2006

Numerical investigations using LES: exploring flow physics and mass exchange processes near groynes

Andrew William McCoy
University of Iowa

NUMERICAL INVESTIGATIONS USING LES: EXPLORING FLOW PHYSICS AND MASS EXCHANGE PROCESSES NEAR GROYNES

by

Andrew William McCoy

An Abstract

Of a thesis submitted in partial fulfillment
of the requirements for the Doctor of
Philosophy degree in Civil and Environmental Engineering
in the Graduate College of
The University of Iowa

December 2006

Thesis Supervisors: Assistant Professor George Constantinescu
Associate Professor Larry J. Weber

ABSTRACT

This dissertation presents a detailed numerical study using fully three-dimensional Large Eddy Simulation (LES) simulations of the flow and mass exchange processes in straight channels containing one or multiple embayments with vertical spanwise walls on one side corresponding to the presence of groynes in river reaches. The main focus is on identifying, understanding and quantifying the role played by the coherent structures and large-scale motions in the momentum and mass exchange processes within the embayments and between the embayments and the main channel. Of the three configurations that are studied, the first two contain only one embayment, and the water depth in the embayment area is equal to the one in the main channel. The two groynes are fully emerged in the first configuration and fully submerged in the second. This allows the study of the intensification of the flow three-dimensionality and acceleration of the mass exchange processes between the embayment and the channel due to the top interface and associated detached shear layer that are present in the submerged case. In both cases, the mass exchange across the embayment-channel interface is highly non-uniform across the depth. The third configuration corresponds to a straight channel with multiple groynes and is identical to one of the cases studied experimentally in a previous scaled model study. The mean water depth in the embayment area is about half that in the main channel; the width and length of the embayments are large compared to the depth; and the width over length ratio is relatively large such that a one gyre circulation pattern is observed inside the embayments. The model is validated with the experimental data available at the free surface. Even for shallow emerged embayments, most of the contaminant leaves the embayment through the top layer of the channel-embayment interface. The present study shows that 3D LES simulations can clarify several important aspects of flow past groyne fields that are very difficult or expensive to quantify using experimental techniques.

Abstract Approved: _____
Thesis Supervisor

_____
Title and Department

_____
Date

_____
Thesis Supervisor

_____
Title and Department

_____
Date

NUMERICAL INVESTIGATIONS USING LES: EXPLORING FLOW PHYSICS AND MASS EXCHANGE PROCESSES NEAR GROYNES

by

Andrew William McCoy

A thesis submitted in partial fulfillment
of the requirements for the Doctor of
Philosophy degree in Civil and Environmental Engineering
in the Graduate College of
The University of Iowa

December 2006

Thesis Supervisors: Assistant Professor George Constantinescu
Associate Professor Larry J. Weber

Graduate College
The University of Iowa
Iowa City, Iowa

CERTIFICATE OF APPROVAL

_____

PH.D. THESIS

_____

This is to certify that the Ph.D. thesis of

Andrew William McCoy

has been approved by the Examining Committee
for the thesis requirement for the Doctor of Philosophy
degree in Civil and Environmental Engineering at the December 2006
graduation.

Thesis Committee: _____
George Constantinescu, Thesis Supervisor

_____
Larry Weber, Thesis Supervisor

_____
Ching-Long Lin

_____
Wim Uijttewaal

_____
Richard Stockstill

_____
Thanos Papanicolaou

ACKNOWLEDGMENTS

I would like to thank my wife Sarah for her continued love, support, understanding and sacrifice. I could not ask for a better companion and someone to walk through life with. I truly thank God for her.

I want to thank my family for all of their support. My parents have always provided an example of how to cherish life, to finish difficult tasks, and pushed me to pursue excellence. I want to honor my brother, Matt, for giving me friendship and an example of living life to the fullest.

I would like to thank Larry Weber for his guidance, friendship, assistance, and support during my time at IIHR – Hydroscience and Engineering. He sets an example of professionalism and passion that we should all strive for. I would like to thank George Constantinescu for his direction, drive, and ambition.

I would like to thank Brian Miller and Mark Wilson for providing computer support, Mike Kundert for the technical drawings, and Dan Daly for the assistance in finding references and editing.

I would like to thank the Harland and Genevieve Emerson Foundation in Adel, Iowa for their financial support. I would like to thank Wim Uijttewaal for making experimental data available and I would like to thank the committee members Larry Weber, George Constantinescu, Thanos Papanicolaou, Ching-Long Lin, Richard Stockstill, and Wim Uijttewaal for their input and direction in this work.

Thank you to my Lord and Savior Jesus Christ for providing the grace and mercy to sustain and direct me through this endeavor.

ABSTRACT

This dissertation presents a detailed numerical study using fully three-dimensional Large Eddy Simulation (LES) simulations of the flow and mass exchange processes in straight channels containing one or multiple embayments with vertical spanwise walls on one side corresponding to the presence of groynes in river reaches. The study is performed at Reynolds numbers similar to the ones at which experimental model studies are generally conducted and in which the incoming flow is fully turbulent. The main focus is on identifying, understanding and quantifying the role played by the coherent structures and large-scale motions in the momentum and mass exchange processes within the embayments and between the embayments and the main channel. The first two of the three configurations that are studied contain only one embayment, and the water depth in the embayment area is equal to the one in the main channel. The two groynes are fully emerged in the first one and fully submerged in the second. This allows the study of the intensification of the flow three-dimensionality and acceleration of the mass exchange processes between the embayment and the channel due to the top interface and associated detached shear layer that are present in the submerged case. In both cases, the mass exchange across the embayment-channel interface is determined to be highly non-uniform over the depth. For both configurations, the spatial and temporal evolution of the horseshoe vortex system at the base of the upstream groyne is investigated, and the regions of high bed shear stress where scour starts developing in the case of a loose channel bed are identified. The third configuration corresponds to a straight channel with multiple groynes and is identical to one of the cases studied experimentally in a previous scaled model study. The mean water depth in the embayment area is about half that in the main channel; the width and length of the embayments are large compared to the depth; and the width over length ratio is relatively large such that a one gyre circulation pattern is observed inside the embayments. The model is validated with the experimental

data available at the free surface. The agreement with the experiment for the mean flow and turbulence statistics is found to be superior to steady RANS predictions. Though the flow inside the embayments is determined to be quasi two-dimensional, the flow in the interface region is highly three-dimensional, and the distribution of the mean transverse velocity in the interface region is strongly non-uniform over the depth. The fact that the transverse velocity is oriented toward the channel over most of the layer close to the free surface in the interface region explains why the mass exchange coefficients determined based on free surface measurements using floating particles consistently overpredict the values determined based on depth-averaged dye concentration measurements. It is also found that even for shallow emerged embayments, most of the contaminant leaves the embayment through the top layer of the channel-embayment interface. The LES simulation shows that most of the mass exchange between the main recirculation eddy inside the embayment and the channel takes place via injection of low-concentration, high-vorticity fluid as a result of the interaction of the mixing layer eddies with the downstream groyne in each embayment and via highly vortical structures that are randomly created and destroyed in the interface region. These structures allow penetration of low-concentration fluid inside the embayment over distances of the order of the main channel depth, followed by small scale mixing as these larger structures are stretched and break into small scale turbulence. For the case in which a contaminant is introduced into one of the upstream embayments of the groyne field, a relatively large amount of contaminant ejected into the mixing layer is re-entrained into the downstream embayments for significant periods of time before being finally ejected into the main channel and leaving the groyne field region. The present study shows that 3D LES simulations can clarify several important aspects of flow past groyne fields that are very difficult or expensive to quantify using experimental techniques.

TABLE OF CONTENTS

LIST OF FIGURES

LIST OF SYMBOLS

Notation

A_f = face area

a_m = mean water depth

a_i = depth at the interface

b = groyne width

B = width of channel

C_o =initial contaminant concentration

C = (grid) filtered non-dimensional scalar (contaminant) concentration

d_{50} = median sediment size

D = depth of main channel (spur height in submerged case)

f = frequency

F1-F6 = fluxes through interfaces between embayment and main channel

h = channel depth

h/D = relative submergence

k = non-dimensional exchange coefficient (D/(UT))

k_e = emerged non-dimensional exchange coefficient (l/Dk)

k_s = submerged non-dimensional exchange coefficient (l/(l+D)k)

l = embayment width, groyne length

M = contaminant mass fraction (or mean concentration) in the embayment

M_e = pollutant mass fraction (or mean concentration) in the embayment

M_r = contaminant mass fraction in main channel

MT1 = temporal variation of the mass in top layer as a flux

MT2 = temporal variation of the mass in middle layer as a flux

MT3 = temporal variation of the mass in bottom layer as a flux

n^+ = distance from wall in wall units ($n^+ = nu_\tau / \nu$)

Re = Reynolds Number (=*UD*/*ν*)

Re = Reynolds Number (=Uh/ν)

S = space between mid-plane of each groyne

Sc = viscous Schmidt number

S = absolute value of strain rate tensor ($|S| = 2\sqrt{S_{ij}S_{ij}}$)

S_{ij} = components of strain rate tensor ($S_{ij} = \frac{1}{2}\left(\frac{\partial u_i}{\partial x_j} + \frac{\partial u_j}{\partial x_i}\right)$)

St = Strouhal Number (St = fU/D)

t = simulation time

τ_0 = non-dimensional bed shear stress ($\rho u_{\tau 0}^2$)value in the incoming channel flow

τ_{cr} = critical bed shear stress

τ =bed shear stress

T = characteristic decay time

U = bulk velocity in main channel

u_r = main channel velocity

u_τ = friction velocity

u_k = filtered (resolved) velocity component in the 'k' direction

w = embayment width

x,*y*,*z* =Cartesian coordinates

y^+ = distance from wall in wall units ($y^+ = yu_\tau / \nu$)

Symbols

ν = molecular viscosity

α_{SGS} = subgrid scale diffusivity

ν_{SGS} = subgrid scale viscosity

Δ = characteristic length of grid cell

$\overline{\Delta}$ = test filtered value of the cell size

ϕ = Passive Scalar

ϕ_{CV} = value of the scalar

ϕ_{face} = value of scalar at face

V_{CV} = volume of cell

υ_n =face-normal velocity

CHAPTER 1

INTRODUCTION

1.1 Background and Motivation

River structures that extend from the bank into the river are known synonymously in the literature as spur dikes, groynes, barbs and wing dams. For the present purposes, all structures of this nature will be referred to as groynes. Pictures of these structures in rivers located in Europe and the U.S.A. are shown in Figures 1.1-Figure 1.3.

The main three-dimensional flow phenomena induced by the presence of groynes include the recirculation eddies and vortex system in the embayment area in between two successive groynes, the mixing layer at the interface between the groyne field and the channel, the recirculation regions upstream of the first groyne and downstream of the last groyne and, in some cases, the formation of a horseshoe vortex (HV) system at the base of the groynes.

Building groynes in natural channels is one of the most effective engineering solutions for:

1. Maintaining channel navigability by increasing the mean velocity in the center of the channel as well as the efficiency of sediment transport;
2. Protecting against flooding by increasing the ability of the river reach to pass a relatively large amount of flood flow;
3. Minimizing bank erosion especially in river reaches with incised banks;
4. Restoring fish habitat to degraded streams (Shields et al., 1995); and
5. Enhancing the diversity of the river ecosystem by providing dead zones in the embayment region between successive groynes that provide favorable conditions for accelerating phytoplankton growth and for the growth of vegetation (Reynolds, 1988, Engelhardt et al., 2004).

A related area of interest is the role played by the groyne field in the exchange of dissolved matter (e.g., suspended particulates, organic matter, contaminants) with the main channel / stream. These exchange processes can substantially modify the transport and dispersion of a pollutant cloud (e.g., due to accidental spills of dissolved matter) past the groyne field region. Accurate prediction of the travel time and maximum concentration and spreading of a pollutant cloud requires accurate quantification of the exchange processes between the main channel and the dead water zones. Quantitative knowledge of these exchange processes allows estimation of global exchange parameters (Wallast et al., 1999, Weitbrecht and Jirka, 2001a) and longitudinal dispersion coefficients that can be used in forecasting models for river pollution (Weitbrecht and Jirka, 2001b, Weitbrecht et al., 2003).

Thus, knowledge of the fundamental flow and mixing phenomena present in the flow around series of groynes is important to maximize their efficiency with respect to one or several of the aforementioned river engineering problems.

Even in seventeenth century Rome, engineers recognized the benefits of installing groynes for additional bank protection and river training. For example, a project performed by Corneiles Meijer addressed severe bank erosion on the Tiber River (Meijer, 1685). Figure 1.4 and Figure 1.5 show the pre and post-project renderings of the river reach in which groyne-like structures were installed. In a more recent example, the U.S. Army Corps of Engineers maintains a 9-ft channel in the Mississippi River for navigational purposes. In pool 16, a 41-km reach of river bordering Iowa and Illinois (see Figure 1.6), over 125 groynes are present.

A problem that commonly arises when groynes are installed in rivers concerns their effects on the surrounding environment during flooding. In many rivers, flooding occurs several times a year, which causes most groynes to become submerged. The momentum convected into the embayment between successive groynes by the flow overtopping the groyne crest can significantly alter the whole circulation pattern inside

and around the embayments. Thus, it is crucial to study the effects of submergence on the momentum and mass transfer processes at groyne fields. The height of the groyne crest is usually selected to closely approximate the yearly averaged water level in the river. As discussed in Uijttewaal (2005), a crest built too high can lead to an unnecessary high flow resistance at flood conditions, while a crest built too low decreases the capacity of the groynes to confine the flow at normal water levels.

Compared to the flow around an emerged groyne field where the momentum and mass exchange take place only laterally at the interface between the embayment and the main channel, the hydrodynamics of the flow around a submerged groyne field is far more complicated as part of the flow convected toward the groyne region overtops the groyne crest and exchanges momentum with the embayments vertically as well as horizontally. The recirculatory motions present in the emerged case near the free surface, in particular the fairly 2D horizontal eddies observed in shallow embayments, are practically absent at high submergence levels. The height of the groyne crest can be considered a design parameter optimized to insure the main functions of a groyne field. Recently, the study of the flow past submerged groynes and the associated mass exchange processes has attracted much more attention from hydraulic engineers and river ecologists.

Another problem that is not well understood for groyne fields is the local scour phenomena that develop over time (especially when flooding occurs) and can endanger the structural stability of the groynes. In most cases, the main mechanism driving the evolution of the local scour is the formation of a HV system at the base of the groynes. Its overall effect increases the mean values of the bed shear stress and of the pressure and velocity fluctuations in the corresponding region near the bed. Figure 1.7 illustrates the HV system and associated flow phenomena around an isolated groyne structure. For isolated groynes, it was shown (Melville, 1997, Chrisohoides et al., 2003) that if the length of the groyne is not very long compared to the local water depth, the eddies that

populate the upstream recirculation region can affect the formation and strength of the HV system. Unfortunately, much less information is known for the case in which a series of groynes is present. Typically, it is expected that the largest scour will occur at the base of the first groyne in the series due to the strong adverse pressure gradients and downflow introduced by the presence of the first groyne in the stream. In particular, a detailed qualitative and / or quantitative description of the mean bed shear stress distribution in the groyne field region, of the unsteady flow phenomena responsible for the amplification of the bed shear stress around the base of the groynes and of the structure of the HV system (if present), is lacking.

There is considerable interest and debate on how to optimize groynes' shape, spacing and orientation to increase their efficiency while avoiding severe local scour phenomena that can endanger the stability of the structure. The flow hydrodynamics in and around the groyne field region and the associated mass exchange processes are yet to be fully comprehended. Understanding the three-dimensional (3D) flow dynamics and mass exchange processes will allow for a better groyne design to fulfill one or several of the above mentioned design objectives over a wider range of flow conditions in the river.

1.2 Research Needs and Objectives

Though recent experimental investigations (e.g., Uijttewaal et al., 2001, Kurtze et al, 2002, Uijttewaal, 2005) have offered a much better understanding of the effects of groynes in a channel (e.g., by elucidating the flow patterns at the free surface including the interaction between the mixing layer eddies and the embayment flow, estimating the global mass exchange rates between the embayments and the channel), several qualitative (e.g., to what extent the free surface flow is representative of the large scale motions within the embayments and the mixing layer for shallow and deep embayments) and quantitative aspects of the flow in a channel with groynes remain unclear. A three-dimensional characterization of the flow and mass exchange processes and their non-

uniformity over the depth is still lacking. In the case of the mass exchange, this is mainly because the experimental methods measuring the mean (depth-averaged) dye concentration fields do not provide any quantitative information on the variation of the dye concentration over the embayment depth and, in many cases, are limited to emerged groynes. Related to the flow patterns, the details of the flow inside the embayment affect the deposition of sediment and determine local residence times of algae and other organic matter that are important for the biodiversity of the river. As previously stated, there is practically no quantitative information available from these experimental studies on the bed shear stress distribution that determines the formation and evolution of scour phenomena. Knowledge of the distribution of the transverse mean velocity component at the interface between the embayments and the main channel is of paramount importance for understanding how a contaminant introduced into the embayment will be transported into the channel.

LES has the advantage that it can capture the dynamics of the energetic coherent structures that are thought to control the momentum and mass exchange at the channel-embayment interface and allows an investigation of the 3D flow features at no additional cost, provided that a sufficiently fine mesh is used and the numerical dissipation in the code is kept at a minimum. The ability to capture the large-scale turbulence content of the mixing layer, in particular the turbulence originating at the head of the groynes, is required to accurately simulate the flow and contaminant transport processes through a groyne field.

LES provides the full 3D flow fields, turbulent fluctuations and the bed shear stress distribution that determine the evolution of the scour around the groynes. This is an important advantage over previous experimental studies that primarily focused on the flow dynamics and turbulence characteristics at the free surface and then assumed the free-surface flow to be representative of the flow inside the embayment (2D effects are predominant). This assumption obviously fails for submerged groynes but, as will be

shown in the following chapters, even groyne fields with shallow embayments, where 2D effects are thought to be dominant, contain regions where 3D effects cannot be neglected and where the flow is strongly non-uniform over its depth. In the long term, a better understanding of the flow hydrodynamics and mass exchange processes in a groyne field using both experimental and numerical investigations will facilitate the optimization of groyne design.

The most important design parameters in optimizing the groyne's shape are the groyne length, spacing, the ratio between length and spacing (l/S), orientation to the flow, relative submergence and cross sectional shape. The spacing between groynes is the key parameter when designing bank protection. If the spacing is too small, the project will become too expensive. In other words, the bank will be over-protected. However, if the spacing is too large, bank erosion will still occur because flow separated at the groyne tip will reattach along the river bank. Groyne spacing also affects the character of the mass exchange process and residence times inside the area between two groynes. The present study will consider embayments with a ratio between length and spacing close to 0.5 for which the mean flow inside the embayment (emerged groynes) changes from a one gyre pattern (>0.5) to a two gyre pattern (<0.5).

Though the flow in a river with groynes is affected by many geometrical parameters the present study will exclusively focus on two generic configurations related to flow over river groynes. The primary points of interest will be the processes and phenomena that are thought to be relevant to most groyne fields present in channels and natural rivers. Related to the mass transfer processes, the present work considers only dissolved phase contaminants with no entrainment at the bed. Thus, the findings related to the dispersion of these contaminants do not apply to suspended sediments as the settling velocity term is absent in the advection-diffusion equation for the contaminant concentration and no entrainment or deposition can take place at the channel bottom.

In the first configuration, only one embayment is considered, in which the water depth in the embayment region is equal to that in the channel and the embayment depth, length and width are comparable. The groynes are either fully emerged (Figure 1.8) or fully submerged (Figure 1.9) and non-permeable. The main objectives are to:

1. Visualize and understand the interaction among the main large-scale flow structures present in the region around the groynes and their role in the mass exchange between channel and embayment;
2. Study the structure of the HV system at the base of the upstream groyne, its effect on the bed shear stress distribution and eventually on the bed morphology changes;
3. Quantify the exchange of dissolved matter between the embayment and the main channel by studying the ejection of a passive contaminant from the embayment volume;
4. Understand how mixing takes place over the embayment depth;
5. Estimate based on LES results the mass exchange coefficients used in simple mass exchange models based on dead-zone theory; and
6. Understand the differences between the emerged and submerged case related to how the mass exchange transpires between the embayment and the surrounding flow, determine the predominant nature of the interactions between the coherent structures in the detached shear layers and the downstream groyne, and comprehend the differences in the bed-shear stress distributions, etc.
7. Create a comprehensive data base containing the 3D and 2D (depth-averaged) statistics, the 3D data sets used to specify inflow conditions in LES and their statistics needed to specify equivalent inflow boundary conditions in RANS models (e.g., distributions of the TKE, turbulent dissipation, and other quantities for which a transport equation is solved in RANS), and representative

instantaneous flow and concentration fields for the two test cases. Besides the mean velocity components, the data base will include higher order statistics (e.g., Reynolds stresses, pressure fluctuations, etc.) that are difficult to measure experimentally for use in future numerical model validation studies. The information contained in the instantaneous flow fields and the statistics would be available for use in future investigations of the flow physics beyond the scope of the present work. The flow set up and the corresponding archived data sets can constitute a very relevant test case for the assessment of the predictive capabilities of 3D models using unsteady or steady RANS approaches, hybrid RANS-LES approaches, or for 2D depth-averaged models using LES or RANS closures use to calculate flow around hydraulic structures, in particular flow around emerged and submerged groyne fields.

In the second generic configuration, a groyne field with six embayments is considered (see Figure 1.10). It corresponds to simplified, but still realistic, groyne field configuration typically encountered in rivers. The water depth in the embayment region is equal to half the channel depth; the embayment bottom is tilted toward the channel side; and the embayment length and width are much larger than the mean embayment depth. The groynes are fully emerged, non-permeable and do not penetrate into the main channel. The main objectives are to:

1. Validate the numerical model using data from the scaled model study (Uijttewaal et al., 2001);
2. Obtain a detailed characterization of the mean flow and *TKE* distribution over the flow depth and of the quasi-2D motions inside the embayments;
3. Understand the role of 3D effects especially near the embayment-channel interface;

4. Describe the main mechanisms of momentum and mass exchange between the quasi-2D flow in the center of the embayment and the channel, in particular the role played by the large-scale coherent structures in the interface region;
5. Identify the regions where erosion is likely to start developing inside the embayment, as local scour around the groyne tip can endanger its stability;
6. Study qualitatively and quantitatively (e.g., by estimating global exchange coefficients used in dead zone theory models) the removal of contaminant introduced initially into the various embayments of the groyne field, its subsequent dispersion into the main channel and its interaction with the downstream embayments; and
7. Evaluate the degree of non-uniformity over the depth of the mass exchange process at the interface between the embayment and the channel and investigate the physics of the large-scale contaminant transport inside the embayment volume and in the interface region.
8. Develop a data base similar to the one for the first generic configuration that can be used along with the experimental measured data for validation of 3D numerical models using simpler turbulence closures or of 2D depth-averaged models using LES or RANS closures.

1.3 Thesis Overview

The outline of the thesis is as follows. Chapter 2 provides a review of previous field, laboratory and numerical studies of flow around groynes and associated mass exchange processes. Chapter 3 describes the numerical algorithm, including the subgrid scale model, used to conduct the present numerical simulations and discusses previous validation of the LES code. Chapter 4 discusses results of the simulation in the one-embayment geometry with emerged groynes, while Chapter 5 presents a similar investigation for the submerged case including a discussion of the changes in the

different flow features and the characteristics of the mass exchange processes as the groynes become submerged. Chapter 6 presents the results for the simulation of flow past a groyne field containing six embayments including validation with experimental data of Uijttewaal et al. (2001). The mass exchange processes are studied by considering the removal and subsequent dispersion into the channel of a passive contaminant introduced in embayments 2 and 5 of the groyne field. Chapter 7 summarizes the main findings of the study and offers recommendations for future work.

Figure 1.1. Spur-dike on Odra River (IIHR)

Figure 1. 2. Wing dams on the Mississippi (GLRC)

Figure 1.3. Groyne on Elbe River (BTU Cottbus)

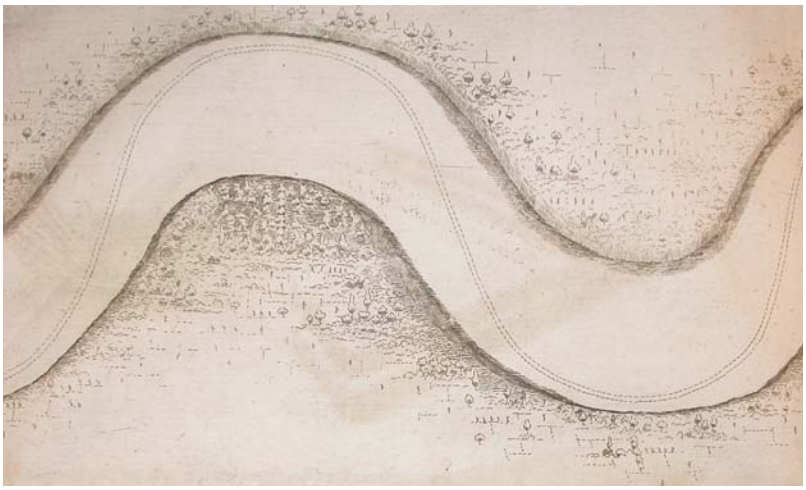

Figure 1.4. A reach of the Tiber River before groyne-like structures were introduced

Source: Meijer, 1685

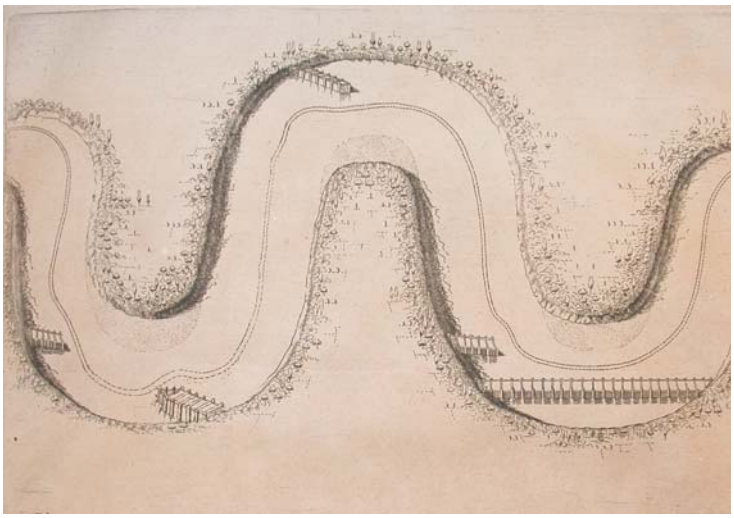

Figure 1.5. A reach of the Tiber River in which groyne-like structures were introduced to protect the river banks

Source: Meijer, 1685

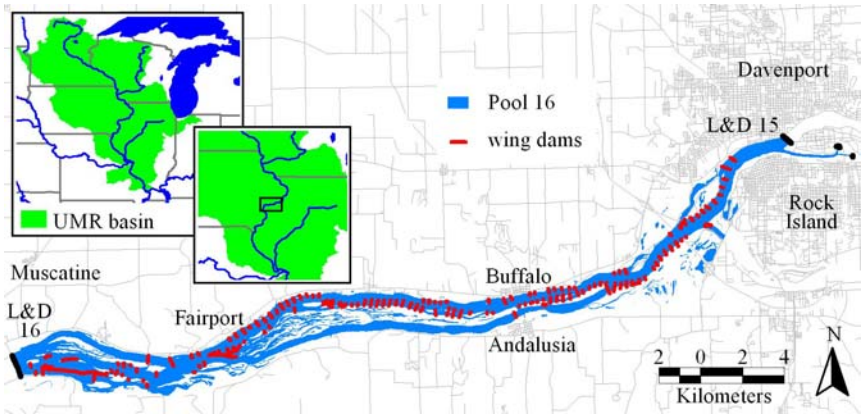

Figure 1.6. Wing dams in pool-16 of Mississippi River

Source: Young, 2006

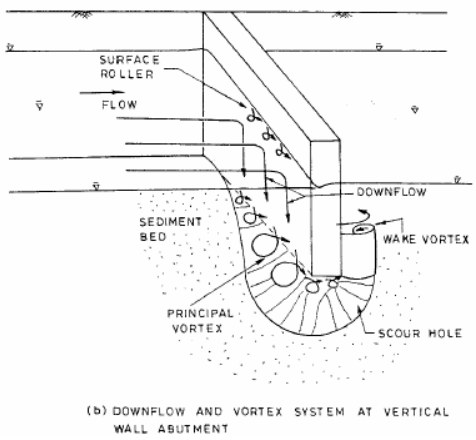

Figure 1.7. Horseshoe vortex system and scour related phenomena in the flow around an isolated groyne

---

Source: Kwan, 1984

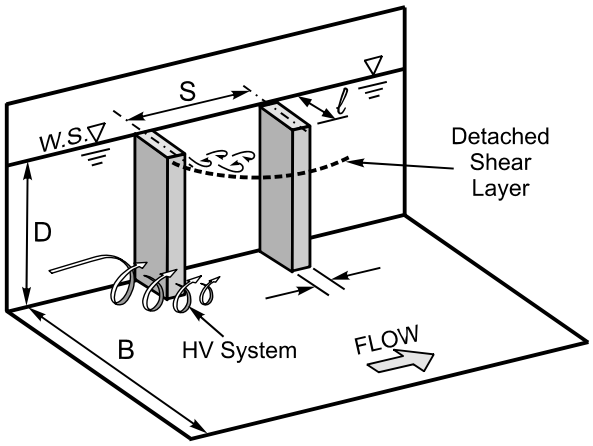

Figure 1.8. Channel flow with two vertical emerged groynes mounted on one side of the channel

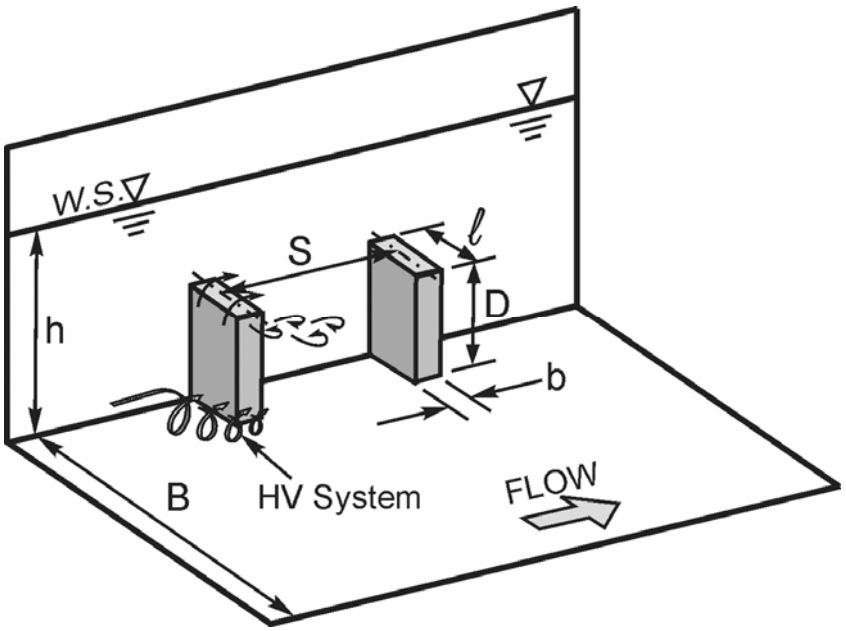

Figure 1.9. Channel flow with two vertical submerged groynes mounted on one side of the channel

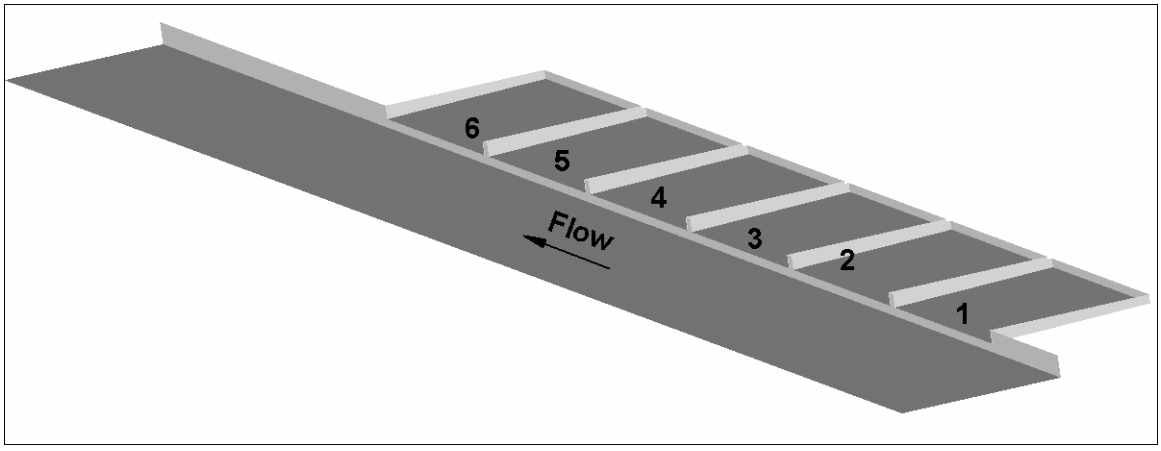

Figure 1.10. Channel flow with multiple emerged groynes mounted on one side of the channel

CHAPTER 2

LITERATURE REVIEW

2.1 Hydrodynamics of the Flow around Groynes

2.1.1 Experimental Investigations and Field Studies

There are numerous experimental studies of the flow around single and multiple groynes in river channels. In some of these studies, a systematic characterization of the effects of the groyne geometry and / or groyne submergence on the flow was undertaken. The relative submergence is the ratio of the total channel depth, h, to the groyne height, D, and is the main parameter distinguishing among cases of varying submergence. It is important to note that in most of the scaled laboratory experiments, the channel Reynolds number was in the range of 5,000 to 50,000 and the incoming flow was fully turbulent. Most laboratory experiments have been completed with a smooth channel bed.

The presence of groynes in a series causes the area between two groynes (embayment) to become a dead zone where the mean velocities are significantly lower than in the main channel, which leads to an increase in mixing and a decrease in transport velocity. One of the main goals of most recent investigations of the flow past multiple groynes was to describe the interaction via the mixing layer at the embayment-channel interface.

Several investigators used Particle Image Velocimetry (PIV) techniques to investigate the hydrodynamics of flow around groynes. For instance, Tominaga et al. (2001) studied how submergence affects the velocity fields in both horizontal and vertical planes in a straight regular channel with two lateral vertical groynes. The channel Reynolds number in the investigation was close to 14,000. Six levels of relative submergence (h/D) were examined 4, 2.67, 2, 1.6, 1.33, and 1.0. The authors also reported on the mass exchange processes based on time averaged vertical and transverse

velocities at the lateral and roof interfaces between the embayment volume and the main channel. The presence of strong vortices shed from the first groyne parallel to the lateral and roof interfaces was observed. These vortices correspond to the eddies that populate the horizontal and vertical detached shear layers (DSLs). The deflection of the horizontal DSL became larger with the increase of the relative height of the groyne. Compared to the emerged case (h/D=1.0), the momentum and mass exchange were observed to be larger in the submerged cases. For relative submergence depths less than two, a large increase of the inflow velocities in the region upstream of the second groyne and of the outflow velocities in the region downstream of the first groyne were observed at the two interfaces. Consistent with other experimental investigations, the vortical structures were strengthened in the submerged cases.

Muto et al. (2002) used large-scale PIV to investigate the instantaneous and mean free surface flow in the vicinity of a groyne field situated in a complex river bathymetry. A scaled model study of the flow past a groyne field of similar geometry was also conducted. The effects of the aspect ratio and water depth on the velocity distributions were analyzed and turbulence characteristics at the embayment interface were clarified. The embayment aspect ratio (width over length) was 0.33 in both the river and the laboratory. The channel Reynolds number for the natural river bathymetry was near 1,000,000, while it was close to 4,000 in the experiment. The PIV data collected in the field study showed the flow was highly unsteady inside the recirculation zone. For example, at a certain time a large recirculation region was observed to develop within the embayment and a small counter rotating recirculation zone was present in the downstream corner. A few minutes later, the size of the large recirculation diminished significantly. The bulging into the main stream no longer existed, but, instead, the main flow entered into the embayment. It was deduced that a significant mass exchange between the channel and the embayment can occur through this process. The laboratory experiments did not exhibit these same unsteady characteristics. The flow patterns were

more or less steady with time in consecutive embayments. The authors concluded that complex bathymetry can initiate unsteadiness along the embayment interface.

Using PIV at two conditions, Nezu et al. (2002) investigated the velocity and turbulence fields in a channel with a series of groynes. In the first instance, the bed was flat (start of the scouring process), and in the second, the bed shape corresponded to equilibrium scour conditions. The aspect ratio of the embayment was 0.5 and two channel Reynolds numbers (31,000 and 62,000) were considered. The experiment was conducted at both flow conditions for both bed conditions. The TKE and time-averaged velocity vectors were compared for both cases. The authors concluded that the vortices induced by the shear instability were diminished in the equilibrium bed scour configuration, especially in the region where the bed was raised.

Sukhodolov et al. (2004) conducted a field study investigation of the 3D turbulence structure, distribution of suspended particulate matter, riverbed scouring and distribution of deposited fine sediments in a groyne field on the Elbe River in Germany. Additionally, the effects of barge traffic on flow structure and sediment resuspension were studied. The groynes were 30-40m long and spaced 100-150m apart. An acoustic Doppler velocimeter (ADV) was used to measure the three velocity components at several positions within the groyne field. The authors found that the horizontal velocity distributions in the groyne field can be well approximated by a power law distribution over the depth, but the values are larger near the free surface due to additional turbulence from the wind. It was shown that barge traffic can increase the concentration of suspended matter by up to 17 percent. A related study by Sukhodolov et al. (2002) examined the spatial distribution of the suspended sediment within the embayment for different groyne aspect ratios.

Elawady et al. (2000) investigated the effects of submergence on the water surface and velocity profiles in the vicinity of a single spur-dike oriented at different angles to the main direction of flow.

The effect of water surface oscillations in a channel with two embayments was studied experimentally by Ohmoto et al. (2003). PIV was used to quantify the effects of water surface oscillations on the mean flow and turbulence quantities. The authors found that water surface oscillations peak when the distance between the groynes is twice as long as the length of the groynes. For this configuration, the lateral velocity fluctuations are also larger and, thus, one expects the mass transfer to intensify.

Uijttewall (2005) studied experimentally the effects of submergence, groyne geometry and groyne permeability on the mean flow field, recirculation patterns and the intensity of vortex shedding in the mixing layers for a multiple-embayment configuration representative of groyne fields encountered in large European rivers. The free-surface velocities were measured in a 1:40 scaled model using Particle Tracking Velocimetry (PTV). Two levels of relative submergence were considered (1.16 and 1.28) and several groyne designs were examined. Overall, the effect of groyne submergence was to increase the intensity of the 3D effects and thus to make the flow more complex. In some of the test cases considered (relatively low submergence depth), it was observed that the momentum that enters the groyne field via the vertical mixing layer can interrupt the recirculating pattern within the embayment typically observed in the emerged case. The flow inside the groyne field then becomes relatively parallel to the flow in the main channel and after a while shifts back to a recirculating pattern. Compared to the emerged case, substantially higher velocities were present in the upper layers of the groyne field. Strong eddies were convected into the vertical mixing layer originating at the groyne crest. The author concluded that for accurate simulation of the flow past submerged groynes, a fully 3D LES model is needed to represent the complex 3D behavior of the large scale flow structures.

In a related study of a similar configuration, Yossef and Uijttewall (2003) collected velocity data using electromagnetic flow meters and PTV. The flow pattern in the relatively low submergence case was found to alternate between the overtopping flow

and the dominant lateral flow in the embayment region. The time series showed that large-scale velocity fluctuations were present in all the cases, but the turbulence characteristics in the submerged case differed considerably from those in the emerged case. The width of the horizontal mixing layer was determined to be larger in the submerged case.

ADV velocity measurements were performed by Fox et al. (2005a) in an experiment featuring a submerged barb (a groyne-like structure composed of large angular riprap protruding from the bank into the channel with the purpose of repelling currents away from the bank). The velocity time series were utilized to study the spatial and temporal scales of the flow eddies at multiple locations of interest near the barb. A methodology was proposed to enable identification of both small and large scale eddies and, more importantly, to provide a detailed description of the turbulence in the vicinity of the barb. A related experiment (Fox et al., 2005b) investigated fluid-sediment dynamics near the barb with fixed and mobile bed conditions.

In the case of experiments conducted with a loose bed, the main purpose of most investigations of the flow past groyne-like obstacles was to measure the evolution of the scour hole and then to develop equations for predicting the maximum scour depth and in some cases the scour hole geometry. For example, empirical equations to predict maximum scour depth have been developed for abutments and groynes in wide channels for both clear-water and live-bed scour conditions by Lim (1997) and Lim and Cheng (1998), while Coleman et al. (2003) proposed an empirical expression to predict the time to maximum scour depth. The effects of submergence and opening ratio (groyne length to channel width) on the local scour development and on predicting the maximum scour depth were investigated by Elwady et al. (2001). Rajaratnam et al. (1983) showed that the increased channel constriction due to the presence of a groyne-like obstacle can amplify the bed shear stress at the groyne head between 3 to 5 times. Kothyari et al. (2001) studied the evolution of scour in the rapidly changing flow environment during

flooding events. Kwan and Melville (1994) tried to describe the effect of the HV system and of the downflow on the local scouring process based on the time averaged velocity fields at equilibrium conditions. A good review of this kind of study for single groyne-like obstacles (e.g., bridge abutments) is given in Melville (1997). Relatively few investigations have been performed to understand the nature and the role of the large scale coherent structures in the scouring process. Chrisohoides and Sotiropoulos (2003) performed a detailed visualization study of the flow in the recirculation region upstream of a single groyne in a rectangular channel. Their experiments found that large-scale eddies in this region undergo complex interactions among themselves and with the channel walls.

Currently, there is considerable interest in restoring fish habitat in incised channels by installing groynes. The environmental benefits of installing groynes as a means to restore complex bathymetry channels include creating large stable pools and scour holes for increasing aquatic habitat (Shields et al. 1995). Empirical formulas that predict the total scour volume based on the effective groyne width and submergence were proposed by Kuhnle et al. (1997, 1999 and 2002).

A groyne field along a river reach in the Elbe River in Germany was selected by Engelhardt et al. (2004) to measure phytoplankton abundance, three-dimensional velocity vectors and channel bathymetry. Specifically, the effects of the groyne field layout and flow structure at high and low flow conditions on the spatial distributions of phytoplankton (e.g., see Figure 2.1) were studied. The structure of the turbulent flow was investigated by calculating the turbulence spectra for the velocity components. Figure 2.2 shows the turbulence spectra for the three velocity components at a point inside the shallow embayment. The velocity spectrum for the transverse component in Figure 2.2b displays a -5/3 decay range indicative of the inertial subrange associated with the energy cascade from larger to smaller scales. However, a -3 decay range associated with quasi-

two dimensional shallow flows is also present. This range was absent in velocity spectra measured outside the shallow embayment region.

2.1.2 Numerical Investigations

With the increase in computational power and development of more accurate numerical methods, the potential for prediction of flow past groynes has increased substantially in recent years. However, the inherent three-dimensionality and complexity of the flow (e.g., the presence of massive separation, adverse pressure gradients and unsteady vortex shedding) still present major challenges for numerical algorithms and turbulence models. Most of the previous numerical investigations of the flow past single and multiple groynes utilized steady RANS models with wall functions that cannot accurately capture some of the above mentioned flow phenomena and focused exclusively on describing the flow hydrodynamics without explicitly considering the mass exchange processes.

Liu et al. (1994) used a depth-averaged viscous solver with the k-ε model to simulate the flow around a single groyne for different groyne orientation angles. Two-dimensional depth-averaged models with mixing length or k-ε turbulence models were used by Biglari and Sturm (1998) and Kimura et al. (2001, 2003) to calculate flow in channels containing two spur dikes.

Ouillon and Dartus (1997) used a steady 3D RANS solver with the k-ε model to study the flow past a groyne including the free surface deformations. Xu et al. (2002) studied the effect of the RANS turbulence model (mixing length, linear or non-linear k-ε model) on the prediction of flow past a submerged dike in a curved channel. A modified version of the non-linear k-ε model was shown to give the best agreement with the experimental data. Other numerical RANS model studies of flow in channels containing groynes were conducted by Kawahara et al. (1998), Kimura et al. (2003) and Peng et al. (1999a). A 3D steady RANS solver was utilized by Scott et al. (2001) to predict the flow

in a 15-km natural river channel containing groynes. Away from the groynes and the channel bed, the calculated velocities were found to be in good agreement with the field measurements. However, the numerical predictions were relatively poor near the bed and region around the groynes.

Marson et al. (2003) simulated the flow around a groyne at equilibrium bed conditions using FLUENT. The steady RANS equations were closed with the standard k-ε turbulence model. The channel Reynolds number was 38,000. Velocity vectors compared favorably with the measured data at several vertical planes extending out from the groyne. Near the bottom, the agreement between the calculated velocity vectors and the corresponding measurements was relatively poor. Miller et al. (2003) conducted a similar numerical investigation of the flow past a groyne with vertical walls and past a groyne with sloping sides. The channel Reynolds number was 60,000. The steady RANS model was closed using the k-ω model. The simulations of Mason et al. (2003) and Miller et al. (2003) captured the formation of a HV system at the base of the groyne. However, the accuracy of these predictions was not quantitatively assessed.

The flow past single and multiple submerged groynes was also studied by means of 3D simulations using several RANS models by Peng et al. (1997, 1999a). As expected, the flow was shown to be highly three-dimensional in the groyne region. An upward motion was observed around the crest of the first groyne associated with the overflow. In the case of an isolated submerged groyne, the size of the downstream recirculation region was found to decrease in the vertical direction with the distance from the bed. Their numerical investigations found that although the simulations, especially the one using a non-linear model, were able to capture some of the main flow features observed in experiments, all the models underpredicted the velocity in the tip region of the groyne and near the opposite sidewall of the groyne field.

The next class of methods corresponds to time-accurate RANS models. These methods should capture at least some of the large-scale unsteadiness of the flow and are

expected to provide more accurate results compared to steady 3D RANS models. Chrisohoides et al. (2003) conducted an integrated experimental and computational investigation of the flow past an isolated emerged groyne present in a straight channel with a flat bed. The time-accurate numerical model was based on an unsteady RANS (URANS) solver with the k-ω turbulence model. The channel Reynolds number was 100,000. Instantaneous flow fields including mean velocity and vorticity contours, free surface and limiting streamlines, and 3D particle paths were used to analyze the complex, three-dimensional character of the flow in the vicinity of the isolated groyne. They found that the vortices present in the upstream recirculation region were highly unsteady and were connected to the HV system at the base of the groyne. The numerical simulations also captured the large scale unsteady interactions in the massively separated wake behind the groyne.

Scour and deposition that occur in the vicinity of groynes can cause navigation and structural stability problems. Peng et al. (1999b) performed RANS simulations of the flow around single and multiple groynes with loose bed. The sediment transport model accounted for gravitational bed slope effects and used the Meyer-Peter-Muller formula to calculate the bed load transport rate. The bed elevation was calculated from the continuity equation for the 2D sediment transport. The local scour and deposition patterns around submerged spur dikes were calculated and compared with experimental data. The location and magnitude of the maximum scour depth near the groyne nose were reasonably captured, although the pattern of local scour and deposition showed some differences with the experiment.

Eddy resolving techniques using LES models represent a better way to numerically simulate these flows as they can accurately capture and predict massively separated flows if a sufficiently fine mesh is used and the numerical dissipation is much smaller than the one provided by the subgrid scale model. As the computational price of full 3D LES simulations is very high, earlier attempts have used 2D depth averaged

models coupled with a Smagorinsky based LES model. Such a model (Delft3D-FLOW) was applied to predict the flow past an array of groynes with a fixed bed by Uijttewall and van Schijndel (2004). Both the emerged and submerged cases were considered. To model the effect of the submergence on the groynes, an additional local roughness was added to the model. The flow separation and the areas of high turbulence intensity were better reproduced by HLES compared to results obtained using the k-ε model. The model predictions for the submerged case were poorer than those obtained for the emerged case. It was concluded that the high three-dimensionality of the flow in the submerged case limited the applicability of a 2D depth-averaged model.

Eddy resolving techniques (a 2D horizontal LES model) coupled with a depth averaged morphological model were used by Yossef and Klaassen (2002) to predict flow and bathymetry evolution (in particular the scouring around the base of the groynes) in a channel with groynes disposed on both sides of the channel. The results of the numerical simulation were compared qualitatively with field measurements in the Rhine River.

Hinterberger (2004) used full 3D LES to predict the flow in an infinite array of groynes situated in a straight channel with lateral walls. A finite volume LES code using generalized curvilinear coordinates was used. In the simulations, the groynes were fully emerged and the water depth in the embayment area was equal to the one in the main channel. The channel Reynolds number was around 7,300. At this Reynolds number, the flow is turbulent inside the channel and embayment. The classical constant Smagorinsky subgrid scale model was used. A detailed investigation of the instantaneous and mean flow fields was provided. The mass exchange processes were studied by considering the ejection of a passive scalar introduced instantaneously into one of the embayments. More details are given in section 2.2.2.

2.2 Mass Exchange Processes in a Channel with Multiple Groynes

Several experimental and numerical investigations studied the mass exchange processes between the embayment regions and the main channel generally using a passive contaminant / scalar (e.g., colored dye in experiments) introduced instantaneously inside one of the embayments. The decay in time of the mass of contaminant within the embayment was measured, and global exchange coefficients based on dead-zone theory models were estimated.

The Reynolds numbers in practically all the scaled model laboratory studies were in the range of $5{,}000<Re<50{,}000$. Though this range of Reynolds numbers is a couple of orders of magnitude lower than the range characterizing flow past groyne fields in a real river environment, these studies are thought to be relevant to the understanding of the flow in rivers or channels with groyne fields primarily because the flow upstream of the embayment area was turbulent in all of these experiments. It is expected that the flow physics would not change considerably with the Reynolds number provided the incoming flow and the attached boundary layers are turbulent. The situation is similar for numerical investigations conducted in the range of Reynolds numbers encountered in scaled model studies.

2.2.1 Experimental Investigations

Flow and exchange of dissolved matter between a main channel and an array of shallower emerged groyne fields were investigated in laboratory models by Uijttewaal et al. (2001) and Wallast et al. (1999) for different aspect ratios and groyne shapes. Figure 2.3 shows a sketch of the groyne field layout considered in their experiments. The water depth in the embayment region was lower than the channel depth. The channel Reynolds number varied from 18,000 to 35,000. Instantaneous and mean velocity fields at the free surface were determined using a Particle Tracking Velocimetry (PTV) method.

In some of the cases studied, the PIV visualizations of the flow at the free surface captured the formation of large coherent structures in the lateral mixing layer. These structures can enter the embayment and merge with the primary recirculation zone. This process is illustrated in Figure 2.4 and is considered one of the main mechanisms responsible for the mixing between the embayment and the channel in the case in which more than one recirculation eddy is present on average inside the embayment. Floats were used to measure the mass exchange at the surface while colored dye provided a depth-integrated characterization of the exchange process. For most experiments, it was observed that the exchange velocity at the surface was significantly higher than the exchange velocity integrated through the whole depth. Consequently, the authors concluded that especially for shallow embayments, the surface float method is not sufficiently accurate because of strong secondary motions and three dimensional flow structures. This led to the calculation of the mass decay inside the embayment using depth integrated dye concentration fields obtained from pixel gray values (see Figure 2.5) rather than using information from surface floats. Exchange coefficients were calculated for each case.

It was found that the embayment aspect ratio plays a key role in determining the overall strength of the mass exchange process. Consistent with the previous discussion, for embayments with an aspect ratio (width over length) close to 0.3, large eddies shed from the upstream groyne tip were able to penetrate deeply into the primary recirculation zone. For embayments with an aspect ratio equal to 0.7, this phenomenon was absent and the mass exchange occurred at a significantly slower rate. The results of the experiments showed that decreasing the water depth in the channel leads to a more pronounced influence of bottom friction which slows down the mass exchange process near the bottom. Increasing the main stream velocity was found to accelerate the decay of the mean dye concentration inside the embayment, as shown in Figure 2.6. The effect of the embayment rank for a groyne field containing embayments with an aspect ratio of 0.7

was found to have a relatively minor effect on the overall decay in time of the mean dye concentration inside the embayment (see Figure 2.7).

The same research group investigated the spectral content and the dominant frequencies of the velocity oscillations in the mixing layer and the embayment (Yossef and Uijttewall, 2003). Velocity components in the horizontal plane were measured at various points in these regions.

Similar experiments were conducted by Weitbrecht et al. (2003) and Kurtze et al. (2002). They used a Lagrangian Particle Tracking Method (Weitbrecht et al., 2002) coupled with PIV for velocity and turbulence measurements at the water surface. The method allowed the estimation of transport characteristics (longitudinal dispersion coefficients, skewness coefficient of the pollutant cloud, etc.) in the far field of a pollutant spill in a river with emerged groyne fields (Weitbrecht et al., 2003). A grayscale analysis method similar to Uijttewaal et al. (2001) that can be applied to submerged and emerged groynes was used to calculate the time-dependent depth-averaged dye concentrations needed to measure the contaminant mass decay in time and to estimate global exchange coefficients. Additionally, the PIV-measured transverse velocities along the channel-embayment interface were used to calculate a mean exchange velocity that was thought to be representative of the depth-averaged transverse velocity at the interface. This method, though less accurate in predicting the global exchange coefficient in dead-zone models, does not necessitate the use of dye measurements. The PIV based method was found to be reliable in most cases. Both methods were applied to study the flow in a channel with a series of groynes at a channel Reynolds number around 7,500, and it was found that the aspect ratio has a profound effect on the formation of circulation cells within the embayment and thus on the strength of the mass exchange process. The same group studied the effect of the aspect ratio and inclination of groynes on the dispersion of a pollutant cloud (Weitbrecht and Jirka,

2001b, Kurtze et al., 2002). As expected, the strongest mass exchange was found to occur in the case in which the groynes were inclined against the flow.

2.2.2 Numerical Investigations

The LES simulations of the flow around an infinite array of groynes in a straight channel performed by Hinterberger (2004) included the prediction of the mass exchange processes. A fully three-dimensional well-resolved LES simulation was performed along with several 2D depth-averaged LES simulations. The typical ratio of the grid sizes between the 3D and 2D simulations was around 15. The predicted values of the mass exchange coefficient were found to be in good agreement with the values estimated from experiments. This was especially true for the 3D LES simulation.

Engelhardt et al. (2004) performed a field study of the flow structure and characteristics of mixing in a river reach with irregular groynes and complex bathymetry. Mass decay (Figure 2.8) and particle residence times (Figure 2.9) were estimated using three-component acoustic Doppler velocity meter (ADV) measurements inside the embayment coupled with a numerical random-walk model to mimic the behavior of a tracer particle within a fluid. The numerical tracer was dispersed uniformly over the embayment volume and the trajectories of the particles were recorded. Based on this information, the time variation of the mean concentration of the particles within the embayment volume was estimated. For a groyne field with one dominant gyre (aspect ratio greater than 0.5 corresponding to high flow conditions), two regimes of exponential decay were present (Figure 2.8a). The authors associated the first regime with the mass exchange through the mixing layer and the second with the recirculating flow inside the embayment. In a groyne field with two gyres (aspect ratio lower than 0.5 corresponding to low flow conditions), three regimes of exponential decay were present (Figure 2.8b).

2.3 The Role of Groynes in Ecohydraulics

Riparian zones associated with alluvial stream systems are the most biologically productive zones in rivers. When riparian conditions become impaired, such as when a channel becomes highly incised or laterally unstable, rehabilitation is necessary because channel incision severs a stream from its traditional land water interface, the floodplain, depriving the stream of carbon and nutrients. Incised channels usually contain extremely degraded aquatic habitat characterized by shallow sandy runs, little or no woody debris, and sparse riparian vegetation. Restoration through land use management is preferable for rehabilitation, but that is not always possible. In these situations, structural solutions are required. Installing river groynes is one of the most popular solutions to address these problems. In many cases, the goal of the rehabilitation process is to provide conditions necessary for natural growth of the vegetation in the river (Van Haveren et al., 1986).

Biological species diversity correlates with diversity of habitat parameters. The ecological condition of many trained rivers is poor. Aquatic organisms respond to physical changes in stream habitats such as changes in spatial and temporal distribution of depth, velocity, bed material, and cover. For example, fish habitat may be enhanced by introducing in-stream structures such as groynes or spur dikes. Especially at low flow conditions, the presence of groynes can provide a wide spectrum of flow conditions and variable channel bathymetry due to scour (Skelnar et al. 2002).

Shields et al. (1994, 1995) showed that the complex bathymetry added by scour and deposition regions adjacent to the dikes provided for fish habitat in the form of hiding cover and shelter from high velocities. The authors describe results of a restoration project in which extensions were added to existing transverse dikes to improve aquatic habitats by accelerating natural processes, promoting the recovery of channel equilibrium, channel vegetation, and stream-flood plain interaction. The channel size and geometry remained fairly stable, but the pool habitat increased five fold due to the additional scour and deposition. The biological response included an order of

magnitude increase in fish biomass, doubling the number of fish species found in the reach, and an increase in average fish length. Design criteria for in-stream bed stabilization structures (e.g., groynes) that also provide an aquatic environment benefit were provided. In a related study, Shields and Cooper (1997) showed that stone spurs (transverse groynes) provide more scour holes and a superior aquatic habitat compared to the more inexpensive longitudinal stone toe structures.

Tamai et al. (1996) performed field observations of sediment scour and deposition around spur dikes coupled with field measurements of flow patterns at low discharge and flood discharge and fish sampling. The goal was to identify the role spur dikes play in fish habitat improvement and to maximize their design with respect to this criterion.

Submerged groynes can also be used to protect freshwater mussels. Rivers in North America have historically supported a large population of freshwater mussels. However, over the last couple of decades numbers have been dwindling and many species have become extinct or are now listed as endangered. There is recent evidence that mussel beds (defined as the near-bed region where the mussel density is 10 to 100 times larger than the density outside the bed) tend to be located in areas that have low shear stresses and stable sediments during flooding events. Submerged spur dikes tend to provide this type of environment. Understanding how different flow regimes, turbulent flow structures at micro and macro scales, and the presence or absence of spur-dikes affect the mussel populations is a critical part of explaining the disappearance of the mussels and can guide resource management decisions in the future (Strayer et al. 2004).

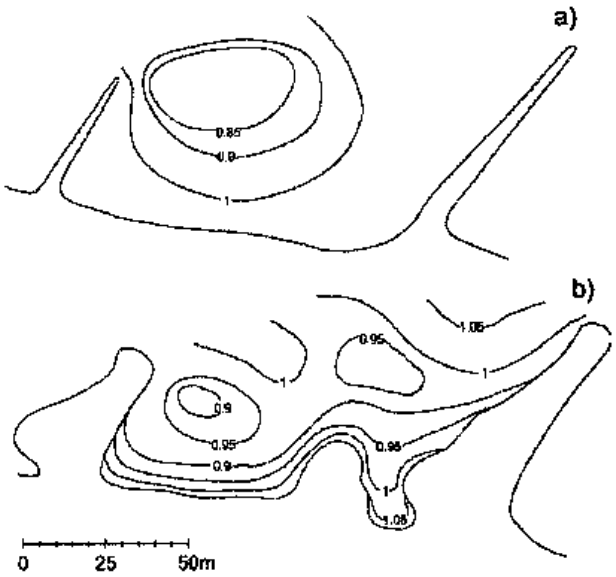

Figure 2.1. Distribution of phytoplankton content over groyne field area; a) high flow conditions (embayment aspect ratio greater than 0.5); b) low flow conditions (embayment aspect ratio less than 0.5).

Source: Engelhardt et al., 2004

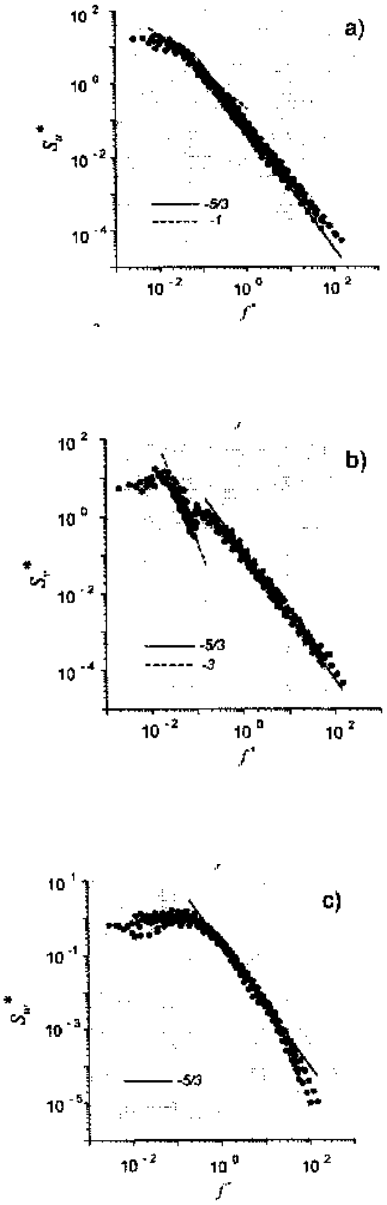

Figure 2.2. Velocity spectra for three velocity components at a station situated inside the embayment at low discharge conditions. a) streamwise; b) transverse; c) vertical.

Source: Engelhardt et al., 2004

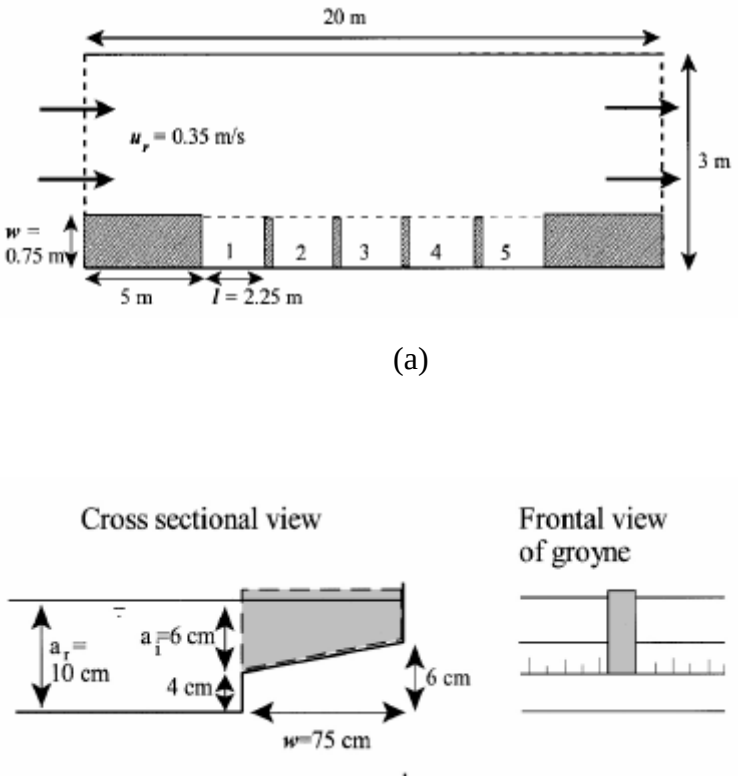

Figure 2.3. Groyne field configuration studied by Uijttewaal et al. (2001). a) horizontal view; b) cross sectional view; c) frontal view of groyne.

Source: Uijttewaal et al., 2001

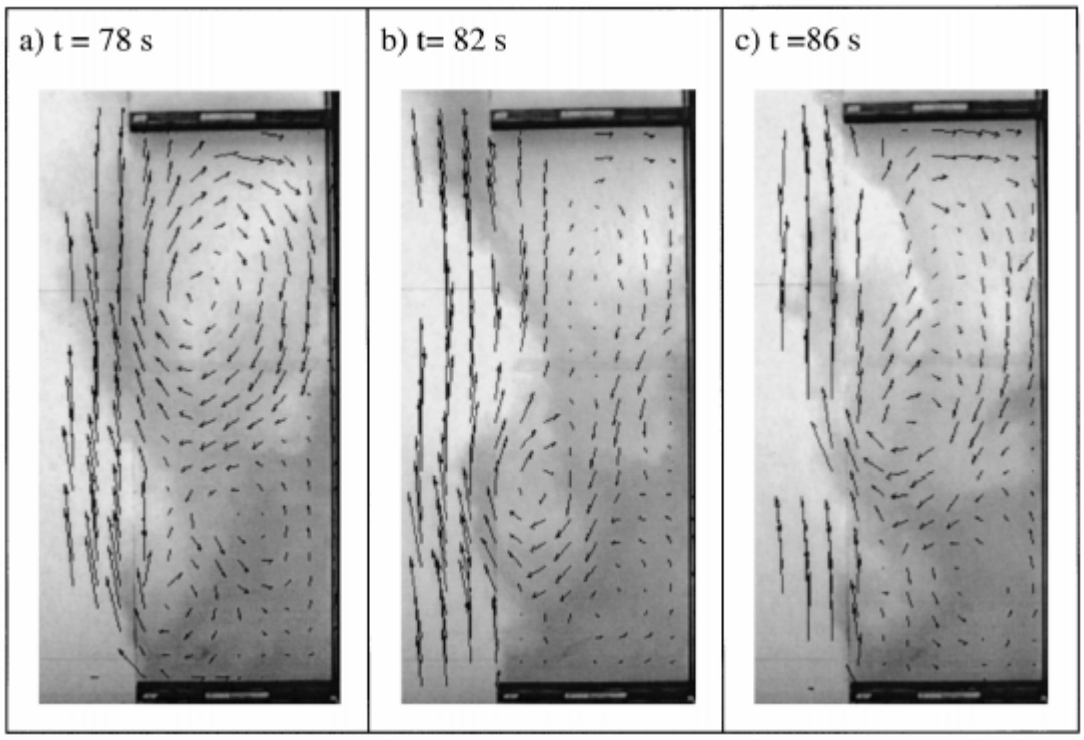

Figure 2.4. Instantaneous velocity fields at the free surface in one of the embayments of the groyne field investigated experimentally by Uijttewaal et al. (2001).

Source: Uijttewaal et al., 2001

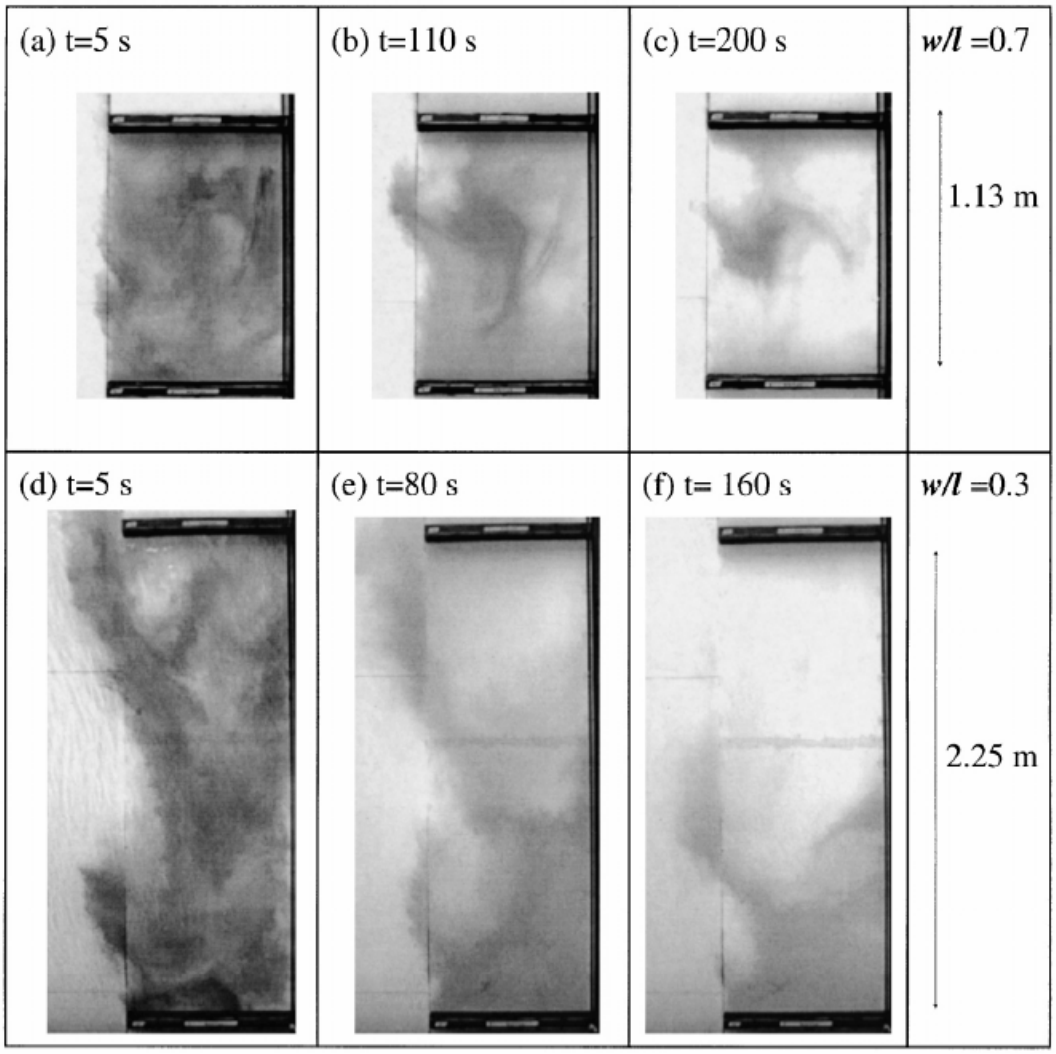

Figure 2.5. Instantaneous dye concentration fields in one of the embayments of the groyne field investigated experimentally by Uijttewaal et al. (2001). a) to c) embayment aspect ratio of 0.7; d) to f) embayment aspect ratio of 0.3.

Source: Uijttewaal et al., 2001

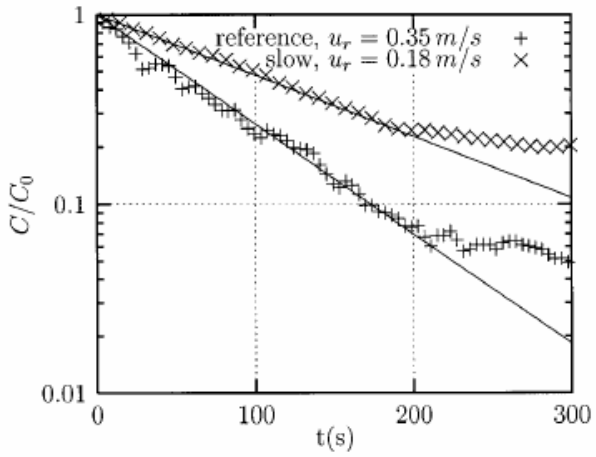

Figure 2.6. Temporal variation of normalized mean dye concentration in one of the embayments of the groyne field studied by Uijttewaal et al. (2001). The two curves correspond to mean channel velocities of 0.18m/s and 0.35m/s.

Source: Uijttewaal et al., 2001

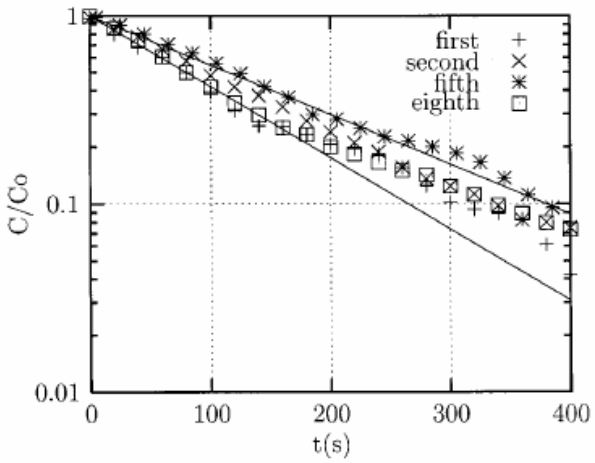

Figure 2.7. Temporal variation of normalized mean dye concentration in successive embayments of the groyne field studied by Uijttewaal et al. (2001). The embayment rank is marked on the figure.

Source: Uijttewaal et al., 2001

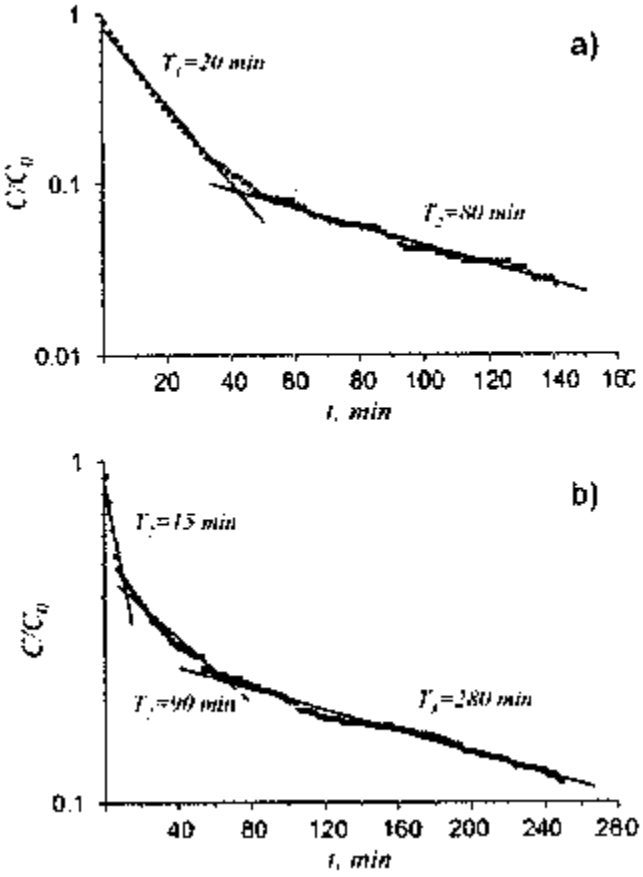

Figure 2.8. Temporal variation of the dimensionless tracer concentration inside the embayment. a) high flow conditions (embayment aspect ratio greater than 0.5); b) low flow conditions (embayment aspect ratio less than 0.5).

Source: Engelhardt et al., 2004

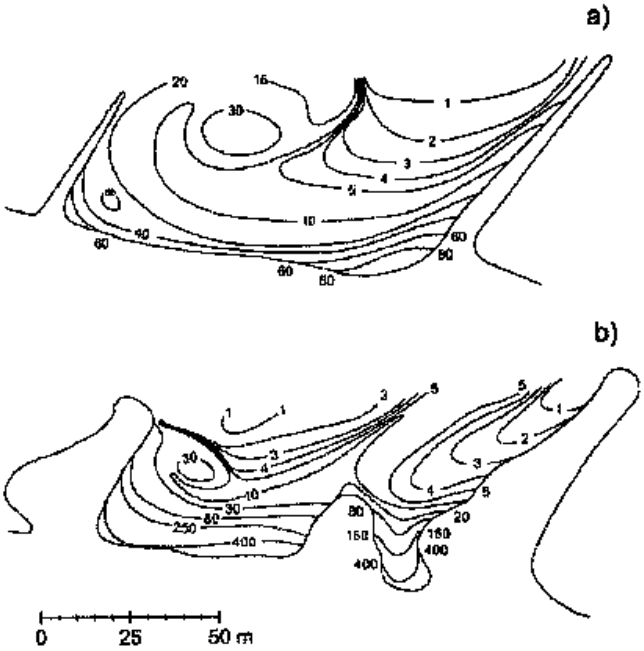

Figure 2.9. Distribution of residence times over groyne field area. a) high flow conditions (embayment aspect ratio greater than 0.5); b) low flow conditions (embayment aspect ratio less than 0.5).

Source: Engelhardt et al., 2004

CHAPTER 3

COMPUTATIONAL METHODOLOGY

3.1 LES vs. RANS Methods for Prediction of Flow and Transport Processes in River Engineering

Most predictions of engineering flows are obtained using the so-called Reynolds Averaged Navier-Stokes (RANS) approach in which the effect of most of the scales (eddies, vortices) on the mean flow is accounted for via a RANS turbulence model. By contrast, in LES, the dynamically important scales in the flow are directly computed, and only the effect of the filtered small scales on the large scales is modeled.

The interest in LES is primarily motivated by its superior accuracy as compared to RANS; e.g., its ability to better predict turbulent transport and mixing. Specific examples include prediction of fate and transport of pollutants, stratified flows mixing due to thermal or salinity gradients, thermal-effluent diffusion, prediction of massively separated flows (e.g., flow around representative hydraulic structures found in rivers and coastal areas like bridge pier/abutments, spur dikes, etc.) and prediction of particulate transport in two phase flows (e.g., particle laden flows). These advantages of LES over RANS make it especially appealing for hydraulics and river engineering modeling applications. LES is the most advanced modeling tool currently available for prediction of realistic complex flows. LES can accurately simulate the coherent structures in turbulent flows as opposed to only the mean flow, as is the case with most of the models (RANS) currently being used in engineering. However, LES is computationally much more expensive compared to RANS and even to unsteady RANS.

3.2 Basic Description of LES for Incompressible Flows and Related Discrete Energy Conservation Ideas

The Navier-Stokes and continuity equations for incompressible flow are:

$$\frac{\partial u_i}{\partial t}+\frac{\partial u_i u_j}{\partial x_j}=-\frac{\partial p}{\partial x_i}+\upsilon\frac{\partial^2 u_i}{\partial x_i \partial x_j} \quad , \quad \frac{\partial u_i}{\partial x_i}=0 \tag{3.1}$$

where the constant density is absorbed into the pressure. In LES, the unsteady, three-dimensional Navier –Stokes equations are spatially filtered, the resolved scales of motion are directly computed, and the influence of the filtered scales on the resolved scales is modeled. Spatial filtering (denoted by the "~") of the Navier-Stokes equations with a filter that commutes with the spatial and temporal derivatives yields the filtered Navier Stokes equations used in LES:

$$\frac{\partial \tilde{u}_i}{\partial t}+\frac{\partial \tilde{u}_i \tilde{u}_j}{\partial x_j}=-\frac{\partial \tilde{p}}{\partial x_i}+\upsilon\frac{\partial^2 \tilde{u}_i}{\partial x_i \partial x_j}+\frac{\partial \tau_{ij}}{\partial x_j} \quad , \quad \frac{\partial \tilde{u}_i}{\partial x_i}=0 \tag{3.2}$$

Here $\tau_{ij}=\overline{u_i u_j}-\tilde{u}_i\tilde{u}_j$ is the subgrid stress and has to be modeled in LES. In the following discussion, all of the quantities are grid filtered and the symbol "~" is omitted.

By definition, the dissipative scales are not resolved by the grid in LES. In practice, this leads to numerical instability if straightforward, non-dissipative central difference schemes are used. The instability is related to aliasing errors that occur when non-linear products are computed in physical space (see, e.g. Moin, 2001). One solution to this problem is to develop non-dissipative numerical schemes that discretely conserve not only first-order quantities such as momentum but also second-order quantities such as kinetic energy (e.g. Mansour et al., 1991). Discrete energy conservation ensures that the flux of kinetic energy $\sum_{CVS} u_i \partial(u_i u_j)/\partial x_j$ has contributions exclusively from the boundary elements (the summation is over all the control volumes of the mesh), which makes the solution robust without the use of numerical dissipation. Note that satisfying one constraint discretely does not ensure the other – both constraints have to be simultaneously enforced when deriving the algorithm. The Harlow-Welch algorithm (Harlow and Welch, 1965) possesses this property on the structured grids and has therefore been widely used for LES on structured grids in simple geometries.

3.3 Discrete Energy Conservation for Algorithms on Collocated Meshes

The basic idea is that the robustness at high Reynolds numbers is determined essentially by the numerical discretization of the convection term, while robustness on skewed grids is determined by both discretization of the convection and the pressure-gradient terms. For incompressible flows, discrete energy conservation refers to the fact that the convective and pressure terms in the discrete kinetic energy equation are expressible in divergence form. In collocated or non-staggered formulations, the Cartesian velocity components and pressure are stored at the centroids of the cells. In the method used to conduct the present LES simulations, the face-normal velocities are treated as independent variables that are stored at the centroids of the faces. Spatial discretization of the convective term is illustrated by the simplified passive scalar equation:

$$\frac{\partial \phi}{\partial t} + \frac{\partial}{\partial x_i} \phi u_i = 0 \tag{3.3}$$

Multiplying by ϕ and using the continuity equation yields:

$$\frac{\partial \phi^2}{\partial t} + \frac{\partial}{\partial x_i} \phi^2 u_i = 0 \tag{3.4}$$

i.e., conservation of ϕ implies conservation of ϕ^2 in the continuous case. However, discretely, conserving ϕ does not automatically imply conservation of ϕ^2. Integrating eqn. (3.3) over a cell (in the following discussion the mesh can be structured or unstructured) and using the divergence yields:

$$V_{CV} \frac{d\phi_{CV}}{dt} + \sum_{faces\ of\ CV} \phi_{face} \upsilon_n A_f = 0 \tag{3.5}$$

where ϕ_{CV} and V_{CV} denote the value of the scalar and the volume of cell 'cv', A_f is the face area, and υ_n denotes the face-normal velocity in the direction of the outward normal at each face. Note that the incompressibility condition requires that $\sum_{faces} \upsilon_n A_f = 0$.

Also, ϕ is discretely conserved regardless of how ϕ_{face} is computed. However, ϕ^2 will discretely be conserved only if the values of ϕ at the faces are calculated as a simple arithmetic mean of the values at the two cells that have that a particular face in common; i.e.,

$$\phi_{face} = \frac{\phi_{CV} + \phi_{nbr}}{2} \tag{3.6}$$

The discrete equation for ϕ^2 is obtained by multiplying eqn. (3.5) with ϕ_{CV} to obtain

$$V_{CV}\phi_{CV}\frac{d\phi_{CV}}{dt} + \frac{\phi_{CV}}{2}\sum_{faces\ of\ CV}(\phi_{CV} + \phi_{nbr})\upsilon_n A_f = 0 \tag{3.7}$$

which may be rewritten as

$$\frac{V_{CV}}{2}\frac{d\phi^2{}_{CV}}{dt} + \frac{\phi^2{}_{CV}}{2}\underbrace{\sum_{faces\ of\ CV}\upsilon_n A_f}_{=0} + \frac{1}{2}\sum_{faces\ of\ CV}\phi_{CV}\phi_{nbr}\upsilon_n A_f = 0 \tag{3.8}$$

Summation over all the cells in the computational domain yields

$$\sum_{volumes} V_{CV}\frac{d\phi^2{}_{CV}}{dt} + \sum_{volumes}\sum_{faces\ of\ CV}\phi_{CV}\phi_{nbr}\upsilon_n A_f = 0 \tag{3.9}$$

The contributions from the interior faces cancel out in the second term such that

$$\sum_{volumes} V_{CV}\frac{d\phi^2{}_{CV}}{dt} + \sum_{boundary\ faces}\phi_{CV}\phi_{nbr}\upsilon_n A_f = 0 \tag{3.10}$$

where if the boundary conditions for the scalar ϕ are specified on the boundary faces, one can define ϕ_{nbr} as $\phi_{nbr} = 2\phi_{face} - \phi_{CV}$. The above property is a statement of robustness since there is no production of energy (ϕ^2) due to discretization.

Note that discrete energy-conservation is implied in the absence of time-discretization errors. The discretization will also have dispersive error to leading order, whose magnitude needs to be small to compute such phenomena as turbulent mixing. In computations of turbulent flow fields, dissipative errors show up at the level of kinetic energy, while dispersive errors show up in higher order statistics. This motivates the

choice of schemes that are non-dissipative, yet robust at high Reynolds numbers. In particular, for $\phi = u_i$, equation (3.10) (after summation over i is performed) indicates that the only net convection of kinetic energy fluxes occurs through the boundary, or in other words there is no production of kinetic energy in the computational domain due to the numerics in the absence of time-discretization errors.

The interpolation $\phi_{face} = (\phi_{CV} + \phi_{nbr})/2$ is second-order accurate on uniform grids. On non-uniform grids, the interpolant could be weighted by the distances between the faces and the neighboring volumes. However such weighted interpolation comes at the cost of not being discretely energy-conserving. Numerical examples show that on grids that vary rapidly, weighted interpolants can be unstable since the weights reflect the underlying grid roughness. The symmetric interpolation, on the other hand, is both energy-conserving and stable for arbitrarily non-uniform meshes, properties which are of prime importance for obtaining meaningful solutions in very complex geometries, where mesh irregularities cannot always be avoided.

There is considerable incentive to utilize LES on unstructured grids. In addition to reducing the number of mesh nodes, unstructured grids significantly reduce the amount of time spent on grid generation. The finite-volume viscous flow solver (Mahesh et al., 2004) used to perform the LES simulations in the present work discretely conserves energy and can employ hybrid unstructured meshes. The solver uses a non-staggered formulation similar to the one described in the previous section for a simplified advection equation. All operators in the finite-volume formulation of the Navier Stokes equations are discretized using central schemes including the convective ones. The convective terms in the scalar transport equation employed to calculate the non-dimensional contaminant concentration, C, are discretized using a second-order WENO scheme (Jiang and Peng, 2000, Ham, 2003). A collocated, fractional-step scheme is used to solve the filtered Navier-Stokes equations with a dynamic Smagorinsky model (Pierce and Moin, 2001). The convective and viscous operators in the momentum (predictor step) equations

and in the scalar transport equation are discretized in time using the Crank-Nicholson scheme. The system resulting due to the implicit time discretization is solved using the SOR method. The discrete pressure equation is solved using the conjugate gradient method with preconditioning. The code was parallelized using MPI and has shown good scalability on various platforms (PC clusters, IBM SP3, Origin 3000, etc.).

3.4 Subgrid Scale Model

In the case in which an isotropic Smagorinsky-like subgrid-scale model is used, equations (3.2) can be rewritten as:

$$\frac{\partial u_i}{\partial x_i} = 0 \tag{3.11}$$

$$\frac{\partial u_i}{\partial t} + \frac{\partial (u_i u_k)}{\partial x_k} = -\frac{\partial p}{\partial x_i} + \frac{\partial}{\partial x_k}(\nu + \nu_{SGS})\left(\frac{\partial u_i}{\partial x_k} + \frac{\partial u_k}{\partial x_i}\right) \tag{3.12}$$

in which, to simplify the equations, the symbol "~" corresponding to a filtered quantity was dropped from the equations (u_i still represents the filtered velocity). The Navier-Stokes equations are solved in non-dimensional form, in which case u_i represents the non-dimensional filtered velocity component in the i direction and ν is replaced by 1/Re, where Re is the Reynolds number. Similarly, the transport equation for the filtered non-dimensional concentration, C, can be written as:

$$\frac{\partial C}{\partial t} + \frac{\partial (C u_k)}{\partial x_k} = \frac{\partial}{\partial x_k}\left(\left(\frac{\nu}{Sc} + \alpha_{SGS}\right)\frac{\partial C}{\partial x_k}\right) \tag{3.13}$$

where Sc is the molecular Schmidt number.

A dynamic procedure is used to estimate the subgrid scale viscosity (ν_{SGS}) and diffusivity (α_{SGS}) in the present simulations. Their expressions are:

$$\nu_{SGS} = C_d \Delta^2 |S| \tag{3.14}$$

$$\alpha_{SGS} = C_\alpha \Delta^2 |S| \tag{3.15}$$

The dynamic parameters C_d and C_α have the following form:

$$C_d\Delta^2 = \frac{1}{2}\frac{L_{ik}M_{ik}}{M_{ik}M_{ik}} \tag{3.16}$$

$$L_{ik} = -\overline{u_i u_k} + \bar{u}_i\bar{u}_k \tag{3.17}$$

$$M_{ik} = \left(\bar{\Delta}/\Delta\right)^2\left|\bar{S}\right|\bar{S}_{ik} - \overline{|S|S_{ik}} \tag{3.18}$$

$$C_\alpha\Delta^2 = \frac{L_i M_i}{M_i M_i} \tag{3.19}$$

$$L_i = -\overline{u_i C} + \bar{u}_i\bar{C} \tag{3.20}$$

$$M_i = (\bar{\Delta}^2/\Delta^2)\,|\bar{S}|\frac{\partial\bar{C}}{\partial x_i} - \overline{|S|\frac{\partial C}{\partial x_i}} \tag{3.21}$$

where $|S| = 2\sqrt{S_{ij}S_{ij}}$ and $S_{ij} = \frac{1}{2}\left(\frac{\partial u_i}{\partial x_j} + \frac{\partial u_j}{\partial x_i}\right)$. In the previous expressions, the grid filter width Δ is a measure of the local grid spacing, and the ratio of the test (denoted "-") to grid filter width was taken equal to 2, as is common. The grid filter width is defined as $V^{1/3}$ where V denotes the element volume. This yields a grid filter width of $\left(\Delta_x\Delta_y\Delta_z\right)^{1/3}$ for a Cartesian grid with cell dimensions Δ_x, Δ_y and Δ_z. The <> operator refers to local filtering that replaces the usual averaging done in the homogeneous directions in simple flows. The test filter is assumed to be a top-hat filter which uses information from the neighboring volumes. The dynamic Smagorinsky model can predict negative values of ν_{SGS} and α_{SGS}. Thus, if necessary, the values of the subgrid-scale contributions are clipped such that the total viscosity and total diffusivity remain positive within the domain at all times. The governing equations are integrated up to the wall ($\Delta n_1^+ \sim 1$ for the first cell off the wall, where $n^+ = nu_\tau/\nu$, n is the wall normal distance, u_τ is the bed-friction velocity) in the simulations discussed in the present work.

The use of the dynamic Smagorinsky model (Lilly, 1992) as opposed to the classical constant coefficient Smagorinsky model and of grids that resolve the viscous

sublayer have several important advantages. For example, it eliminates the need to specify the value of the model constant which becomes a function of space and time and is calculated from the resolved variables without any empirical input, eliminates the need for near-wall viscosity corrections (e.g., Van Driest damping functions) in the near-wall region as the model coefficient decays to zero automatically in the vicinity of solid boundaries and eliminates the use of empirical modifications to account for the effect of 'extra strains', if present. As seen from equations (3.14) and (3.15), the values of ν_{SGS} and α_{SGS} are calculated independently based on the instantaneous, resolved velocity and concentration fields. The dynamic procedure eliminates the need to specify, a priori, a value for the turbulent Schmidt number. Only the molecular Schmidt number has to be specified in equation (3.13).

3.5 Previous Validation Studies of the Numerical Method and Code Used in the Present Work

Extensive validation results for internal and external flows (including massively separated flows) are described in Mahesh, Constantinescu and Moin (2004), Mahesh et al. (2006) and several reports of the Center for Turbulence Research in Stanford University (2001-2004). Specific direct numerical simulation (DNS) and LES validation test cases (in some of the cases detailed comparison with Laser-Doppler-Velocimetry (LDV) or Particle-Image-Velocimetry (PIV) data was performed) include isotropic turbulence (Mahesh et al., 2004), turbulent channel flow (Mahesh et al., 2004), massively separated flow around cylinders at different Reynolds numbers (Mahesh et al., 2004), swirling flow in a coaxial geometry (Mahesh et al., 2004, Mahesh et al., 2006, Apte et al., 2003a), spatially evolving jets (Babu and Mahesh, 2005) and jets in cross-flow (Muppidi and Mahesh, 2005a, 2005b). Validation studies for turbulent flows in highly complex geometries (e.g., Pratt Whitney jet aircraft engine combustors) are described in Ham et al. (2003) and Mahesh et al. (2006). Validation for particle laden swirling flows is discussed

in Apte et al. (2003b) and Apte et al. (2004). The code was recently used to calculate the flow through a realistic geometry water pump intake bay (Tokyay and Constantinescu, 2005a, 2005b, 2006) and successfully validated using detailed PIV experimental data. The code is also being applied to simulate flow around hydraulic structures like bridge piers (Kirkil et al., 2005a, 2005b, 2006) and bridge abutments (Koken and Constantinescu, 2006) for which large-scale PIV was used to validate the numerical predictions at the free surface.

CHAPTER 4

COHERENT STRUCTURES AND MASS EXCHANGE PROCESSES IN CHANNEL FLOW WITH TWO EMERGED GROYNES

4.1 Introduction

In this section, Large Eddy Simulation (LES) is used to investigate the instantaneous and mean flow fields around two fully emerged groynes in a flat-bed open channel with lateral vertical walls and the mass exchange processes between the embayment and the main channel. The depth in the embayment and channel are equal. The present generic geometry has been studied in Japan both experimentally (Chen and Ikeda, 1997, Tominaga et al., 2000, 2001a, 2001b) and numerically using RANS models (Kimura et al., 2001, 2003) in the context of the investigation of flow around river groynes. The flow around the first embayment of a groyne field is of particular interest because of the strong horseshoe vortex (HV) system that develops around the tip of the upstream groyne. In virtually all the cases when groyne fields are present in a river reach, the strongest erosion occurs around the most upstream groyne. As seen in most of the scaled model studies of the flow around groyne fields, the extrapolation to full scale of the results of the present numerical investigation, conducted at a relatively low Reynolds number, should be made with care despite the fact that the incoming channel flow was fully turbulent.

The main topics discussed in the results section are: 1) a description of the vortical structure of the flow in the upstream recirculation region, the embayment, the horizontal detached shear layer (DSL) and the downstream recirculation region using the averaged and instantaneous flow fields; 2) a detailed study of the structure of the turbulent HV system and of the instantaneous and mean bed shear stress distributions; 3) a discussion of the interactions among the dominant coherent structures that play an integral role in the mass exchange between main channel and embayment; 4) a

quantitative study of the exchange of dissolved matter (passive contaminant) between the embayment and the main channel; 5) an investigation of how the mass exchange at the channel-embayment interface occurs over the embayment depth and a description of the contaminant transport within the embayment; 6) an estimation based on LES results of the mass exchange coefficients used in simple mass exchange models for the present geometry; and 7) a description of the advection inside the main channel of the contaminant removed from the embayment volume.

4.2 Computational Domain and Mesh

4.2.1 Computational Domain

The geometry of the channel with two lateral groynes considered in the present study is shown in Figure 4.1. The depth of the main channel, D, is used as the length scale. In this case, the channel depth is equal to the groyne height. The mean velocity in the main channel, U, is used as the velocity scale. The two groynes (obstructions) extend up to the free surface. The physical domain extends 2D upstream of the first obstruction and 14D downstream of the second obstruction. The channel Reynolds number is Re=13,600. The width of the channel is B=3.75D. The length, l, and width, b, of each obstruction are 0.625D and 0.25D, respectively. The space between obstructions is S=1.5D (see also Figure 4.1). The embayment has a length to width ratio close to 0.5. The obstructed area is 17% of the total channel section. In the computational domain, x is the streamwise direction, and its origin is at the inflow section (the centers of the two obstructions are situated at x/D=2.0 and x/D=3.5). The normal direction, z, is measured from the channel bottom.

4.2.2 Boundary and Initial Conditions

At the inflow section of the open channel, the flow fields corresponding to a precalculated, fully-developed LES periodic open channel simulation at the same channel Reynolds number were fed in a time-accurate way. The fields corresponding to the statistically steady periodic channel solution were collected over a non-dimensional time of 80D/U. The non-dimensional distributions of the mean streamwise velocity and Reynolds shear stress (not shown) were found to agree well with the profiles measured (Hussain and Reynolds, 1975, Wei and Willmarth, 1989) in wide channels (top and bottom boundaries were walls in the experiments) at Reynolds numbers (defined with the channel half depth to be consistent with the definition of the Reynolds number in the case of an open channel) in the same range (10,000-20,000). The comparison with the same experimental data for the profiles of the velocity fluctuations in all three directions is shown in Figure 4.3 in the bottom wall region ($y^+<100$) where the effects of imposing a symmetry boundary condition on the top surface (e.g., this forces the vertical fluctuations to be zero at the free surface) are small. These conditions ensured that the incoming flow was fully turbulent at the location of the upstream obstruction.

A convective outflow boundary condition was used at the exit section, which has the advantage of allowing the coherent structures to leave the computational domain in a physical way and to reduce the distortions and numerical noise associated with the interaction between the coherent structures and the outflow boundaries. The velocity boundary conditions on all walls including the lateral wall opposite to the embayment side are no-slip. The free surface was simulated as a rigid lid (open channel). The shear stresses in the horizontal directions and the normal velocity were set equal to zero at the free surface.

The mass exchange between the embayment and the main channel was investigated by considering the ejection of a passive scalar that was introduced instantaneously at a certain time (after the velocity fields become statistically steady)

inside the embayment domain (results and description to follow in section 4.4). The non-dimensional scalar concentration, C, was initialized as C=1 inside the embayment and C=0 outside of it. The time at which the scalar was introduced was formally taken as t=0D/U. The simulation was continued for another 90D/U until approximately 98% of the contaminant initial situated inside the embayment had exited. At the inflow, C was set to zero. The mass flux was set to zero on all solid surfaces and at the free surface.

4.2.3 Computational Mesh

The unstructured mesh (see Figure 4.2) contains approximately 3 million hexahedral elements and was generated using a paving technique (Fluent Manual, 2003) which allows rapid variation in the characteristic size of the elements while maintaining high overall mesh quality and low stretching ratios. Figure 4.2a shows a partial view of the mesh in the free surface plane. Figure 4.2b shows a detailed view around the embayment, and Figure 4.2c shows a detailed view of the mesh around the tip of the upstream groyne. The aspect ratio of the cells away from the solid surfaces was kept as close to unity as possible. The first row of cells from the solid surfaces including lateral walls is located within the viscous sublayer ($\Delta y^+<1$). In the vertical direction (42 grid points), the mesh spacing varies between 0.5 wall units at the bottom to 21 wall units at mid depth and to around 42 wall units at the free surface, based on the channel Reynolds number and assuming $u_{\tau 0}/U\sim0.05$. The vertical resolution near the free surface may not be sufficient to capture some of the turbulence and anisotropy effects in that region. Though this is not expected to substantially modify the nature of the mass exchange processes between the embayment and the main channel (at least inside the embayment, the physical Reynolds number and thus the grid spacing in wall units is smaller by a factor of two or more as the velocity magnitude is smaller than the one inside the main channel), it is important to acknowledge this limitation of the present simulation.

The mesh size in the regions around (horizontal cell size is close to 50 wall units at point c1 outside the embayment region in Figure 4.2a) and within the embayment (horizontal cell size is close to 9 wall units at point c2 in Figure 4.2b) is expected to allow the simulation to capture the dynamically important coherent structures present around the embayment region. The typical dimension of the mesh cells around the tip of the upstream groyne (point c3 in Figure 4.2c), where the vortex tubes form and are shed in the detached shear layer, is close to 3 wall units. This is essential to accurately capture the dynamics of these coherent structures (see discussion of Figure 4.7, Figure 4.8, and Figure 4.10b) that play an important role in the dynamics of the momentum and mass exchange around the interface.

The time step in the simulation was 0.002D/U. The Courant number inside a typical element within the embayment (point c2 in Figure 4.2 where velocity magnitude is around 0.3U) was 0.04. Outside the embayment region (e.g., point c1 in Figure 4.2 where velocity magnitude is around 1.0U), the Courant number was about 0.025. The non-dimensional cut-off frequency (given in the form of a Strouhal number) defined with the local velocity magnitude and characteristic cell length in the direction of the velocity vector is around 12 in the middle of the main channel, around 20 inside the embayment (point c2) and around 200 near the origin of the detached shear layer (point c3 in Figure 4.2). At the channel Reynolds number at which the simulation is conducted (Re=13,600), the frequency associated with the shedding of the vortex tubes (which is dependent on the Reynolds number) is conservatively estimated to be less than 20. In fact, results in Figure 4.10b show that the dominant non-dimensional frequency (St=fD/U, f is the frequency) associated with the shedding of these coherent structures is close to 7. In the same figure, an inertial range is also observed at stations situated inside the main channel and embayment. The other large-scale unsteady phenomena within the embayment, recirculation regions and wake are expected to take place at much smaller frequencies and thus should be captured by the present simulation. The energy spectrum was

observed to have between a 4 and 6 decade decay for all variables (e.g., see results in Figure 4.10 for the pressure). The above arguments show that the mesh density is reasonable for the present simulation to be sufficiently resolved for the purpose of studying the mass exchange processes between the embayment and the channel.

4.3 Analysis of Mean and Instantaneous Flow Structure

4.3.1 General Qualitative Description of Vortical Flow Structure Using Two-Dimensional Streamlines

Mean velocity streamlines are used to educe the mean vortical structures in the flow. The mean velocity fields were averaged over 75 D/U, a time period long enough to ensure convergence of the velocity statistics.

One should also note that the presence of a certain flow structure in the mean flow field does not necessarily mean a corresponding structure of similar shape is present at most of the times in the real flow (instantaneous LES flow fields in the present case). Though most of the large vortical structures present in the mean flow correspond to a fairly stable coherent structure in the instantaneous flow, this is not always the case. Sometimes a mean vortical structure is just an artifact of averaging over a highly unsteady flow field (e.g., where irregular vortex shedding is present). Thus, concurrent analysis of the averaged and instantaneous flow fields is necessary to fully elucidate the physics of the flow.

Figure 4.4 shows the streamlines in three horizontal planes situated near the free surface, at mid-depth level (z/D=0.6) and near the bottom (z/D=0.1). They help to visualize the recirculation pattern inside the embayment as well as the extent of the recirculation regions upstream of the first groyne and downstream of the embayment at three depths in the channel. Several large-scale coherent structures are present throughout the channel in the mean flow.

Corner vortices are found upstream of the first groyne and downstream of the second groyne, near the junction between the lateral wall and the groynes. The streamline patterns within the embayment vary along the depth. For example, an eddy is present at mid-depth level and the free surface in the upstream part of the embayment. The recirculation eddy in the embayment-channel interface region observed in Figure 4.4a-b corresponds to the DSL. In reality, vortex tubes are shed in this region and convected downstream. The recirculation eddy observed in the mean flow field is just a consequence of the time averaging process (see also discussion of Figure 4.6). The recirculation eddy corresponding to the wake behind the downstream groyne extends around 9 groyne lengths downstream. This is consistent with the experimental results of Fox et al. (2005) who studied the flow past stream barbs and observed a value of this ratio close to 8. It is observed that as the free surface is approached, the reattachment point of this recirculation region moves downstream corresponding to an increase in the size of this eddy. In fact, this recirculation eddy looks similar to a tornado-like vortex originating near the bottom.

Compared to the statistically averaged flow structures, visualization of the instantaneous coherent structures in Figure 4.5 highlights the differences between the mean and instantaneous flow and illustrates even more clearly the complexity of the interactions among the structures within the flow. As expected, the vortical flow structure as shown by the instantaneous velocity fields is more complex with a wider range of scales and vortices present. The main time-averaged flow structures in these horizontal planes can still be observed in Figure 4.5, but it is immediately apparent that the upstream (corner) vortex system contains additional secondary vortices when the instantaneous flow fields are used for visualization. The same is true for the embayment region, especially for the region between the embayment-channel interface and the outer surface associated with the detached shear layer where instead of a smooth elongated

vortex, several vortical structures are observed within the same region (especially near the free surface) in the instantaneous fields.

4.3.2 Vortical Structure of the Flow in the Detached Shear Layer and Embayment Region

The instantaneous streamlines in Figure 4.6 indicate that several coherent structures are present in the embayment-shear layer region. In fact, these structures are observed in most of the collected instantaneous flow fields. Their formation is at least partially due to the merging of the small vortex tubes that are shed from the tip of the upstream groyne. Noticeably, these structures appear to extend only through the upper half of the channel depth, and their coherence is lost in the bottom part of the channel. The path followed by these coherent structures is not always the same, and vorticity animations show that similarly to 2D cavity flows (flow is homogeneous in the third direction) they can be advected over the embayment area without crossing the interface (total escape event). In some cases, they can cross the interface (partial or total clipping event) and convect high vorticity fluid inside the embayment (see Lin and Rockwell, 2001, Chang et al., 2005a, 2005b,2006). The coherence of these coherent structures is usually lost in the bottom part of the channel. Interestingly, the upstream eddy in Figure 4.6a appears to entrain fluid toward the free surface while the opposite is true for the downstream structure.

Though these vortices are intermittent, their circulation can be very high. Thus, they can play a central role in the mass exchange process between the embayment and the channel. In the context of removing contaminant from the embayment, these coherent structures have from time to time been observed to engulf fluid with higher concentrations from the upper layers of the embayment and advect it downstream of the second groyne (total escape event). Due to the averaging process, these structures are not captured in visualizations using mean velocity flow fields. This example highlights the

limitations of analyzing the mass exchange processes based solely on the mean flow fields.

Before quantitatively analyzing the mass exchange process, it is important to focus on the dynamics of the coherent structures within and around the embayment area. As similarly observed in previous dye visualization experiments (e.g., Weitbrecht and Jirka, 2001b), it is found that the region around the embayment-channel interface is characterized by the fairly random interaction between the channel flow, the structures that populate the detached shear layer and the eddies inside the embayment. As a result of these interactions, the instantaneous flow structure in the region around the interface can vary considerably over time scales of the order of several D/U.

The vortical structure of the instantaneous DSL is clearly captured in Figure 4.7 which shows the instantaneous values of the out-of-plane vorticity component at four horizontal planes over the depth of the channel. The presence of the obstructions induces massive separation around the embayment. The horizontal DSL starts at the leading edge of the upstream groyne and extends along the interface between the embayment and main channel. High instantaneous vorticity values are observed in the upstream recirculation area, in the DSL and downstream of the embayment region. Small tube-like vortices form due to growth of Kelvin-Helmholtz instabilities and are shed from the upstream obstruction head. As these vortices are convected along the DSL, their size increases in part due to merging of consecutively shed vortices. This phenomenon is clearly captured in animations of the vorticity field at the free surface. Strongly coherent vortex tubes are evident especially near the mid-depth point of the groyne (Figure 4.7b-c). Due to the interaction with the bottom and the near-wall turbulence, the vortex tubes lose coherence as they approach the channel bottom (Figure 4.7d).

Figure 4.8 illustrates the distributions of the mean vorticity magnitude, TKE, pressure fluctuations and resolved primary shear stresses in a plane (z/D=0.5) situated at the mid-depth of the groynes. The information in these figures is provided in part

because it may be used to validate RANS or hybrid RANS/LES models. In the plane z/D=0.5, very high values of the out-of-plane vorticity magnitude (Figure 4.8a) are predicted inside the upstream part of the separated shear layers. However, the vorticity levels are relatively small at x/D~3.5 (near the downstream groyne). This is in stark contrast to what is observed in the instantaneous vorticity fields in Figure 4.7, where patches of high vorticity are convected inside the DSL over the whole extent of the channel-embayment interface.

The distribution of the pressure fluctuations in Figure 4.8c shows that the turbulence inside the upstream part of the DSL originating at the tip of the upstream obstruction dominates the background turbulence associated with the fully turbulent flow in the incoming channel. The TKE levels are also relatively high inside the horizontal DSL. However, relatively large values of the TKE are observed inside the main recirculation eddy downstream of the embayment. Finally, the distribution of the resolved shear stress, $\overline{u'v'}$, shows a continuous region of relatively high values inside the DSL and the downstream recirculation region but relatively low values inside the embayment.

Evidence of high levels of turbulence amplification over the whole vertical extent of the horizontal DSL is given in Figure 4.9a, which shows the TKE distribution in a vertical section (x/D=2.75) situated at mid distance between the groynes. The embayment-channel interface is marked with a dashed line (y/D=3.12). Starting at z/D~0.15, the turbulent fluctuations inside the separated shear layer are larger by at least one order of magnitude compared to the ones inside the embayment or on the channel side. It is also important to note the low levels near the lateral wall on the left. In fact, the level z/D~0.15 corresponds approximately to the thickness of the bottom wall boundary layer (see also the streamwise and spanwise vertical velocity profiles at the mid channel-embayment interface in Figure 4.9b). The strong reverse flow observed in the upper half of the streamwise velocity profile in Figure 4.9b is due to the recirculation

eddy (see Figure 4.4a-b) associated with the mixing layer (see also Figure 4.6a) forming between the outer flow (outside the DSL) and the flow inside the embayment. This eddy disappears near the channel bottom, and the flow in the channel-embayment interface region is oriented in the positive streamwise direction, as observed in Figure 4.4c.

Pressure power spectra (see Figure 4.10b) determined from the simulated flow fields at points situated very close to the tip of the upstream groyne (e.g., see point B in Figure 4.8a) show the presence of a fairly broad turbulent spectrum with two dominant frequencies corresponding to Strouhal numbers (St=fD/U) of 3.8 and 7.5, respectively. The larger Strouhal number is associated with the initial shedding of vortex tubes from the upstream obstruction. The smaller Strouhal number corresponds to the dominant frequency in the detached shear layer once consecutively shed vortices have merged just downstream of the tip of the groyne (the value of the lower frequency is roughly half of the larger one). This process is quasi-periodic and is clearly captured in Figure 4.11, where two consecutively shed vortices, a and b, are shown to merge over a time interval of 0.32 D/U. This corresponds to a Strouhal number of 3.2 which is close to the dominant frequency St=3.8 present in the power spectrum.

Besides the DSL, strong localized patches of vorticity are shed and advected in the region around the downstream groyne on the embayment side (e.g., see point C in Figure 4.8a). This feature of the instantaneous vorticity field is in fact observed consistently in animations and is related to a more complex, relatively regular, shedding process that takes place near the tip of the downstream groyne and is influencing the mass exchange between the embayment and the channel. Figure 4.12 shows a typical sequence that corresponds roughly to a shedding cycle. The four instantaneous out-of-plane vorticity fields are spaced 1D/U in time and reflect the wide range of eddies in the embayment area. Patches of clockwise rotating vorticity (e.g., red patch of vorticity marked as b in Figure 4.12a) are shed from the downstream groyne tip into the embayment. Once formed, vortex b moves roughly along the diagonal of the

embayment, as observed in Figure 4.12b-d (in the same figure the patch of vorticity denoted as a corresponds to the previously shed vortex). As the patch of vorticity is advected, it interacts with other eddies inside the embayment area and is strongly stretched and deformed. Because of the small-scale turbulence and different time scales associated with some of the large-scale unsteadiness, the evolution of the patches of vorticity shed from the tip of the downstream groyne is not identical. However, a certain periodicity can be inferred from animations and visualizations. In Figure 4.12d, a new patch of positive vorticity denoted c is already present and corresponds to patch b in Figure 4.12a. The sequence illustrated in the four frames of Figure 4.12 suggests that the process takes place over a time interval of 3.0 D/U. Indeed, the pressure spectrum at point C (Figure 4.10c) has its most energetic peak centered near St = 0.33, confirming the value of the period associated with the shedding deduced based on flow visualizations. Though the St=0.33 and St=0.4 frequencies are also present in the spectrum at point D (Figure 4.10d) inside the main recirculation eddy downstream of the embayment (Figure 4.8a), no dominant frequency is present at that location. This is also the case for the spectrum at point A (see Figure 4.8a and Figure 4.10a) upstream of the embayment region.

The two vortex shedding phenomena discussed in Figure 4.11and Figure 4.12 are found to play an important role in the removal of the high concentration embayment fluid present in the upper layers of the embayment. This is inferred from the comparison of the corresponding vorticity and scalar concentration fields shown in frames a-d and e-h of Figure 4.12. A first observation is that the patches of vorticity associated with the shedding from the tip of the downstream groyne contain low concentration fluid. This makes sense as most of these eddies are entraining fluid from the region downstream of the second groyne (see also mean 3D streamlines in Figure 4.17a in the region near the free surface around the tip of downstream groyne). These pockets of high vorticity magnitude tend to be surrounded by higher concentration fluid (red areas in the

concentration fields in Figure 4.12). The vortical eddies are advected along the diagonal of the embayment along with the associated low concentration fluid. While engulfment and small eddies locally increase the mixing between these patches of vorticity and the surrounding higher concentration fluid, the main consequence of the advection of these patches of vorticity toward the upstream embayment corner is to dislocate high concentration fluid already present in the embayment. Part of this higher concentration fluid is pushed parallel to the upstream groyne face toward the tip of the groyne (e.g., see Figure 4.12a) and from there into the horizontal DSL (Figure 4.12b). Once in the DSL, it is engulfed by the vortex tubes and advected (Figure 4.11 and Figure 4.12) away from the embayment area. In reality, the process is more complicated than that mainly because of the vertical contaminant transport which is on average toward the free surface, though as shown in Figure 4.17a, part of the low concentration fluid convected toward the upstream embayment corner near the free surface is advected downwards where it mixes with and dislocates high concentration fluid from the bottom area. However, the above described scenario appears to partially explain the mixing in the region close to the free surface.

4.3.3 Mean and Depth-Averaged Velocity Fields

The mean flow fields (u/U, v/U, w/U) are shown in three horizontal planes through the channel depth along with the depth-averaged distributions in Figure 4.13 to 4.15. They are useful for validation of simpler 3D RANS models or 2D depth-averaged RANS or LES models that are used to predict flow past groyne-like geometries. Observe the large three-dimensionality of the flow in and around the embayment region as shown by the mean vertical velocity distributions. Though the distributions of the horizontal components are qualitatively similar, significant quantitative differences between the free surface and the bottom regions are observed. This is consistent with the significant three-dimensionality of the momentum and mass exchange processes in the embayment region that are subsequently discussed.

4.3.4 Coherent Structures in the Mean and Instantaneous Flow Fields

Figure 4.16a visualizes the statistically averaged corner vortex system using 3D streamlines released in the vicinity of the junction between the lateral wall and the first groyne, upstream of the embayment. Figure 4.16b-e more vividly details the vortex structure throughout the depth using in plane 2D streamlines. The streamlines indicate that, in the mean, two vortical structures exist, the upstream vortex being weaker than the more dominant vortex present right next to the junction line. The vortices appear to be independent near the surface. Around z/D=0.4, the coherence of the upstream vortex decays and streamlines suggest that the secondary vortex merges with the primary vortical structure. Also in the vicinity of the z/D=0.4 plane, the orientation of the axis of the main vortex begins to transition from being perpendicular to the channel bed to being parallel with the channel bottom. For this channel configuration (l/D = 0.625, l/B = 0.1667), the corner vortex connects into the horseshoe vortex (HV) system. Thus, one can speculate that the dynamics of the corner vortex may have an important effect on the dynamics of the HV system, at least for groynes whose length is relatively small compared to the depth. As will be discussed later, the instantaneous structure of the upstream corner vortex is more intricate and complex.

Figure 4.17a shows the coherent structures in the embayment area using 3D streamlines released in the upstream embayment half. Figure 4.17b-e shows the vortex structure throughout the depth as seen in horizontal planes. A clockwise vortex dominates the upstream half of the embayment and is present through most of the depth. Its role is to transfer fluid from near the surface toward the channel bottom. The extent of this vortex structure is limited by the presence of the horizontal DSL. Streamlines indicate that fluid feeding into this system originates near the tip of the downstream groyne (especially near the surface) and from the vortex oriented parallel to the channel bottom located in downstream half of the embayment (Figure 4.18a). The upstream

embayment vortex loses its coherence near the channel bottom but clearly plays a role in the entrainment of fluid from the embayment toward the main channel. Fluid exiting the embayment volume near the channel bottom becomes entrained in the fast moving flow inside the shear layer. Some fluid particles are transported downstream, past the embayment, while other particles are recirculated back into the embayment. Thus, this vortical eddy plays a major role in the movement of fluid between the different horizontal layers inside the embayment and between the embayment and the channel. The presence of this eddy partially explains why the mass exchange process is very non-uniform over the depth of the embayment (see section 4.4). The 3D streamlines in Figure 4.17a also show that low-concentration fluid from the recirculation eddy downstream of the embayment is entrained back into the embayment in the free surface region near the tip of the downstream groyne.

Figure 4.18a captures the strongly coherent vortex just beneath the free surface whose axis is perpendicular to the groynes and lateral wall. This vortex entrains fluid from the bottom part of the embayment and from outside it (see streamlines near the base of the second groyne) and then convects it upwards toward the free surface and then toward the upstream groyne (see Figure 4.17). Once it approaches the face of the upstream groyne, the fluid is eventually convected outside the embayment where it is entrained by the fast moving vortical structures that populate the DSL. This circulation pattern is fully consistent with the above discussion of the mass exchange dynamics within the embayment. Figure 4.18b-e displays more systematically the vortex structure across the embayment width (location of vertical planes is shown in Figure 4.18a). The intensity of the vortex peaks between x/D = 2.8 and x/D = 3.2. Observe also the presence in these vertical planes of a bottom-attached vortex beneath the DSL.

Figure 4.19 shows the extent of the mean vortex system corresponding to the DSL near the embayment-channel interface. As already discussed, in the instantaneous flow this region is populated by vortices that are shed from the tip of the upstream groyne and

whose size increases as they are convected downstream (see Figure 4.5a, Figure 4.5b, Figure 4.6 and Figure 4.11). In fact, even the instantaneous vortex present near the downstream groyne in Figure 4.6a does not correspond to the large vortex in Figure 4.19 situated at virtually the same position, as fluid is convected toward the bottom along the core of the instantaneous vortex structure while the fluid is convected toward the free surface in the time-averaged vortical structure in Figure 4.19. The upstream eddy in Figure 4.6 that entrains fluid toward the free surface appears to be a vortex that resulted through the merging of subsequent vortex structures shed from the upstream groyne tip (see also discussion of Figure 4.11).

Figure 4.19a shows that fluid is entrained upward from a region situated just upstream of the second groyne into a vortex that convects fluid toward the free surface in the DSL region. Fluid particles are also entrained into the vortex from the area inside the embayment close to the channel bottom. Figure 4.19b-e details the tornado-like vortex structure throughout the channel depth. Its axis is fairly vertical over most of the channel depth (up to z/D=0.2) except near the bottom where it curves toward the shear layer interface. It is also important to note the connection with the downstream recirculation zone, especially near the free surface. As shown in Figure 4.17a, some of the fluid particles entrained back into the embayment are coming from the recirculation zone downstream of the second groyne. In fact, they are entering the embayment through the small gap between this vortex and the tip of the downstream groyne.

Figure 4.20 illustrates the extent of the mean vortex system in the downstream recirculation zone. The streamlines indicate that massive separation takes place downstream of the second groyne. The recirculation region is dominated by the presence of one counter-clockwise rotating vortex. The vortex axis is not vertical, i.e., its core moves downstream as depth decreases and the overall movement of the fluid inside the core of the vortical structure is toward the free surface. Near the free surface, the recirculation zone extends up to 10 groyne lengths downstream of the second groyne.

Near the channel bottom, the distance is close to 6 groyne lengths. As previously mentioned, some of the fluid particles entrained in the outer edges of the vortex in the downstream recirculation area are transported upstream along the lateral channel wall and then close to the downstream face of the second groyne. From there they are swept around the head of the second groyne into the embayment. As one approaches the bottom, the entrainment of fluid from the downstream recirculation region into the embayment is reduced significantly.

Figure 4.21 visualizes the structure of the corner vortex system near the junction between the downstream groyne and the lateral channel wall. The streamlines show the presence of a main tornado-like vortex structure located very close to the corner which entrains fluid from the free surface corner region toward the channel bottom. This structure is similar to the upstream corner vortex system but is significantly weaker. Part of the fluid particles entrained in the core of the corner vortex near the channel bottom are swept upstream around the groyne into the embayment. The other fluid particles are entrained into the main tornado-like vortex in the downstream recirculation region. The discussion of Figure 4.16 to 21 shows the highly complex mechanism through which momentum and mass exchange between the embayment and the region around it occur.

The 3D streamlines used to educe the upstream corner vortex system in Figure 4.22 confirm that its instantaneous structure is far more complex compared to the time-averaged one (Figure 4.15). The primary corner vortex situated in the immediate vicinity of the junction is still the strongest, but there are three smaller vortices, upstream of the primary vortex, which interact among each other and with the primary corner vortex. Over time, these smaller vortices can merge among them or with the primary corner vortex and thus indirectly affect the dynamics of the HV system. Though the structure can vary considerably in time, a comparison of Figure 4.15 and Figure 4.22 shows that the averaged flow gives a relatively good description of the flow dynamics in this region. This is in contrast to the DSL region (compare Figures 4.19 and 4.6).

Figures 4.16 to 4.22 serve to visualize the large scale vortical structures in the mean and instantaneous flow. The presence of the small scale eddies and of eddies responsible for local momentum transfer in the channel bottom region (e.g., ejections, sweeps, outward and inward interactions), especially in the regions situated away from the embayment region where the flow is highly three-dimensional, is not clearly observed in these figures. This is because the visualization of the large scale eddies (e.g., the necklace vortices part of the HV system, the vortex tubes shed in the DSL that merge and grow into larger structures as they are convected downstream, the large coherent structures responsible for most of the momentum transfer inside the embayment) has hidden the presence of the smaller scales. Figures 4.23 to 4.26 try to educe these smaller scale eddies using more appropriate quantities. In particular, the presence of outward interactions and sweep events that play an important role in the movement of sediment particles in the case of a loose bed can be visualized using the fluctuating part of the total instantaneous velocity especially in regions where there is a strong mean velocity component (e.g., in the channel away from the embayment).

For example, Figure 4.23 shows the instantaneous velocity flow field in a yz plane situated upstream of the embayment region. One can observe the presence of secondary eddies with length scales of the order of 0.05D to 0.2D as expected for a turbulent channel flow. The length scale of these eddies appears to slightly increase as one moves away from the channel bottom.

The presence of small scales near the free surface in the embayment region where large scale vortices are present is more appropriately visualized by plotting the contours of the vertical velocity component. They are shown in Figure 4.24a along with the instantaneous total velocity vectors (Figure 4.24b) in the same plane (z/D=0.95). The instantaneous velocity vectors show the presence of a strong corner vortex at the junction between the lateral wall and the upstream groyne, the presence of small scales in the formation region of the DSL and of a strong jet-like flow

originating at the tip of the downstream groyne that convects fluid from the channel toward the embayment. However, along with these larger structures the flow contains small scale eddies as inferred from the presence of small patches of positive and negative vertical velocity distributed over the whole embayment area and the interface region. These patches of positive and negative vertical velocity are also associated with upwelling and downwelling motions in the free surface region that can, in some cases, transport a significant amount of contaminant toward or away the free surface.

Figures 4.25 and 4.26 illustrate the presence of outward interaction (u'>0, w'>0) and sweep (u'>0, w'<0) events in the bottom region. These coherent structures play an important role in the local momentum and mass transport especially in the regions situated away from the embayment where larger more energetic eddies are responsible for most of the momentum and mass transport. For example Figure 4.25 shows the presence of an outward interaction event in the y/D=2.4 plane (see Figure 4.25a). Its presence is observed in the in-plane fluctuating velocity vectors and in the streamwise fluctuating velocity contours in Figures 4.25b and 4.25d, respectively. In these pictures a jet like flow associated with the outward interaction event convects fluid from the bottom region toward the free surface. The strength of the jet is relatively high until z/D=0.15 and the angle of the jet with the bottom is close to 30^0. Observe that the presence of the turbulence events is practically impossible to infer by looking at the vectors of the total instantaneous velocity in the same plane (Figure 4.25c) because of the strong mean streamwise velocity component associated with the mean channel flow. The jet associated with the turbulence event convects not only momentum but also mass. In the case of the jet visualized in Figure 4.25, a patch of higher concentration fluid is present in the bottom region where the jet is forming. As a result, the jet will convect higher concentration fluid away from the bottom. This is clearly observed in the concentration contours (Figure 4.25g) in the plane z/D=0.05

(the exact area shown is marked in Figure 4.25a) where the localized patch of high concentration fluid corresponds with the center of the jet associated with the outward interaction event. Observe also that in the same plane the fluctuating velocity vectors (Figure 4.25f) show that fluid is convected radially outwards from the center of the jet like flow associated with the outward interaction, such that the higher concentration fluid originating from the bottom region is mixing gradually with the surrounding lower concentration fluid. Observe also the presence of a wide range of small energetic scales in the velocity vectors in Figure 4.25f which are responsible for the rapid mixing between the patch of relatively high concentration fluid convected by the jet originating near the channel bottom and the surrounding lower concentration fluid.

A similar phenomenon is observed in Figure 4.26 but in this case a sweep event is captured in the plane y/D=3.4 (see Figure 4.25a). The associated instantaneous concentration contours suggest that the sweep convects higher concentration fluid from the region around z/D=0.25 toward the channel bottom, though in this case the relative difference between the concentration levels away and very close to the bottom is less than the one observed in the ejection event discussed in Figure 4.25. This is due to the fact that larger scale mixing dominates in this region. In fact this is expected, as the sweep event is localized in the recirculation region downstream of the second groyne where large scale coherent structures are much more energetic than the ejection/sweep events and are thus responsible for most of the mass transfer. This is also the reason why a quadrant analysis generally performed for channel flows with a flat or deformed bed (e.g., bedforms) is not very relevant in the case of flow past groynes.

4.3.5 Horseshoe Vortex System

Another important vortical system in the flow is the highly turbulent necklace vortices that form at the base of the upstream groyne (see sketch in Figure 4.27). Due to the adverse pressure gradients and downflow introduced by the presence of the upstream groyne, the incoming boundary layer separates and its vorticity reorganizes at the groyne base forming what is commonly known as the HV system. Upstream of the groyne, the alignment of the main necklace vortices is approximately perpendicular to the channel wall. As the HV approaches the tip of the groyne, it is stretched and elongated as it starts turning around the groyne head before being lifted from the bottom and then dissipated into the downstream flow.

The complex spatial structure of the HV system is shown in Figure 4.27 using instantaneous streamlines in several vertical sections. The vertical planes progress from a plane making a 25^{o} angle with the lateral channel wall to a plane making a 65^{o} angle, as shown in Figure 4.27. Figure 4.28 shows two main coherent structures, A and B, splitting and reemerging along the axis of the mean HV system (see also Figure 4.29). Their relative strength varies along the axis of the mean HV system due to the splitting (e.g., see Figure 4.28b-c for B and Figure 4.28f-g for A) and remerging (e.g., Figure 4.28f and 4.28g for B) of these vortices. Vortex B appears to also interact with secondary vortices C and D which form immediately downstream of the separating line of the incoming boundary layer. As vortices A and B are lifted away from the channel bottom, the HV system starts losing its coherence and its structure becomes highly complex.

The mean spatial structure of the HV system is visualized in Figure 4.29 at the same vertical sections shown in Figure 4.27. The mean spatial structure is composed of a primary vortex A and a secondary vortex B. The mean primary vortex A corresponds to the instantaneous vortex A observed in Figure 4.28. The mean vortex B occupies a region that corresponds to the one over which the instantaneous vortices B, C and D are present in Figure 4.28. Animations show that the elongated mean vortex B does not

correspond to a particular secondary necklace vortex in the instantaneous flow fields. Rather, it is just a consequence of the averaging process in the region in which secondary vortices form and are shed toward the primary vortex A.

The instantaneous and mean HV system is visualized in two planes inclined at 35^0 (frames a-d) and 45^0 (frames e-h) from the lateral wall in Figure 4.30. The secondary necklace vortices interact with the primary vortex in a highly chaotic fashion and modulate the intensity of the HV system in time. In agreement with experimental studies of junction flows (e.g., see Simpson, 2001, Dargahi, 1990), very high levels of turbulence as indicated by the TKE and pressure fluctuations in Figure 4.30c-d and Figure 4.30g-h are predicted inside the HV region. These fluctuations are thought to be one of the main reasons the HV system will induce and sustain the local scouring process in the case of a loose bed.

Figure 4.31 visualizes the evolution of the HV system in time over a period of 0.6D/U. Attention is focused on the plane making a 45^o angle with the lateral channel wall (turbulence statistics are displayed in Figure 4.30c-d for same plane). The large amplification of the velocity and pressure fluctuations shows that the flow inside the HV system is highly turbulent compared to the incoming fully turbulent channel flow. Monitoring the flow over very large time intervals (~150D/U) showed that the HV system was always present, though its overall structure and strength were found to vary significantly. In particular, in Figure 4.31, one can observe the subsequent merging and splitting of vortices L and M (corresponding to the primary necklace vortex A in Figure 4.28) and of the secondary vortex N. Though in the frames of Figure 4.31, vortex M appears to be consistently larger and stronger than L, and at other times the situation is reversed. Sometimes L is practically absent. The secondary vortex N was found to be relatively stable over long time periods and at irregular times to shed smaller vortices that move toward the primary vortex M and eventually merge with it (N1 and M2 in Figure

4.31g and Figure 4.31h). At other times, N appears to lift itself from the floor. The overall structure is changing in time mostly due to the merging and destruction of eddies. Figure 4.32 shows the time history and power spectrum of the streamwise velocity, u, for point p1 situated inside the main vortex M (see Figure 4.31e). The pressure power spectrum is also shown at points p1 and p2 (situated inside the floor attached vortex N). It is evident that the time series in Figure 4.32a contain a wide range of relatively energetic velocity oscillations consistent with the chaotic nature of the motions inside the HV system. The pressure and streamwise velocity spectra at p1 display a range of energetic frequencies between St=0.1 and 10 corresponding to a broad spectrum. Clear peaks are observed in the u-velocity spectrum for p1 at St~0.11 and its first two sub-harmonics (0.22 and 0.33) due to strong non-linear interactions between the primary vortex and the secondary vortices. The main low frequency component (St~0.11 for p1) is quite strong and may be due to the presence of aperiodic oscillations inside of the HV system similar to those observed experimentally by Simpson (2001) for turbulent flow past surface mounted cylinders. A secondary peak at St=0.53 is observed in the pressure spectra at both points.

4.3.5 Bed Shear Stress Distribution

Figure 4.33 shows the contours of the mean non-dimensional bed shear stress relative to the mean value ($\tau_0 = \rho u_{\tau 0}^2, u_{\tau 0}/U = 0.052$) corresponding to fully turbulent flow in a channel of identical section without spanwise obstructions. Maximum values of τ/τ_o are close to 16, which illustrates the large effect of these obstructions on sediment entrainment at the start of the scouring process. As expected, the highest values are recorded around the tip of the upstream groyne in the strong acceleration region and beneath the main HV system. For reference, the critical bed shear stress, τ_{cr}, corresponding to entrainment conditions was calculated using Shield's diagram for a sediment size of d_{50}=0.45mm (the other dimensional parameters were D=0.08m,

U=0.171m/s consistent with the channel Reynolds number). The critical shear velocity was estimated at 0.016m/s ($u_{\tau cr} / u_{\tau 0} \sim 1.8$) and the particle Reynolds number at 6.13, which gives a critical bed-shear stress for sediment entrainment of $\tau_{cr}=0.035\rho U^2$. It corresponds to a value of τ_{cr}/τ_o of 3.3. Figure 4.33b shows the instantaneous distribution of the non-dimensional bed shear stress. Areas of entrainment for the mean and instantaneous flow are shown in Figure 4.33c-d. The largest instantaneous bed shear stress values can be as high as 22. Figure 4.33e-g shows time series of the instantaneous non-dimensional bed shear stress. The positions of points p11, p12 and p13 are given in Figure 4.33c. The instantaneous values at these representative points situated beneath the HV system can be as much as 60 to 100 percent higher than the mean values.

Despite the fact that most of the large values of the instantaneous bed shear stress are recorded beneath the HV system, high values are also present beneath the DSL. These relatively large values are induced by the convection of the high-vorticity eddies that populate the DSL. A comparison between the mean and the instantaneous bed shear stress illustrates a profound point with regard to scour prediction for groyne fields with a loose bed. The instantaneous distribution of the bed shear stress suggests that sediment transport models which predict entrainment based only on the condition that the mean bed shear stress is larger than a critical value would not be very accurate when applied to complex junction flows like the flow past a channel with groynes. Successful prediction of sediment transport and scour requires use of models that can account for the turbulence characteristics near the bed, including the effect of coherent structures, and for the temporal variability in the distribution of the bed shear stress at least in a statistical way (e.g., variance and the mean bed shear stress value should be predicted by the model). Use of time-accurate eddy-resolving techniques which have the ability to capture these phenomena (e.g., macro-turbulence events) as part of the simulation will automatically reduce the amount of modeling needed in the equations that describe the sediment transport and bed evolution.

4.4 Mass Exchange Processes

4.4.1 General Description

Based on the previous analysis of the dynamics of the coherent structures, the primary mass exchange mechanism is due to the eddies shed from the groyne tip that are transported along the horizontal DSL and interact with the coherent structures within the embayment and with the tip of the downstream groyne (partial or total clipping events). A secondary mechanism (see discussion of Figure 4.12) is due to the eddies that are shed from the tip of the downstream groyne into the embayment. It was shown that these eddies transport low-concentration fluid from the region around the head of the downstream groyne into the embayment. These eddies are convected along the diagonal of the embayment, dislocating areas of higher-concentration fluid that is pushed parallel to the upstream groyne face into the upstream part of the DSL. The patches of high concentration fluid are then engulfed by eddies contained within the DSL and advected rapidly into the region downstream of the embayment.

Details of the mixing process in the free surface plane are inferred from Figure 4.34 that shows contours of the instantaneous contaminant concentration at different times. The temporal evolution of the concentration fields illustrates the dispersion of the contaminant as it is removed from the embayment region and advected downstream. Most of the contaminant which exits the embayment area is then trapped in the wake behind the embayment. At t=60D/U (Figure 4.34j), 97% of the initial mass of contaminant has left the embayment. The concentration scale is different in frames i and j such that the flow structures and the concentration fields behind the embayment can be easily observed.

The visualizations of the concentration fields confirm that the mass exchange occurs primarily as the higher concentration fluid within the upper layer of the embayment is pushed parallel to the face of the upstream obstruction toward its head and

from there inside the DSL. Additionally, through interactions between the eddies advected inside the DSL with the embayment, pockets of higher concentration fluid from the interface region are sometimes entrained into the DSL and from there into the channel.

The entrainment of low concentration fluid back into the embayment near the tip of the downstream groyne as a result of the shedding occurring at the tip of the obstruction (see discussion of Figure 4.12) is captured in Figure 4.34c, where a wisp of very low concentration fluid is advected into the surrounding higher concentration fluid. Most of the contaminant which exits the embayment area is then advected in the wake behind the embayment. Additionally, as observed especially in Figures 4.34i and 4.34j, mixing takes place laterally by the large-scale structures that engulf the surrounding fluid near the interface between the channel fluid and the higher concentration fluid in the wake past the embayment. In particular, large scale intrusions of wisps of low concentration fluid are observed in Figure 4.34j. Their characteristic length scale is of the order of the groyne width, l.

Though the purging of the contaminant is an unsteady process, it is interesting to analyze the time series of the concentration and the associated range of high frequency fluctuations induced by the turbulence. The concentration time series at point B inside the separated shear layer and at point D (see Figure 4.8a) inside the main recirculation eddy downstream of the embayment are shown in Figure 4.35 along with the concentration power spectrum at point D. The mean decay of the concentration at point B is modulated by a wide range of energetic frequencies ($2<St<10$). As a consequence of the entrainment of wisps of zero concentration fluid inside the separated shear layer, the concentration at point B decays to values very close to zero during these high frequency oscillations. Downstream of the embayment, at point D, the mean concentration peaks at around 25D/U and then decays practically exponentially. Similar to point B, high frequency oscillations around the mean (filtered) time variation are observed in the time

history of the concentration, but the frequencies associated with these oscillations are lower (0.3<St<3) and correspond to the larger eddies containing relatively well mixed fluid that are convected past the embayment.

4.4.2 Temporal Variation of the Mean Contaminant Concentration within the Embayment

In practice, predictive one-dimensional transport models that rely on empirical dispersion coefficients based on dead-zone theory are utilized to globally characterize the mass exchange between channel and embayment. The equation that is generally used to describe the 1D mass exchange between the embayment and the main channel (Uijttewall et al. 2001) is:

$$\frac{\partial M}{\partial t} = -\frac{1}{T}\left(M_r - M\right) \tag{4.1}$$

This practically reduces to assume an exponential decay of the mean concentration (mass of contaminant inside embayment) in time of the form:

$$\frac{M - M_r}{(M_0 - M_{r0})} = \exp(-\frac{1}{T}\Delta t) = \exp\left(-\frac{\Delta t \cdot U / D}{T \cdot U / D}\right) = \exp\left(-\frac{\Delta t \cdot U / D}{k}\right) \tag{4.2}$$

where T is the characteristic decay time, k is the non-dimensional exchange coefficient related to the characteristic decay time T, M is the contaminant mass fraction (or mean concentration) in the embayment, and M_r is the contaminant mass fraction in the channel which is assumed to be zero. The index zero corresponds to the values of the variables at t=0.

Defining *k* as simply D/(UT) allows a direct comparison of the decay rates in the emerged and submerged cases (see Chapter 5). The value of *k* can be estimated directly from the decay rate of the mass of contaminant in time plotted in a log-linear scale. This was done in Figure 4.36 where the decay of the mean contaminant concentration in time is plotted. In the case of a groyne field in which the bottom elevation inside the

embayment region is constant and equal to that inside the main channel, the nondimensional exchange coefficient is often defined for fully emerged groynes (Uijtewaal et al., 2001) as

$$k_e = l/(UT) = l/D\,k \qquad (4.3)$$

where l is the embayment width (=0.625D). To facilitate a comparison with submerged groynes (see Chapter 5), the values for k will be used in the following discussion.

As shown in Figure 4.36, the decay in the contaminant mass within the embayment can be described fairly accurately by such an equation provided that the exchange coefficient assumes different values in the initial phase (k=0.10 up to 12D/U) and final phase of decay (k=0.05). In general, the boundary between the two regimes is expected to depend on the particular geometry of the embayment and flow conditions. However, for the present embayment aspect ratio for which a one gyre circulation pattern (one dominant recirculation eddy) is observed at the free surface, the presence of two regimes of exponential decay is somewhat expected (see also Engelhardt et al., 2004). The fact that in the later stages of the decay the exchange coefficient is sensibly smaller (by a factor of two for the geometrical setup and flow conditions considered in the present work) is related to the presence of the bottom boundary which slows the process considerably. This is also supported by results of simulations of the flow in cavities without bottom walls (flow is homogeneous in the vertical direction) where it was shown that the contaminant mass decay within the cavity can be approximated by an exponential function with a unique constant over the whole length of the removal process (Chang et al., 2006).

4.4.3 Non-Uniformity of the Mass Exchange Process over the Embayment Depth

Visualizations of the concentration fields at practically all stages of the contaminant removal process strongly suggest that the mass exchange process is highly

non-uniform over the depth. For example, Figure 4.37 shows instantaneous concentration contours at the free surface, mid-groyne depth, near the channel bottom (z/D=0.1) and at mid distance between the two groynes (x/D=2.75) in the embayment area at t = 15.0D/U. Clearly, more high concentration fluid is situated near the channel bottom than near the free surface, as observed from comparison of frames a, c and d in Figure 4.37. This is due to the presence of the bottom boundary layer where the velocities, in particular the transverse component toward the channel in the interface region, are lower. The main effect is that the contaminant ejection from the embayment through the corresponding (bottom) part of the channel-embayment interface is slowed down. Intrusions of low concentration fluid into the embayment near the tip of the downstream groyne are observed in Figure 4.37a-b consistent with the 3D streamline patterns observed in Figure 4.17 near the free surface. Figure 4.37d visualizes the non-uniformity over the depth of the instantaneous concentration field.

The instantaneous velocity and concentration fields from LES are used next to understand the overall mass transport within the embayment and between the embayment and the channel. This is important, as even advanced experimental methods are not able to quantify the non-uniformity of the mass exchange process over the depth. To quantify the mass exchange between different levels within the embayment, it was subdivided into three layers of equal volume corresponding to the top, middle and bottom regions.

Figure 4.38 shows the contaminant mass decay in each of the three layers in log-log scale. The exchange coefficient k is found utilizing equation (4.2) for each layer. In each zone, distinct values of the exchange coefficient characterize the mass exchange during the contaminant removal process. At the start of the mass exchange process (up to ~4-5D/U), the decay of pollutant in the three layers is transpiring at very different rates. The equivalent exchange coefficient in the bottom, middle and top layers is equal to 0.05, 0.10 and 0.16, respectively. After t=20D/U, the value of k drops to values around 0.05 in all three layers, with the top layer displaying the highest variability. However, as shown

in Figure 4.36, the value of the exchange coefficient for the whole embayment volume becomes equal to 0.05 after 12D/U mainly because the average value of *k* in the top and bottom layers is practically equal to the value in middle layer which is already close to 0.05.

Figure 4.39 analyzes the fluxes through the different open surfaces of the three layers, enabling a better understanding of the large-scale circulatory motions within the embayment and between the embayment and the main channel. The time derivative of the mass decay (-MT) is considered positive when it corresponds to a reduction in the total mass inside the corresponding layer, while the fluxes through the embayment-channel interface (F1, F2 and F3) are positive when contaminant is leaving the embayment. The scale of the contaminant mass flux was changed for t>30D/U in Figures 4.39b, 4.39d and 4.39f to facilitate visualization of the contaminant flux variations in the later stages of the purging process.

In Figure 4.39a-b, -MT1 is the rate of change of the mass within the top embayment layer, F1 is the flux into the main channel through the top interface region and F5 is the flux through the bottom surface (F5 is positive when it corresponds to contaminant moving upwards into the top layer). F5 is usually oriented toward the free surface (-F5<0), but there are times when this flux is reversed, especially during the initial part of the mixing process (t<4D/U) when contaminant is convected toward the middle layer at about half the rate at which it exits the embayment. This also explains the very high value of the exchange coefficient in the top layer during this period. The flux toward the main channel (F1) is usually larger in magnitude than the flux through the bottom surface (F5), and for t>5D/U, a high correlation between their variations can be observed indicating some sort of equilibrium regime where an important part of the contaminant that leaves the top layer via the channel-embayment interface is not originating in the top layer but is rather advected from the lower embayment regions by

the large-scale 3D motions. The difference accounts for the overall decrease of the mass within the top layer during the final phase of decay.

In the bottom layer (Figure 4.39c-d), the contaminant flux through the embayment plane is denoted F3 and the flux through the top surface is denoted F4 (F4 is positive when the flux direction is toward the bottom). Most of the time, F3 is oriented toward the channel, though there are periods when F3 is negative (e.g., around 12D/U, 24D/U and 33D/U) and a small amount of contaminant is reentering the embayment through the bottom part of the interface. The flux F4 is oriented generally toward the free surface (-F4>0), but there are small time intervals (e.g., around 2D/U, 21D/U and 38D/U) when the flux direction is reversed. The magnitude of F3 is considerable smaller than that of F4 except near the start of the mixing process when some of the contaminant from the middle layer is convected toward the bottom. For t>5D/U, there is a fairly high correlation between the large scale fluctuations of F4 and those of the rate of change of the contaminant mass within the bottom layer, -MT3, showing that the decay of the mass of contaminant in the bottom layer is largely due to the contaminant leaving this layer through the top surface toward the middle layer.

Finally, in the middle volume (Figure 4.39e-f), the flux through the embayment interface (F2) is virtually always oriented toward the main channel. The fluxes through the top surface (F5) and bottom surface (F4) are generally oriented in the same direction toward the free surface. However, near the start of the mixing process (t<4.5D/U), F5 is oriented toward the bottom. With the exception of a couple of short time intervals, the mass of contaminant in the middle layer is decaying in time (-MT2>0). Several periods are observed when the fluxes through the bottom and top surfaces are near equilibrium (F5~-F4) and values of the interface flux F2 and -MT2 are relatively small, denoting that the primary transport process consists of advection of contaminant from the bottom layer toward the top layer and from there into the main channel (e.g., for 10D/U<t<19D/U). During other time periods (e.g., t~37D/U), -MT2 and F2 are relatively larger than the

magnitudes of F4 and F5, and the primary transport process consists of contaminant being advected into the channel through the embayment interface. A third, less frequent situation occurs when the flux toward the top layer and the contaminant mass decay within the middle layer are small. In this case, the primary transport consists of contaminant from the bottom layer entering the middle layer and then being advected into the main channel.

The aforementioned scenarios illustrate the role played by the 3D vertical motions inside the embayment and the effect of the bottom surface on the mass exchange between the embayment and the main channel. The overall effect of these motions and of the transverse velocity profile at the channel-embayment interface is to produce a non-uniform cumulative mass transport into the main channel respective of the layers within the embayment. Figure 4.40 shows the cumulative mass (time integral of the interface flux) transferred into the main channel from the three layers. The mass is normalized by the initial mass of contaminant present inside the embayment (M_0=0.78 D^3C_0). The total amount of contaminant passing through the top, middle and bottom embayment-channel interfaces is 0.384, 0.258 and 0.128D^3C_0 respectively, (0.492, 0.329 and 0.163 normalized). If the flow were homogeneous in the vertical direction or the channel were very deep, the mass of contaminant exiting all the layers would be the same for all the three layers and equal to the original mass of contaminant within each layer. This is obviously not the case for the present embayment where after t = 75D/U, 151%, 99.5% and 49.5% of the initial mass of contaminant (0.26 D^3C_0) present in the top, middle and bottom embayment layers has been purged from the embayment through the corresponding interfaces into the channel.

4.4.4 Mass Transport through the Channel

Figure 4.41 illustrates how the contaminant is transported and dispersed through the channel. Figure 4.41a compares the cumulative mass of contaminant passing through

the embayment plane and through each of the seven cross sections situated downstream of the embayment. Their positions are shown in Figure 4.41e. The cumulative mass is non-dimensionalized by the total mass of contaminant present initially inside the embayment.

Figure 4.41c to 4.41f quantify the mass flux variation in time through each cross section. As expected, at the embayment plane the flux is the largest in the initial phases of the mixing. The maximum value is $0.09D^2UC_0$ (ρ=1). Subsequently, the contaminant mass decay is fairly exponential. At the channel cross sections, there is a delay time needed for the cloud of contaminant to start reaching that section (the delay time is easily inferred from Figure 4.41a) followed by a relatively short time interval where there is a sharp increase of the flux to its maximum value. Because turbulent diffusion spreads the contaminant as it is transported downstream, the maximum flux in each successive cross section is decreasing. At the x/D=17 section, the maximum recorded flux is only 0.038 $D^2U\ C_0$. After the peak value is reached, there is a final period over which the mass flux is decaying fairly slowly. Though the overall decay in the final period appears to be exponential at all sections monitored, large fluctuations due to large scale mixing phenomena, in particular engulfing, are present and reflect the turbulent nature of the flow and the presence of large shed eddies and vortices downstream of the embayment region.

4.5 Summary

The dynamics of the large scale structures in the vicinity of the embayment region of a channel with two fully emerged groynes and the role of these structures in the momentum and mass exchange between the embayment and the channel were investigated using the mean and instantaneous flow fields. The averaged and instantaneous three-dimensional features of the vortex systems upstream, within and

downstream of the embayment were clarified. The upstream recirculation area was found to contain a dominant vortex residing in the lateral wall-groyne junction region. This main vortex interacts with multiple smaller vortices whose structure is highly variable in time. For the geometric configuration considered in this chapter, the main tornado-like corner vortex feeds fluid and momentum into the HV system. It can be speculated that this connection will become weaker as the length of the groyne increases.

The eddies that are shed from the tip of the upstream groyne and their interactions with the embayment fluid in the interface region and with the tip of the downstream groyne were found to play an essential role in the momentum and mass transport processes. The interaction between the eddies inside the DSL and the embayment is such that some of the fluid inside the downstream recirculation zone can be transported from downstream of the second groyne back into the embayment, and from there, after a complex recirculation process, back into the high speed DSL area.

The simulations demonstrated that a strongly turbulent HV system is present at the base of the upstream groyne. The time-averaged values of the bed shear stress showed that the largest values were reached in the strong acceleration region near the tip of the upstream groyne and beneath the main necklace vortex of the HV system. The instantaneous distributions of the bed shear stress showed that large oscillations around the mean values are quite common and that large bed shear stress values can be induced by the eddies advected inside the DSL.

To elucidate the mass exchange processes, the dispersion of a passive contaminant, originally introduced instantaneously within the embayment volume, into the main channel was computed and analyzed. The decay of the mass of contaminant within the embayment was quantified, which enabled calculation of a global exchange coefficient used in dead-zone models. It was found that the contaminant removal process is not uniform. In the initial phase of decay over which about 68% of the total mass of

initial contaminant leaves the embayment, the exchange coefficient is about twice the value recorded for the final phase.

The dynamics of the contaminant transport within the embayment and the mass exchange between the embayment and the main channel were studied in detail by analyzing the mass transport in the top, middle and lower layers of the embayment separately, which is very difficult to achieve experimentally. It was found that past the very initial stages of the mixing, part of the contaminant entrained outside the embayment in the middle and top layers does not originate in these layers but, rather, is convected from the bottom region. The process was found to be highly three dimensional, and the bottom of the embayment acted toward delaying the mass exchange process. This also offers a possible explanation for why the exchange coefficient is not single valued over the whole duration of the mass exchange process, as is the case for the flow past '2D' cavities of similar aspect ratio.

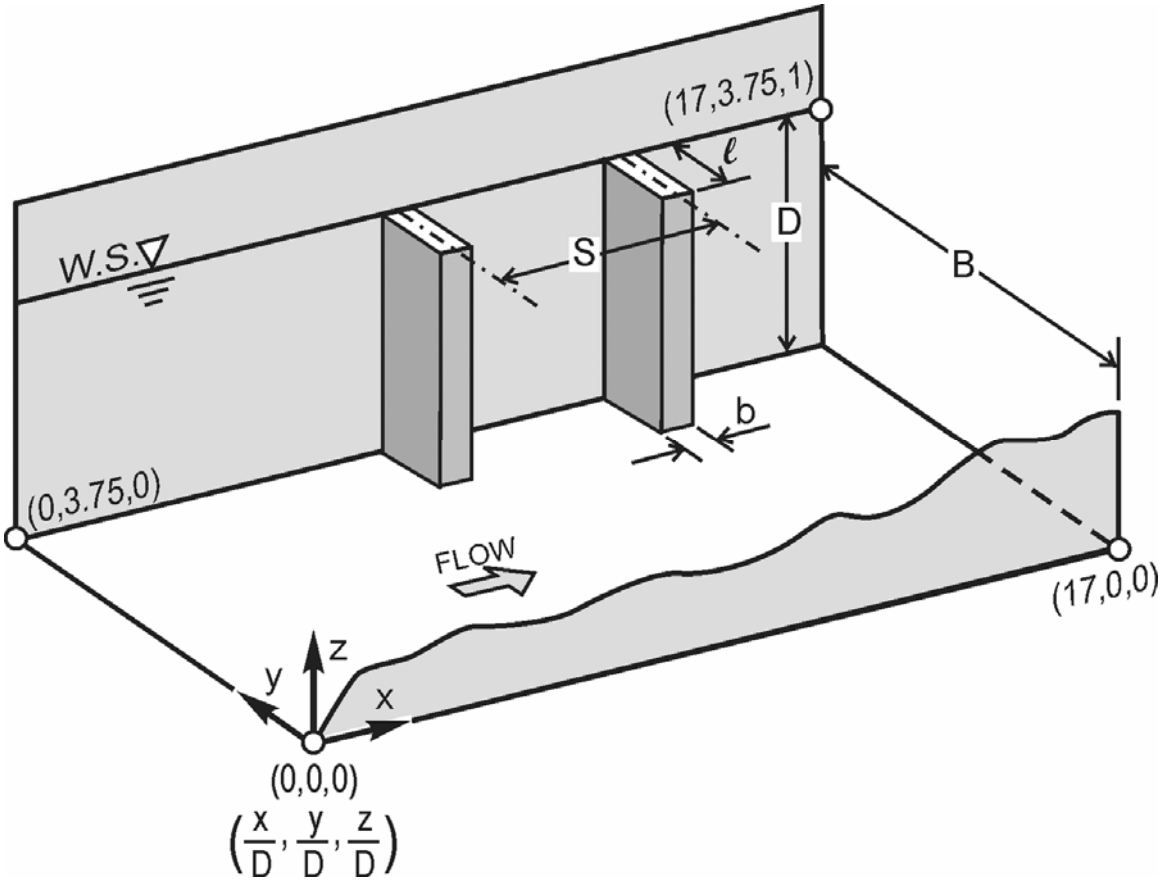

Figure 4.1 Sketch showing channel flow with two emerged groynes (one embayment).

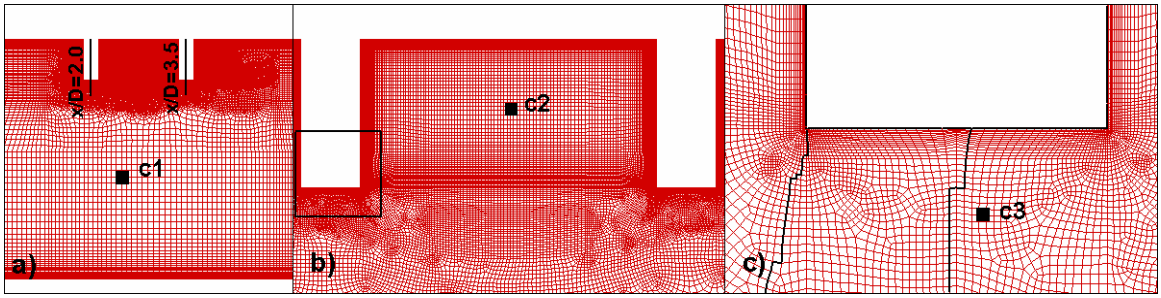

Figure 4.2. Visualization of the mesh in the free surface plane. a) partial view showing complete channel width; b) detail around embayment region; c) detail around groyne tip also showing domain partition on processors.

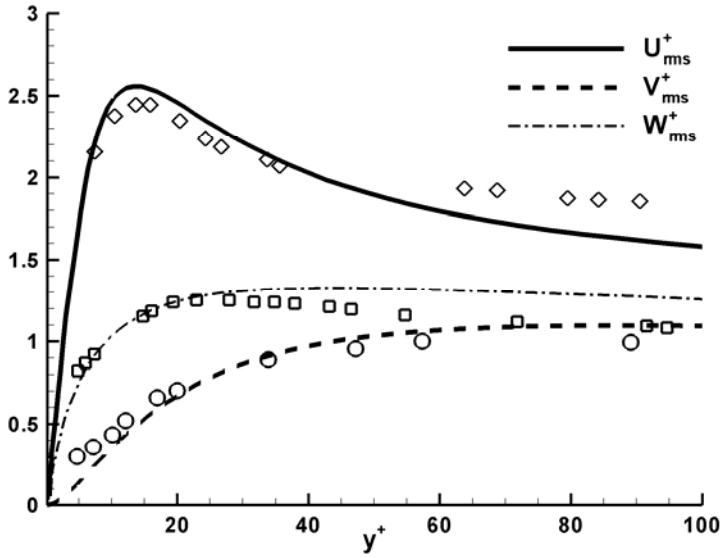

Figure 4.3. Variation of the velocity fluctuations away from the bottom wall ($0<y^+<100$) in the channel flow simulation used to specify inflow velocity conditions. The simulation results are shown with lines. Experimental data (Hussain and Reynolds, 1975, Wei and Willmarth, 1989) obtained in closed channels at comparable Reynolds numbers are shown with symbols.

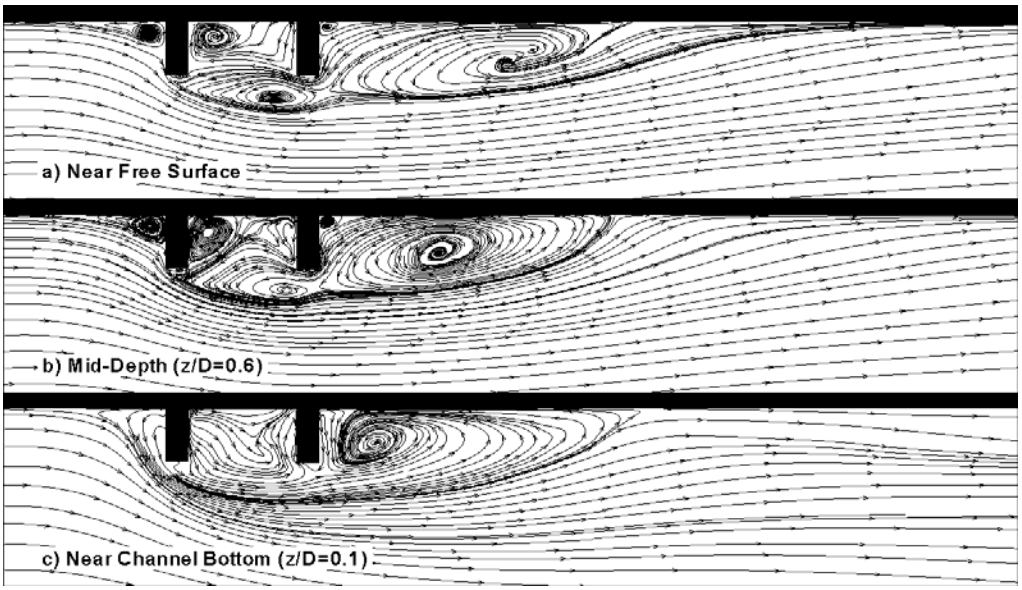

Figure 4.4. Mean velocity streamlines showing flow patterns; a) near the free surface; b) near mid-depth (z/D=0.6); c) near the channel bottom (z/D=0.1).

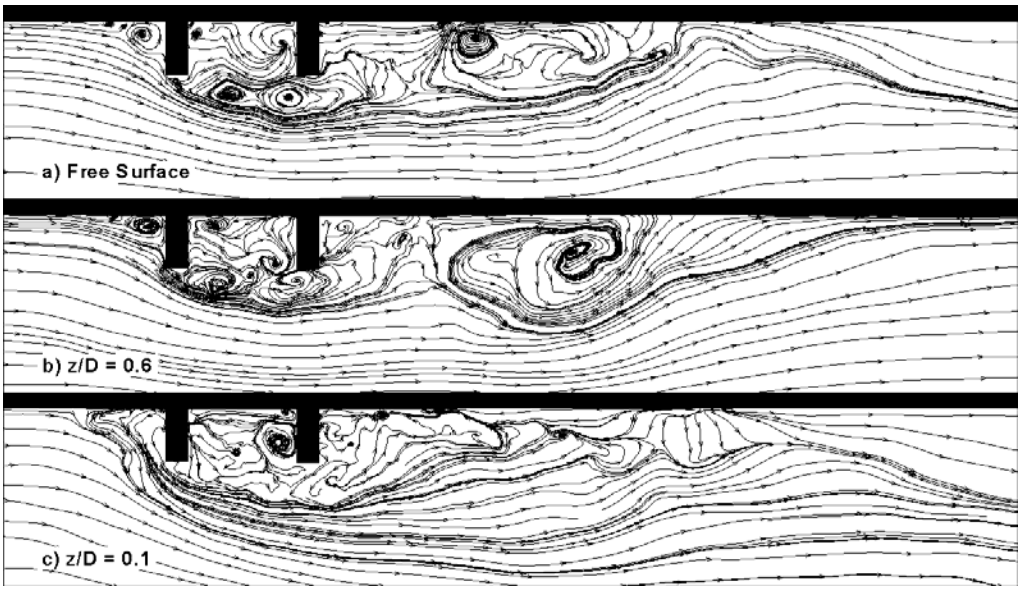

Figure 4.5. Instantaneous velocity streamlines showing flow patterns; a) near the free surface; b) near mid-depth (z/D=0.6); c) near the channel bottom (z/D=0.1).

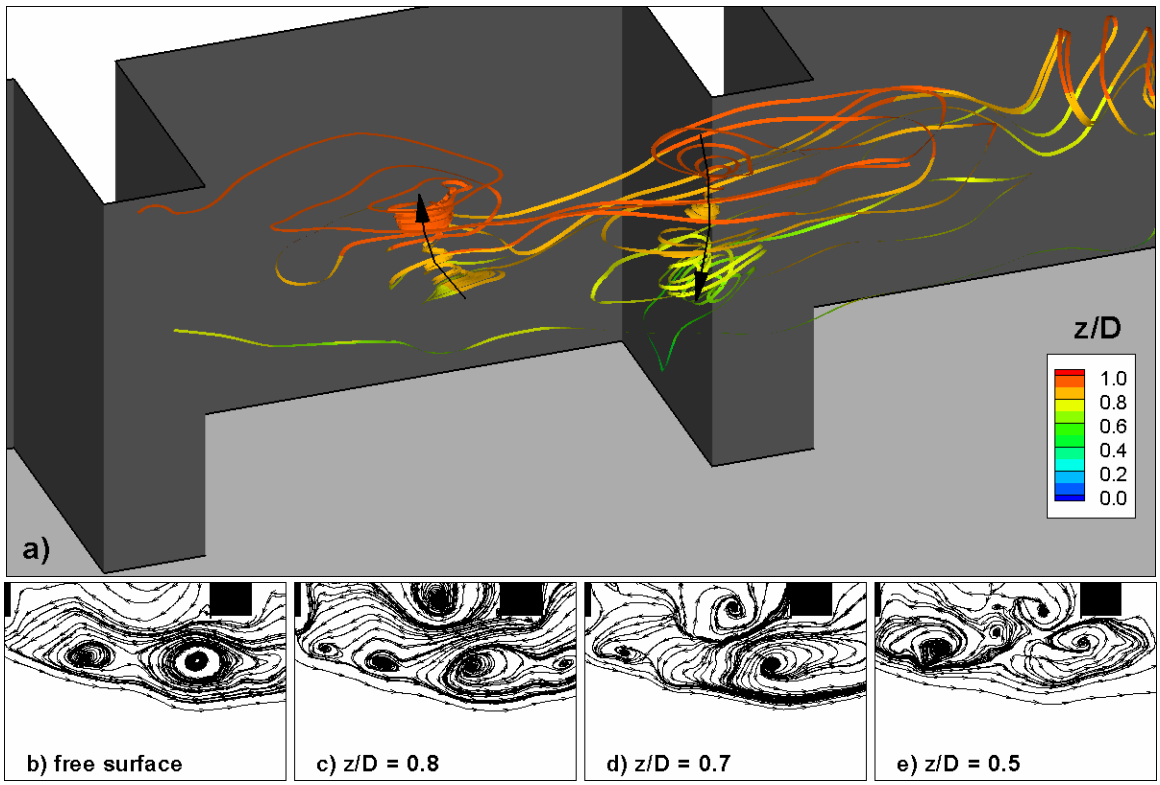

Figure 4.6. Instantaneous velocity streamlines visualizing coherent structures being advected inside the DSL. a) 3D streamlines; and 2D streamlines in horizontal planes: b) free surface; c) z/D=0.8; d) z/D=0.7; e) z/D=0.5.

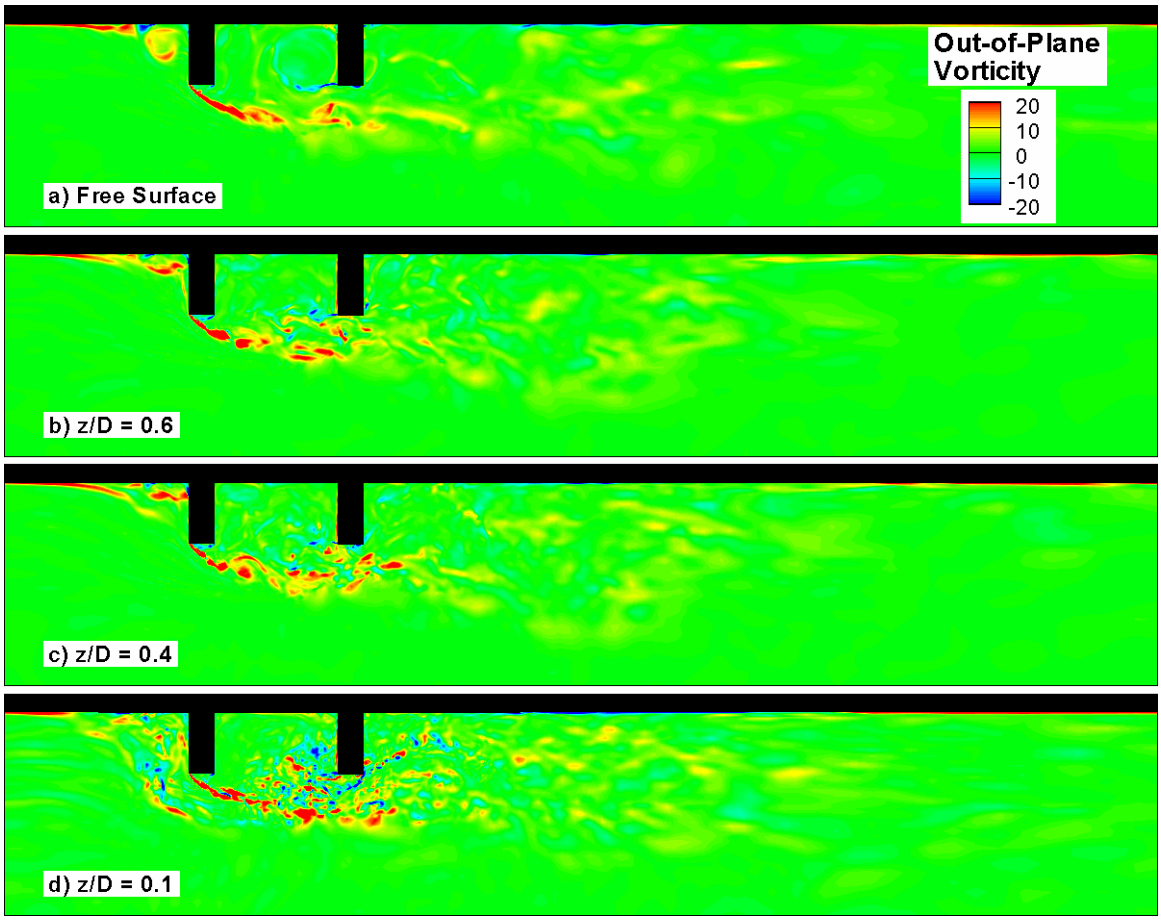

Figure 4.7. Instantaneous out-of-plane vorticity contours. a) free surface; b) z/D=0.6; c) z/D=0.4; d) z/D=0.1.

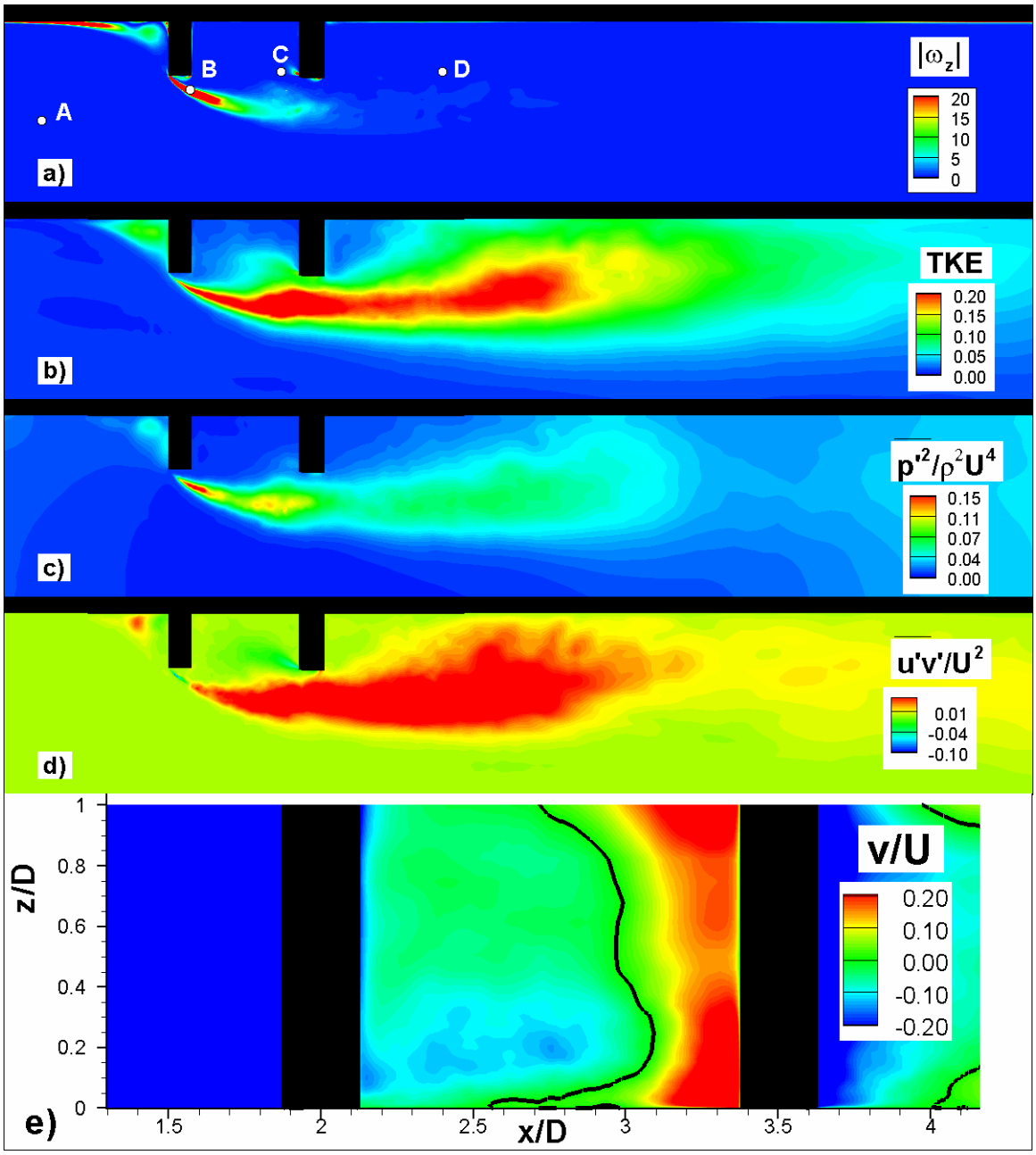

Figure 4.8. Mean flow and turbulence statistics in a plane situated at mid groyne depth (z/D=0.5); a) out-of-plane vorticity magnitude; b) TKE; c) pressure fluctuations; d) $\overline{u'v'}/U^2$; e) transverse velocity at embayment interface (y/D=3.125).

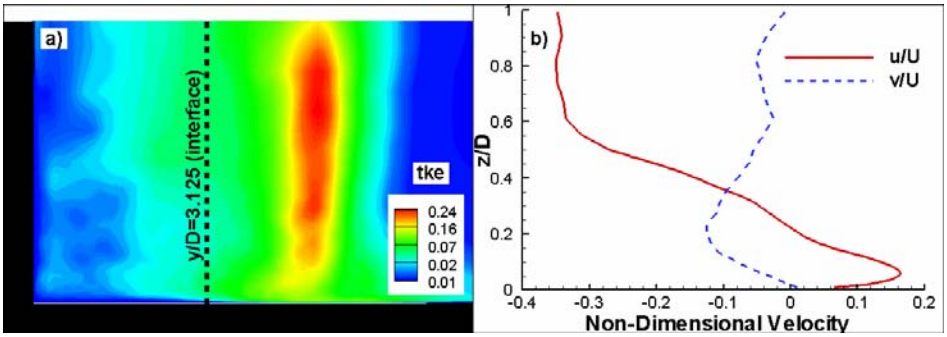

Figure 4.9. Visualization of the mean flow in a vertical plane situated at mid-embayment length (x/D = 2.75); a) TKE; b) streamwise and spanwise mean velocity profiles at (y/D=3.125, x/D=2.75).

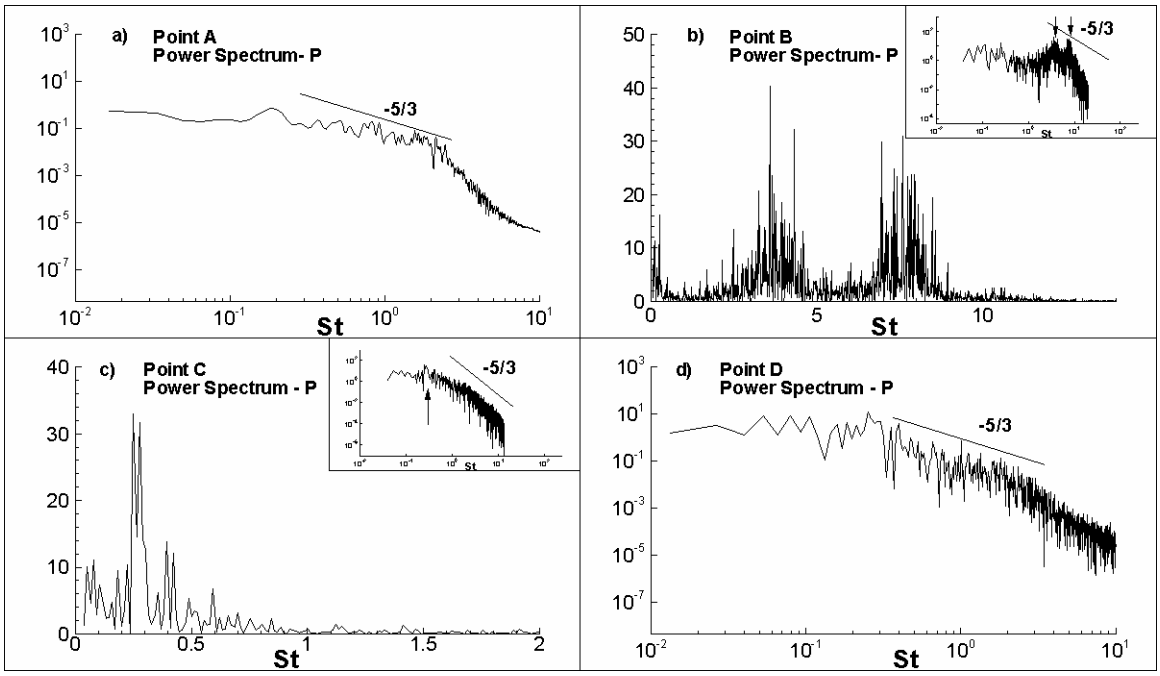

Figure 4.10. Pressure power spectra in the flow domain near the free surface (position of points is shown in Figure 4.8); a) near inflow (point A); b) near tip of upstream obstruction inside separated shear layer (point B); c) inside the embayment near the downstream obstruction (point C); d) in the wake region (point D).

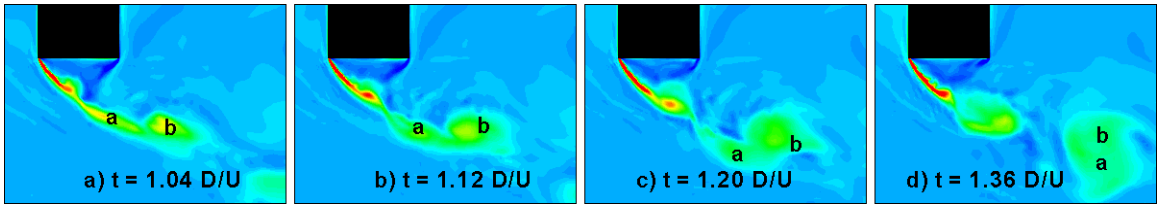

Figure 4.11. Out-of-plane vorticity contours at the free surface showing shedding of vortex tubes from upstream groyne tip and subsequent merging; a) t = 1.04D/U; b) t = 1.12D/U; c) t = 1.20D/U; d) t = 1.36D/U.

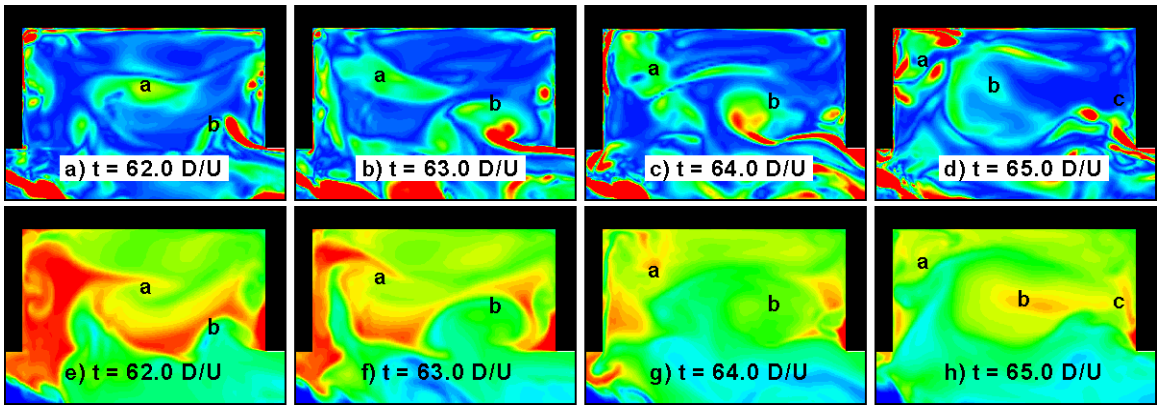

Figure 4.12. Out-of-plane vorticity contours at the free surface plane showing shedding of clockwise vorticity containing low concentration fluid from the tip of the downstream groyne into the embayment; Vorticity contours at: a) t = 62.0D/U; b) t = 63.0D/U; c) t = 64.0D/U; d) t = 65.0D/U; Concentration contours at: e) t = 62.0D/U; f) t = 63.0D/U; g) t = 64.0D/U; h) t = 65.0D/U.

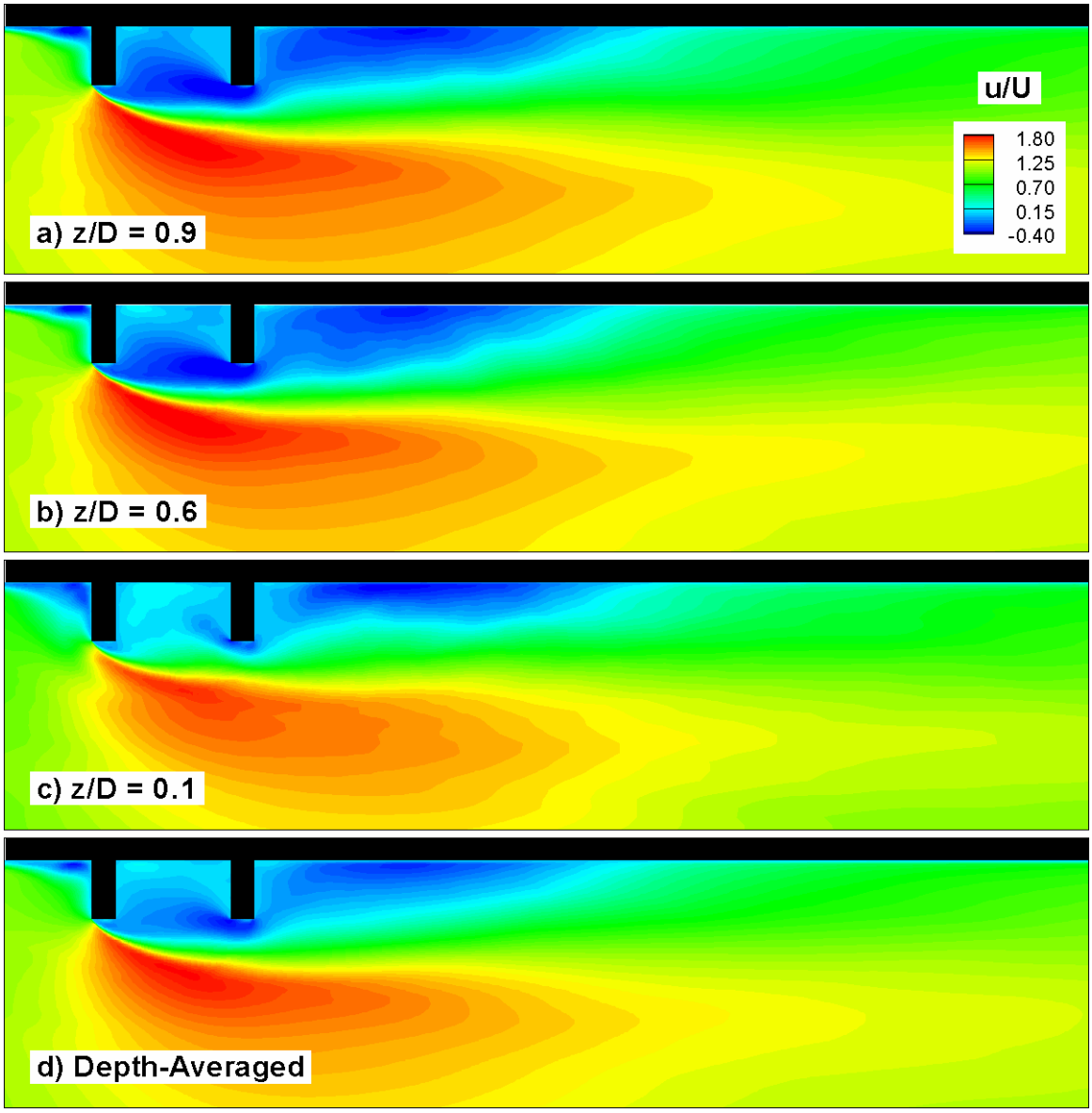

Figure 4.13. Distribution of mean streamwise velocity, u/U, in horizontal planes; a) z/D = 0.9; b) z/D = 0.6; c) z/D = 0.1; d) depth-averaged.

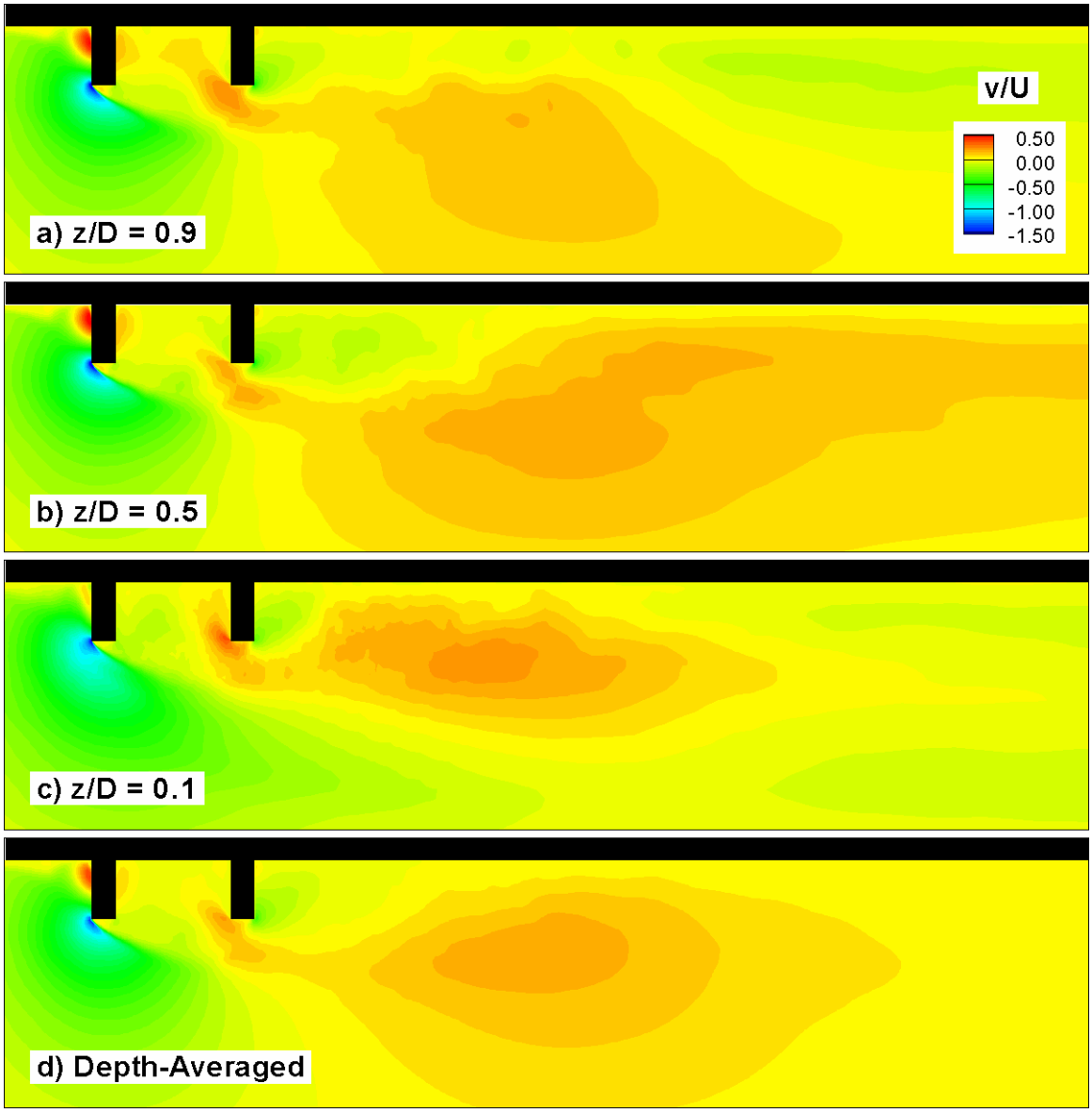

Figure 4.14. Distribution of mean spanwise velocity, v/U, in horizontal planes; a) z/D = 0.9; b) z/D = 0.6; c) z/D = 0.1; d) depth-averaged.

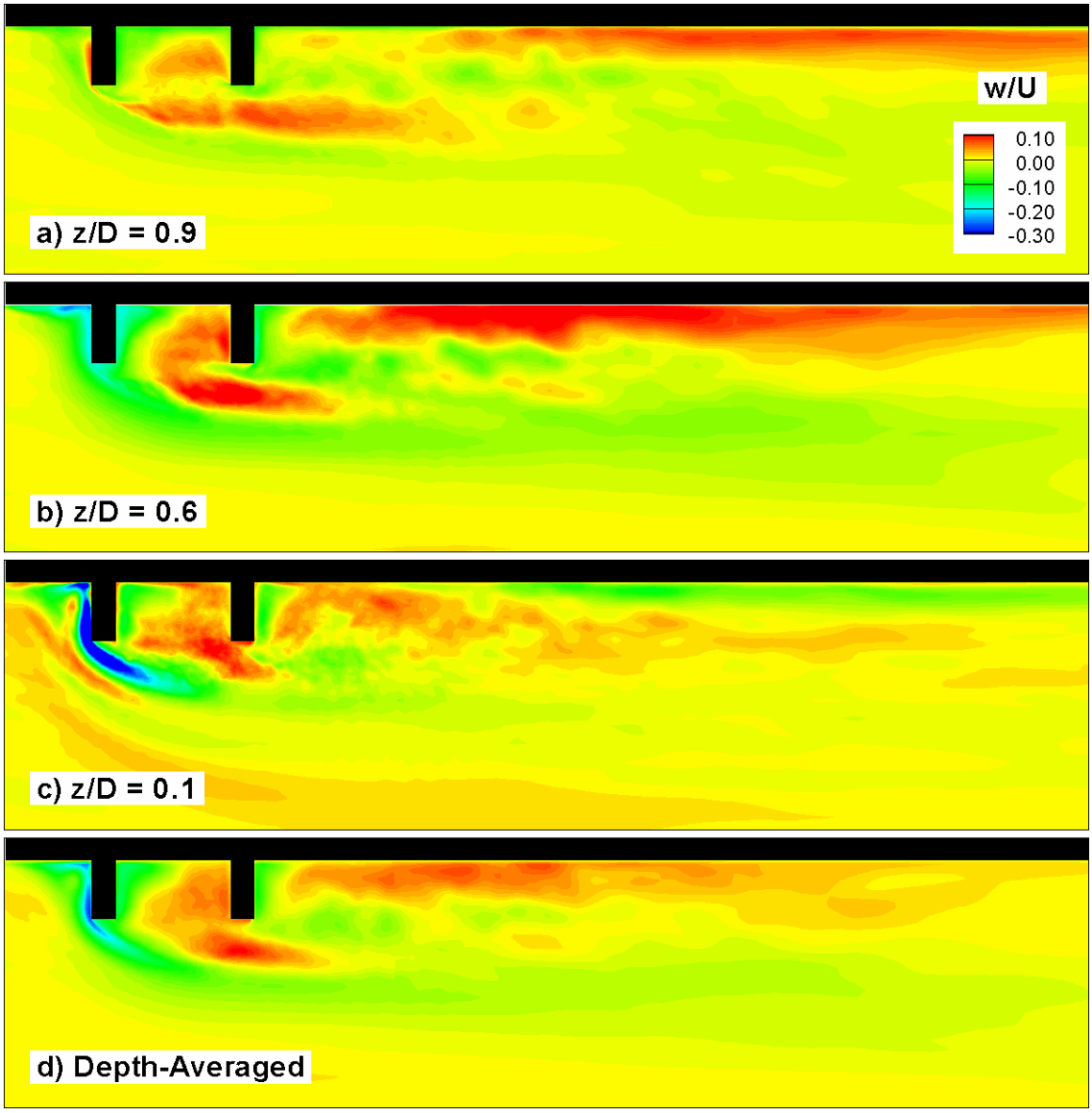

Figure 4.15. Distribution of mean vertical velocity, w/U , in horizontal planes; a) z/D = 0.9; b) z/D = 0.6; c) z/D = 0.1; d) depth-averaged.

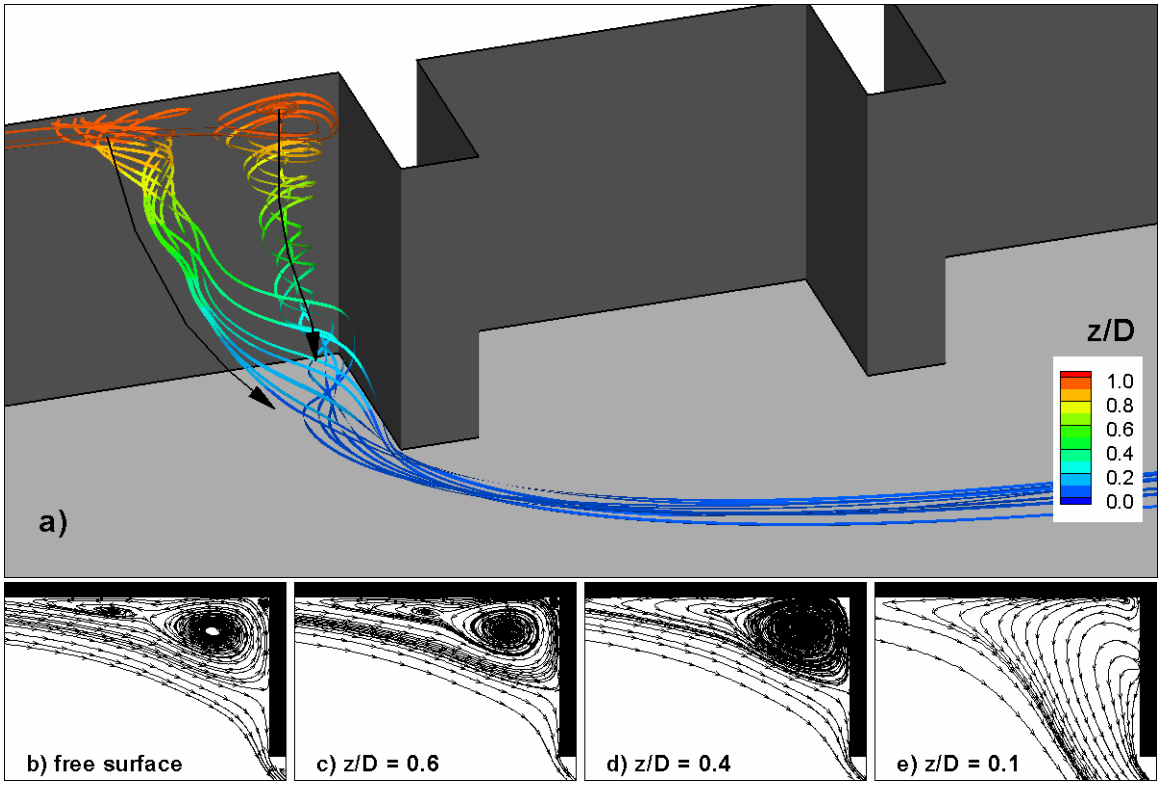

Figure 4.16. Mean velocity streamlines illustrating 3D structure of the flow in the upstream recirculation zone; a) 3D streamlines; and 2D streamlines in horizontal planes: b) free surface; c) z/D=0.6; d) z/D=0.4; e) z/D=0.1.

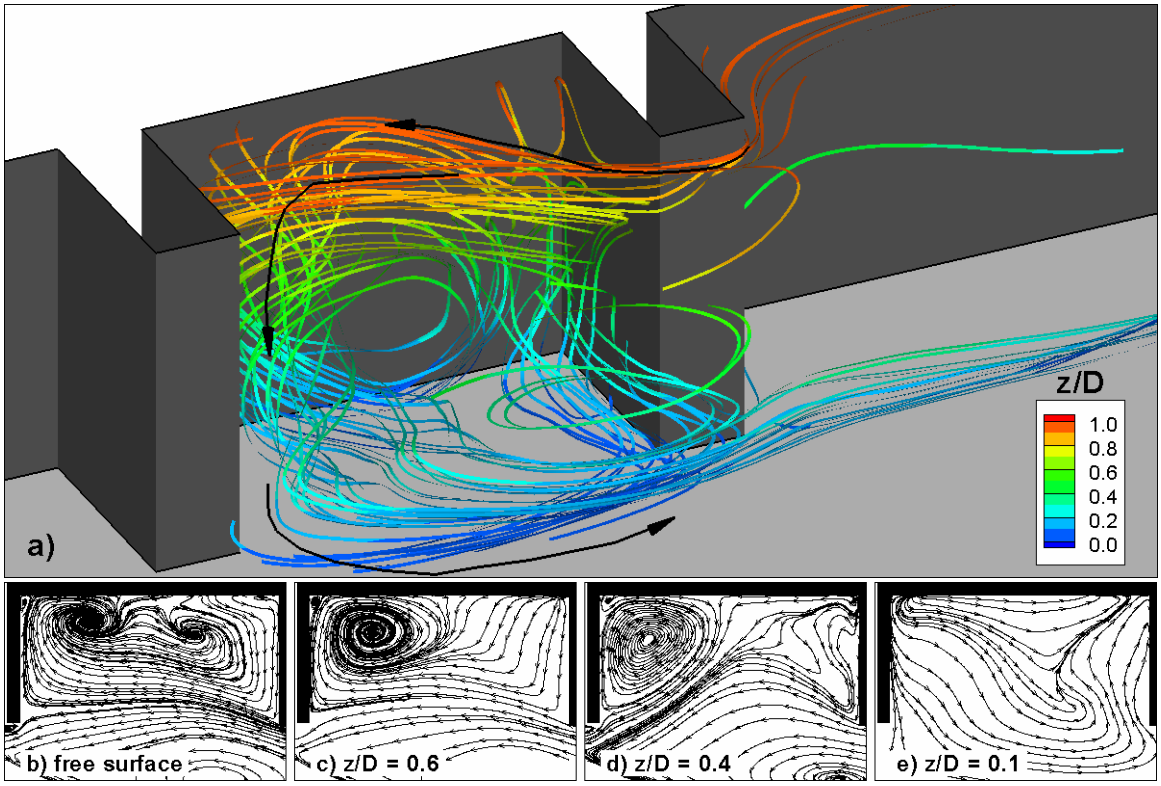

Figure 4.17. Mean velocity streamlines illustrating 3D structure of flow inside embayment; a) 3D streamlines; and 2D streamlines in horizontal planes: b) free surface; c) z/D=0.6; d) z/D=0.4; e) z/D=0.1.

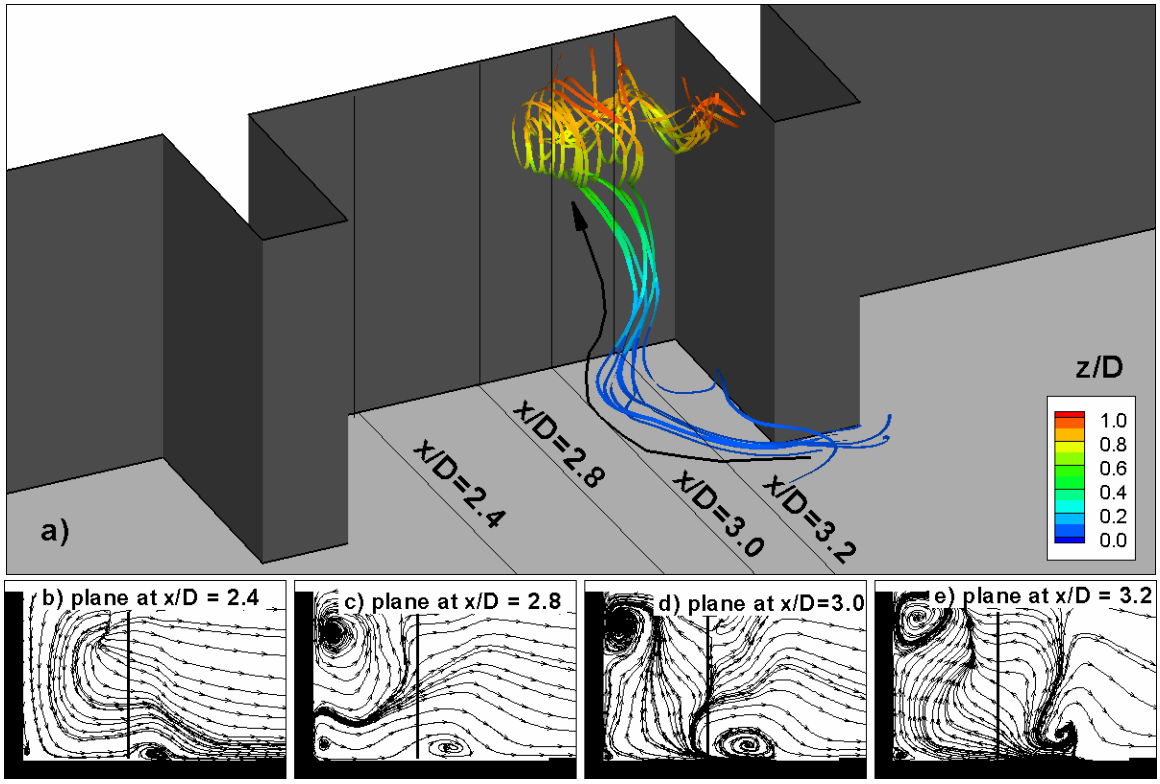

Figure 4.18. Mean velocity streamlines illustrating 3D structure of flow inside the embayment; a) 3D streamlines visualizing a streamwise-oriented vortex near the free surface; and 2D streamlines in vertical spanwise planes: b) x/D=2.4; c) x/D=2.8; d) x/D=3.0; e) x/D=3.2. The channel-embayment interface is depicted by the bold vertical lines in frames b to e.

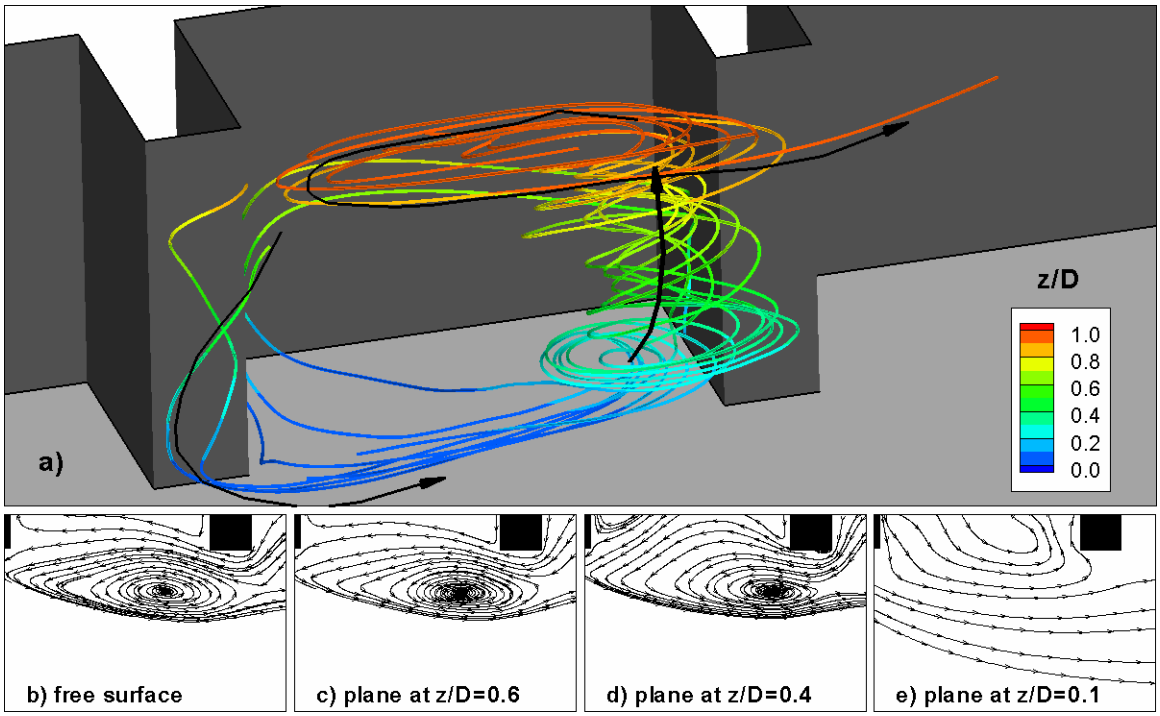

Figure 4.19. Mean velocity streamlines illustrating 3D structure of flow in the channel-embayment interface region; a) 3D streamlines; and 2D streamlines in horizontal planes: b) free surface; c) z/D=0.6; d) z/D=0.4; e) z/D=0.1.

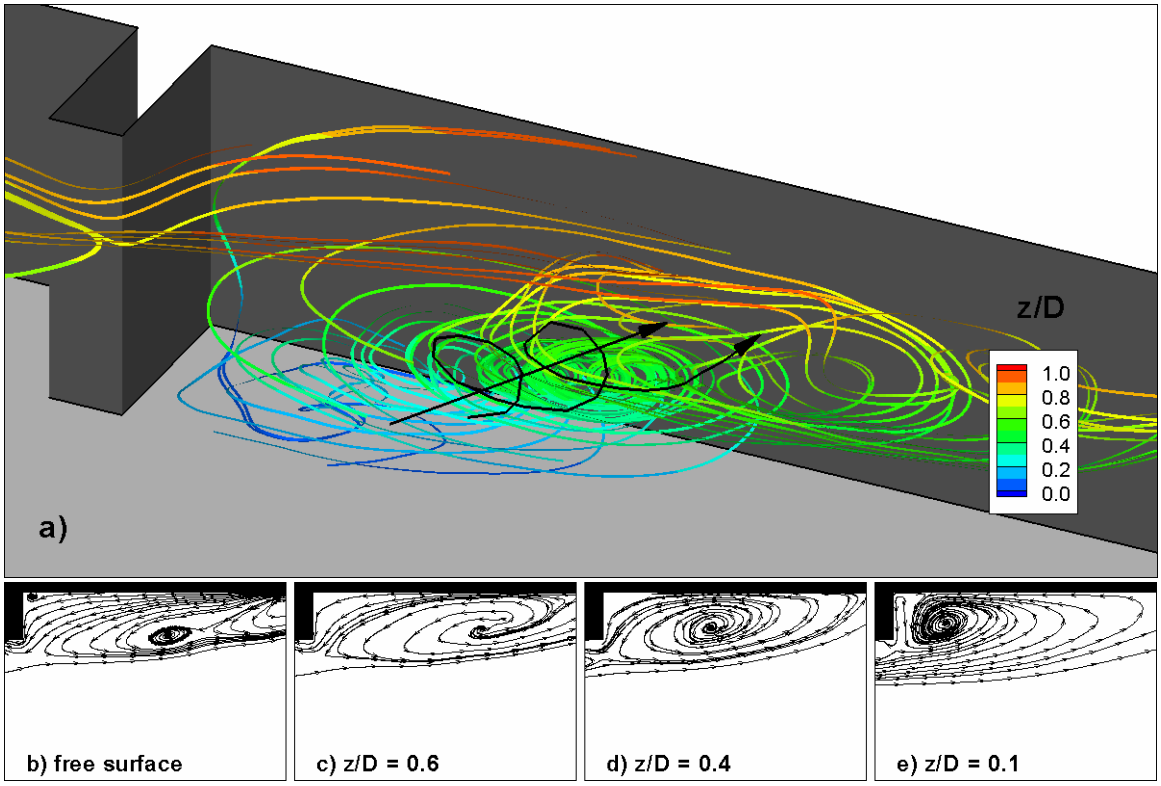

Figure 4.20. Mean velocity streamlines illustrating 3D structure of flow in the recirculation region downstream of the embayment; a) 3D streamlines; and 2D streamlines in horizontal planes: b) free surface; c) z/D=0.6; d) z/D=0.4; e) z/D=0.1.

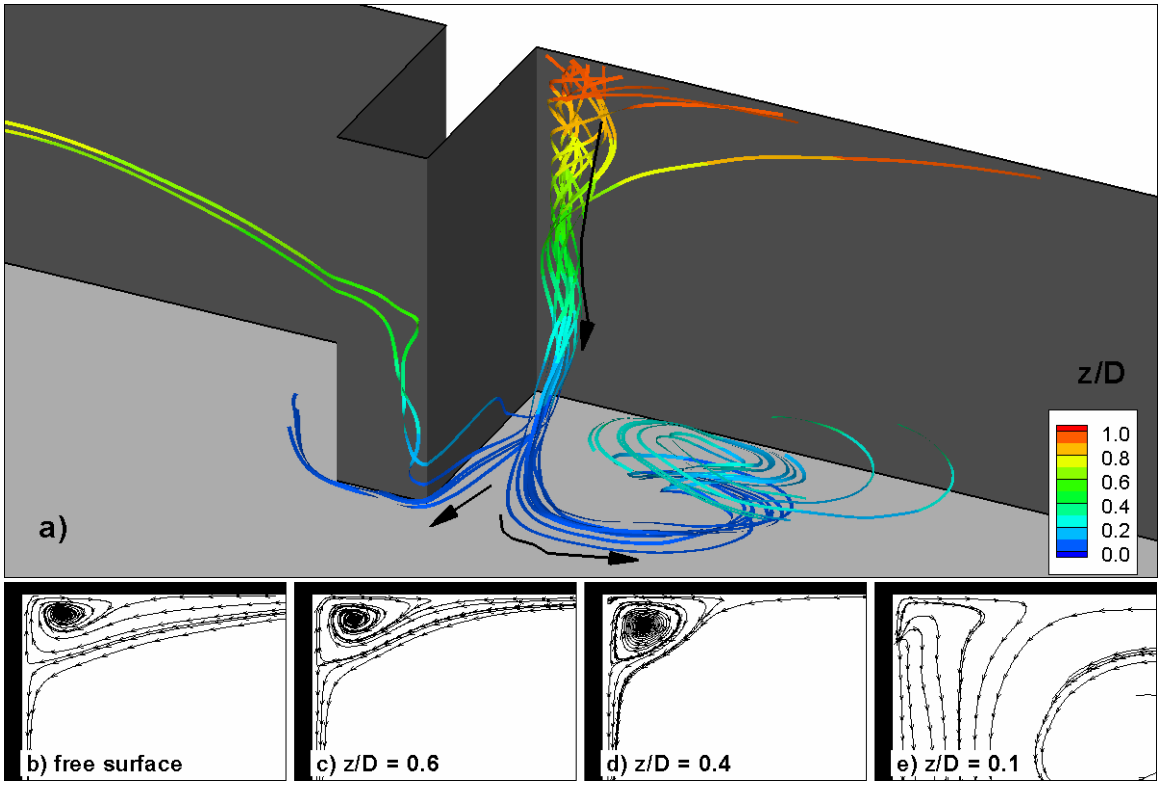

Figure 4.21. Mean velocity streamlines visualizing corner vortex in the recirculation region downstream of the embayment; a) 3D streamlines; and 2D streamlines in horizontal planes: b) free surface; c) z/D=0.6; d) z/D=0.4; e) z/D=0.1.

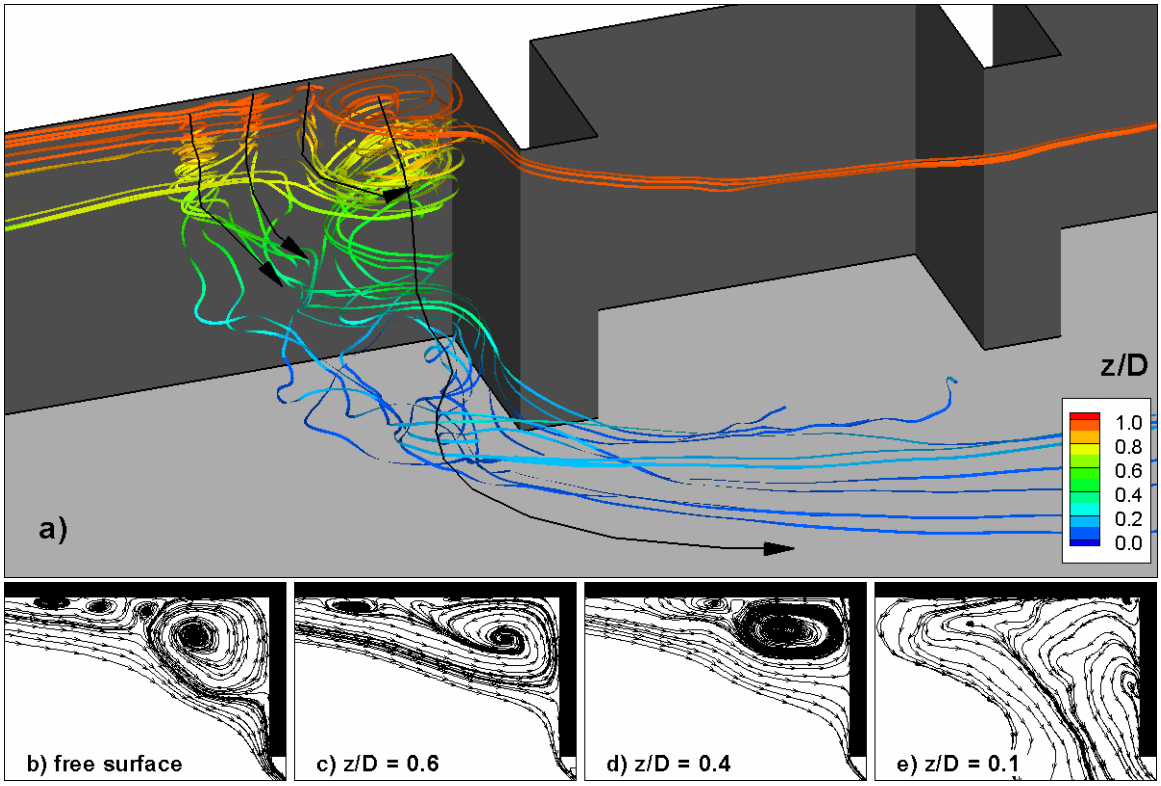

Figure 4.22. Instantaneous velocity streamlines illustrating 3D structure of the flow in the upstream recirculation zone; a) 3D streamlines; and 2D streamlines in horizontal planes: b) free surface; c) z/D=0.6; d) z/D=0.4; e) z/D=0.1.

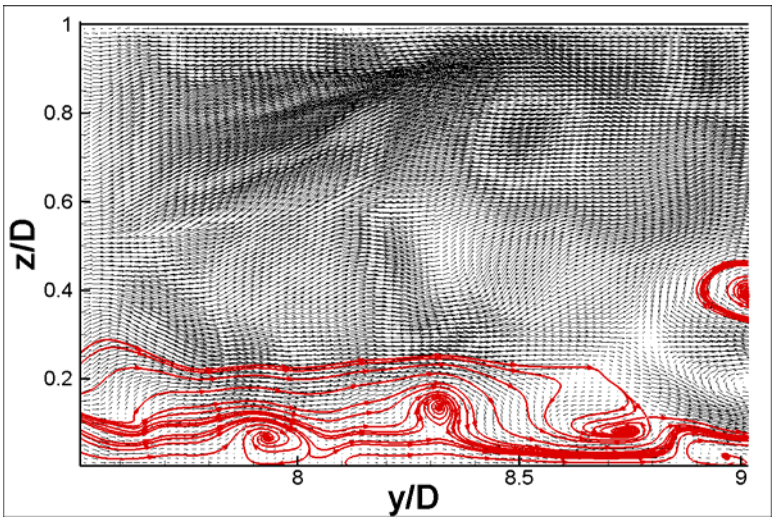

Figure 4.23. Instantaneous velocity vectors and in-plane streamlines in a yz plane situated upstream of the embayment showing presence of small scale eddies.

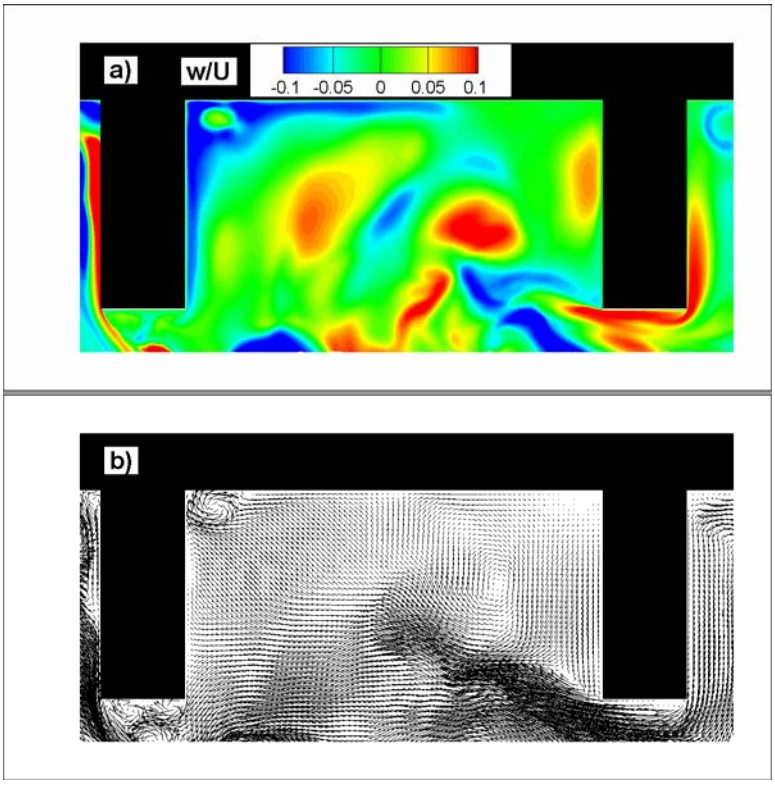

Figure 4.24. Visualization of coherent structures in the embayment region near the free surface (z/D=0.95). a) vertical (out-of-plane) velocity contours; b) instantaneous velocity vectors.

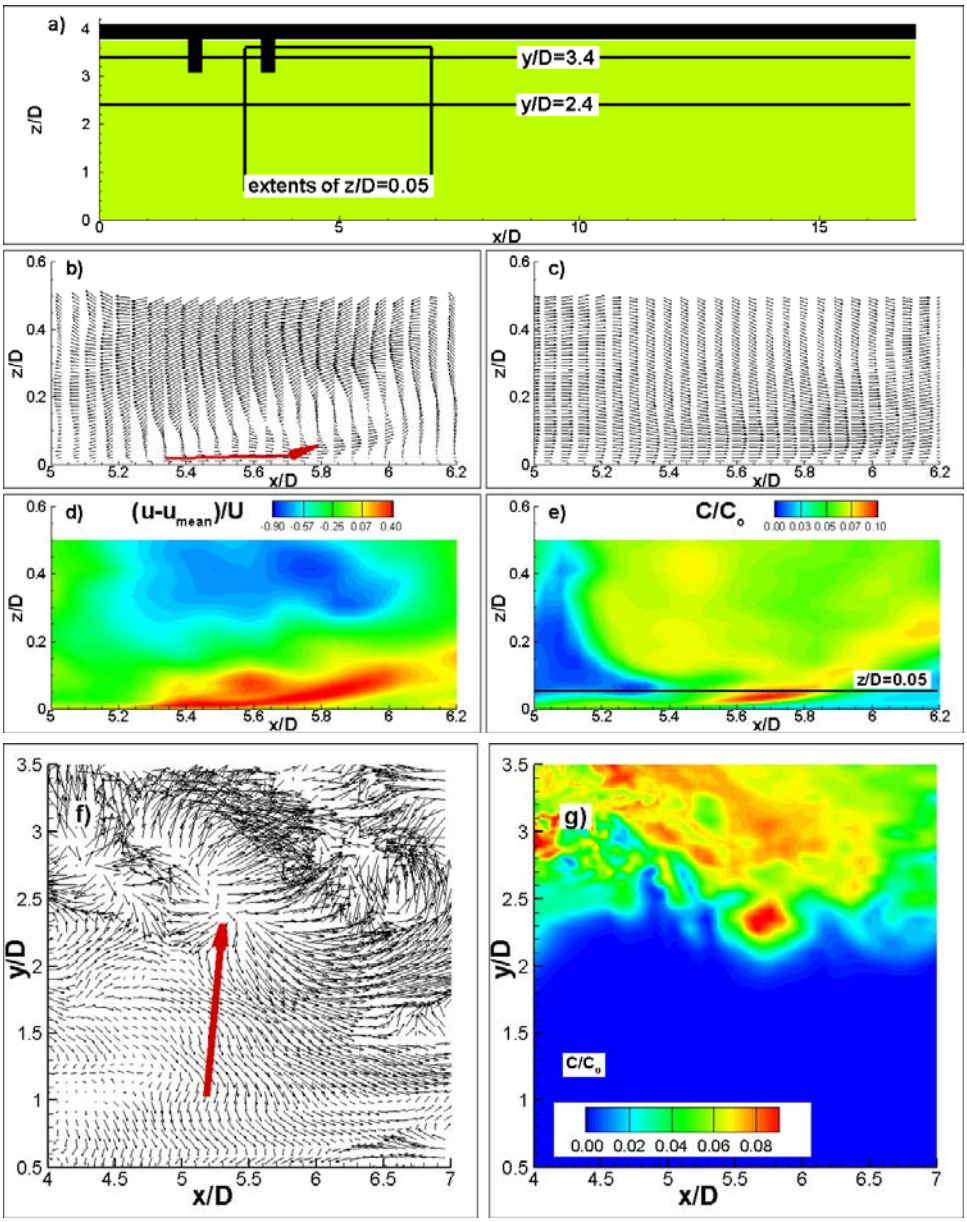

Figure 4.25. Visualization of an outward interaction event near the channel bottom; a) location of planes of interest; b) instantaneous fluctuating velocity vectors in plane y/D=2.4; c) instantaneous total velocity vectors in plane y/D=2.4; d) streamwise fluctuating velocity contours in plane y/D=2.4 ; e) instantaneous concentration contours in plane y/D=2.4; f) instantaneous fluctuating velocity vectors in plane z/D=0.05; g) instantaneous concentration contours in plane z/D=0.05.

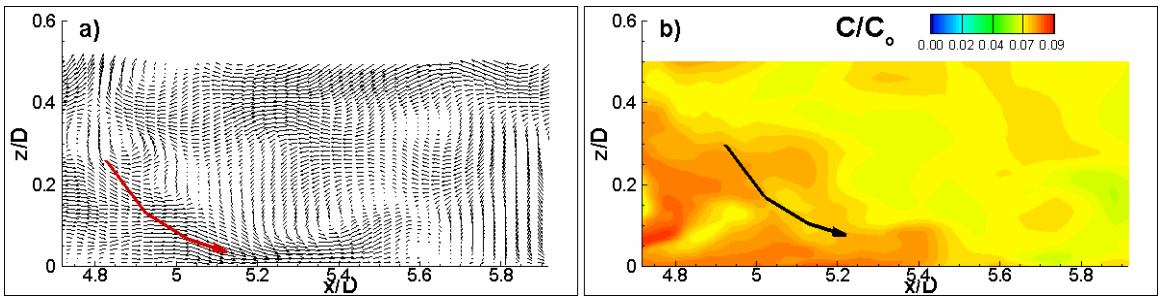

Figure 4.26. Visualization of a sweep event near the channel bottom; a) instantaneous fluctuating velocity vectors in plane y/D=3.4; b) instantaneous concentration contours in plane y/D=3.4.

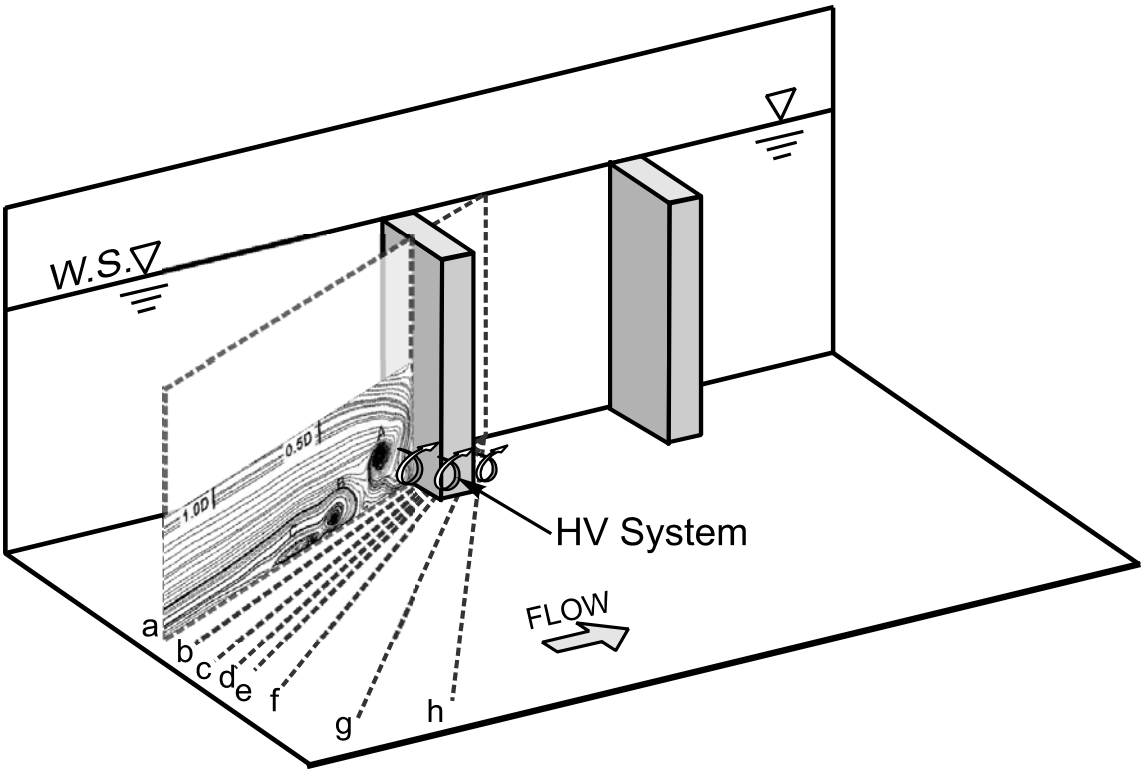

Figure 4.27. Sketch of the one-embayment geometry showing position of the vertical planes used to visualize the HV system around the tip of the upstream groyne.

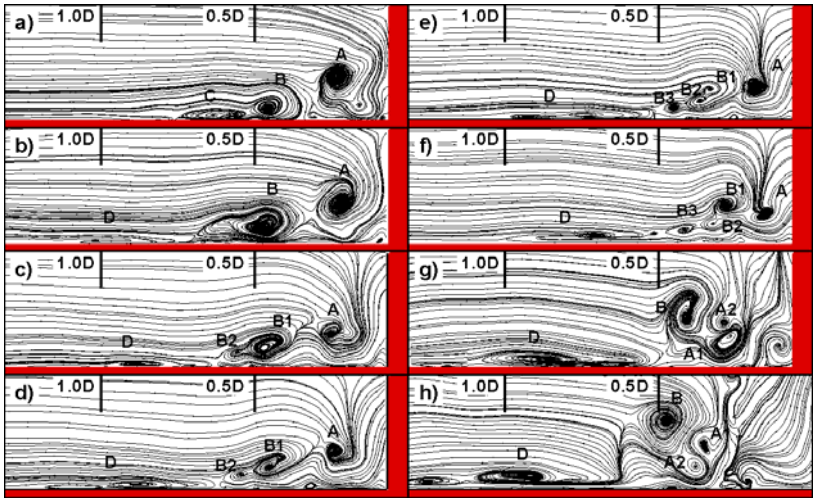

Figure 4.28. Structure of the instantaneous HV system as it wraps around the base of the upstream groyne visualized in vertical planes making an angle with the lateral channel wall of: a) 25°; b) 30°; c) 35°; d) 37.5°; e) 40°; f) 45°; g) 55°; h) 65°. See also Figure 4.27.

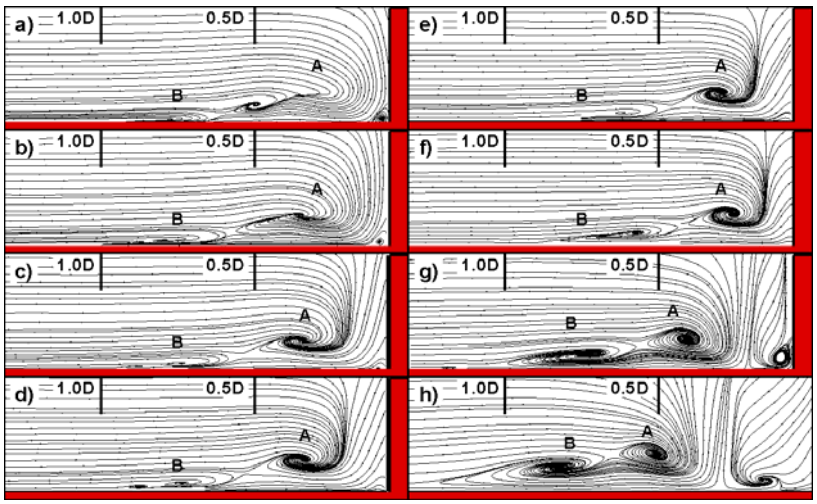

Figure 4.29. Structure of the mean HV system as it wraps around the base of the upstream groyne visualized in vertical planes making an angle with the lateral channel wall of: a) 25°; b) 30°; c) 35°; d) 37.5°; e) 40°; f) 45°; g) 55°; h) 65°. See also Figure 4.27.

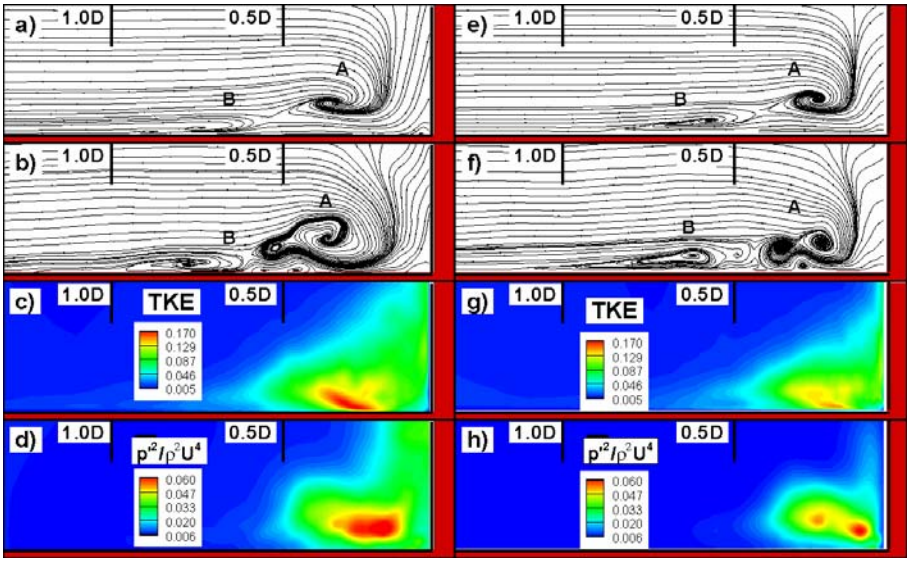

Figure 4.30. Visualization of the HV system at the base of the upstream groyne in vertical planes inclined at 35^o (left) and 45^o (right) from the lateral channel wall; a) mean velocity 2D streamlines; b) instantaneous velocity 2D streamlines; c) TKE; d) pressure fluctuations $\overline{p'^2}$.

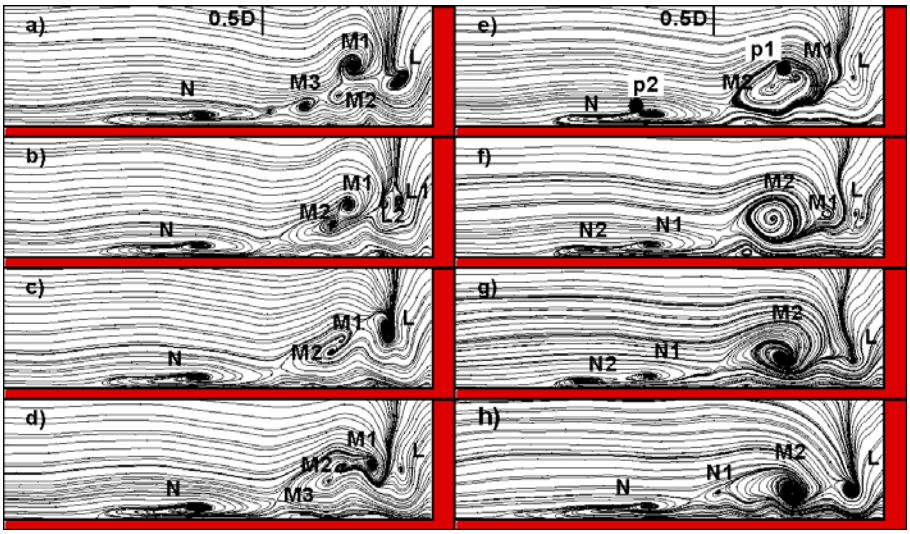

Figure 4.31. Temporal evolution of instantaneous HV system in a vertical plane making a 45^o angle with the lateral channel wall. a) 1.08 D/U; b) 1.20 D/U; c) 1.28 D/U; d) 1.32 D/U; e) 1.36 D/U; f) 1.44 D/U; g) 1.52 D/U; h) 1.68 D/U.

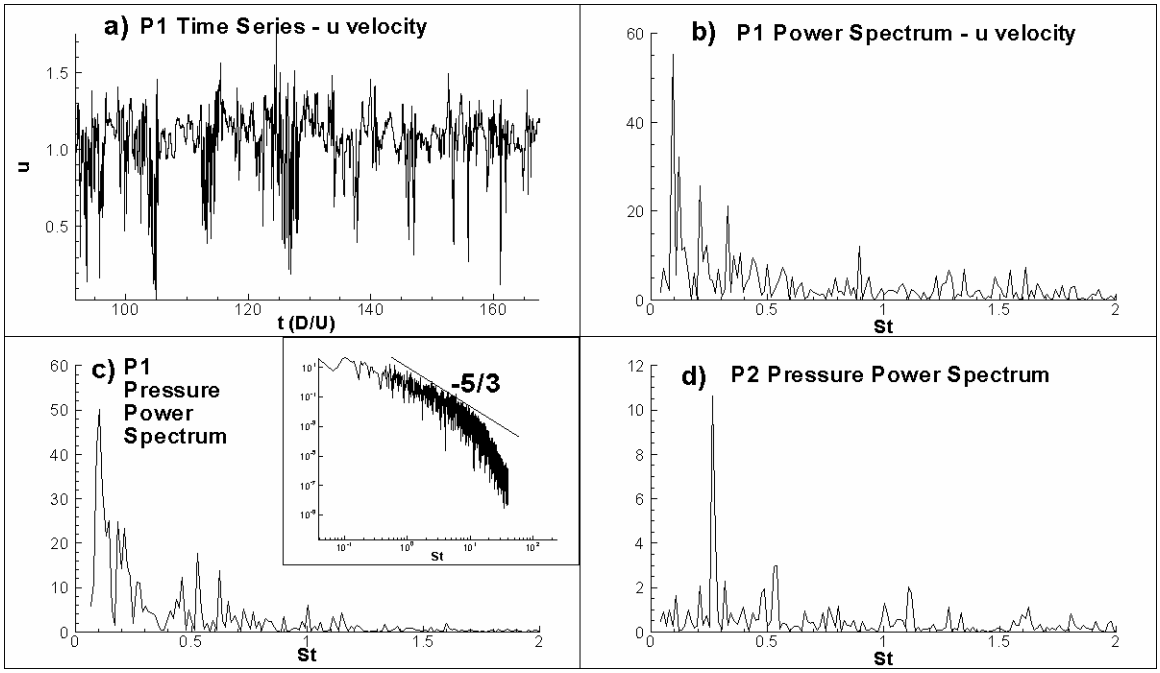

Figure 4.32. Velocity time series and velocity and pressure power spectra within the HV system a) u-velocity time series at p1; b) u-velocity power spectrum at p1; c) pressure power spectrum at p1 (inset shows pressure power spectrum as a log-log plot); d) pressure power spectrum at p2. The position of points p1 and p2 are shown in Figure 4.31e.

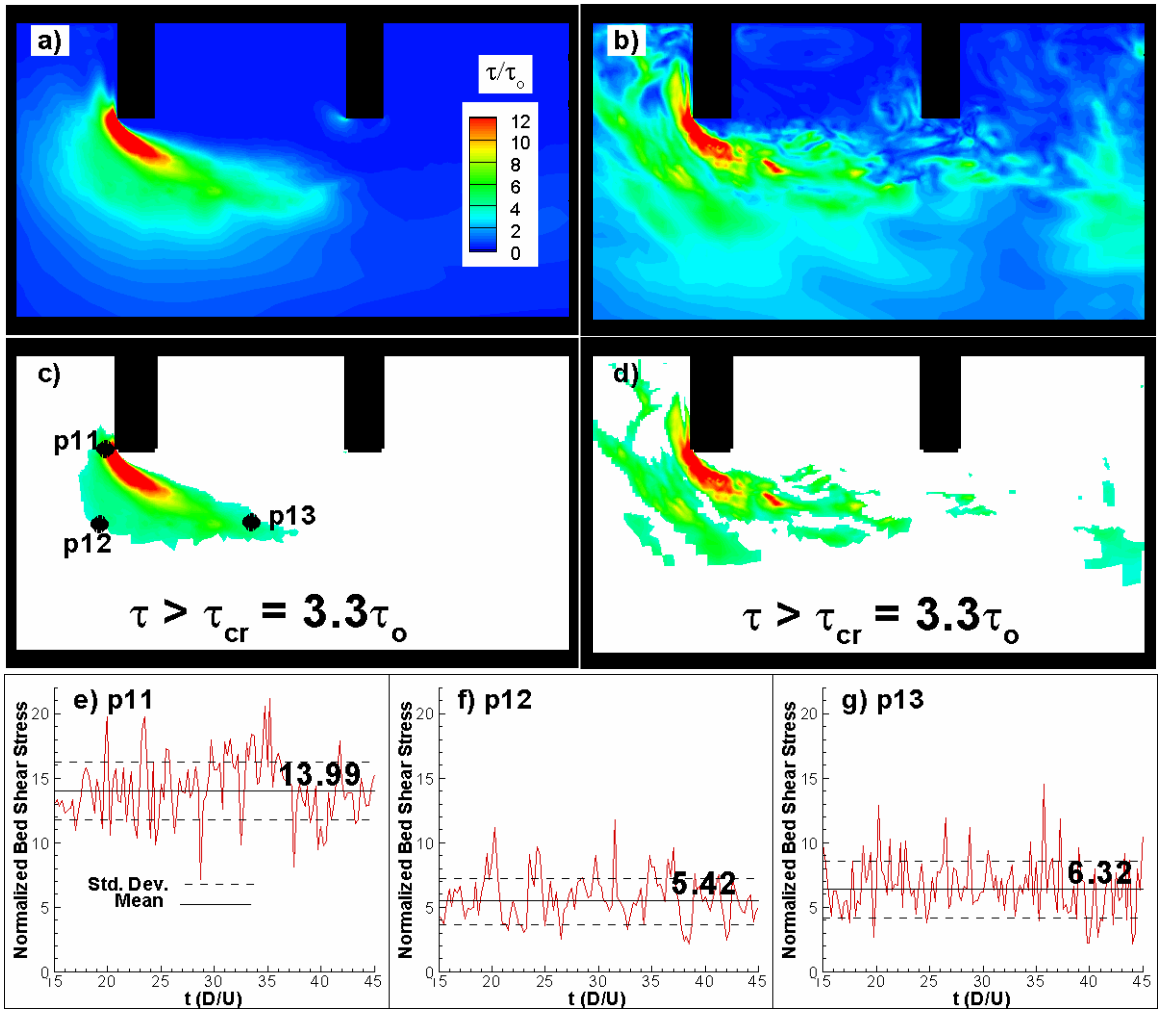

Figure 4.33. Non-dimensional bed shear stress distribution. a) mean values; b) instantaneous values; c) mean values showing entrainment region; d) instantaneous values showing entrainment region; e) bed shear stress time series at point p11; f) bed shear stress time series at point p12; g) bed shear stress time series at point p13. The positions of points p11, p12 and p13 are shown in frame c.

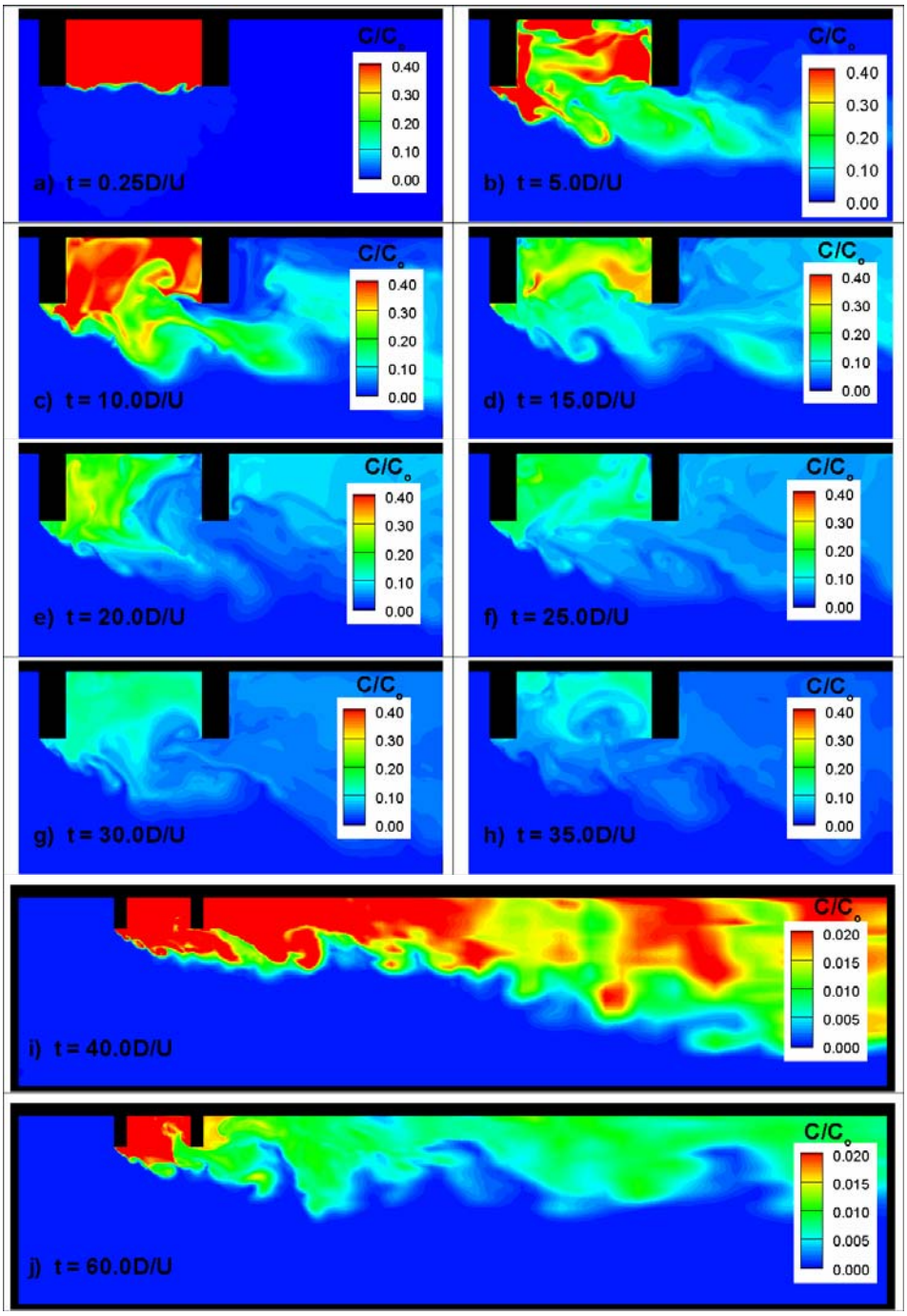

Figure 4.34. Instantaneous contours of contaminant concentration at the free surface. Mixing starts at t=0D/U when the concentration in the embayment is set to C/C_0=1.0; a) t = 0.25D/U; b) t = 5.0D/U; c) t = 10.0D/U; d) t = 15.0D/U; e) t = 20.0D/U; f) t = 25.0D/U; g) t = 30.0D/U; h) t = 35.0D/U; i) t = 40.0D/U; j) t = 60.0D/U.

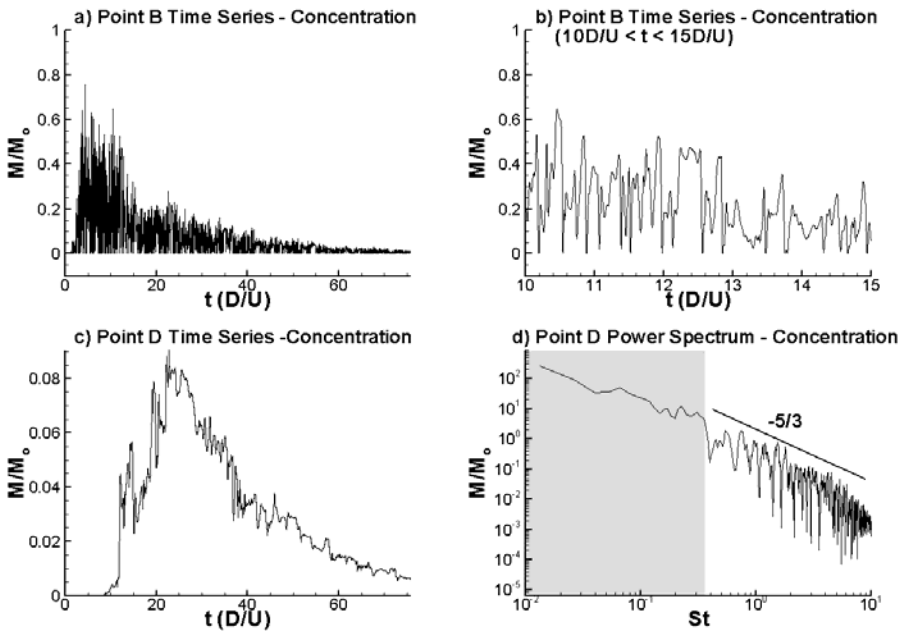

Figure 4.35. Concentration time series and power spectra; a) concentration time series at point B; b) concentration time series at point B between 10D/U and 15D/U; c) concentration time series at point D; d) concentration power spectrum at point D (lower part of the spectrum should be discarded as process is unsteady). The positions of points B and D are shown in Figure 4.8.

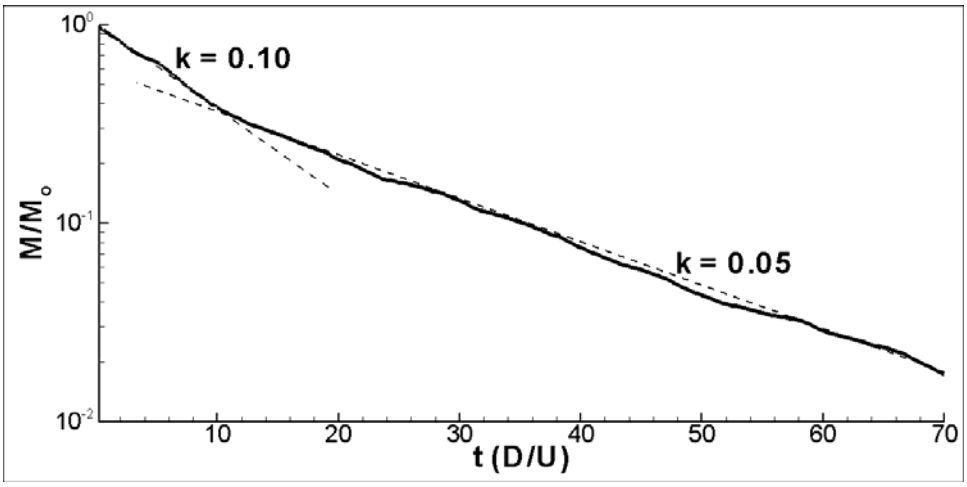

Figure 4.36. Contaminant mass decay within total embayment volume.

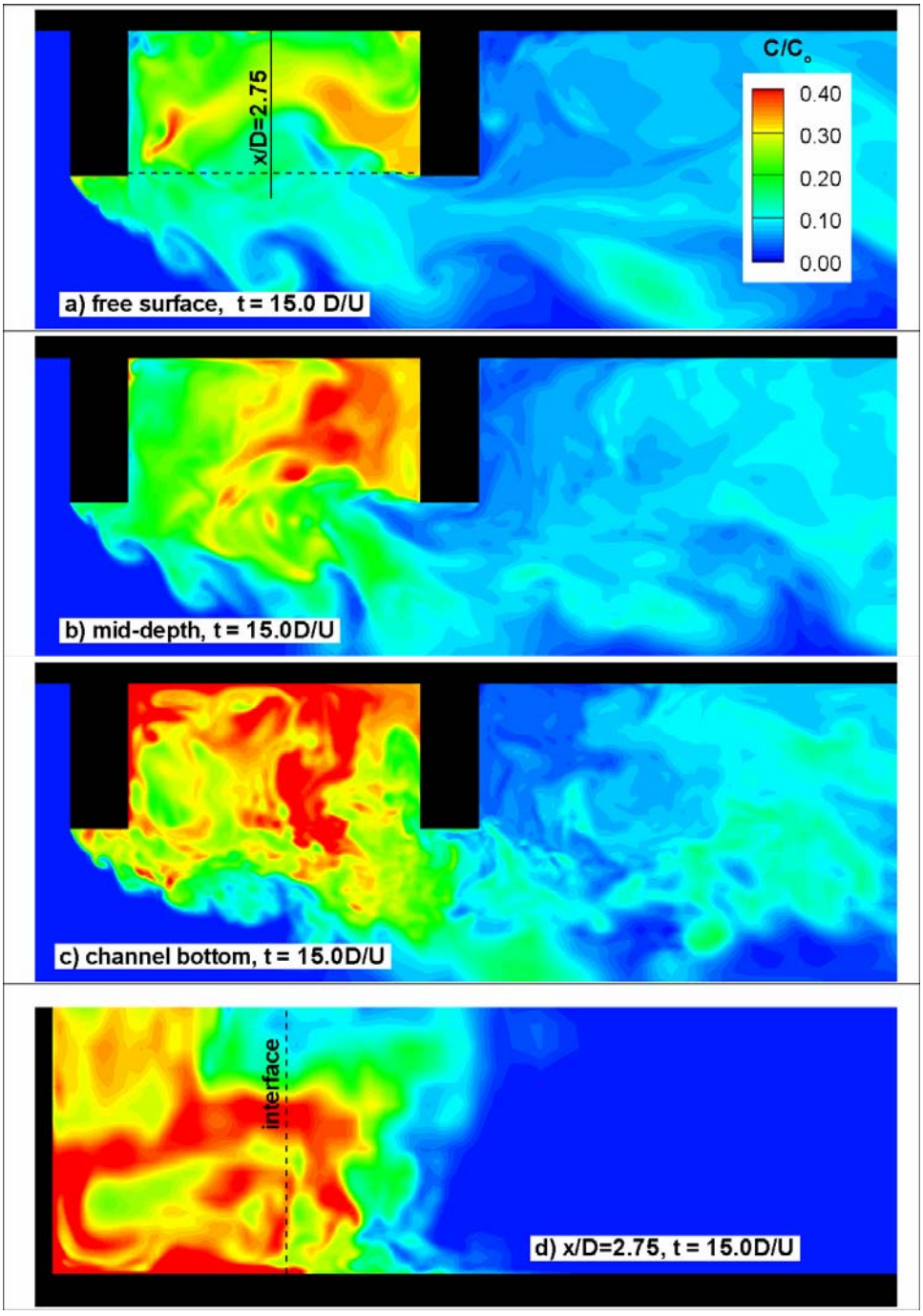

Figure 4.37. Instantaneous contours of contaminant concentration at different levels in the embayment and channel at t=15D/U; a) free surface (z/D = 1.0); b) mid-depth (z/D = 0.5); c) close to channel bottom (z/D = 0.1); d) mid-distance between the two groynes (x/D=2.75).

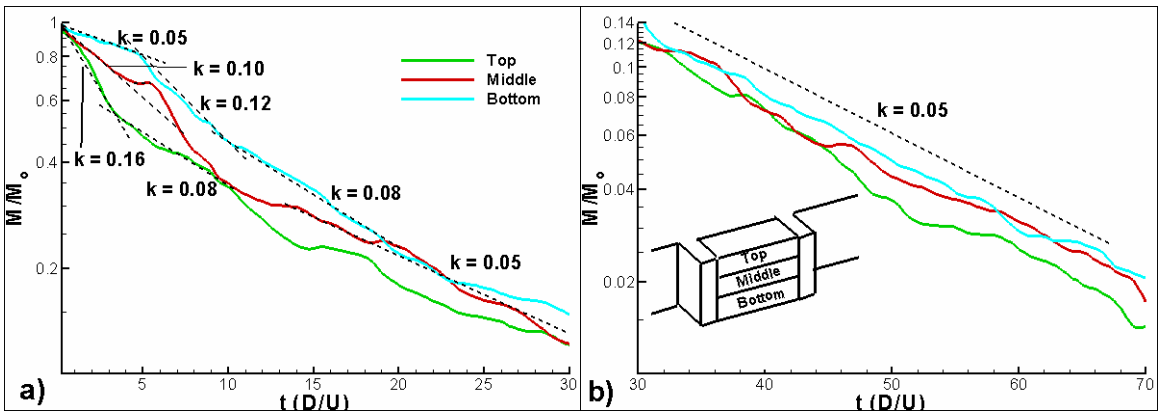

Figure 4.38. Contaminant mass decay within top, middle and bottom embayment layers; a) t = 0 to t = 30; b) t=30 to t=60.

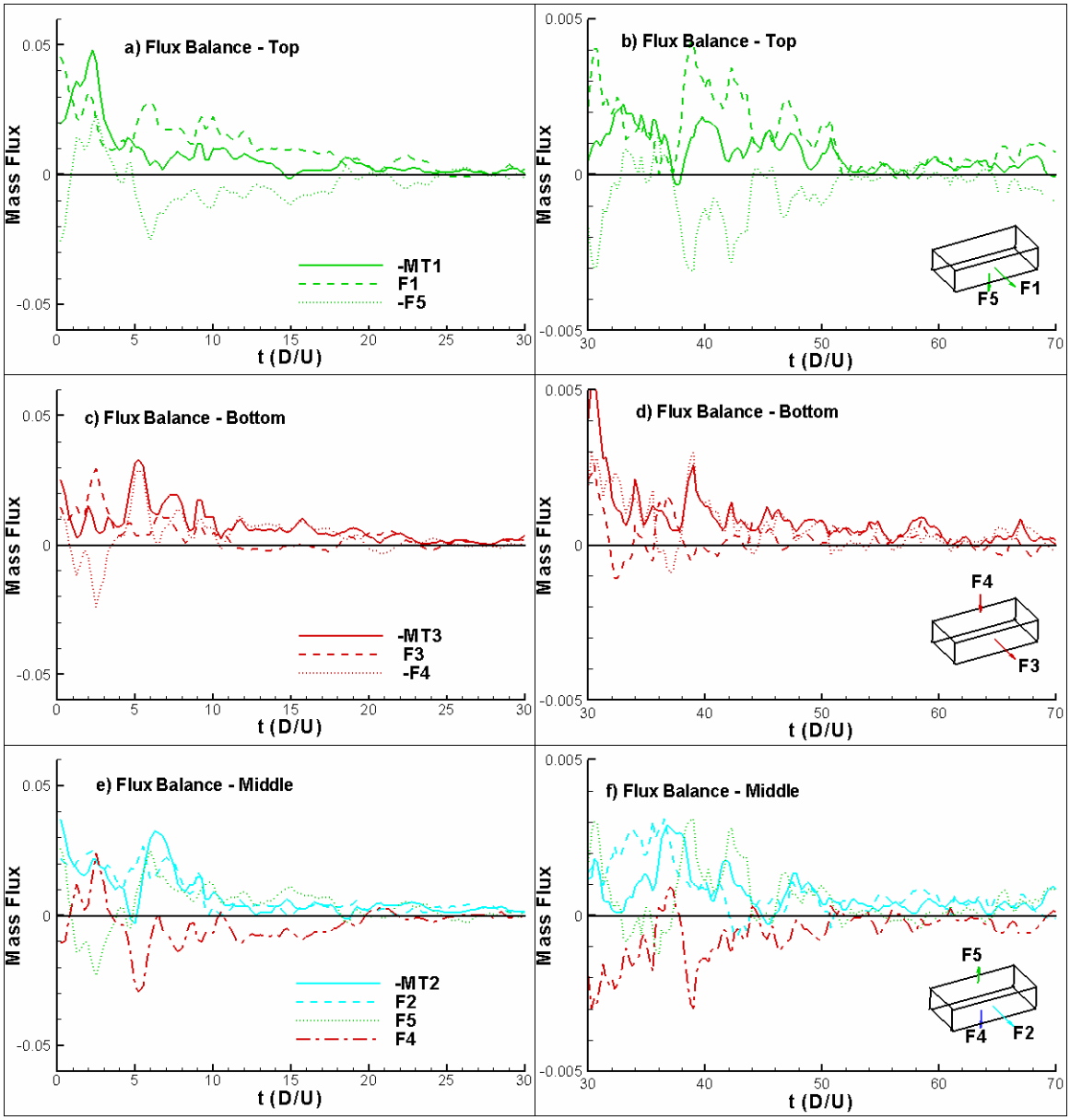

Figure 4.39. Contaminant mass fluxes within each layer of the embayment; a) top (t = 0 to t = 30); b) middle (t = 0 to t = 30); c) bottom (t = 0 to t = 30); d) top (t = 30 to t = 60); e) middle (t = 30 to t = 60); f) bottom (t = 30 to t = 60).

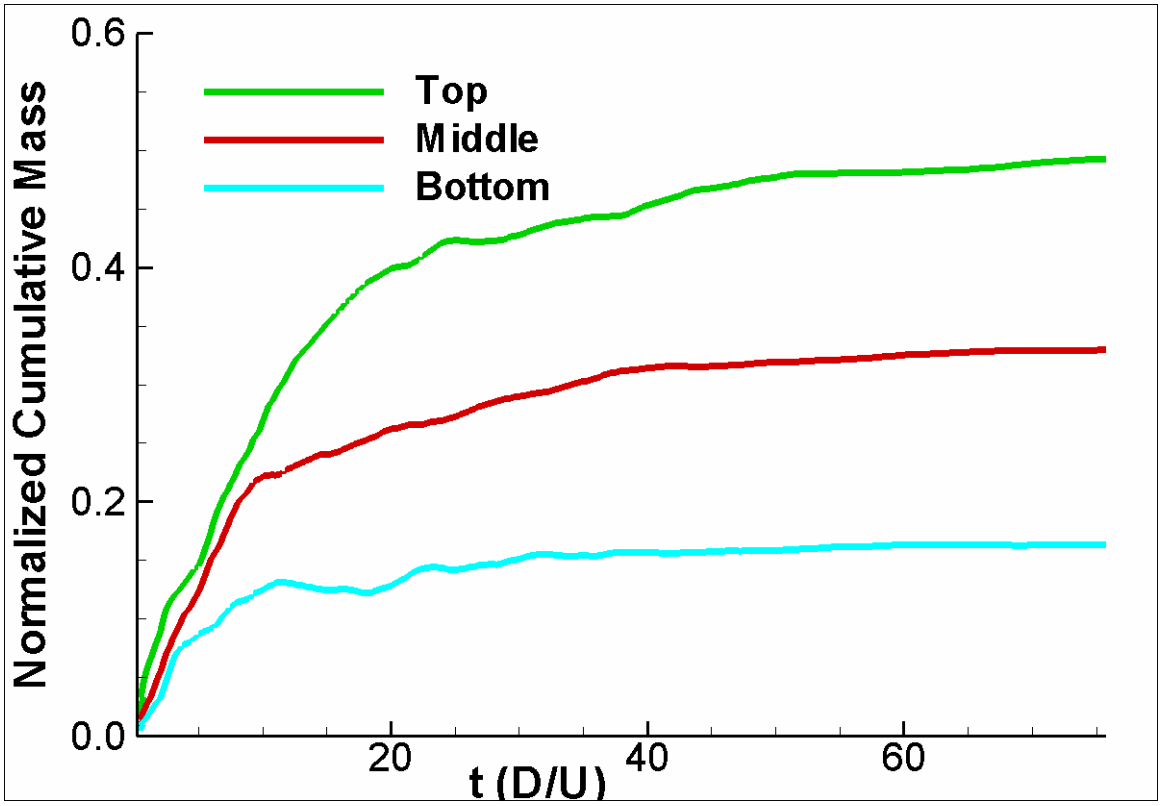

Figure 4.40. Temporal evolution of cumulative contaminant mass transport into the channel through the corresponding embayment-channel interfaces.

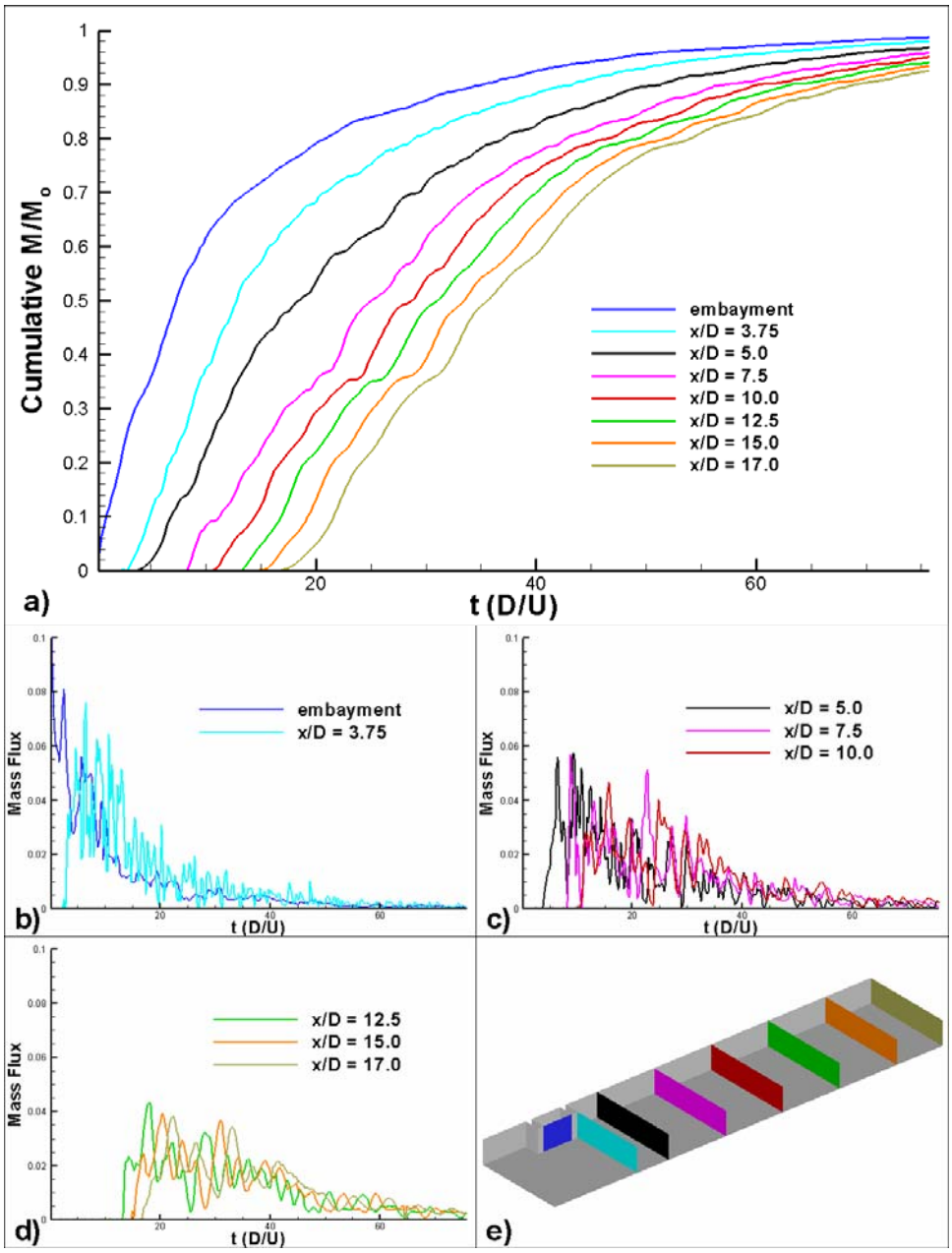

Figure 4.41. Analysis of contaminant advection through main channel; a) cumulative mass of contaminant transported through various cross sections; b) contaminant mass flux through embayment-channel interface and x/D = 3.75 plane; c) mass flux through x/D = 5.0, x/D = 7.5 and x/D=10.0 planes; e) mass flux through x/D = 12.5, x/D=15.0 and x/D = 17.0 planes; f) relative position of the cross sections within the domain. x/D is measured from the inlet section.

CHAPTER 5
COHERENT STRUCTURES AND MASS EXCHANGE PROCESSES IN CHANNEL FLOW WITH TWO SUBMERGED GROYNES

5.1 Introduction

In this section, Large Eddy Simulation (LES) is used to investigate the instantaneous and mean flow fields around two fully submerged groynes in a flat-bed open channel with lateral vertical walls and the mass exchange processes between the embayment and the main channel. The geometry, dimensions and position of the groynes, and the flow conditions are identical to those considered in the case study discussed in Chapter 4. The only difference is that because the water level is 40% higher, the groynes are fully submerged.

The interest in this configuration is motivated by its similarity to flow around groyne fields in natural rivers at flood conditions. Compared to the emerged case, the hydrodynamics of the flow past submerged groynes is far more complicated and the three-dimensional effects are considerably stronger. In addition to the horizontal detached shear layer which plays a similar role in both cases, there is a vertical detached shear layer associated with the flow over the top of the embayment. The contaminant removal process is expected to be faster in the submerged case because of the additional roof interface through which the contaminant can leave the embayment volume.

The main topics discussed in the results section are: 1) a description of the main vortical structures present in the flow inside and around the embayment volume; 2) a study of the structure of the turbulent HV system at the base of the upstream groyne and of the bed shear stress distribution and a discussion of the differences between the emerged and submerged cases; 3) a discussion of the interactions among the dominant coherent structures that play a role in the mass exchange between the embayment and the channel. In particular, the nature of the interactions between the eddy that populate the

horizontal and vertical DSLs are discussed in detail and compared with the emerged case; 4) a quantitative study of the exchange of dissolved matter (passive contaminant) between the embayment and the main channel; 5) an investigation of the non-uniformity of the mass exchange over the embayment depth and of the efficiency of the roof interface compared to the one of the lateral interface in removing contaminant from the embayment volume; 6) an estimation based on LES results of the mass exchange coefficients used in simple mass exchange models for the submerged case; 7) an investigation of the subsequent advection of the contaminant in the main channel, its non-uniformity over the depth and the temporal variation of the contaminant concentration at representative cross sections downstream of the embayment; 8) a comparison of the TKE distributions between the emerged and the submerged case; and 9) a comparison of various depth-averaged quantities (mean velocities, velocity fluctuations, TKE, etc.) between the emerged and submerged cases.

5.2 Computational Domain and Mesh

5.2.1 Computational Domain

The height of the groyne, D, is used as the length scale. The total channel depth is h=1.4D. The mean velocity in the main channel, U, is used as the velocity scale. The physical domain extends 2D upstream of the first groyne and 14D downstream of the second groyne (see Figure 5.1). The Reynolds number defined with D and U is Re=13,600 and is identical to the one used in the emerged case study discussed in Chapter 4. The width of the channel between the two lateral vertical walls is B=3.75D. The length, l, and width, b, of each groyne are 0.625D and 0.25D, respectively. The distance between the mid-planes of the two groynes is S=1.5D such that the embayment length is 1.25D. As in the emerged case, the centers of the two groynes are situated at x/D=2.0 and x/D=3.5.

5.2.2 Boundary and Initial Conditions

Following the procedure used in the emerged case, at the inflow section the flow fields corresponding to a precalculated, fully-developed LES open channel simulation conducted at the same channel Reynolds number with periodic conditions in the streamwise direction were fed in a time-accurate manner. This ensured that the incoming flow was fully turbulent and the turbulent channel flow contained realistic near-wall coherent structures at the location of the upstream groyne.

A convective outflow boundary condition was used at the exit section. The velocity boundary conditions on all walls including the lateral wall opposite to the embayment side were no slip. As in the emerged case, the free surface was simulated as a rigid lid. This is generally accepted as a good approximation if the Froude number is relatively low (<0.5) (Alfrink and van Rijn, 1983). For instance, using the same kind of boundary condition Hinterberger (2004) captured the seiching motions in an array of emerged embayments. Of course the seiching motions were educed by converting the pressure distribution on the free surface into an equivalent water surface elevation using the hypothesis of a hydrostatic pressure distribution close to the free surface. In the present simulation with submerged groynes the Froude number in the channel away from the groynes is near 0.25 but locally, above the groynes, the Froude number is close to 0.9. The fact that even over the groynes the Froude number remains smaller than one means that the groynes do not act as a local control on the flow (e.g., the flow does not resemble that over a weir, no high amplitude waves downstream of the groynes are expected, etc.), so in that sense water surface elevation effects are not important. It is more probable that the resulting pressure distribution on the free surface acts in a similar way on the flow away from the free surface as would the presence of a real deformed free surface. Still, nonlinear coupling phenomena between the free surface and the eddies convected beneath it are probably not accounted for correctly and the results from the present simulation should be interpreted carefully.

Following the procedure used in Chapter 4, the mass exchange between the embayment and the main channel was investigated by considering the ejection of a passive contaminant (conserved scalar) that was introduced instantaneously at a certain time (after the velocity fields became statistically steady) inside the embayment domain. The nondimensional scalar concentration, C, was initialized as C=1 inside the embayment volume (up to the embayment roof) and C=0 outside of it. The time at which the scalar was introduced was formally taken as t=0D/U. The simulation was continued for another 35D/U until less than 1% of the initial mass of contaminant was left inside the embayment. C was set to zero at the inflow. The mass flux was set to zero on all the walls and at the free surface.

5.2.3 Computational Mesh

The unstructured fine mesh which is used to analyze the flow in the results section contains approximately 4 million hexahedral elements and was generated using a paving technique which allows rapid variation in the characteristic size of the elements while maintaining high overall mesh quality and low stretching ratios. Figure 5.2 shows the computational mesh in two planes. The views in Figure 5.2a-c are situated in a horizontal plane located at the top of the groyne (z/D=1.0). Figure 5.2a shows a partial view of the mesh over the whole width of the channel. Figure 5.2b shows a detailed view around the embayment, and Figure 5.2c shows a detailed view (see rectangle in Figure 5.2b) of the mesh around the tip of the upstream groyne (the black lines correspond to the boundaries between the grid partitions corresponding to the processors). Figure 5.2d-f shows the mesh in a vertical plane (mid groyne width, y/D=3.44) over the depth of the channel and details around the embayment region and around the crest of one of the groynes.

The first row of cells from the walls is situated within the viscous sub-layer ($\Delta y^+<1$). In the vertical direction (82 grid points), the mesh spacing varies from 0.5 wall

units at the channel bottom to 22 wall units at the groyne mid (z/D=0.5) height, back to 0.5 wall units at the crest of the groyne (z/D=1) and then increases to 21 wall units at the free surface, based on the channel Reynolds number and assuming the non-dimensional mean friction velocity $u_{\tau 0}/U \sim 0.05$. The mesh size in the regions around (horizontal cell size is close to 50 wall units at point c1 outside the embayment region in Figure 5.2a) and within the embayment (horizontal cell size is close to 9 wall units at point c2 in Figure 5.2b) is expected to allow the simulation to capture the dynamically important coherent structures present around the embayment region. The typical dimension of the mesh cells around the tip of the upstream groyne (point c3 in Figure 5.2c), where the vortex tubes form and are shed in the horizontal DSL, is close to 3 wall units. The resolution inside the upstream part of the vertical DSL (see Figure 5.2e) is similar. This is essential to accurately capture these coherent structures that play an important role in the transport of the momentum and mass around the lateral and roof interfaces.

The time step in the simulation was 0.002D/U. The Courant number inside a typical element within the embayment was 0.06, while outside the embayment region the values were close to 0.04. Based on the above elements, the mesh density can be considered fine enough to resolve the dynamically important coherent structures in the flow.

5.2.4 Grid Independence Study

An additional simulation on a mesh with around 2.4 million cells was performed to check the grid independence of the fine mesh solution. Similar to the fine mesh computation, the viscous sub-layer was resolved and the first cell off the walls was situated at less than 3 wall units. The mesh density in relevant horizontal and vertical planes is shown in Figure 5.3 and can be compared to the mesh density used in the fine mesh simulation in Figure 5.2. Comparison of the mean streamlines in relevant horizontal planes in Figure 5.4 and Figure 5.5 show that the patterns are similar in the

coarse and fine mesh solution. The lateral extent of the horizontal DSL in all planes cutting through the groynes, the position of the main corner vortex upstream of the first groyne and the size of the downstream recirculation region in the horizontal section at z/D=0.1 are close in the two simulations. Additionally, the out-of-plane mean vorticity contours in Figure 5.6a-b at groyne mid-depth level clearly show that the vorticity distribution inside the horizontal DSL and the upstream recirculation region is similar in the two simulations. To better estimate the quantitative differences between the predictions obtained on the two meshes, the spanwise profiles of the vertical vorticity magnitude and streamwise velocity at a point situated at z/D=0.5 (groyne mid height) and x/D=2.75 (mid distance between the two groynes) are compared in Figure 5.7. The profiles on the coarse and fine meshes are similar and do not show any substantial quantitative differences, including in the region cutting through the horizontal DSL around y/D=2.75.

5.3 Analysis of Mean and Instantaneous Flow Structure

5.3.1 General Qualitative Description of Vortical Flow Structure Using Two-Dimensional Streamlines

Mean velocity streamlines are used to describe the main vortical structures in the flow as predicted by the fine mesh solution. Figure 5.1b locates the position of the planes in which the solution is analyzed. The velocity fields over a time interval of 65 D/U were used to calculate statistics.

Figure 5.5 shows 2D velocity streamlines at four depths in the channel (near the free surface z/D=1.3, near the top of the groyne z/D=0.9, near mid-depth z/D=0.6 and near the channel bottom z/D=0.1). As expected, for the fairly high relative submergence (1.4) considered in the simulation, the flow near the free surface (Figure 5.5a) is relatively parallel to the mean flow direction. This is consistent with experimental investigations of the flow patterns at the free surface for submerged embayments. Only

small deformations are observed in the trajectories followed by the streamlines in the region corresponding to the embayment. Past the embayment location, the mean streamlines appear to diverge from the lateral wall at which the groynes are present.

The flow in horizontal planes near the channel bed and up to a level situated near the mid-depth of the groyne (Figure 5.5c-d) resembles the flow observed in the fully emerged case (Figure 4.4). A large recirculation region is observed inside the embayment along with secondary corner vortices near the junction between the groynes and the lateral wall (Figure 5.5c). The shape of horizontal DSL varies with the depth. Near the bottom, the area associated with the main recirculation region situated outside the lateral interface is larger. As one goes away from the bottom, the shape of the DSL becomes relatively flat in the region between the two groynes. Because of the overflow and the associated vertical DSL above the roof interface (z/D=1), the 2D streamline patterns near the crest are very different compared to the ones observed in the fully emerged case (Figure 4.4a). The most obvious difference is that the recirculation eddy downstream of the second groyne has practically disappeared at z/D=0.9 (Figure 5.5b). In the fully emerged case, the size of this eddy and the associated reattachment length are increasing strongly as the free surface is approached. At lower levels, this eddy is present in the submerged case, but its overall size in the streamwise direction is less than half the value observed in the emerged case. Upstream of the first groyne, a relatively weak vortex is observed especially at mid levels near the junction between the groyne and the lateral face. The intensity and size of this vortex appear to be smaller compared to the emerged case.

Comparison of the mean and instantaneous 2D streamlines at z/D=0.6 in Figure 5.5c and Figure 5.8c indicate the differences between the instantaneous and mean flow. The main difference is the presence of several eddies inside the DSL region in the instantaneous flow fields which are shed from the tip of the upstream groyne and are convected downstream. Near the channel bottom, it is the wake region downstream of

the second groyne that contains several smaller vortices in the instantaneous plot showing the 2D streamlines (e.g., compare Figures 5.5d and 5.8d).

5.3.2 Vortical Structure of the Flow in the Detached Shear Layer and Embayment Region

The Q criterion is used in Figure 5.9a to educe the 3D vortex tubes in the instantaneous flow associated with the horizontal DSL (the other vortical structures in the flow were eliminated from the picture). These small elongated vortices result from the growth of the Kelvin-Helmholtz instabilities at the interface between the outerflow and the recirculating embayment flow. Figure 5.9b-e shows 2D streamlines in horizontal planes situated at different distances from the bed. Examination of these frames shows that the vortex tubes are relatively irregular, their cores are not exactly vertical and the individual eddies do not extend uniformly from the top of the embayment to the bottom. As they are convected downstream, these tubes are stretched, and in some cases they merge with another vortex tube over part of their length to form a stronger vortical structure that in many cases maintains its coherence as it approaches the tip of the second groyne. Figure 5.9f-h shows the vertical vorticity component in a horizontal plane at z/D=0.6. The frames illustrate the merging of two vortex tubes a short distance from the formation region, close to the tip of the first groyne. The two vortical structures are distinct in Figure 5.9g, whereas in Figure 5.9h, the merging of the last two eddies shed in the DSL is complete.

The three-dimensionality of the instantaneous flow inside the embayment increases as the crest of the groynes is approached (Figure 5.9c), while at levels very close to the free surface (Figure 5.9b) the instantaneous flow remains relatively uniform. It appears that in the instantaneous flow visualized in Figure 5.9b-e, the vortex tubes inside the horizontal DSL (see also instantaneous vorticity contours in Figure 5.11 and Figure 5.12) are convected inside the embayment (total clipping event) rather than over

the lateral interface area as the mean flow fields would suggest. As discussed later, these coherent structures are responsible for most of the momentum and mass exchange between the embayment and the main channel at both the lateral and roof interfaces. The nature of the interactions with the lateral side and crest of the second groyne (partial clipping, total clipping or total escape events according to the classification by Lin and Rockwell, 2001, for cavity flows) controls the intensity of the recirculation motions inside the embayment. A detailed discussion of the relationship between the occurrence of these events and the pressure fluctuations, vorticity fields and flow patterns inside the cavity / embayment is given in Chang et al. (2006). Similar to the emerged case, as these eddies are not captured in the mean flow, one should exercise caution when trying to explain the dynamics of a flow dominated by large- scale transport based solely on the mean flow fields.

The instantaneous flow fields are utilized to understand the flow physics pertaining to large scale unsteadiness and/or intermittency phenomena. For example, the two main vortices upstream of the first groyne and downstream of the second groyne are more deformed in Figure 5.8c-d when compared to Figure 5.5c-d but still recognizable in the instantaneous flow fields, which suggests that these structures are relatively coherent. Animations of the instantaneous flow fields show that these eddies are virtually always present though the structure of the downstream recirculation eddy can vary significantly in time.

The Q criterion is used in Figure 5.10a to educe the 3D vortex tubes in the instantaneous flow associated with the vertical DSL (the other vortical structures in the flow were eliminated from the picture). The other frames show 2D streamlines in a diagonal plane (Figure 5.1b) and in several vertical planes (Figure 5.10c-e) situated at different distances from the lateral wall. Qualitatively, the vortical structure of the vertical DSL is similar in many respects to that of the horizontal DSL.

Details of the eddy content of the horizontal DSL are shown in Figure 5.11a-e in which the instantaneous values of out-of-plane vorticity component were plotted at five planes over the depth of the channel. The strength and coherence of the vortex tubes is the largest near the mid-depth of the groyne (Figure 5.11c-d). The vortex tubes lose some of their coherence as they approach the transition region near the top of the groyne (Figure 5.11b) and the channel bottom (Figure 5.11e) where they interact with the near-bed turbulence. Figure 5.12 shows similar information for the vertical DSL which is visualized in four vertical planes parallel to the lateral channel wall.

Observe also the wide range of scales and large levels of the instantaneous vorticity associated with some of the eddies present inside the embayment in Figures 5.11 and 5.12. They indicate the strong 3D nature of the flow inside the embayment. However, these medium and small resolved scales are not associated with organized large-scale phenomena, such that the vorticity levels in the mean flow fields (Figures 5.13c and 5.14c) are relatively low inside the embayment everywhere except in the attached boundary layers. In Figure 5.12c, several patches of vorticity are advected parallel to the upstream face of the first groyne toward its crest. Animations show that once they arrive in the crest region, they will jitter the vertical DSL. This will induce a strong disturbance into the way the vortex tubes are shed over some finite amount of time. This is one of the mechanisms responsible for the random switching between the different types of interactions among the vortical structures inside the DSLs and the extremities of the downstream groyne.

Figure 5.13 and Figure 5.14 show the distribution of the TKE, mean primary shear stress and the magnitude of the out-of-plane mean vorticity component in one horizontal plane situated at mid distance between the bed and the roof interface (z/D=0.5) and in one vertical plane situated at mid-distance between the lateral wall and the lateral interface (y/D=3.44). They serve to better illuminate the similarities and differences between the horizontal and vertical DSLs in the mean flow at equivalent locations.

Information provided in these figures is also of interest for validation of 3D RANS or hybrid RANS/LES models.

The main qualitative difference between the two DSLs in the mean flow is the more curved shape of the horizontal DSL as observed from comparison of the TKE and mean vorticity contours. The vertical DSL in the mean flow appears to be flatter and fairly parallel to the roof interface. The levels of these two quantities are strongly amplified inside the DSLs (by about one order of magnitude in the case of TKE compared to the regions away from the embayment region) mainly because of the convection of the vortex tubes which induces high levels of large-scale fluctuations on top of the background turbulence.

The amplification of the TKE inside the embayment in the region close to the crest of the second groyne in Figure 5.14a is due to the partial and complete clipping events. As patches of vorticity are injected inside the embayment through the roof interface near the crest of the second groyne, a wall-attached vertical jet-like flow forms parallel to the upstream face of the second groyne. This explains the large mean vorticity values observed in that region in Figure 5.14c. The partial and complete clipping events are modulating the intensity of this jet-like flow in time.

Evidence of a similar, though weaker, phenomenon that occurs in the horizontal mixing layer where the complete escape events predominate is given by the visualization of the instantaneous out-of-plane vorticity in Figure 5.11c and Figure 5.12c. Three large patches of vorticity associated with vortex tubes are visible inside the horizontal DSL in between the two groynes, and a deformed stretched one is observed downstream of the second groyne. The position of the second and third patches strongly suggests (animations confirmed this) that these structures will be convected past the second groyne without interacting with it.

The vorticity distribution inside the vertical DSL at the same time instant is different. The last patch of vorticity has just been entrained (total clipping event) inside

the cavity while the one behind it will also be totally entrained or at least interact with the crest of the groyne such that part of it will be injected inside the embayment (partial clipping event). Though examination of animations shows that partial clipping and even total clipping events can transpire inside the horizontal DSL, their occurrence is much lower compared to that of the total escape events. In contrast, the total clipping events dominate in the vertical DSL. In fact, the mean flow inside the embayment close to the crest of the second groyne reveals a strong downward flow. Such a flow component (spanwise flow toward the lateral wall) is absent in the mean velocity contours at the equivalent position inside the horizontal DSL.

The other region of high amplification of the mean out-of-plane vorticity is situated at the side extremity/crest of the upstream groyne (Figure 5.13c and Figure 5.14c) where the vortex tubes are shed at a frequency that is strongly dependent on the physical Reynolds number in the horizontal/vertical DSLs. Though the TKE amplification levels in the embayment region in the two DSLs are similar, the decay downstream of the second groyne is somewhat different. The differences are even clearer when the primary resolved shear stress in the corresponding horizontal and vertical planes are compared in Figure 5.13b and Figure 5.14b. Between the two groynes, the amplification of the primary shear stress is higher in the horizontal plane. The shear stress values in the horizontal plane are relatively large up to two embayment lengths downstream of the second groyne at the interface between the DSL and the downstream recirculation region (Figure 5.5c). In contrast, the decay of the shear stress at the downstream part of the vertical DSL is much faster primarily because of the predominance of the total escape events inside the horizontal DSL and of total clipping events in the vertical DSL for the embayment geometry considered in the test case. In the case of total escape events, the highly energetic patches of vorticity will continue to be convected downstream of the second groyne, which will induce larger Reynolds stresses in the horizontal DSL past the second groyne. In the case of the vertical DSL,

most of these patches of vorticity are injected inside the embayment and relatively few of them will be convected past the second groyne.

To make the analysis easier to follow, the above discussion distinguishes between the vertical and horizontal DSLs. In fact, these two DSLs are continuous and one should talk instead about a continuous sheet of vorticity associated with the DSLs originating around the crest and lateral side of the first groyne. Besides the vortex tubes that populate this vorticity sheet, a trailing edge vortex whose direction is predominantly streamwise forms at the corner of the upstream groyne. Figure 5.15 shows the TKE distribution in a spanwise plane (x/D=2.75) situated at mid-distance between the two groynes. The shape of the vorticity sheet as well as the small TKE amplification near the corner associated with the trailing vortex can be inferred from this picture. It appears that at mid-embayment length, the intensity of the turbulent fluctuations inside the vertical DSL is larger compared to the ones inside the horizontal DSL. This can be explained by considering that the fluctuations scale with velocity magnitude. The velocity magnitude in the area of the vertical DSL is nearly 30-percent higher than the velocity magnitude in the corresponding area occupied by the horizontal DSL. This is caused by the constriction of the flow between the upstream groyne and the free surface boundary. It follows that the TKE is nearly 30-percent higher in the vertical DSL than in the horizontal DSL. In cases in which the relative submergence will be higher the differences in the TKE levels in the horizontal and vertical DSLs are expected to diminish.

Details on the trailing edge vortex in the mean flow are given in Figure 5.16 in which the Q criterion educes the position of the vortex relative to the embayment (Figure 5.16a) and 2D streamlines is several sections perpendicular to the mean flow direction are used to obtain more details on its structure (Figure 5.16b-e). The position of the trailing edge vortex in all the sections is situated slightly above and toward the exterior of the embayment volume. The decay in the mean circulation of the vortex is plotted in Figure

5.16f starting at the downstream face of the first groyne. Over a distance of 0.5D from the edge of the first groyne, the trailing edge vortex lost more than 60% of its circulation.

Figure 5.17a-h displays the pressure power spectra at several stations whose position is given in Figures 5.13 and 5.14. The points located near the tip of the upstream groyne show the presence of a broad turbulent spectrum. Velocity and pressure power spectra show that the range of energetic frequencies (f) associated with the shedding of the vortex tubes from the formation region, expressed in the form of a non-dimensional Strouhal number (St=fD/U), is between 3 and 6. In the area past the location where the merging of consecutively shed vortex tubes generally occurs, the range of dominant frequencies is between 1.5 and 2.7 (see spectra at points A and E in Figure 5.17a, 5.17e and 5.17f), consistent with the observed pairing process that takes place in both the horizontal and the vertical DSLs. In the same spectra, the high frequency range $3<St<6$ is still present but is not very energetic. Point G (Figure 5.17h) is located downstream of the embayment. As expected, the power spectrum at G does not contain the high frequency range ($3<St<6$) associated with the initial shedding of vortex tubes inside the DSLs but the spectrum remains broad. The same can be said of the spectra at point C and D inside the embayment volume. The spectra at point D situated close to the upstream face of the embayment contains a fairly broad range of low energetic frequencies ($St<2$) associated with the large-scale recirculating motions inside the embayment. The spectrum at point C situated in the region where the DSL eddies are injected into the jet-like flow parallel to the downstream groyne contains two peaks around St=0.7 and St=0.9 which are probably associated with the occurrence of total or partial clipping events. By comparison, the dominant frequency inside the DSLs is close to St=2 and corresponds to the convection of eddies inside the DSLs regardless of the kind of interaction which will take place when they approach the tip of the downstream groyne.

5.3.3 Mean and Depth-Averaged Velocity Fields

The mean velocity fields (u/U, v/U, w/U) are shown in four horizontal planes through the channel depth along with the depth-averaged velocity distributions in Figure 5.18 to 5.20. Knowledge of the 3D and depth-averaged distribution of the velocity components is useful for validation of simpler 3D or 2D depth-averaged RANS or LES models that are used to predict flow past groyne-like geometries. Observe the large qualitative differences in the distributions of the horizontal velocity components in the section at z/D=1.3 situated between the embayment roof and the free surface and the ones at levels that cut through the groynes (z/D<1). The other important feature of the mean flow field is the presence of a strong downward flow inside the embayment close to the downstream groyne in Figures 5.20b-c. This region of large negative vertical velocities is due to the strong jet-like flow parallel to the downstream groyne produced by the total and partial clipping events that predominate inside the vertical DSL.

5.3.4 Coherent Structures in the Mean and Instantaneous Flow Fields

To better comprehend the mechanisms responsible for the ejection of a passive scalar (contaminant) from the embayment, one should first visualize the main 3D eddies in the embayment area and understand their interaction and ultimately their role in the mass exchange processes between the embayment and the channel. The analysis is quite difficult in the submerged case as the degree of three-dimensionality of the flow is very high and the instantaneous energetic coherent structures can be very different compared to the eddies in the mean flow solution. Nevertheless, animations of the LES flow fields show that some of the 3D structures observed in the mean flow have a clear correspondent in the instantaneous flow.

The 3D and 2D streamlines in Figure 5.21 serve to describe the flow structures in the complex recirculation upstream of the first groyne, in particular the interaction

between the vertical corner vortex and the junction vortex which forms at the base of the first groyne. The incoming attached boundary layer on the lateral wall separates due to the adverse pressure gradients induced by the presence of the first groyne in a similar way to the boundary layer on the bed.

In the emerged case, it was shown that the main role of this corner vortex was to feed fluid and momentum from the upper layers, starting at the free surface, into the main necklace vortex of the HV system forming at the base of the first groyne. In the submerged case, the structure of the system of corner vortices is more complex. As shown in Figure 5.21a, only the fluid being convected from upstream below z/D~0.6 is entrained into the corner vortex that feeds fluid into the HV system, which suggests that the dynamics of the corner vortex may have an important effect on the dynamics of the HV system.

Part of the incoming fluid between z/D~0.6 and z/D~0.9 is also entrained into a corner vortex. However, the flow inside the core of this corner vortex is toward the free surface rather than toward the bottom, as is the case for the corner vortex present at the deeper levels. The core of this corner vortex also changes orientation from being initially vertical to becoming parallel to the lateral wall. In fact, at the junction between the groyne and the lateral wall, close to the crest, an HV system is present. In addition, a secondary weaker vortex is present in the mean flow (see Figure 5.21a and Figure 5.21c) close to the lateral wall and upstream of the main corner vortex. The Q criterion (see inset in Figure 5.21a) shows only one main continuous structure corresponding to the two corner vortices and the two necklace vortices at their ends as well as the secondary vortex at levels close to the free surface. This is somewhat expected if the relative submergence is high, such that in the vicinity of the upstream groyne there is a similarity between the obstructing effect of the groyne relative to the lateral wall and to the bottom given that the incoming flow is parallel to both these surfaces and no stratification effects are considered. This also explains the qualitative similarities observed between the vertical

and horizontal DSL over the roof and lateral interfaces. As for the flow over groynes in a channel, it is the HV system present at the base of the first groyne near the bed surface and the accelerating flow around the groyne tip that create scouring problems. The next section will concentrate on an analysis of its structure. However, for similar reasons, an amplification of the shear stress on the lateral wall is also present near the crest level around the first groyne.

The mean flow fields are much less helpful in understanding the complex interactions taking place within the embayment volume. However, it appears that most fluid particles inside the embayment will follow a helicoidal path induced by a large 3D vortical eddy bounded by the vorticity sheet associated with the horizontal and vertical DSLs. This eddy plays a major role in the movement of fluid between different levels within the embayment. As shown by the 3D streamlines in Figure 5. 22a, its core starts by being perpendicular to the lateral wall and ends being perpendicular to the bottom. The core appears to be situated in a plane parallel to the groynes. The 2D streamlines are shown in sections cutting through the embayment volume, parallel to the lateral and bottom walls and situated at small distances from them and confirm the presence of a large vortical motion induced by the overflow and the lateral flow in these sections. The flow direction inside this mean vortical structure appears to be from the lateral wall and the bottom wall toward the central part of the embayment.

The flow downstream of the second groyne is also more complex than the one observed in the emerged case (Figure 4.20) where a main tornado-like vortex was observed to originate at the bed and increase its section as the free surface was approached. Such a vertical structure is present in the submerged case, as shown by the 3D streamlines in Figure 5.23a, but it extends only up to levels around 0.6D (e.g., it is present in sections situated at z/D=0.1 and 0.5 but not at z/D=0.9 where only a small junction vortex is present, as shown in Figure 5.23b-d). The flow direction inside this vortex is away from the bottom. At higher levels, a vortex originating at the lateral wall

is observed in Figure 5.23a and Figure 5.23e. Its axis is initially perpendicular to the lateral wall. Its center is situated slightly below the crest of the groyne, and the fluid particles entrained into this vortex are convected away from the lateral wall. The core of this vortex curves toward the vertical direction as one moves away from the lateral wall. The end result is that fluid particles entrained into these two recirculation eddies in regions close to the lateral and bottom walls are eventually convected into the main stream somewhere between z/D=0.6 and z/D=0.9. The overall size of the recirculation region associated with these vortices is much smaller compared to the one observed in the emerged case. For instance, the maximum downstream extent is about 2 groyne lengths (l=0.625D) in the submerged case compared to about 7l in the emerged case.

The 3D streamlines used to educe the instantaneous upstream corner vortex system in Figure 5.24 confirm that its instantaneous structure is more complex compared to the time-averaged one. Several vortices whose axes are fairly vertical are observed in the instantaneous flow. The junction vortex is still the strongest, but there are several secondary vortices upstream of it. Though the structure can vary considerably in time, a comparison of Figure 5.21a and Figure 5.24a shows that the averaged flow gives a decent description of the flow dynamics in this region. The instantaneous vorticity contours in Figure 5.11c and d give an idea about the vortical structure in that region at mid groyne depth. One of these vortices (see larger patch of positive vorticity in Figure 5.11c-d) is larger and relatively stable. The others are shed from the separation region and are convected toward the main corner vortex. These eddies are created and destroyed randomly. In some cases, they can merge with the main corner vortex.

The instantaneous 3D streamlines in the embayment shown in Figure 5.25a suggest the general circulation pattern observed in the mean flow in Figure 5.22a is also present in the instantaneous flow fields. However, the instantaneous flow in the embayment region is characterized by the presence of a broad range of eddies which greatly complicate the flow. This is evident from the 2D streamline plots in various

sections in Figure 5.25. The same holds true when the mean and instantaneous flow patterns are compared in Figures 5.23 and 5.26.

5.3.5 Horseshoe Vortex System

The structure and overall intensity of the HV system forming at the base of abutment like structures (in the present case the first groyne) placed in a fully turbulent incoming flow are known to undergo large spatial and temporal variations. Similar to the emerged case, as the flow approaches the first groyne, the incoming boundary layer separates and necklace like vortical structures form around the base of the groyne as a result of the transverse pressure gradients and of the downflow. These vortices are stretched as they are swept around the tip of the groyne. These eddies are thought to largely control the evolution of the scour process which in some cases can endanger the structural integrity of the groyne.

The mean spatial structure of the HV system is shown in Figure 5.27a-h using 2D streamlines in vertical planes (see also Figure 5.1a). Somewhat similar to the emerged case (see Figure 4.25), the mean HV system is composed of a primary necklace vortex A and an elongated eddy upstream of it denoted B in each frame. Vortex A is initially parallel to the upstream face of the groyne. Subsequently, its core changes orientation and follows the curved shape defined by the horizontal DSL near the bed.

Figure 5.28 shows the TKE distribution in the same frames as Figure 5.27 for the emerged case. As discussed in Chapter 4, the TKE is significantly amplified within the region occupied by the main necklace vortex. The vertical patch of high TKE in Figure 5.28g-h corresponds to the cut through the horizontal DSL. The large TKE values in the region associated with the separation of the attached boundary layer are due to the formation of a jet like flow of variable strength beneath the main vortex A. This jet-like flow is the main reason why large scale oscillations of the primary vortex A are observed in the instantaneous flow fields.

By comparison, the TKE amplification in the submerged case shown in Figure 5.29 is smaller (by 20-30%) than the one observed in the emerged case (for the same mean channel velocity) in practically all the sections. This is expected because the flow convected into the upstream recirculation region and feeding into the main necklace vortex starts only at z/D~0.6 in the submerged case compared to z/D=1 (free surface level) in the emerged case. In the submerged case, the flow above z/D~0.6 is eventually convected into the overflow on top of the embayment. However, at flooding conditions, the mean channel velocity is higher, so the dimensional values of the TKE will be higher. Consequently, the effectiveness of the HV system in entraining sediment will be higher in the submerged case as the sediment size remains the same at normal and flood conditions.

The complex spatial structure of the HV system is shown in Figure 5.30 using instantaneous 2D streamlines. The instantaneous streamlines in the same sections as those shown in Figure 5.27 for the mean flow clearly show important differences between the mean and instantaneous structure of the HV system as it wraps around the base of the upstream groyne. The flow inside the HV system is characterized by random interactions among the necklace eddies. Similar to the emerged case, animations in several vertical planes show that the primary necklace vortex A is practically always present though its shape and size can vary considerably over time. The primary vortex A in the mean flow corresponds to the instantaneous vortex A in Figure 5.30. By contrast, no instantaneous vortex in Figure 5.30 can be directly associated with the elongated eddy denoted B in Figure 5.27. This eddy is a result of the averaging process. It is associated with the secondary vortices that are shed from the separation region toward the main necklace vortex A in the instantaneous flow.

No definite frequency can be associated with the shedding of these secondary necklace vortices. The range of Strouhal numbers associated with the convection of these eddies toward the main necklace vortex and with their oscillations is between 0.45 and

2.3. Besides these frequencies, velocity and pressure power spectra show the presence of energetic frequencies between St=0.12 and St=0.29 (see times series and power spectrum of streamwise velocity in Figure 5.33 at a point situated inside the HV system; its position is shown in Figure 5.27e). These lower frequencies are associated with aperiodic oscillations (e.g., see Devenport and Simpson, 1990, Simpson, 2001) of the primary vortex A between what is generally called a zero-flow mode, in which the primary vortex is situated closer to the groyne base and the near-bed jet flow beneath it is weak and separates early, and a back-flow mode in which the near-bed jet flow is stronger and separates at a larger distance from the abutment. In the back-flow mode, the main necklace vortex is convected away from the wall and assumes a more elliptical shape. The oscillations of the necklace vortex A between these two modes are the main reason for the high turbulence intensities observed in the HV region in Figure 5.29.

The instantaneous 2D streamlines in Figure 5.31 and Figure 5.32 (35^{o} section) provide a better understanding of the flow dynamics within the HV system in a section where its overall intensity is close to the peak.

The streamlines in Figure 5.31 illustrate one of the mechanisms that result in a strong modulation of the intensity of the primary vortex A. A comparison of Figure 5.31a and Figure 5.31b reveals that the secondary vortex C is moving toward the tip of the groyne while, as a result of its interaction with the secondary wall-attached vortex, the primary vortex is moving away from the groyne tip. Vortices A and C start interacting and eventually merge in Figure 5.31c. The merging is practically complete in Figure 5.31d, where the following secondary necklace vortex D starts moving toward the new primary vortex A.

Another mechanism that results in a large variation of the structure and intensity of the primary vortex A is illustrated in the successive frames in Figure 5.32. In this case, the interactions with the secondary vortices convected from the separation region of the incoming boundary layer are negligible. As a result of the change in the intensity of the

downflow, the secondary wall-attached vortex, WA, that is present at most times immediately upstream of vortex A grows such that its size and intensity become comparable to that of the primary vortex A (Figure 5.32b). Concomitantly, this secondary vortex is swept away from the bed and starts merging with the primary vortex, as shown in Figure 5.32c. In Figure 5.32d, the merging is complete and the size of the primary vortex A has grown considerably compared to its mean size.

5.3.5 Bed Shear Stress Distribution

Figure 5.34 shows the contours of the non-dimensional bed shear stress relative to the mean value ($\tau_0 = \rho u_{\tau 0}^2$ where $u_{\tau 0}/U = 0.052$) corresponding to fully turbulent flow in a channel of an identical section without groynes. The mean bed shear stress τ/τ_o distributions in the emerged and submerged cases are plotted in Figure 5.34a and 5.34b. Qualitatively the bed shear stress distributions appear similar. The maximum values of τ/τ_o are close to 15 in the submerged case and close to 16 in the emerged case in the strong acceleration region near the tip of the upstream groyne. This is consistent with previous experimental observations of the scour at bridge abutments (isolated spur dike) that show that scour is initiated in the region around the tip of the groyne. Once the scour hole starts forming, the largest bed shear stress values are recorded beneath the main eddy of the HV system. In both simulations, the large amplification of the bed shear stress around the tip of the upstream groyne indicates that severe scour can occur at the base of the first groyne. By comparison, the amplification around the second groyne is very small.

For the mean sediment size of d_{50}=0.45mm, it was shown in section 4.3.5 that the critical bed shear stress value for sediment entrainment, τ_{cr}/τ_o, is equal to 3.3, which is why the values beneath $3.3\tau_0$ were blanked in Figure 5.34a-c. Observe that the entrainment area is slightly larger in the emerged case. This may appear counterintuitive knowing that scour is generally more intense at flood conditions. However, the present

results are consistent with this observation. The two non-dimensional distributions in Figure 5.34a and Figure 5.34b automatically take into account the additional water depth at flood conditions while the mean incoming velocity is assumed to be identical. However, this is not the case when flooding occurs. Typically, the mean velocity in the channel is higher (roughly proportional to the hydraulic radius at power 2/3) and thus the same is true for the Reynolds number in the submerged case. Assuming scale effects are relatively small between the Reynolds numbers corresponding to normal and flood conditions (the incoming flow is fully turbulent in both cases), the distribution of the dimensional bed shear stress will show that higher values are predicted and the entrainment region is larger in the submerged case which is associated with real flood conditions.

Similar to the emerged case, the instantaneous distribution of τ/τ_o for the submerged case in Figure 5.34c shows the large variability of the bed shear stress distribution and the direct correspondence between the intensity of the coherent structures above the bed (e.g., coherent structures being convected inside the DSL, primary and secondary necklace vortices whose intensity vary along their axes) and the bed shear stress value. Typical variations of the instantaneous bed shear stress values around the mean value are of the order of $1.5\tau_0$ in the region of high bed shear stress amplification beneath the HV system and in the upstream part of the horizontal DSL, as observed from the time series of the nondimensional bed shear stress in Figure 5.34d-f. The positions of points p11, p12 and p13 are shown in Figure 5.34a.

One of the quantities of real interest for sediment transport is the probability distribution function (pdf) of the local instantaneous bed shear stress, especially over the range of values comparable to the mean critical value for sediment entrainment given by the Shields diagram. To estimate this quantity one has to first compute the histograms of the instantaneous bed shear stress. Figures 34g to 34i show the pdf plots (histograms) for

the emerged case and Figures 34j to 34l display the probability plots for the submerged case at the same points (see Figure 5.34a).

Entrainment of sediment particles from the bed occurs with a certain non-negligible probability when τ is comparable with τ_{crit}. As already discussed, if the same channel bulk velocity is present in both the emerged and submerged cases, than the overall intensity of the HV system and the associated bed shear stress levels are expected to be higher in the emerged case. This is clearly seen by comparing the corresponding histograms for the emerged and submerged cases in Figure 5.34.

In the following paragraphs an introductory discussion about more modern approaches to determine the criterion for incipient motion, which go beyond the deterministic way in which the local mean value of the bed shear stress is the only parameter used to determine whether or not sediment particles will start being entrained at the bed (e.g., using Shields diagram), are briefly presented following for the most part the review in Papanicolaou et al. (2002). This is an interesting and needed approach as incipient motion criteria based only on the time-averaged bed shear stress were shown to underpredict sediment transport (Papanicolaou et al., 2002). One of the first to point out that Shields diagram for the mean bed shear stress should be modified to take into account the probabilistic nature of the entrainment process was Gessler (1971). He assumed that fluctuations of the shear stress about the mean are normally distributed and if the value of the mean bed shear stress at the bed is equal to the critical value for that sediment size than the probability of motion for the sediment particles is 50%. However, his theory did not account for the presence of near bed turbulent structures that play a determinant role in local entrainment (e.g., sweep events, etc.).

In these stochastic approaches the role of the near-bed turbulent structures and, in some cases, the bed packing density (Dancey et al., 2002, Papanicolaou et al., 2002) are accounted for. The main idea behind these approaches is that turbulent stresses and intermittant phenomena such as turbulent bursting are mainly responsible for the initial

entrainment of sediment particles along with initial bed packing conditions (especially for gravel bedstreams) and other sediment properties (e.g., distribution of the pressure fluctuations in the near bed region). Criteria for the initiation of motion of sediment in loose bed channels were proposed, among others, by Neil and Yalin (1969), Shividchenko and Pender (2000) and, very recently, by Dancey et al. (2002) who also investigated the role of sediment packing density on the critical shear stress and the bed load transport rate for conditions close to the threshold of sediment motion. In the approach proposed by Dancey et al. (2002), the probability at the threshold of motion was determined such that the measured Shields parameter under these conditions was comparable to that measured in the literature for isolated grains. Their experiments showed that at conditions close to the threshold of motion the bed load transport rate, the fraction of moving sediment particles and the Shields parameter increase with increasing packing density.

Most of these models (e.g., Engelind and Fredsoe, 1976, Fredsoe and Deigaard, 1992, Cheng and Chiew, 1998, Keshavarzy and Ball, 2000) try to estimate the probability of sediment entrainment (pick up probability function defined as the probability that the lift on the particle is larger than the weight). For instance, in the model of Cheng and Chiew (1998), the Shields criterion for the definition of threshold condition for sediment transport is equivalent to a value of 0.6% for the pick up probability (percent of the particles on a given area that are moving under the threshold condition of sediment transport set by Shields criterion), at least for high particle Reynolds numbers (>500). In these models the normal and shear Reynolds stresses as well as the hydrodynamics forces and moments are assumed to be well represented by a normal distribution. However, in some more recent models (e.g., Papanicolaou et al., 2002), based also on recent experimental investigations of channel flows, a more complex non-symmetrical distribution is assumed (e.g., a general non-central chi-squared distribution or a log-normal distribution). It was also shown that the shape of the distribution is related to the

changes in the bed microtopography (bed packing conditions). One should also point out that the expressions proposed for the probability of sediment entrainment in these studies are generally deduced based on experiments conducted on flat beds with uniform sediments.

In the approach proposed by Keshavarzy and Ball (2000) the classical Shields diagram was modified through adding a pdf. A pdf for the intermittent instantaneous bed shear stress and a pdf of particle entrainment from the bed were derived. These two pdf's were used to modify the Shields diagram through the addition of the pdf of particle motion. To incorporate the pdf of the shear stress into the Shields diagram, the magnitude of the shear stress for the sweep event and for a 50% exceedance probability were selected and computed. Then, a 50% exceedance probability was selected and used to add information on the instantaneous shear stresses and the percentage of entrainment area to the Shields diagram. This way information on the initiation of motion was added to the Shields diagram such that the entrainment of sediment particles (given a certain particle size) with a certain probability of occurrence can be obtained from the diagram. Close to the original Shields curve for the mean bed shear stress the percentage of area entrained was found to be around 10% given an exceedance probability of 50%. This result also showed that Gessler's (1971) assumptions were too conservative.

The simpler approach proposed by Keshavarzy and Ball (2000) for the estimation of particle motion given a certain instantaneous value of the bed shear stress and a certain particle size can be used in numerical models in which the near bed turbulence is resolved (e.g., as is the case in the present LES model in which at each location the instantaneous bed shear stress is known from the simulation and a pdf can be calculated as was done in Fig. 5.34) to get a more realistic estimation of the sediment entrainment in the case in which the channel bed is loose. For example, for the sediment size of 0.45 mm assumed in the present discussion of flow past a single embayment for which the particle Reynolds number is 6.13 at critical conditions (based on the mean bed shear

stress), one can use the correlation curves in Figure 12 of the study of Keshavarzy and Ball (2000) to deduce the probability of sediment entrainment (% of area entrained) given a certain value of the instantaneous bed shear stress. For example, for values of the ratio between the instantaneous stress and the time averaged one corresponding to critical conditions (d_{50}=0.45mm) of 1.028, 0.892, 0.649, 0.563 and 0.408, the probability of sediment entrainment will be 12.5%, 11%, 8%, 6.8%, 5%, 3%, respectively. The same information can be used together with the deduced pdf's of the local bed shear stress distributions in Fig. 5.34 to estimate the mean probability of sediment entrainment at a given position based on LES simulations.

Observe also that the range of recorded bed shear stress values around the mean (the variance) is larger in the emerged case. This large variance is also expected to be present at points where the mean bed shear stress is smaller than the critical value. If a classical RANS model would be used then the model would predict no sediment entrainment to occur at that position. This is obviously wrong, as entrainment of sediment particles can occur at those locations in an intermittent fashion (with a lower probability). Thus variance of the bed shear stress along with the mean bed shear stress distribution should be used with simpler RANS models to determine whether or not sediment will be entrained locally. Models for estimation of the variance are still to be proposed for complex geometry flows in which massive separation is present. In this regard LES or hybrid LES-RANS models that resolve the variations of the bed shear stress induced by the passage of the resolved large-scale coherent structures can account for these phenomena without need for extra modeling and are more appropriate for applications in which prediction of sediment entrainment from the bed is of interest.

Based on the results in Figure 5.34, in the emerged case the bed shear stress at point 11 (Figure 5.34g) has a cumulative probability (calculated by integrating the probability up to the threshold value from the histograms shown in Figure 5.34) of 1.0 for being greater than the critical bed shear stress. At point 12 the cumulative probability is

close to 0.90 (Figure 5.34h) and at point 13 is close to 0.93 (Figure 5.34i). In the submerged case the cumulative probabilities at points 11, 12 and 13 are equal to 1.0, 0.45and 0.69, respectively.

5.4 Mass Exchange Processes

5.4.1 General Description

Details of the contaminant ejection and dispersion are visualized in Figure 5.35 to Figure 5.37, which show contours of the instantaneous concentration as the contaminant is leaving the embayment in a horizontal plane situated at groyne mid depth (Figure 5.35), in a vertical plane situated at groyne mid length (Figure 5.36) and in a vertical plane situated at embayment mid length (Figure 5.37). The non-dimensional times with respect to the start of the ejection process are marked on these figures. The concentration levels in frames g and h of these figures (maximum contour level is 0.03) are different compared to the ones used in frames a to d (maximum contour level is 0.1) such that the structures and concentration distribution can be clearly identified in the embayment region and the main channel in the later stages of the removal process.

Examination of animations of the concentration fields shows that most of the contaminant leaves the embayment area by being entrained into the horizontal and vertical DSLs. As low-concentration fluid from the channel is entrained within the embayment over the downstream part of the lateral and roof interfaces (e.g., observe the difference in concentration between the upstream and downstream parts in Figure 5.35b and Figure 5.36b), higher concentration embayment fluid is pushed parallel to the downstream face of the first groyne toward the lateral side or the crest. Once it approaches the upstream part of these DSLs in which patches of vorticity that correspond primarily to the vortex tubes are convected, wisps of high concentration fluid are entrained in between these structures and then carried with them further downstream. This process is illustrated in Figure 5.38, which shows the vortex tubes visualized using

instantaneous out-of-plane vorticity contours and the corresponding concentration contours in a vertical plane cutting through the vertical DSL at two time instances. As the wisps of high concentration fluid are advected, they mix with the surrounding low concentration channel fluid due to the intense stretching of the coherent structures that populate these DSLs and their subsequent breaking into small scale turbulence (recall that the DSL region is characterized by high levels of the TKE).

As a relatively high number of the coherent structures inside the DSLs are advected totally or partially over the second groyne, most of the contaminant entrained into the DSLs over the upstream part of the lateral and roof interfaces will be convected past the embayment region rather than being re-entrained into the embayment. Part of this higher concentration fluid is then trapped into the recirculation region downstream of the second groyne, as clearly shown by the relatively high concentration observed for t>12.5D/U in Figure 5.35 and Figure 5.36. Even at t=33D/U when practically all the contaminant was ejected from the embayment volume, contaminant is still trapped immediately downstream of the second groyne. In fact, the maximum concentrations within the channel are observed to occur in this region rather than inside the embayment for t>18D/U. A considerable amount of the high concentration fluid trapped into the downstream recirculation region appears to be entrained by the large scale eddies in the wake past the embayment toward the free surface (e.g., see Figure 5.36d) before being convected downstream in the channel. For the relative submergence considered in this simulation, most of the mixing between the pollutant and the channel fluid downstream of the embayment region takes place laterally (see Figure 5.35b-d) by the action of the large scale structures associated especially with the horizontal DSL. These structures engulf patches of higher concentration fluid and then mix it with the higher speed channel fluid.

The depth averaged concentration contours are shown in Figure 5.39 at several time instances. Comparisons of the depth-averaged distributions with the corresponding

ones in Figure 5.35 (groyne mid depth level) show that the distributions are qualitatively similar. The depth-averaged distributions can be used to validate 2D depth averaged models that try to predict exchange processes in channels with submerged groyne fields.

The concentration contours in Figure 5.37 indicate that the mass exchange process is highly non-uniform over the depth. Though the same was true for the emerged case (see discussion in Chapter 4), there is an important difference. In the emerged case, it was shown that over practically the whole duration of the ejection process the concentration within the embayment volume was higher in the bottom layer. An important part of the contaminant from this bottom layer was first advected at higher levels within the embayment before leaving the embayment volume. The overall flux of contaminant within the embayment was from the bottom toward the free surface. In the submerged case (e.g., see Figure 5.37d where the color scale allows to differentiate between the concentration levels within the embayment), the higher concentration fluid is usually situated in the upper layers of the embayment. Past the initial stages of the ejection process, the lower layer contains lower concentration fluid and, as will be discussed later, the flux of contaminant leaving the embayment through the channel-embayment interface corresponding to the bottom layer is much larger compared to the emerged case.

5.4.2 Temporal Variation of the Mean Contaminant Concentration within the Embayment

The procedure employed in section 4.4.2 for the emerged case will be implemented to characterize the mass exchange between the groyne field and the channel. . Equations 4.1 and 4.2 are valid for the submerged case. The non-dimensional exchange coefficient, *k*, defined simply as D/(UT) allows a direct comparison of the decay rates in the emerged and submerged cases. Similar to relation 4.3 shown to be valid for emerged groynes, one can define a non-dimensional mass exchange coefficient

for the submerged case in a more physical way which accounts for the fact that the contaminant leaves the embayment volume (=S*l*D) through the lateral and roof interfaces. Its expression is:

$$k_s = lD/(l+D)^x 1/(UT) = l/(l+D)k \quad (5.1)$$

The decay of the mean concentration within the embayment is plotted in Figure 5.40 for both the submerged and emerged cases. The faster decay observed in the submerged case is simply a result of the fact that the contaminant can leave the embayment volume not only though the lateral interface (same area in both cases) but also through the roof interface. In both cases, a change in the slope of decay is present when the mean concentration inside the embayment becomes less than 35-40% of its initial value. This change in the slope of decay occurs at around 3D/U in the submerged case and at 11D/U in the emerged case. The fact that for both cases the decay over the initial and final phases is practically linear in the log-linear plot means that the concentration decay is exponential. The estimated values of *k* over the two phases of decay are 0.29 and 0.18 in the submerged case. The corresponding values for the emerged case are 0.1 and 0.05.

Figure 5.41 gives more information on the mass transfer at different levels within the embayment by separating the volume into three equal volumes corresponding to the bottom, middle and top layers. After 6D/U, the exponential decay rate is practically the same in all three layers. However, over the initial stages of the contaminant ejection process, the rate at which the contaminant is removed from these three layers differs greatly. In particular, the middle and bottom layers lose contaminant much faster compared to the top layer especially for $1<tD/U<3$. The reason for this variation will be explained in the context of the global mass balance for these layers that is discussed in Figure 5.41.

The presence of two regimes of exponential decay was also observed by Engelhardt et al. (2004) in a field study of the mixing processes around irregular river groynes (the changes in bed elevation between the channel and embayment area were gradual) in a reach of the River Elbe for which a one-gyre pattern (one main recirculation eddy inside the embayment) was predominant in the velocity fields. Their results are consistent with the present results. For an embayment in which a two-gyre pattern was predominant, the number of regimes characterized by different values of the exchange coefficient was found to be three.

5.4.3 Non-Uniformity of the Mass Exchange Process over the Embayment Depth

In the submerged case, there is considerable movement of contaminant among different regions within the embayment before it exits the embayment through the lateral or roof interfaces. Similar to the emerged case, the embayment volume was subdivided into three layers of equal volume (at the start of the ejection process all the layers contain a third of the total mass of contaminant introduced into the embayment) corresponding to the top, middle and bottom layers to study in a more quantitative way the mass fluxes at the interfaces between these layers and the mass decay within these layers. The temporal variation of the rate of change of the mass of contaminant within each of these layers (MT1, MT2, MT3 for the top, middle and bottom layers), the instantaneous fluxes through the corresponding part of the lateral interface (F2, F4 and F6), the flux through the roof interface (F1), the one between the middle and top layers (F3) and the one between the bottom and middle layer (F5) are represented in Figure 5.41. The vertical scale is modified in Figure 5.41 for t>15D/U to better capture the variations of these quantities. The rate of change of the contaminant mass (-MT) is considered positive when the total mass within the layer is decaying in time. The fluxes through the roof and

lateral interfaces are positive when contaminant is leaving the embayment. The fluxes F3 and F5 are considered positive when they are oriented toward the bottom.

In the top volume layer (Figure 5.41a-b), -MT1 is always positive, indicating that the top volume is always losing mass. The flux through the roof interface, F1, is always oriented upward as, on average, contaminant is leaving the embayment through this surface. Generally, the flux through the lateral interface, F2, is toward the main channel, except for some small time intervals (e.g., for 2.7<tU/D<3.7). The flux through the bottom surface, F3, is usually toward the free surface (F3<0), but there are times when this flux is reversed (e.g., for 2.7<tU/D<4.8) and the contaminant is moving from the top layer into the middle layer. The flux through the roof interface, F1, is usually larger in magnitude than the flux through the lateral interface, F2. This means that at most times more contaminant leaves the embayment through the roof interface compared to the top third of the lateral interface. The magnitude of the flux through the bottom surface, F3, seems to be highly correlated with the magnitude of the flux through the roof, F1 (F1~-F3). This means that a substantial part of the flux of contaminant through the roof interface is contaminant that has been convected from the middle layer, rather than being linked to a decay of –MT1. In the initial 1D/U, the decay is very fast. Most of this decay is due to the engulfment of high concentration fluid at the top interface by the DSL eddies (-MT1~F1 while F2 and F3 are small). Between 1D/U and 2D/U, the mass decay within the top layer is small (the value of *k* inside the top layer over this time period is only 0.13) as -F3~F1+F2.

In the bottom layer (Figure 5.41c-d), -MT3 is also usually positive. Close to 4D/U, –MT3 is negative mainly because of the incoming flux of contaminant through the top interface of the bottom layer, F5, that is larger than the flux leaving through the lateral interface F6. The flux F6 is oriented toward the channel during the whole duration of the ejection process. The flux F5 changes orientation quite often. However, its predominant direction is toward the free surface (out of the bottom layer). Most of the

time, the majority of the mass decay within the bottom layer is due to contaminant exiting the volume through the lateral interface as F6 is sensibly larger than –F5. Over the first 3.5D/U, the mass decay within the bottom layer is very high (k~0.56 substantially higher compared to the mean value k=0.29 for the whole embayment over the same time period). This is due mostly to the high values of F6 coupled with the non-negligible contribution from F5 whose direction is into the bottom volume.

In the middle volume (Figure 5.41e-f), -MT2 is almost always positive. The flux through the lateral interface, F4, is usually oriented toward the main channel but there are several time periods (e.g., for 3.7<tU/D<5.1 and for 20.5<tU/D<21.3) where the flux is reversed and contaminant is advected back into the middle layer from the channel. The variations of F3 and F5 have already been discussed. Of the three fluxes contributing to the overall mass balance within the middle layer, the flux through the top surface, F3, has the largest magnitude and is oriented most of the time toward the free surface. The other two fluxes have much smaller magnitudes and usually tend to cancel out, as when one is oriented into the middle layer volume the other is oriented out of it. Thus, the main cause of the decay of –MT2 is the contaminant lost through the top surface. Over the first 3D/U, the mass decay within the bottom layer is high (k~0.46) due to the high values of F3, as the contributions of the other fluxes over this period cancel out (F4~-F5).

The temporal evolution of the relative amounts of the cumulative mass of contaminant is shown in Figure 5.42. The cumulative mass is defined as the integral of the flux of contaminant passing through one of the surfaces corresponding to the roof and lateral interfaces normalized by the total amount of contaminant initially present inside the embayment, M_0=0.78 D^3C_0. The cumulative mass advected at the end of the contaminant removal process through the roof interface and the top, middle and bottom lateral interfaces is 44%, 15%, 12% and 29%, respectively.

Another way to interpret the results in Figure 5.42 is to look at the relative mass advected through the interfaces of these volumes relative to the initial mass in each of

these volumes. At the end of the removal process, 173%, 35%, and 91% of the initial mass of contaminant present in the top, middle, and bottom embayment layers has been convected into the main channel, respectively. This shows in a quantitative way the non-uniformity of the contaminant removal process and highlights the role played by the 3D vertical motions inside the embayment.

If the fact that a substantial amount of contaminant leaves the embayment through the top interface (44%) was somewhat expected, it appears that on average the extra amount of contaminant comes from the middle layer. The amount of contaminant leaving the bottom layer through the bottom lateral interface (29%) is very close to the initial mass of contaminant in that layer (33%). This is in complete contrast to the emerged case when the mass of contaminant exiting the embayment through the bottom was much smaller than the initial mass of contaminant in that layer (the mass of contaminant exiting through the bottom, middle and top lateral interfaces were around 17%, 33% and 50%, respectively). In the submerged case, it is the middle lateral interface that is the less effective in removing contaminant from the embayment. The roof interface accounts for roughly the same amount of contaminant leaving the embayment as the sum between the middle and bottom lateral interfaces at all stages of the ejection process, as observed by comparing the curves labeled as roof+top and top+middle+bottom in Figure 5.42. Another interesting observation is that most of the contaminant leaving the embayment through the top and middle lateral interfaces does that during the initial phase ($t<3D/U$). After 3D/U, relatively little contaminant leaves the embayment through these interfaces. This is in contrast to the contaminant transport through the roof and bottom lateral interfaces.

The results in Figure 5.42 allow a comparison of the effectiveness of the horizontal and vertical DSLs to remove contaminant from the embayment. About 57% of the total initial mass of contaminant passed through the lateral interface ($0.445\ D^3C_0$) and 43% passed through the roof interface ($0.336\ D^3C_0$). The roof interface has an area of

$0.78125D^2$ and the lateral interface has an area of $1.25D^2$. The mass yield of the roof interface is calculated as 0.430 DC_0 and the mass yield of the lateral interface is 0.356 DC_0, which reveals that for the present geometry the vertical DSL is about 20% more effective than the horizontal DSL in removing contaminant from the embayment.

5.4.4 Mass Transport through the Channel

The temporal variation of the width-averaged concentration profiles are shown in Figure 5.43 at several sections (x/D=5, 7.5 and 15, the position of these sections is shown in the sketch in Figure 5.43a) situated downstream of the embayment. These profiles give an idea of the vertical distribution of the concentration in time at different locations downstream of the embayment and can be used to assess the level of pollution and times associated with the occurrence of dangerous levels of contamination within the channel. The profiles in each of the three sections (Figure 5.43b-d) is shown at different time instances between t=5.4D/U and t=27.4D/U. These time instances are labeled with numbers (1 to 6) to more easily follow the time variation of the vertical concentration profiles in these sections. The corresponding instantaneous distributions of the concentration in these sections are shown in Figure 5.44 (x/D=5), Figure 5.45 (x/D=7.5) and Figure 5.46 (x/D=15).

In the first section at x/D=5 (Figure 5.44), a short time after the start of the ejection process, the cloud of contaminant starts being convected through the section. The contaminant is initially highly nonuniformly distributed over the depth. The larger concentrations at t=5.4D/U are observed to occur between the roof interface level (z/D=1) and the free surface and are associated with the initial scouring of the high concentration fluid in the roof interface region by the eddies inside the vertical DSL. The lowest concentrations are observed in the middle of the channel. As discussed in Figure 5.42, this is due to the small amount of contaminant leaving the embayment volume through the lateral interface at mid-depth levels. The overall concentration levels at subsequent

times start decaying, and the variability in the concentration distribution over the depth decreases strongly such that for t>12D/U the contaminant can be considered relatively uniformly distributed over the depth. In the later stages of the dispersion process, the largest concentrations are observed near the groyne mid-depth level and are mostly due to the advection of high concentration contaminant trapped in the recirculation region downstream of the second groyne. In the lateral direction, the contaminant cannot diffuse past the horizontal DSL, including above the interface level. This explains the very small concentrations observed in these sections more than two groyne lengths from the lateral wall.

In the section situated at x/D=7.5 (Figure 5.45), there is an initial time until the cloud of contaminant reaches that section. Initially (e.g., at t=5.4D/U), the contaminant distribution is very nonuniform in the section and the concentration is larger near the free surface. By t=7.4D/U, the flux of contaminant peaks in this section and the width-averaged concentration distribution is relatively uniform over the depth, though most of the concentration variation in the section is due to large scale transport in the wake of the embayment. As the average concentration in the section start to decay, the largest values of the concentration are observed in the layers close to the free surface (e.g., at t=12.4D/U and 17.4D/U). Eventually, the width-averaged concentration profile becomes more uniform in the vertical direction for t>22D/U. The diffusion of the contaminant in the lateral direction is still comparable to the one observed in the x/D=5 (Figure 5.44) section mainly because the curvature of the horizontal DSL is relatively small between the two sections.

The situation changes substantially in the x/D=15 section (Figure 5.46) where the region in which relatively high concentration contaminant intrudes extends more than 3.5 groyne lengths from the lateral wall, once the cloud of contaminant starts being convected through the section (t>10D/U). When the overall concentration levels in the sections are the highest, most of the high concentration fluid is situated near the free

surface (t=17.4D/U). Beyond that, the concentration distribution becomes more uniform over the depth, and the largest values tend to be observed near the channel bottom (z/D<0.05). Overall, the concentration distributions in Figure 5.44-46 show that the peak concentrations are observed near the free surface downstream from the embayment region.

5.5 Comparison of the Mean and Depth-Averaged Solutions for the Emerged and Submerged Cases

Depth-averaged quantities are compared in Figure 5.47 between the emerged and submerged cases to more effectively highlight the overall differences between the two cases. The 2D streamlines and distribution of the TKE integrated between the bed and the free surface is shown in Figure 5.47a-b for the emerged case and in Figure 5.47c-d for the submerged case. The same quantities integrated only from the bed (z/D=0) to the roof interface (z/D=1) are shown in Figure 5.47e-f for the submerged case to facilitate comparison of the two cases. This is necessary because, as shown in Figure 5.47c, the large value of the relative submergence depth (1.4) induces a strong overflow that explains why the depth-averaged flow pattern in the embayment region does not contain much information on the recirculation pattern around and between the submerged groynes.

The 2D streamlines in the depth averaged flow show that only a perturbation of the incoming parallel flow is present over the groyne region, similar to the case of a channel flow with bottom roughness elements. By contrast, the 2D streamlines obtained by averaging only over the depth of the embayment in the submerged case (Figure 5.47e) give a good idea of the mean flow pattern and main recirculation motions induced by the groynes over the embayment height and are more appropriate compared with the depth-averaged streamlines in the emerged case (Figure 5.47a).

Several important differences between the flow patterns are observed. The size of the main upstream and downstream recirculation eddies is much larger in the emerged case. For instance, the downstream recirculation eddy reattaches on the lateral wall after 2*l* from the downstream groyne in the submerged case and after approximately 6.5*l* in the emerged case. The recirculation eddies in the region bordered by the embayment and the horizontal DSL are more complex in the emerged case. The larger size of the downstream recirculation eddy and the larger values of the TKE in the DSL past the embayment in the emerged case are due to the fact that the shape of the horizontal DSL is such that most of the eddies shed inside the DSL are convected past the embayment region, while in the submerged case, a larger part of the vortex tubes are either entirely or partially entrained inside the embayment, as evidenced by comparison of the TKE distributions where a larger part of the streak of high TKE associated with the DSL is diverted toward the embayment around the tip of the second groyne (Figure 5.47d) in the submerged case. This phenomenon is practically absent in Figure 5.47b. The number of coherent structures and the streamwise momentum past the second groyne are larger and consequently the decay of the TKE is slower in the emerged case. Even in the region between the two groynes, the TKE levels are around 30-40% larger inside the DSL in the emerged case.

Comparison of the TKE distributions in the submerged case depth averaged over the channel depth (Figure 5.47d) and over the embayment depth (Figure 5.47f) gives an indication of the importance of the overflow and vertical DSL. The TKE values inside the horizontal DSL are smaller in Figure 5.47d. This is expected because the horizontal DSL is absent between the crest of the groynes and the free surface. However, the overall TKE distribution is similar in the two pictures. The only difference is observed over the embayment, in particular over the upstream part of it and over the top of the second groyne where the values are higher in Figure 5.47d. This is due to the contribution of the vertical DSL. The TKE values are very large over the top of the

second groyne because the local water depth is only 0.4D in that region and the vertical DSL extends vertically over the whole local flow depth.

The TKE distributions for the two cases in several horizontal planes enhance understanding of the overall distribution of the TKE over the depth of the embayment and inside the overflow for the submerged case. As observed from comparing the corresponding distributions in Figure 5.48 and Figure 5.49 near the bottom (0.1D), middle (0.6D) and top (0.9D) of the groynes, in both cases there is a substantial amplification of the TKE in the vertical direction between the near bed levels and the mid depth levels, followed by a mild decay of the TKE in the horizontal DSL near the top of the groynes.

Qualitatively, the TKE distribution between the bottom and the crest of the groyne is similar in both cases. In the emerged case, the TKE is amplified at z/D=0.1 near the tip of the second groyne similar to what occurs in the submerged case over the whole depth of the embayment. This suggests that more coherent structures present inside the DSL are injected inside the embayment near the bottom in the emerged case. In the submerged case, the trend is the opposite as the TKE amplification inside the embayment, close to the second groyne, increases as the top of the groyne is approached. The TKE distribution in the submerged case at z/D=1.3 close to the free surface (Figure 5.49a) is somewhat unexpected and suggests that the 3D interaction between the vertical DSL and the lateral wall is important. The amplification of the TKE between the lateral wall and the extremity of the groynes over and past the embayment is very far from uniform in the spanwise direction. Rather, the TKE is amplified in an elongated region that starts at the lateral wall between the two groynes and makes a small angle with it.

Figure 5.50 and Figure 5.51 show the depth-averaged normal Reynolds stresses components for the emerged case and the submerged case, respectively. The highest depth-averaged normal velocity fluctuations are found in the emerged case. This is consistent with the TKE distributions in Figure 5.48 and Figure 5.49. However, as

pointed out earlier, at flood conditions one expects the mean velocity to be higher in the submerged case, in which case the dimensional values of the normal stresses can become higher in the submerged case.

Figure 5.52 and Figure 5.53 show the instantaneous distributions of the concentration in several horizontal planes along with the depth-averaged ones for the emerged and submerged cases, respectively. In the emerged case, though the concentration distribution over the depth is clearly non-uniform especially inside the embayment, the horizontal distribution of the depth-averaged concentration is qualitatively similar to the one observed at various levels between the bed and the free surface. Outside the embayment, where the contaminant is more uniformly distributed over the depth, the agreement is quite good. The situation changes substantially in the submerged case where the depth-averaged levels inside the embayment are substantially lower than the one observed in horizontal planes cutting through the groynes. This is because the overflow over the roof interface contains relatively little contaminant compared to the fluid inside the embayment. The situation is similar in the recirculation region downstream of the second groyne where the concentration levels are relatively very high compared to the mean concentration in the flow at $z/D>1$. The situation is reversed at more than three embayment lengths past the second groyne as the highest concentrations are observed to occur near the free surface. Thus, in the submerged case, the depth averaged distribution of the concentration gives only limited information on the overall distribution of the concentration in and around the embayment.

5.6 Summary

The dynamics of the coherent structures in the flow past two vertical submerged groynes (one embayment) mounted on one of the lateral walls of a flat-bed channel were studied and compared with results from a similar investigation in which the groynes were fully emerged.

As expected, it was found that the three-dimensionality of the flow in the groyne region was much stronger and the overall vortical system inside and around the embayment was more complex when compared to the emerged case due to the momentum transport occurring at the roof interface. The driving force behind the flow dynamics around the roof interface is the coherent structures that populate the vertical DSL. Qualitatively, the development of the coherent structures, their interaction with the corresponding embayment interface and their role in the mass exchange processes between the channel and embayment were found to be similar for the horizontal and vertical DSLs. However, for the geometry considered in the present paper it was found that the coherent structures inside the vertical DSL had a larger chance to be totally or partially entrained into the embayment close to the second groyne compared to the ones convected inside the horizontal DSL. The relative submergence depth was high enough such that the mean flow at the free surface was close to parallel to the mean flow direction in the channel.

The structure and intensity of the HV system at the base of the upstream groyne and the associated bed shear stress distributions were investigated. Consistent with previous experimental investigations of the HV system forming at the base of abutments or isolated groynes, it was found that the turbulence and pressure fluctuations were strongly amplified inside the HV system and that the highest bed shear stress was induced beneath the main necklace vortex and in the strong acceleration region near the tip of the upstream groyne. For the same incoming mean channel velocity, the intensity of the turbulent HV system and the values of the bed shear stress around the tip of the upstream groyne were found to be slightly smaller in the submerged case.

The removal of a passive contaminant introduced instantaneously inside the embayment was studied using an advection-diffusion equation, and the temporal variation of the mean concentration inside the embayment was calculated. Similar to the emerged case (Chapter 4) and to the field study conducted by Engelhardt et al. (2004), for

an embayment with a one-gyre recirculation it was found that the decay process was exponential but cannot be described by a unique value of the exchange coefficient over the whole duration of the contaminant ejection process. The switch between the initially faster exponential decay and the final slower phase occurred after about 60% of the initial mass of contaminant left the embayment, close to the emerged case result. Compared to the emerged case, the contaminant removal process was much faster (by about 3 times) due to the additional roof interface and the action of the vortex tubes advected in the vertical DSL.

The LES simulation allowed a detailed study of the nonuniformity of the mass exchange process over depth, something that is not possible to quantify experimentally using techniques that solely estimate the depth-averaged concentration. The decay of the contaminant mass in the top, middle and bottom layers of the embayment and the mass exchange through the corresponding embayment-channel interfaces were studied in detail. It was found that about 44% of the total initial amount of contaminant left the embayment through the roof interface and less than half of the mass of contaminant initially situated inside the middle layer left the embayment through the corresponding lateral interface. A mass of contaminant close to the one introduced initially inside the bottom layer was found to exit the embayment through the corresponding lateral interface. This shows that a mean upward contaminant motion is present within the top two thirds of the embayment depth.

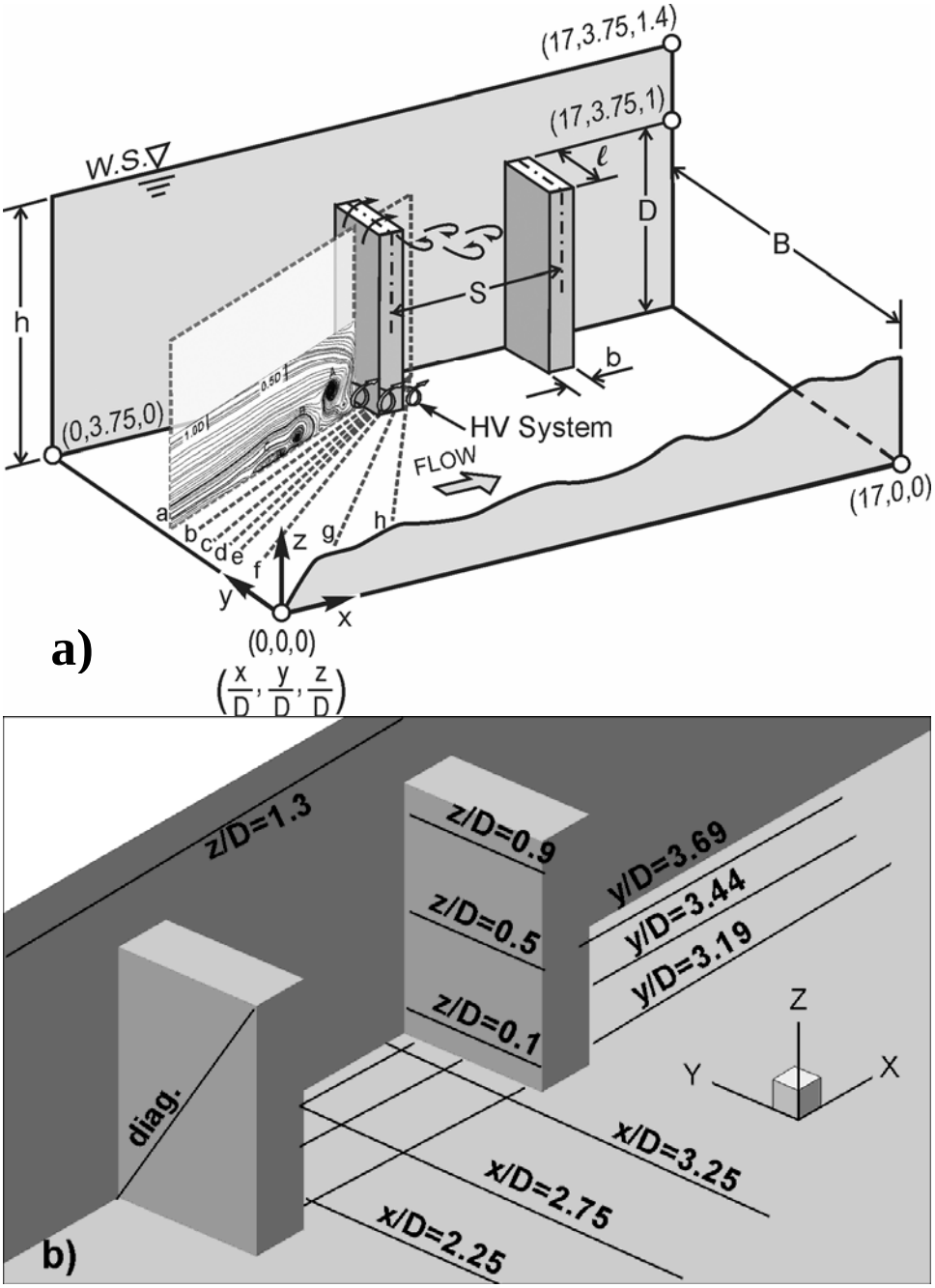

Figure 5.1. Sketch showing channel flow with two submerged groynes. a) geometry and main flow features; b) position of the planes where solution is analyzed.

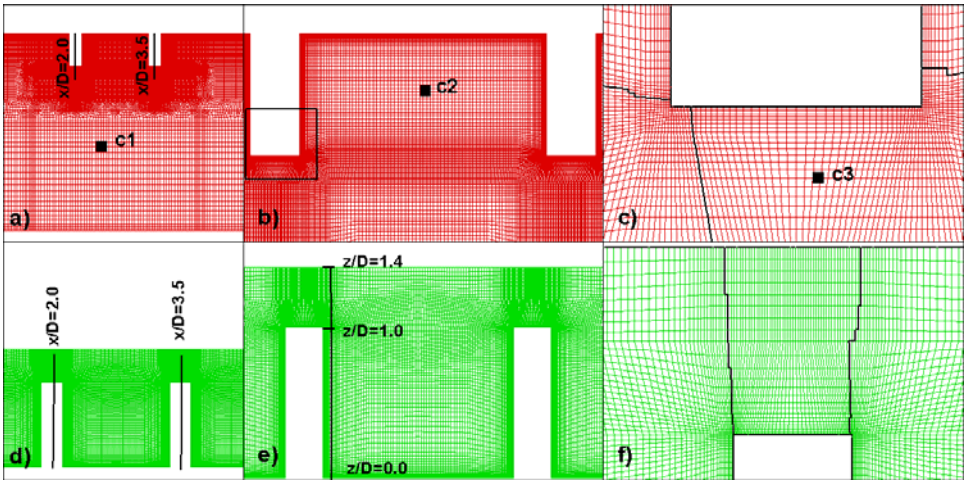

Figure 5.2. Visualization of the mesh. a) partial view showing complete channel width in a horizontal plane cutting through the groynes; b) detail around embayment region; c) detail around groyne tip also showing domain partition on processors; e) partial view in a vertical plane cutting through the groynes; f) detail around embayment region in vertical plane; g) detail around groyne tip in vertical plane also showing domain partition on processors.

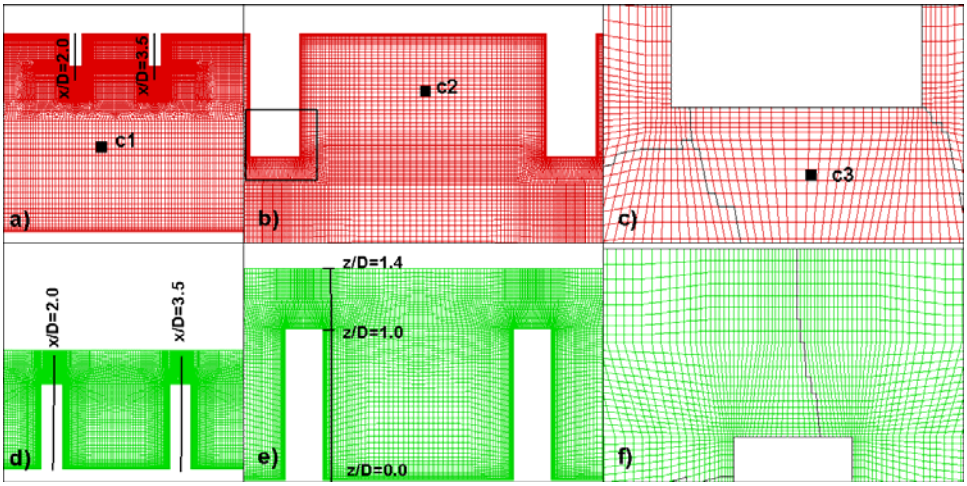

Figure 5.3. Visualization of the coarse mesh. a) partial view showing complete channel width in a horizontal plane cutting through the groynes; b) detail around embayment region; c) detail around groyne tip also showing domain partition on processors; e) partial view in a vertical plane cutting through the groynes; f) detail around embayment region in vertical plane; g) detail around groyne tip in vertical plane also showing domain partition on processors.

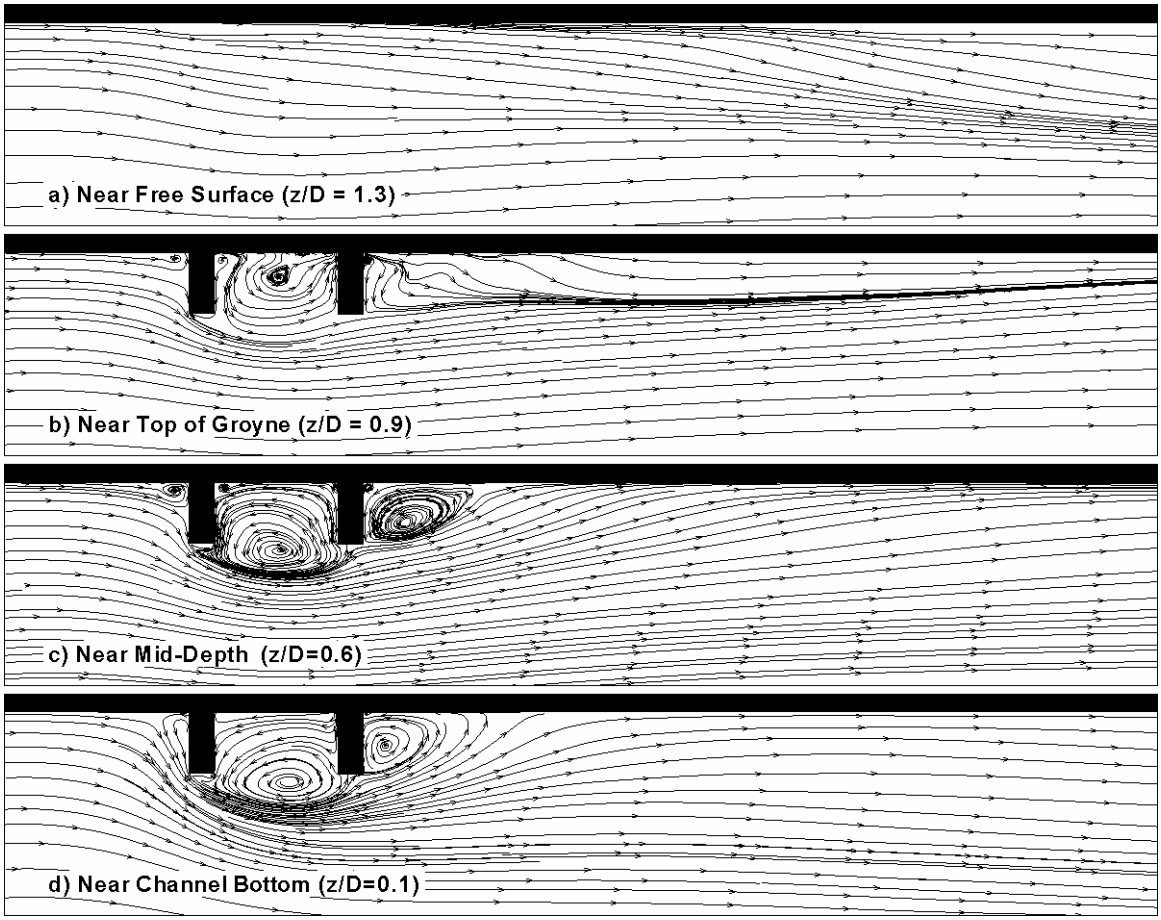

Figure 5.4. Visualization of flow structure using 2D mean velocity streamlines (fine mesh solution). a) near the free surface (z/D=1.3); b) near the groyne top (z/D=0.9); c) near mid-depth (z/D=0.6); d) near the channel bottom (z/D=0.1).

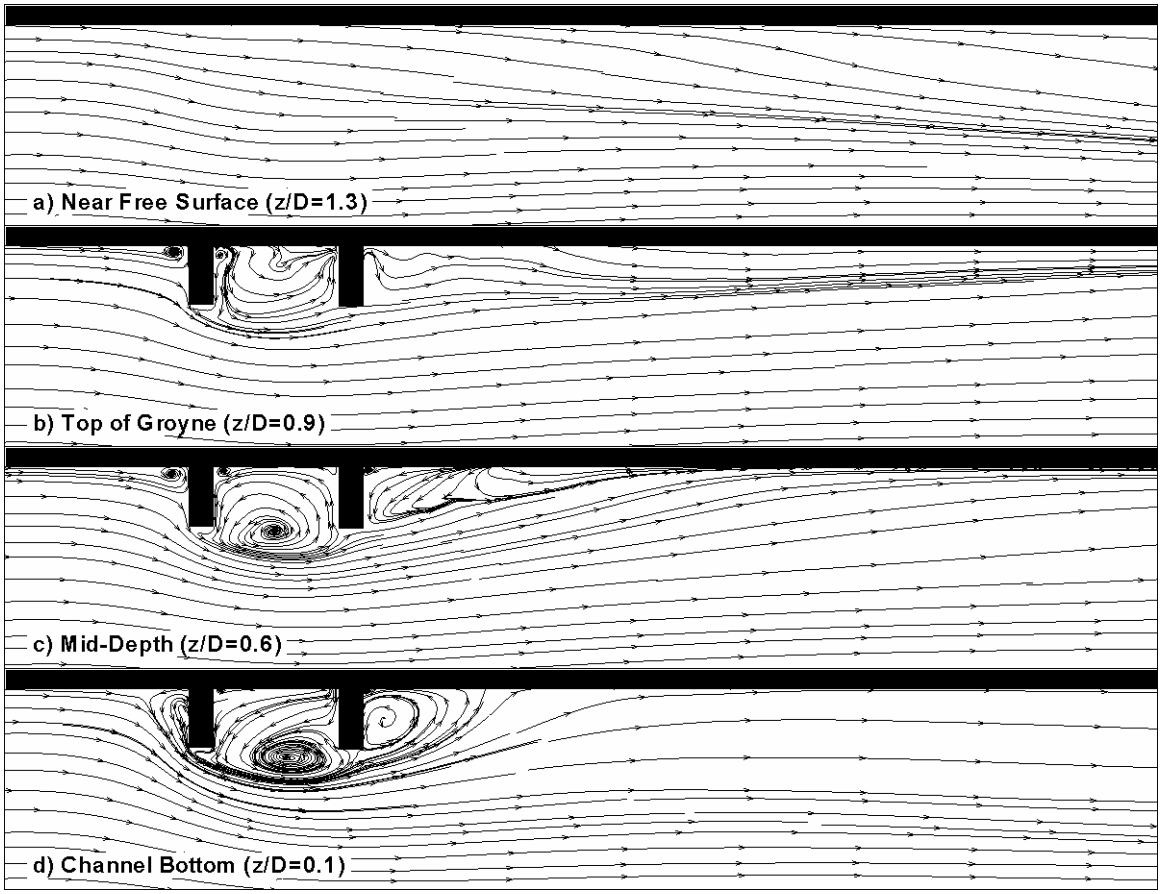

Figure 5.5. Visualization of flow structure using 2D mean velocity streamlines (coarse mesh solution). a) near the free surface (z/D=1.3); b) near the groyne top (z/D=0.9); c) near mid-depth (z/D=0.6); d) near the channel bottom (z/D=0.1).

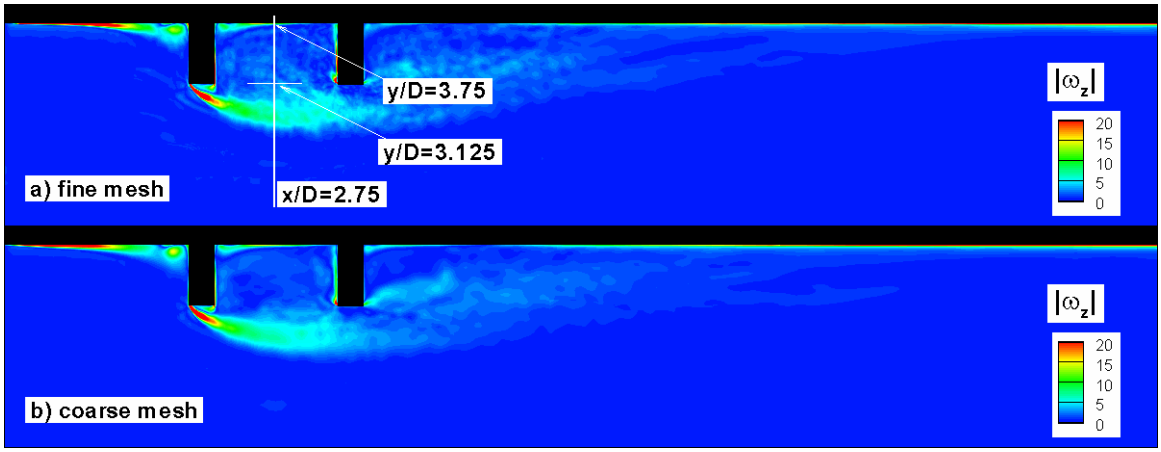

Figure 5.6. Comparison of out-of-plane mean vorticity magnitude at the groyne mid-depth level (z/D=0.5); a) fine mesh solution; b) coarse mesh solution.

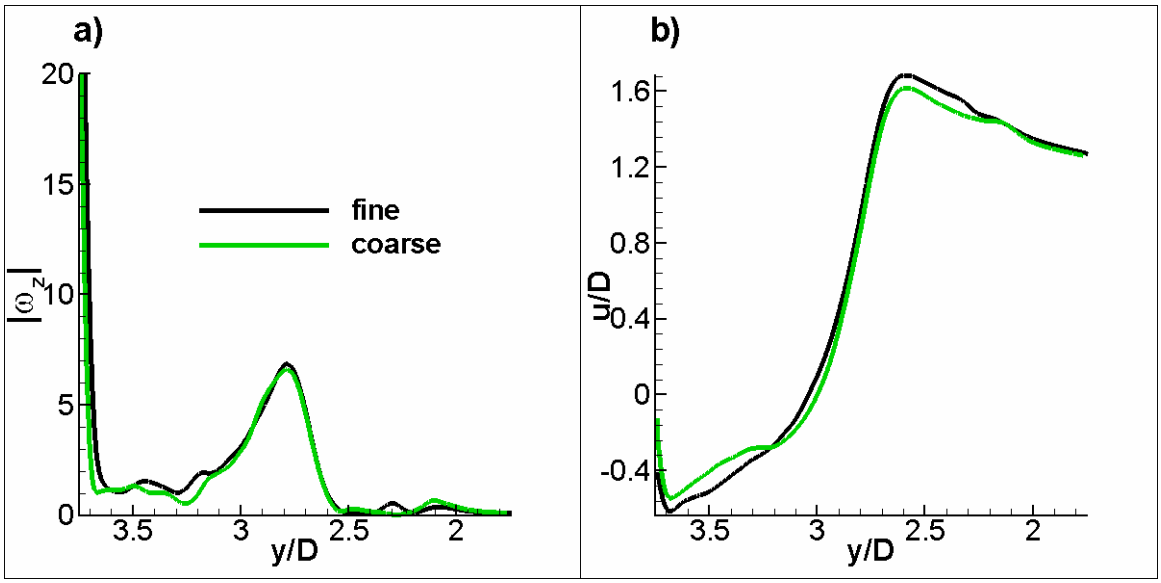

Figure 5.7. Comparison between fine and coarse mesh solutions on a line parallel to the y direction (z/D=0.5, x/D=2.75). a) out-of-plane mean vorticity magnitude; b) mean streamwise velocity.

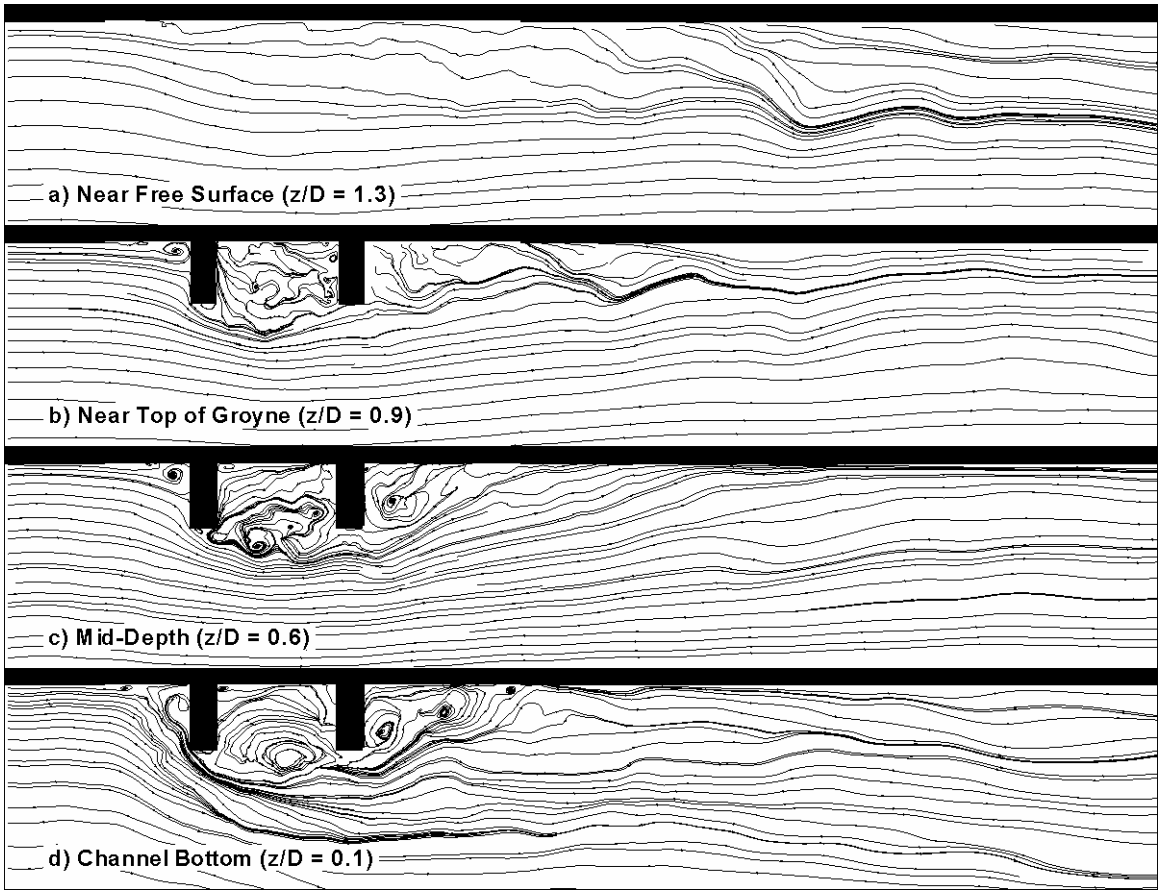

Figure 5.8. Visualization of instantaneous flow structure using 2D instantaneous velocity streamlines (fine mesh solution). a) near the free surface (z/D=1.3); b) near the groyne top (z/D=0.9); c) near mid-depth (z/D=0.6); d) near the channel bottom (z/D=0.1).

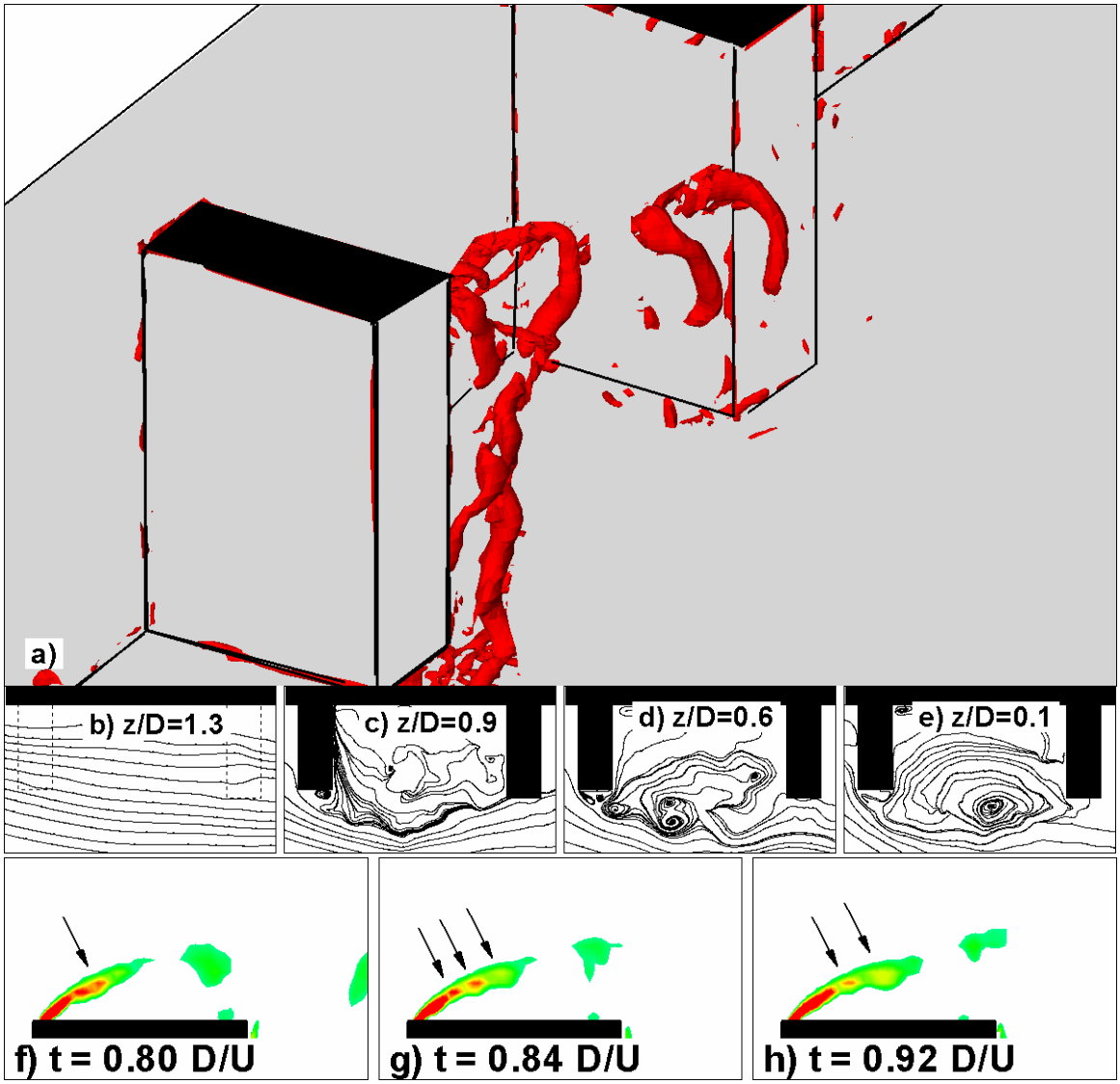

Figure 5.9. Visualization of vortex tubes in horizontal DSL (instantaneous fine mesh solution). a) Q criterion; 2D streamlines in horizontal planes at: b) z/D=1.3; c) z/D=0.9; d) z/D=0.6; e) z/D=0.1; out-of-plane vorticity contours at z/D=0.5 at various time instances: f) t=0.80D/U; g) t=0.84D/U; h) t=0.92D/U.

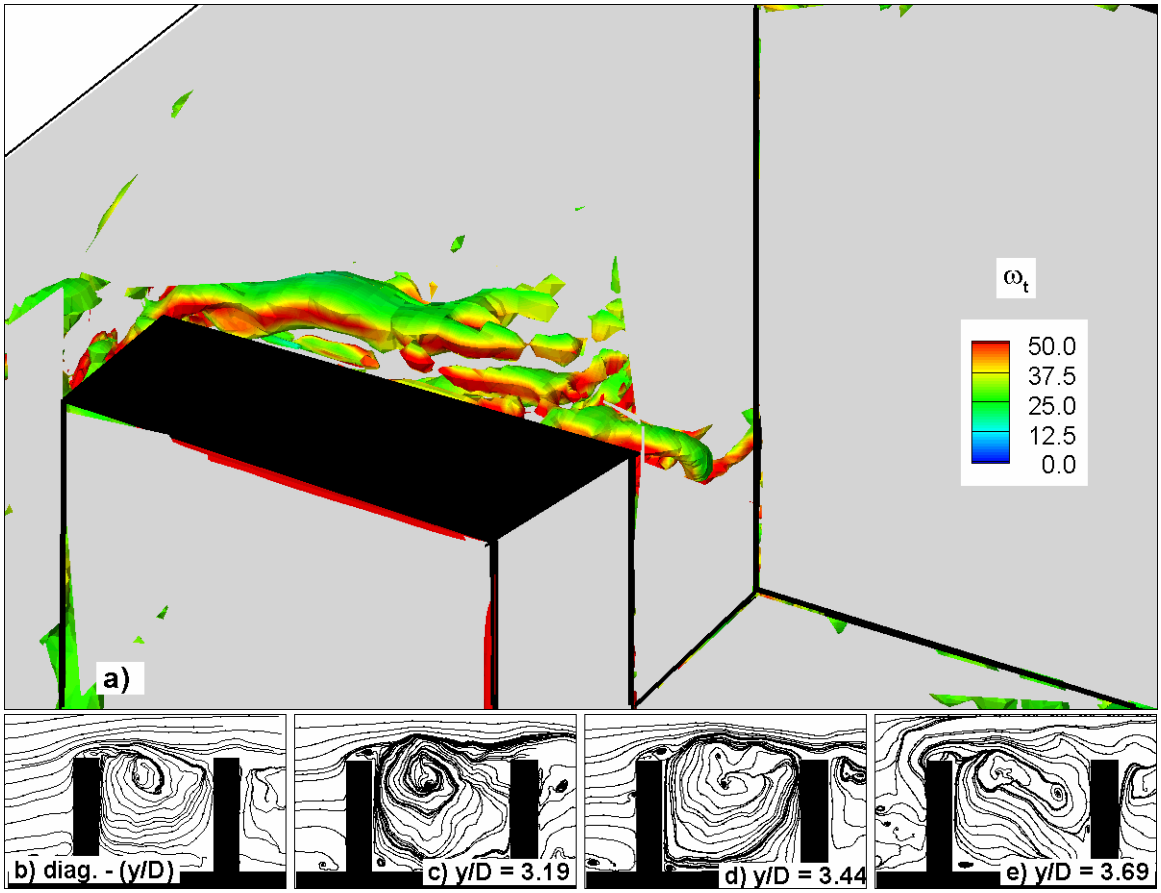

Figure 5.10. Visualization of vortex tubes in vertical DSL (instantaneous fine mesh solution). a) Q criterion; 2D streamlines in various planes at: b) diagonal (Figure 5.1.b); c) y/D=3.19; d) y/D=3.44; e) y/D=3.69.

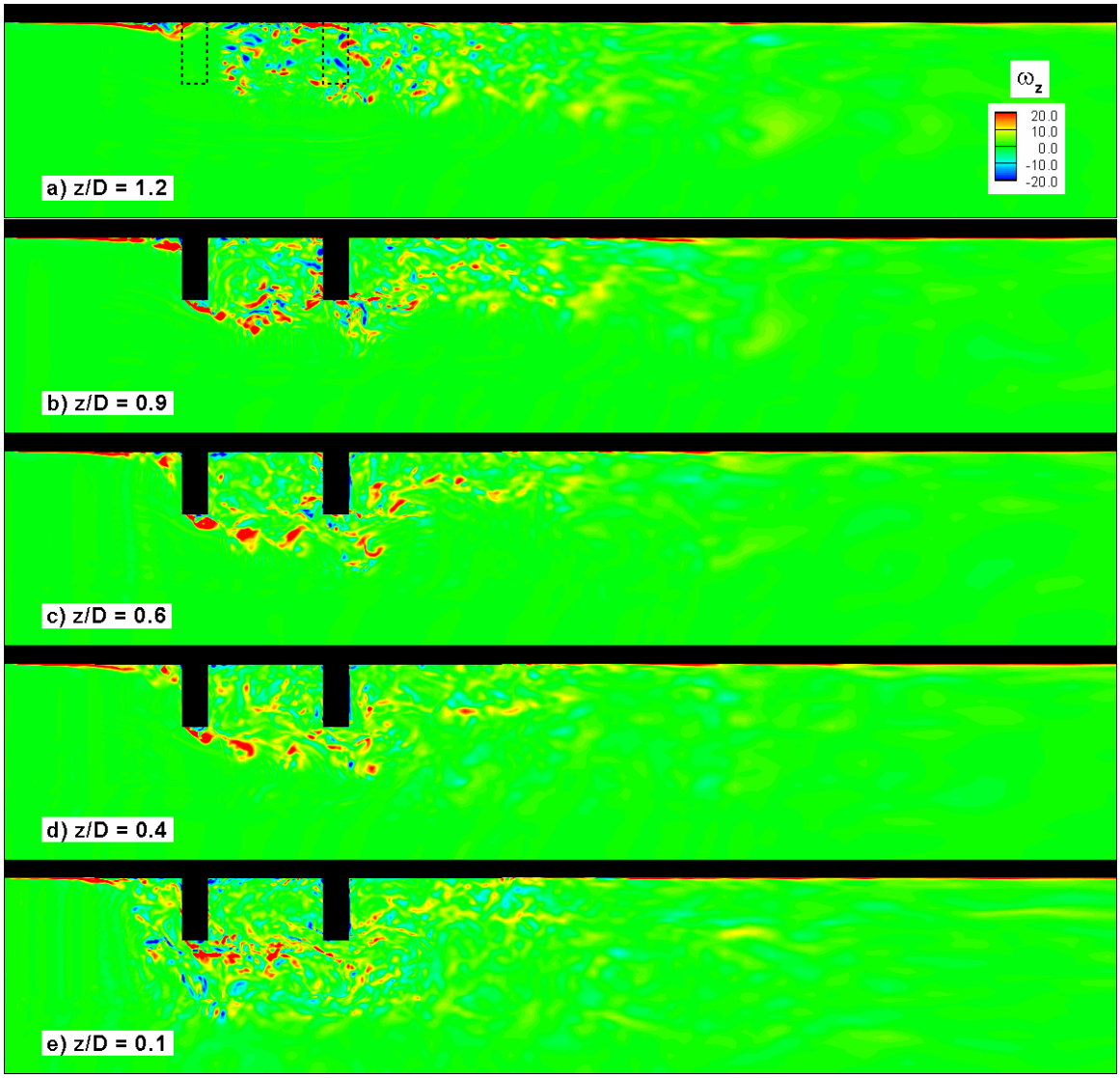

Figure 5.11. Instantaneous out-of-plane vorticity contours in horizontal planes showing vortical content of the flow. a) z/D=1.2; b) z/D=0.9; c) z/D=0.6; d) z/D=0.4; e) z/D=0.1.

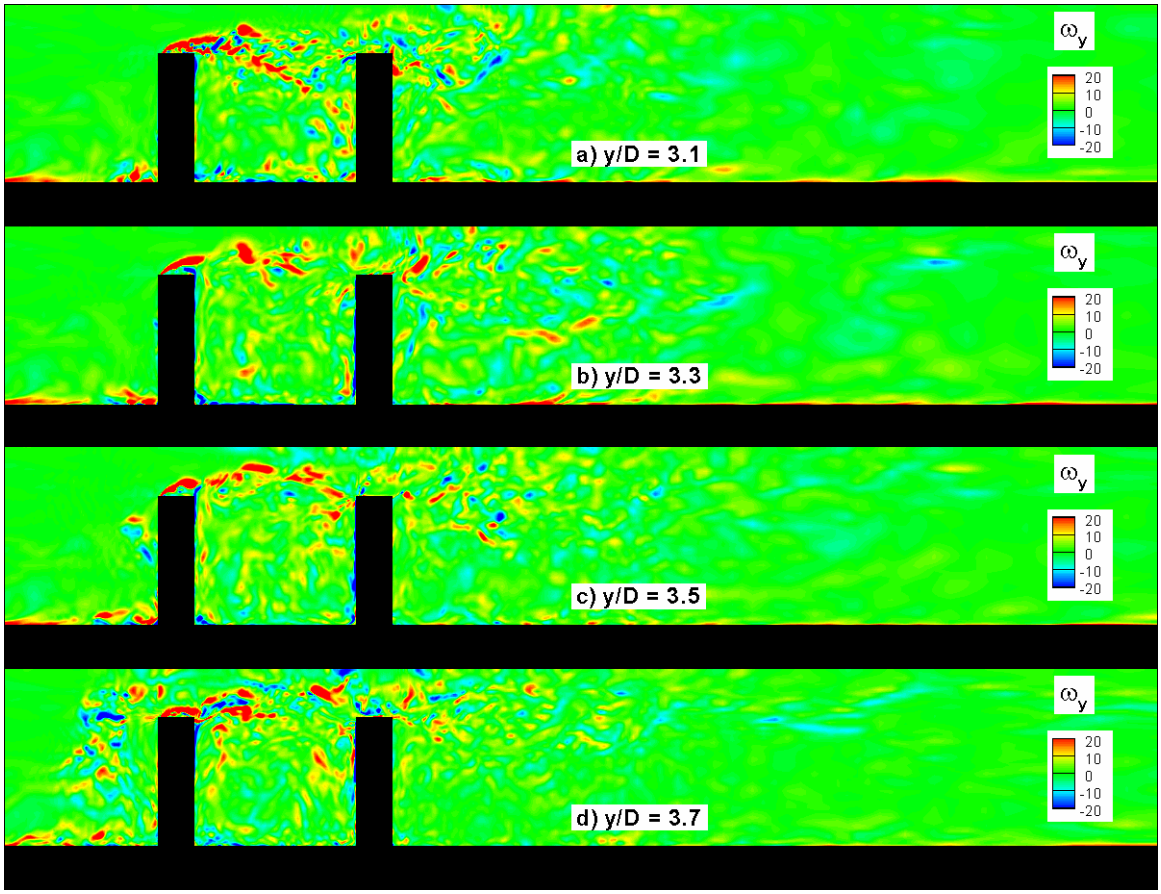

Figure 5.12. Instantaneous out-of-plane vorticity contours in vertical planes showing vortical content of the flow. a) y/D=3.1; b) y/D=3.3; c) y/D=3.5; d) y/D=3.7.

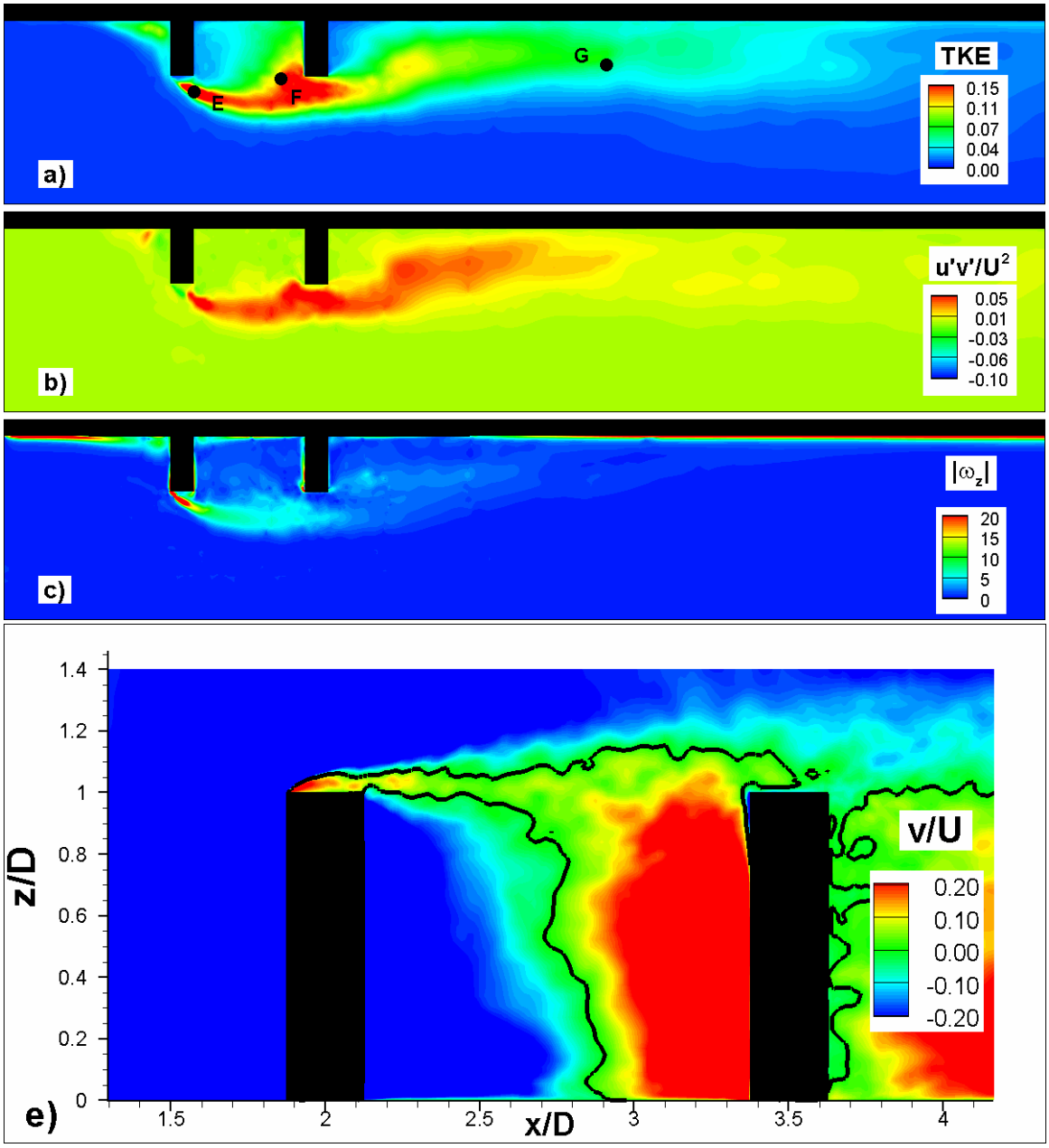

Figure 5.13. Vorticity and turbulence quantities in a plane situated at mid-groyne depth (z/D=0.5). a) TKE; b) $\overline{u'v'}/U^2$; c) out-of-plane mean vorticity magnitude; d) transverse velocity at embayment interface (y/D=3.125).

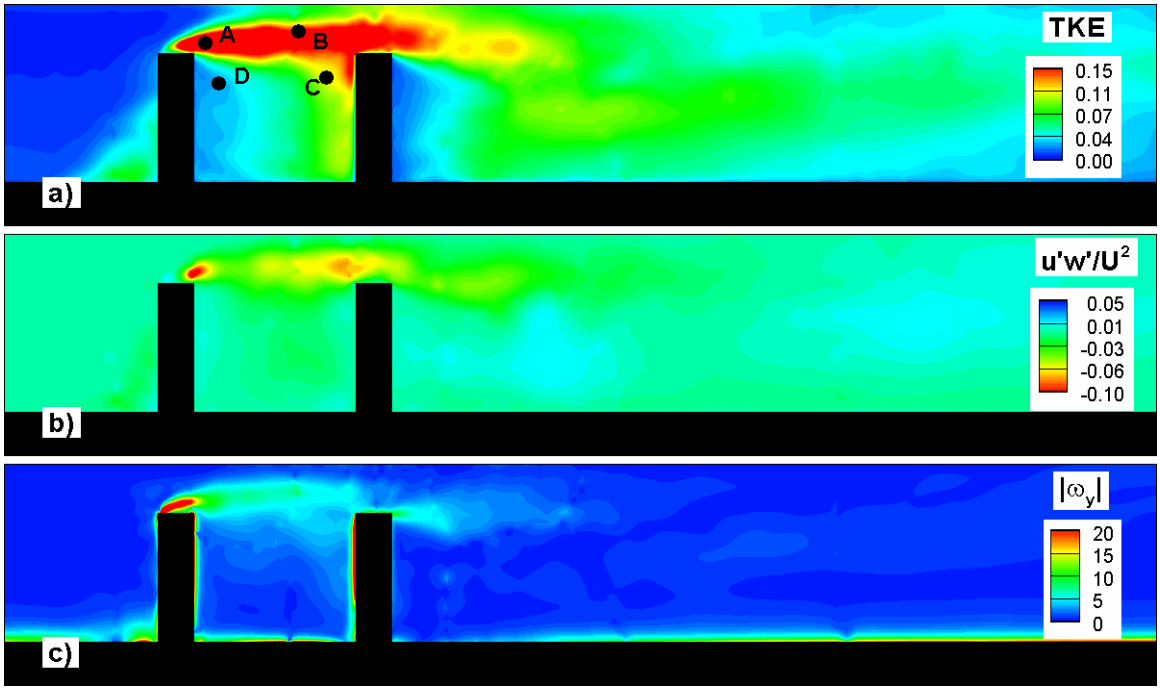

Figure 5.14. Vorticity and turbulence quantities in a plane situated at mid-groyne width (y/D=3.44). a) TKE; b) $\overline{u'w'}/U^2$; c) out-of-plane mean vorticity magnitude.

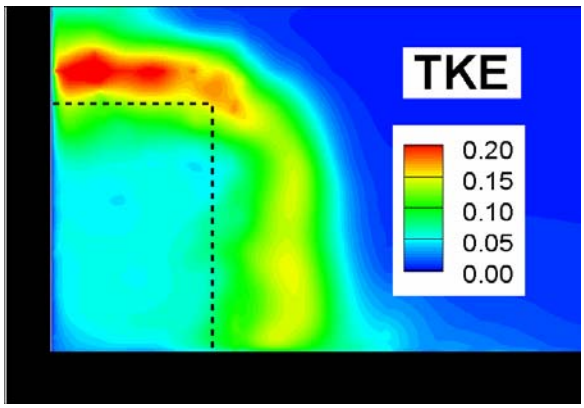

Figure 5.15. TKE in a plane situated at mid-embayment length (x/D=2.75).

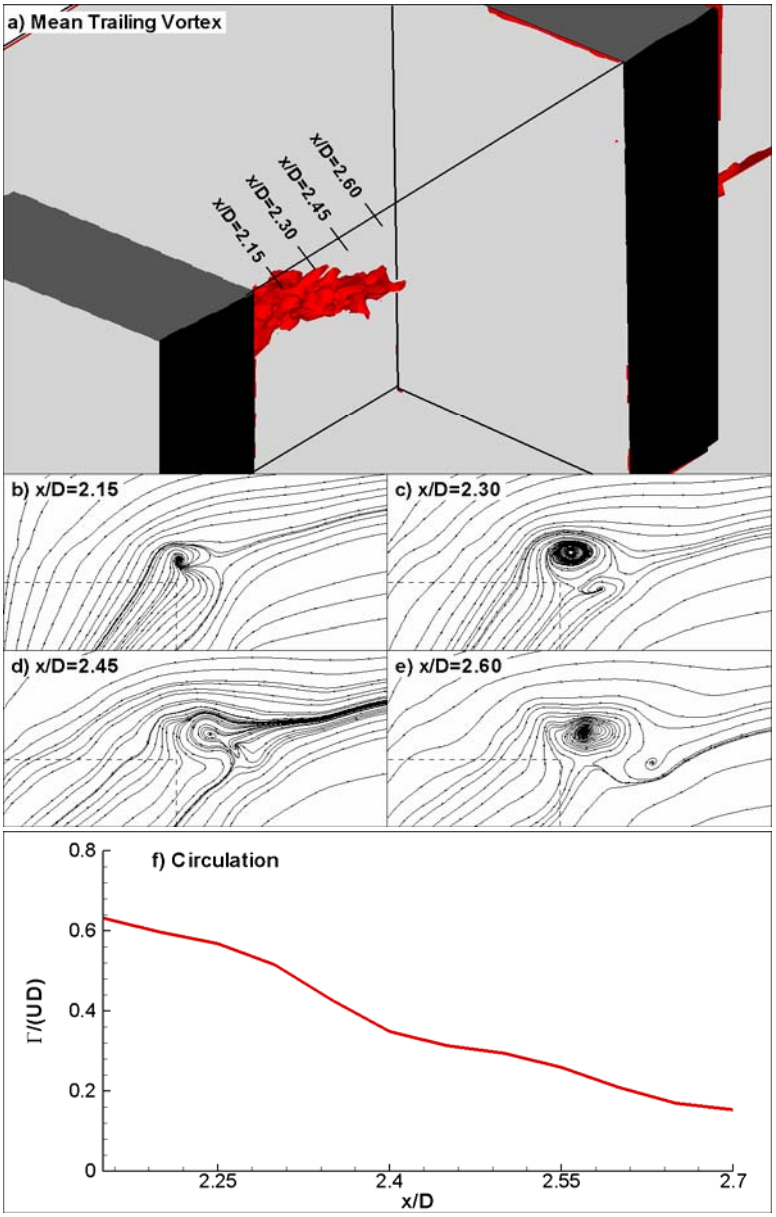

Figure 5.16. Visualization of the structure of the trailing vortex in the mean flow; a) 3D visualization using a streamwise vorticity iso-surface; 2D streamlines in vertical spanwise planes: b) x/D=2.15; c) x/D=2.3; d) x/D=2.45; e) x/D=2.6; f) streamwise variation of the mean circulation along the axis of the trailing vortex.

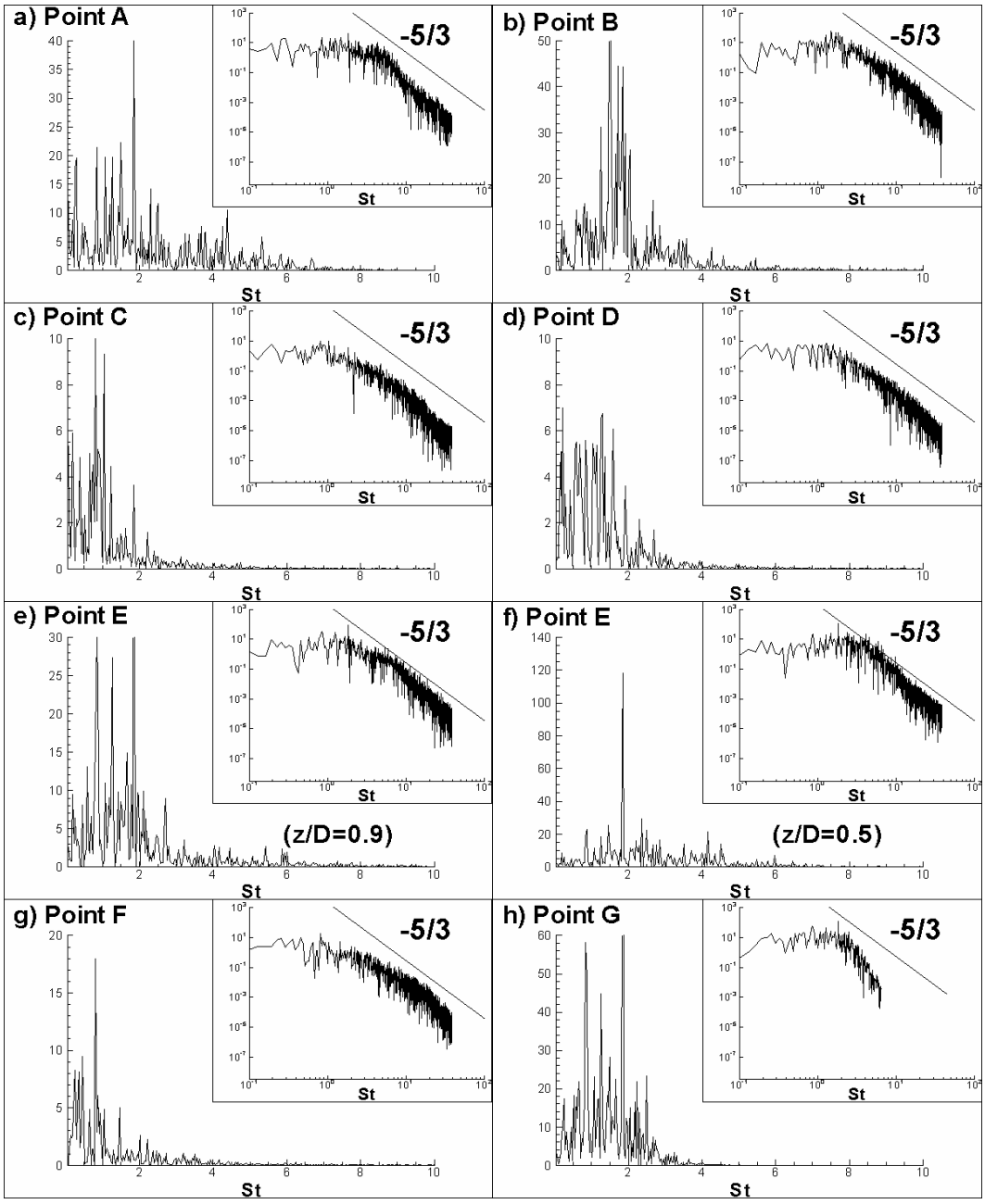

Figure 5.17. Pressure power spectra in the flow domain (position of points is shown in Figures 5.13a and 5.14a). a) point A; b) point B; c) point C; d) point D; e) point E (z/D=0.9); f) point E (z/D=0.5); g) point F; h) point G.

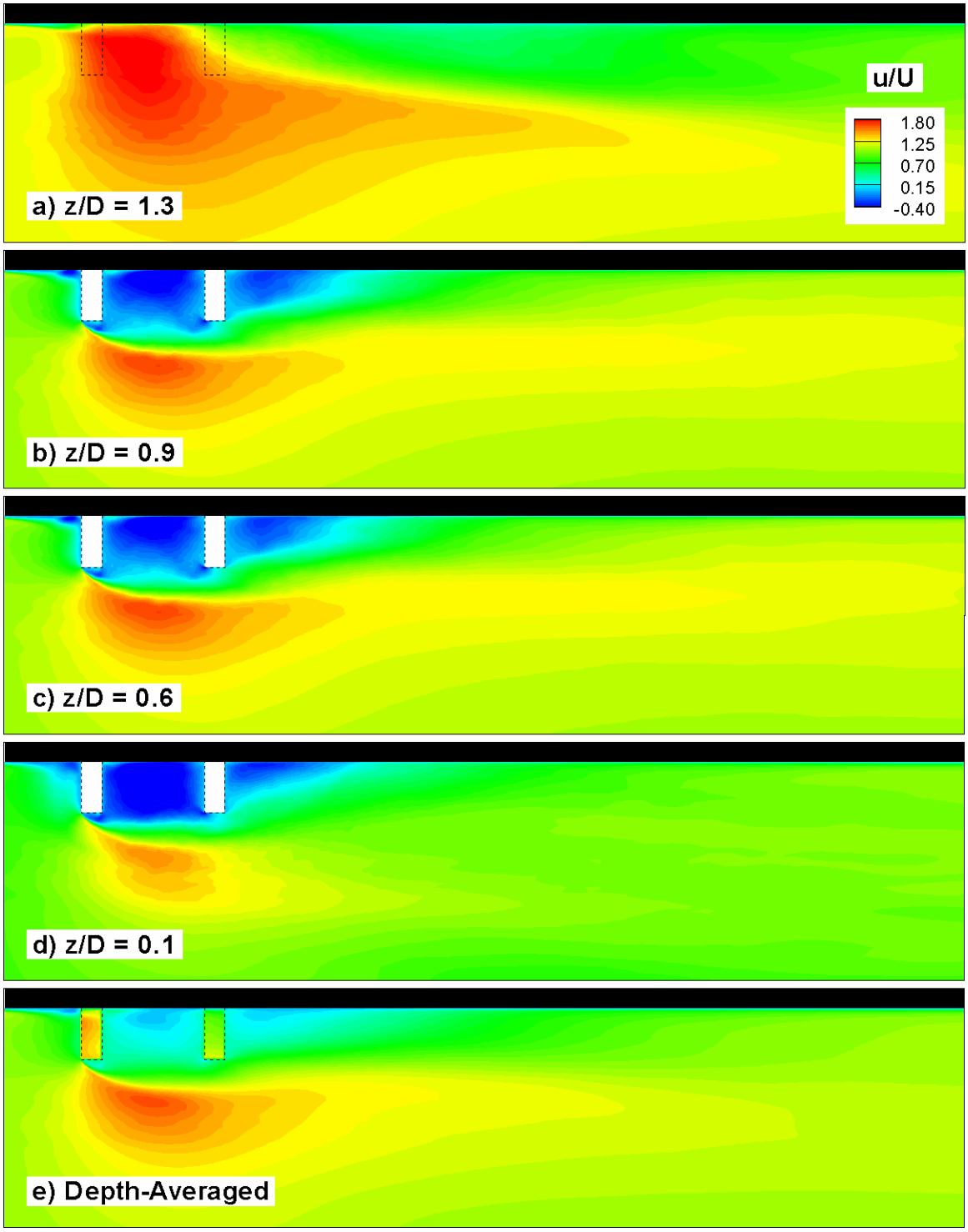

Figure 5.18. Distribution of mean streamwise velocity, u/U, in horizontal planes. a) z/D = 1.3; b) z/D = 0.9; c) z/D = 0.6; d) z/D = 0.1; e) depth-averaged.

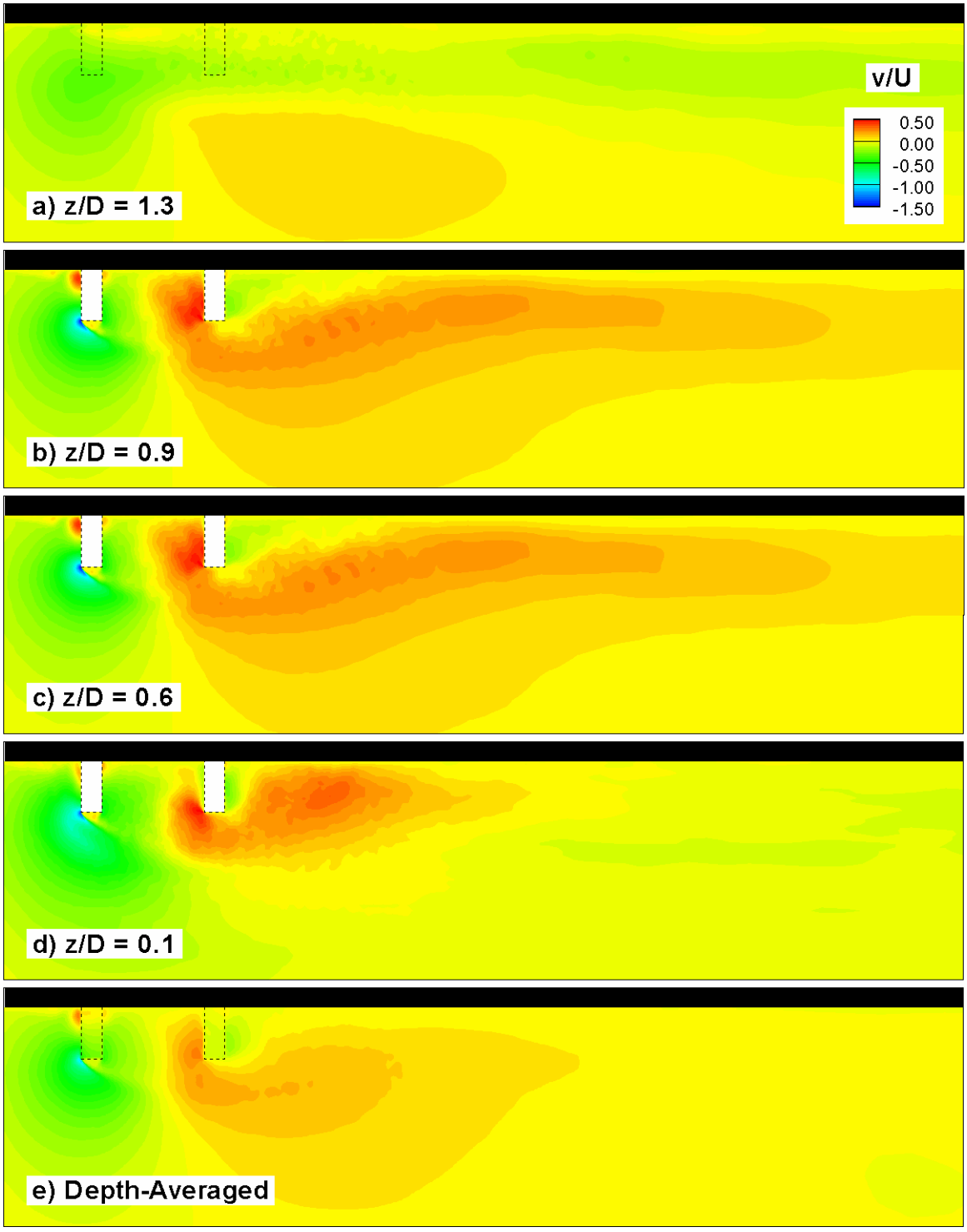

Figure 5.19. Distribution of the mean spanwise velocity, v/U, in horizontal planes. a) z/D = 1.3; b) z/D = 0.9; c) z/D = 0.6; d) z/D = 0.1; e) depth-averaged.

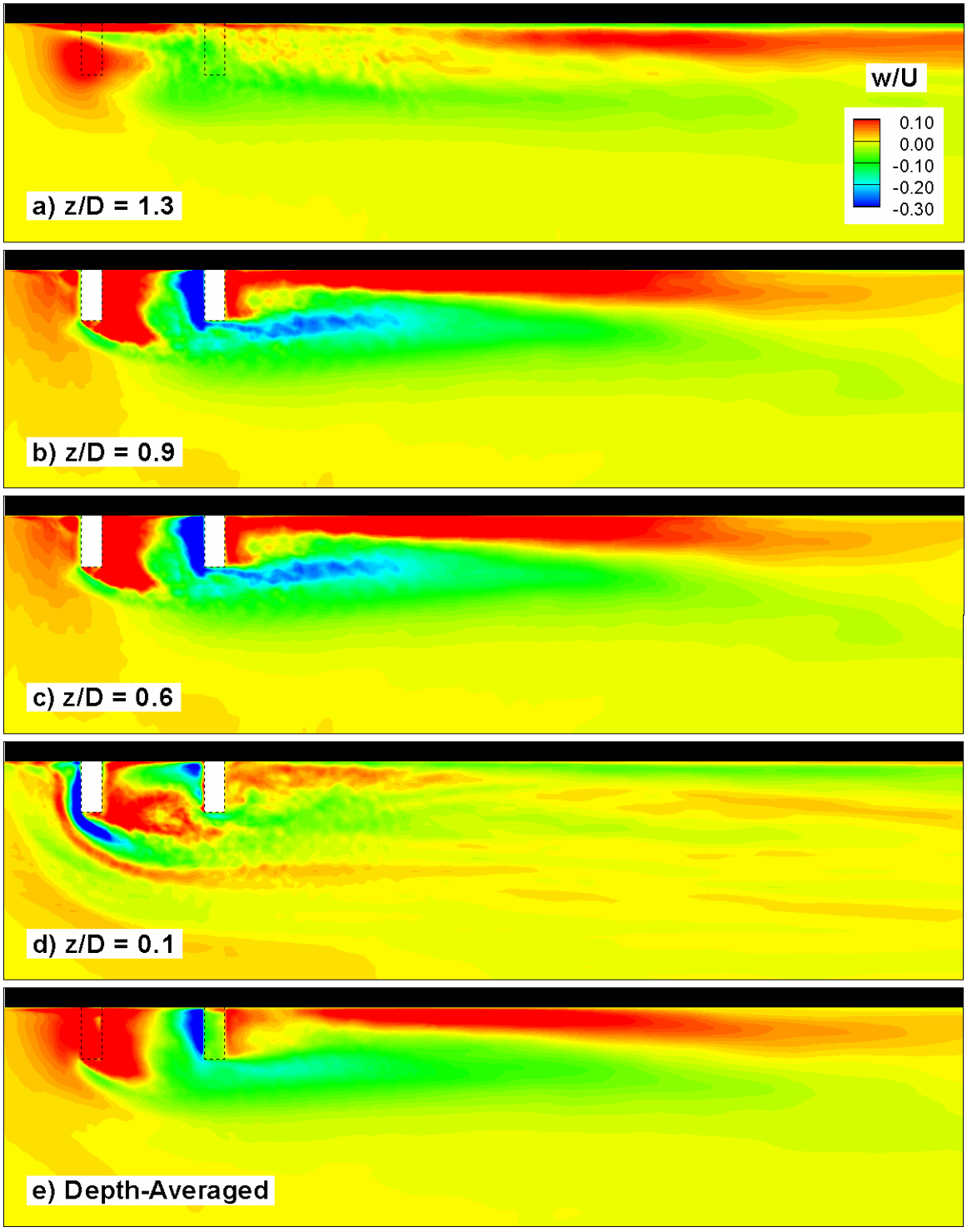

Figure 5.20. Distribution of the mean vertical velocity, w/U , in horizontal planes. a) z/D = 1.3; b) z/D = 0.9; c) z/D = 0.6; d) z/D = 0.1; e) depth-averaged.

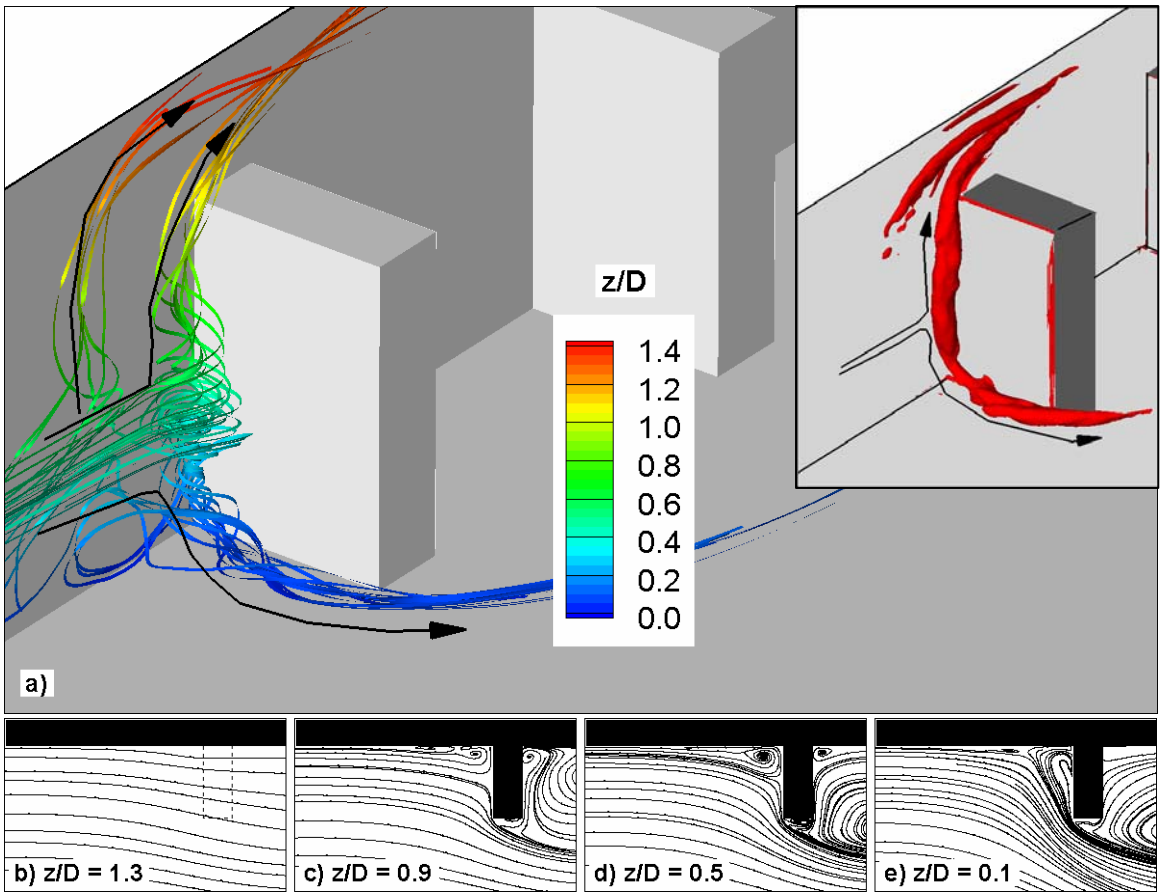

Figure 5.21. Mean velocity streamlines visualizing vortex system in the upstream recirculation region. a) 3D streamlines with inset showing vortical structures educed using Q criterion; 2D streamlines in vertical planes at: b) z/D=1.3; c) z/D=0.9; d) z/D=0.5; e) z/D=0.1.

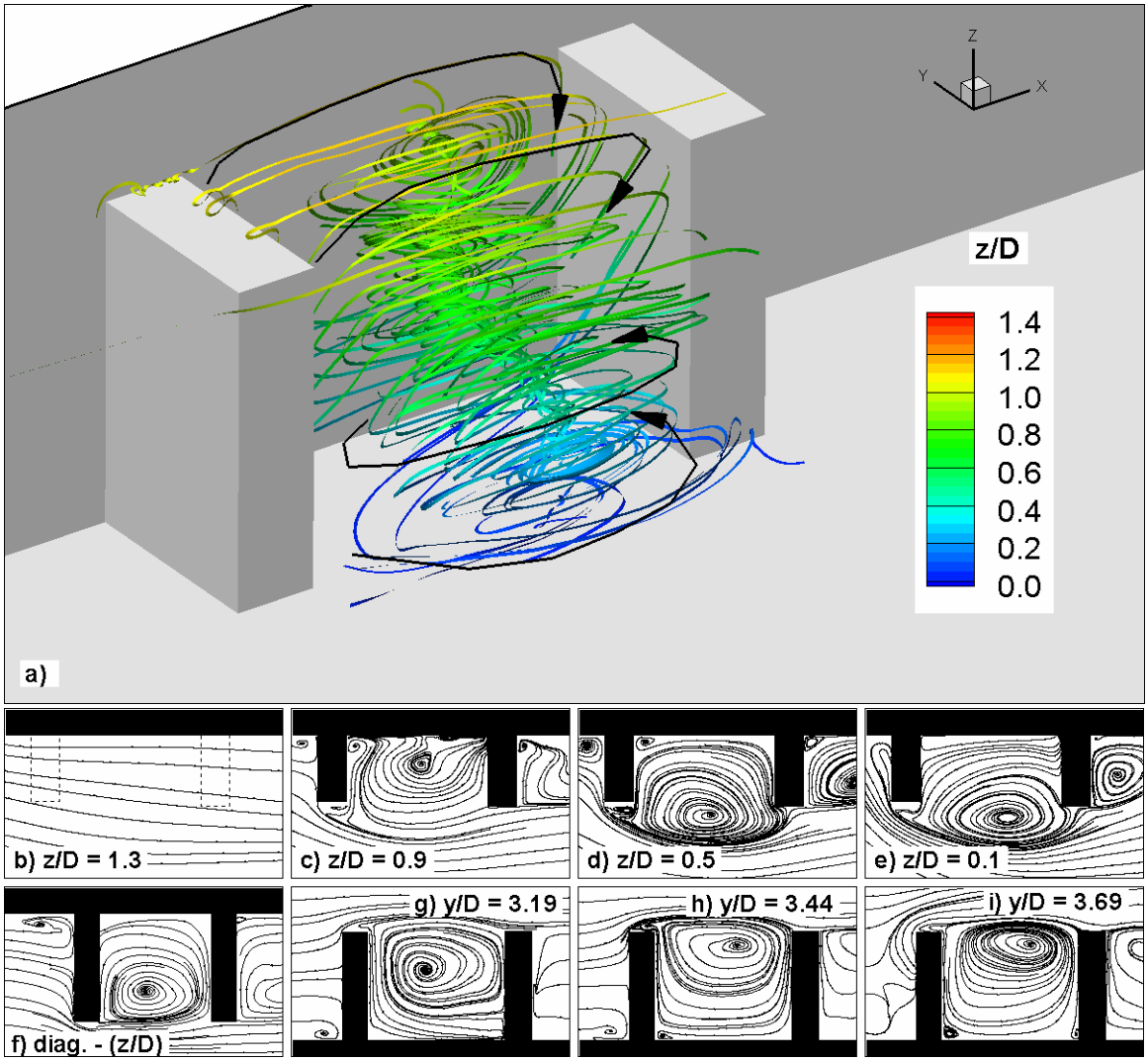

Figure 5. 22. Mean velocity streamlines visualizing vortices inside the embayment region. a) 3D streamlines; 2D streamlines in planes situated at: b) z/D=1.3; c) z/D=0.9; d) z/D=0.5; e) z/D=0.1; f) diagonal section (see Fig. 5.1b); g) y/D=3.19; h) y/D=3.44; i) y/D=3.69.

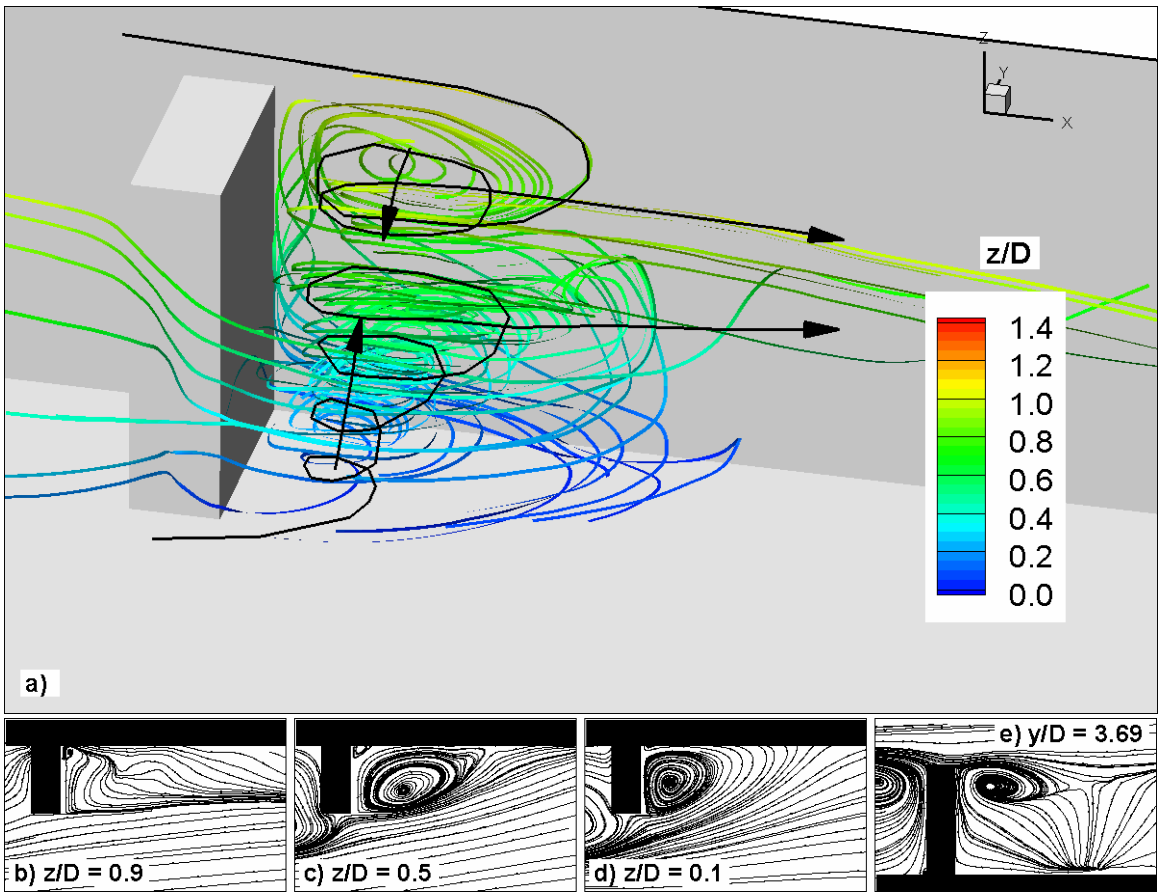

Figure 5.23. Mean velocity streamlines visualizing vortex system in the downstream recirculation region. a) 3D streamlines; 2D streamlines in planes situated at: b) z/D=0.9; c) z/D=0.5; d) z/D=0.1; e) y/D=3.69.

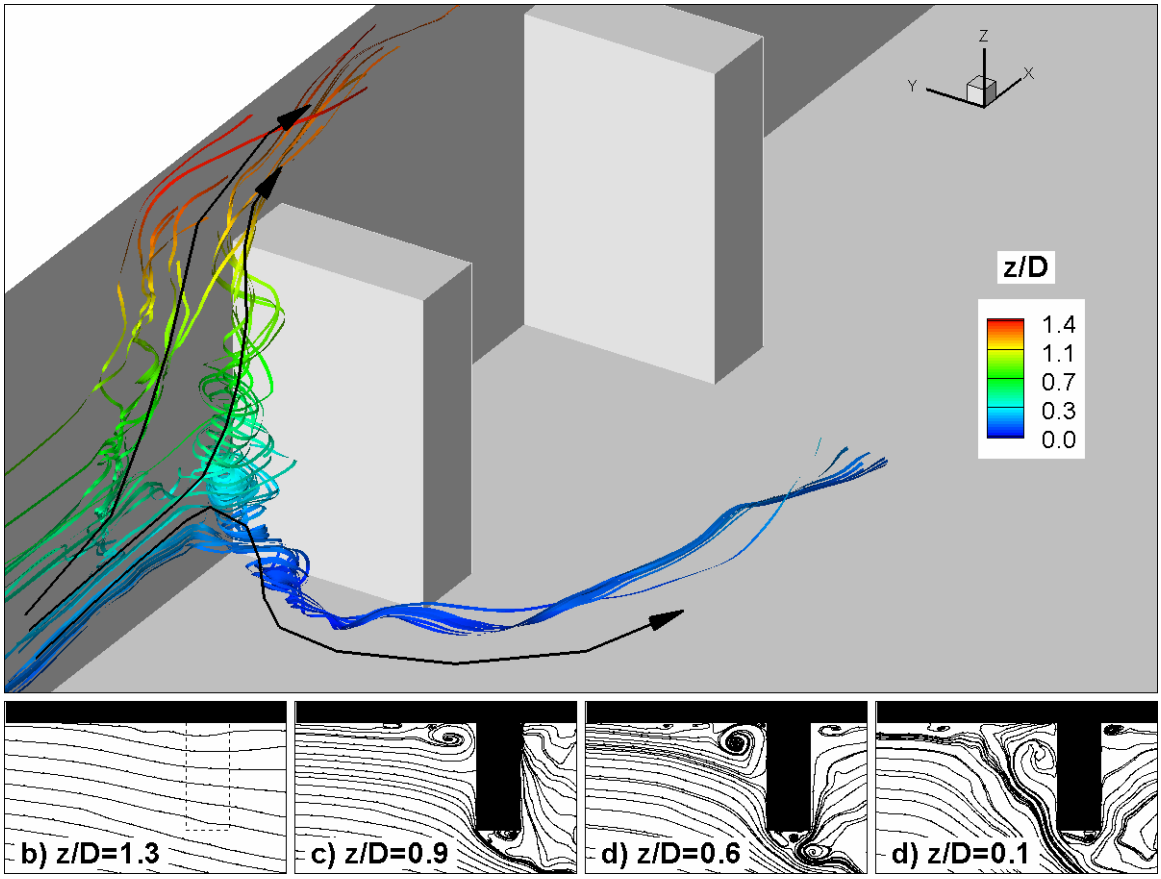

Figure 5.24. Instantaneous velocity streamlines visualizing vortical structure in the upstream recirculation zone and HV system; a) 3D streamlines; 2D streamlines in horizontal planes situated at: b) z/D=1.3; c) z/D=0.9; d) z/D=0.5; e) z/D=0.1.

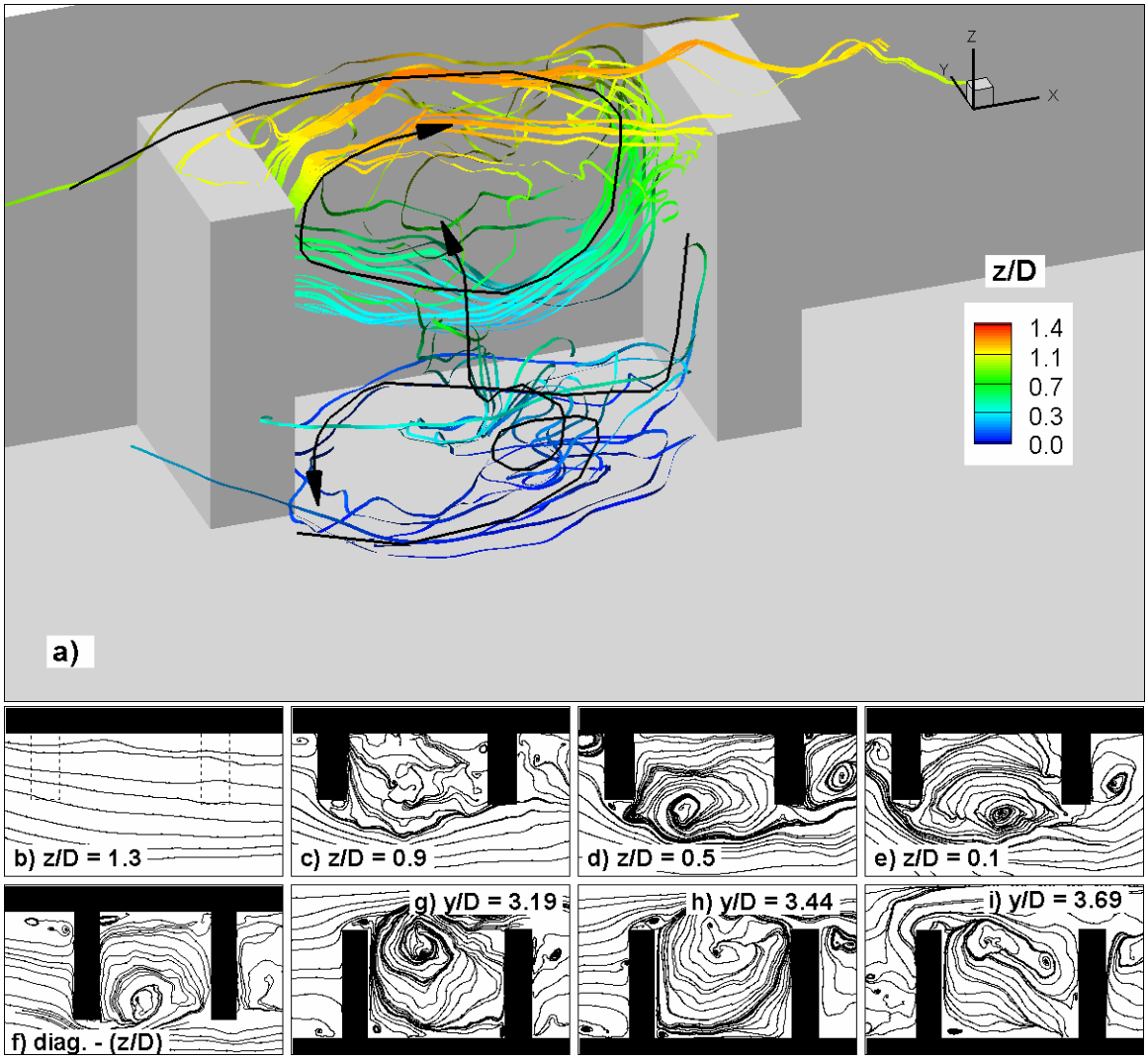

Figure 5.25. Instantaneous velocity streamlines visualizing vortices inside the embayment region. a) 3D streamlines; 2D streamlines in planes situated at: b) z/D=1.3; c) z/D=0.9; d) z/D=0.5; e) z/D=0.1; f) diagonal section (see Fig. 5.1b); g) y/D=3.19; h) y/D=3.44; i) y/D=3.69; j) plane perpendicular to vortex core; k) y/D=3.19; l) y/D=3.44; m) y/D=3.69.

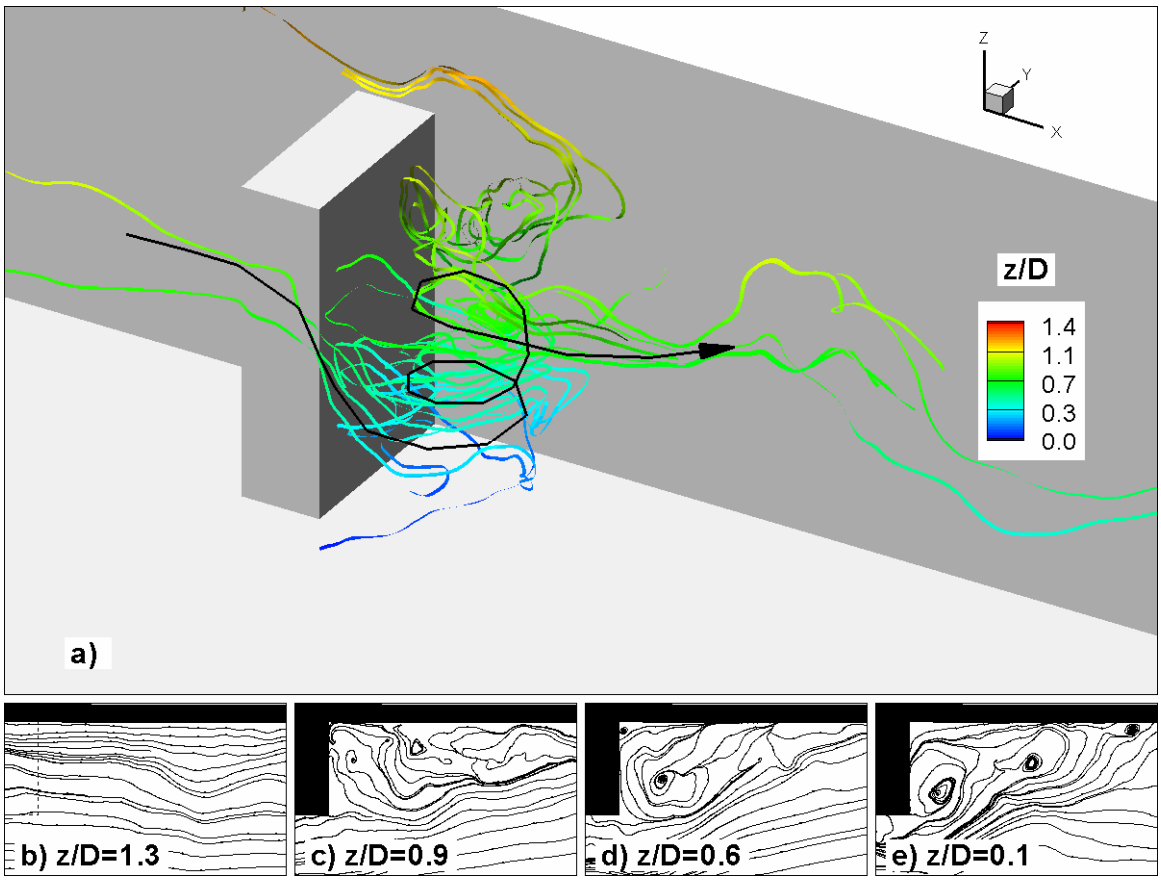

Figure 5.26. Instantaneous velocity streamlines visualizing vortex system in the downstream recirculation region. a) 3D streamlines; 2D streamlines in planes situated at: b) z/D-1.3; c) z/D=0.9; d) z/D=0.5; e) z/D=0.1.

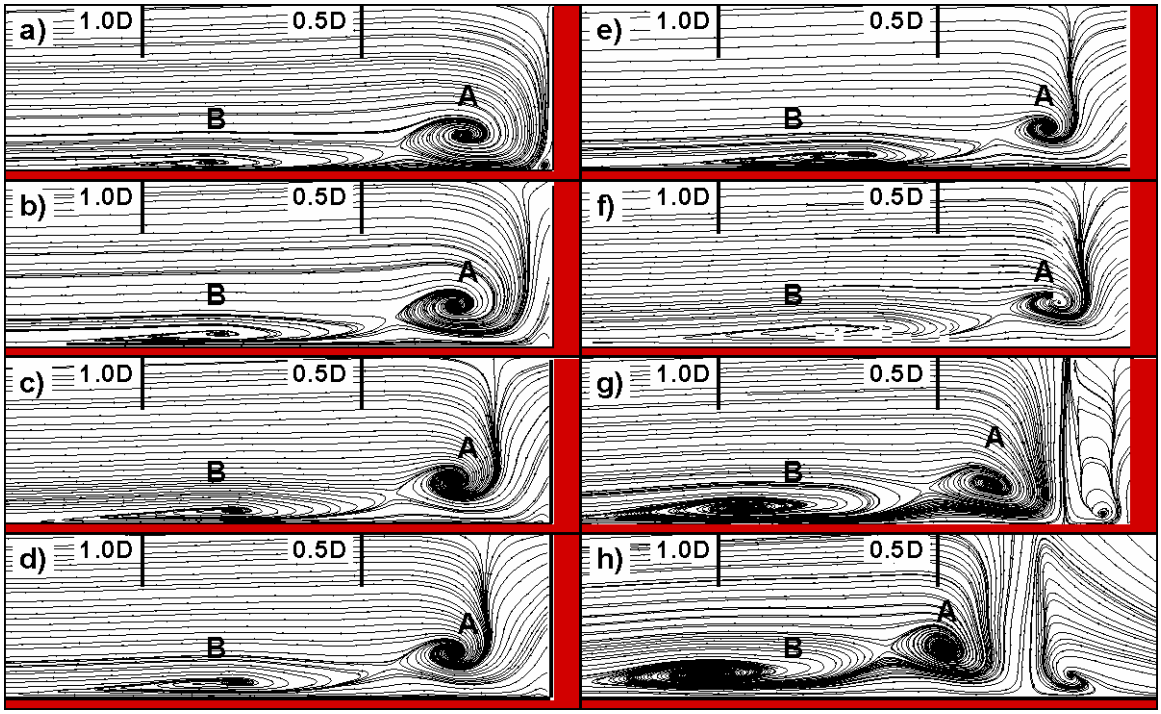

Figure 5.27. Structure of the mean HV system as it wraps around the base of the upstream groyne visualized in vertical planes making an angle with the lateral channel wall of: a) 25°; b) 30°; c) 35°; d) 37.5°; e) 40°; f) 45°; g) 55°; h) 65°. See also Figure 5.1 for plane location.

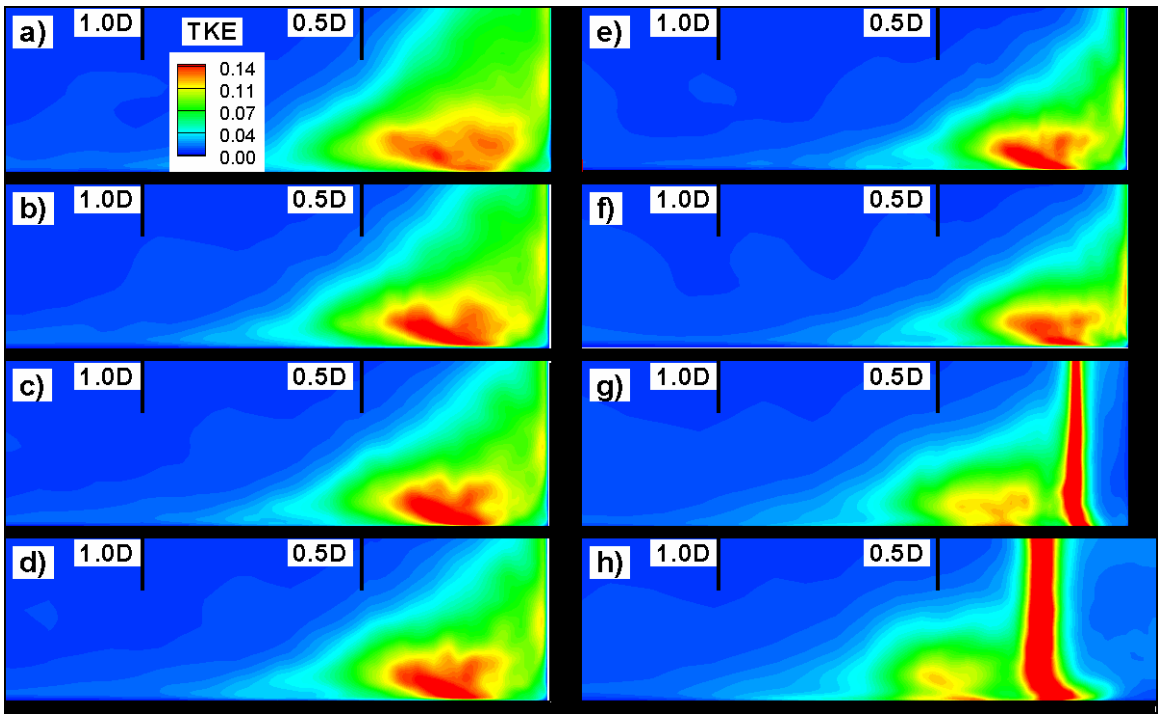

Figure 5.28. TKE distribution inside the HV system region (emerged case) in various vertical planes making an angle with the lateral channel wall of: a) 25°; b) 30°; c) 35°; d) 37.5°; e) 40°; f) 45°; g) 55°; h) 65°. See also Figure 5.1 for plane location.

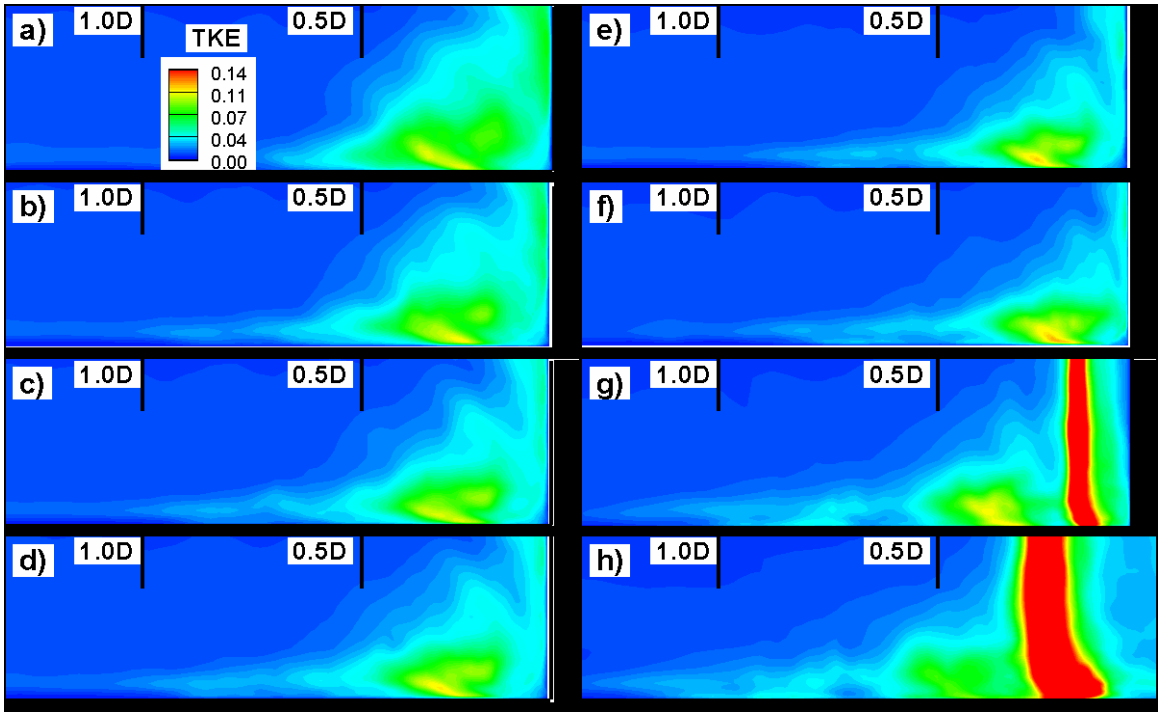

Figure 5.29. TKE distribution inside the HV system region (submerged case) in various vertical planes making an angle with the lateral channel wall of: a) 25°; b) 30°; c) 35°; d) 37.5°; e) 40°; f) 45°; g) 55°; h) 65°. See also Figure 5.1 for plane location.

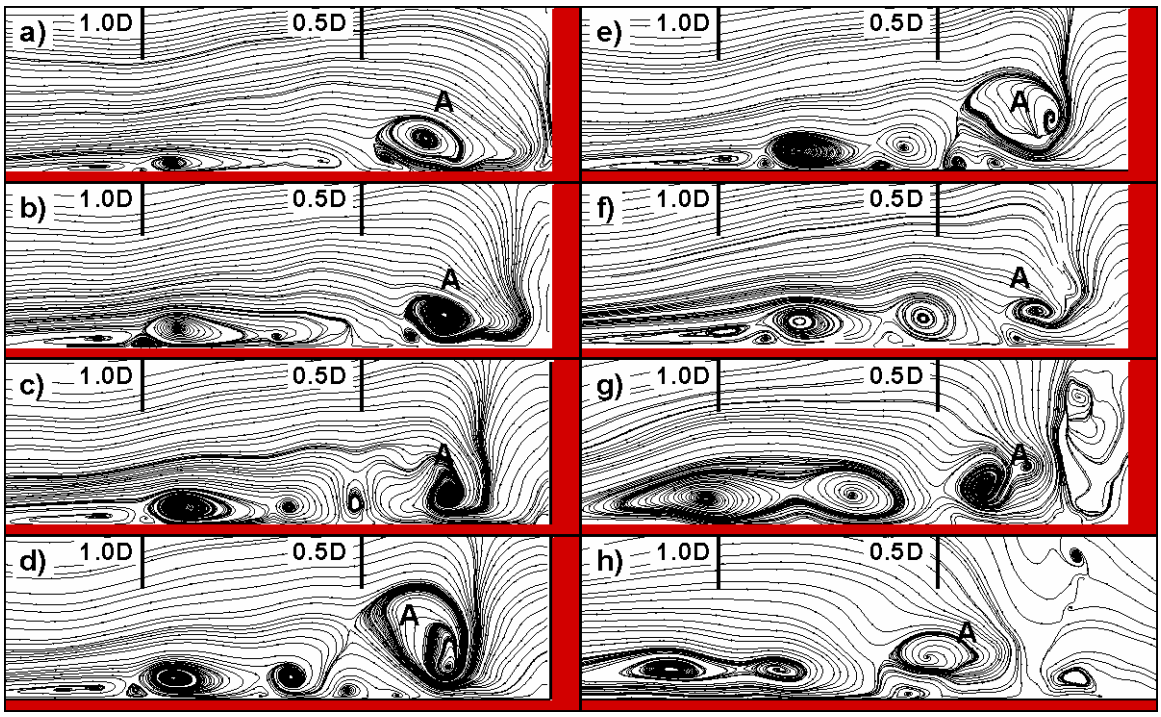

Figure 5.30. Structure of the instantaneous HV system as it wraps around the base of the upstream groyne visualized in vertical planes making an angle with the lateral channel wall of: a) 25^o; b) 30^o; c) 35^o; d) 37.5^o; e) 40^o; f) 45^o; g) 55^o; h) 65^o. See also Figure 5.1 for plane location.

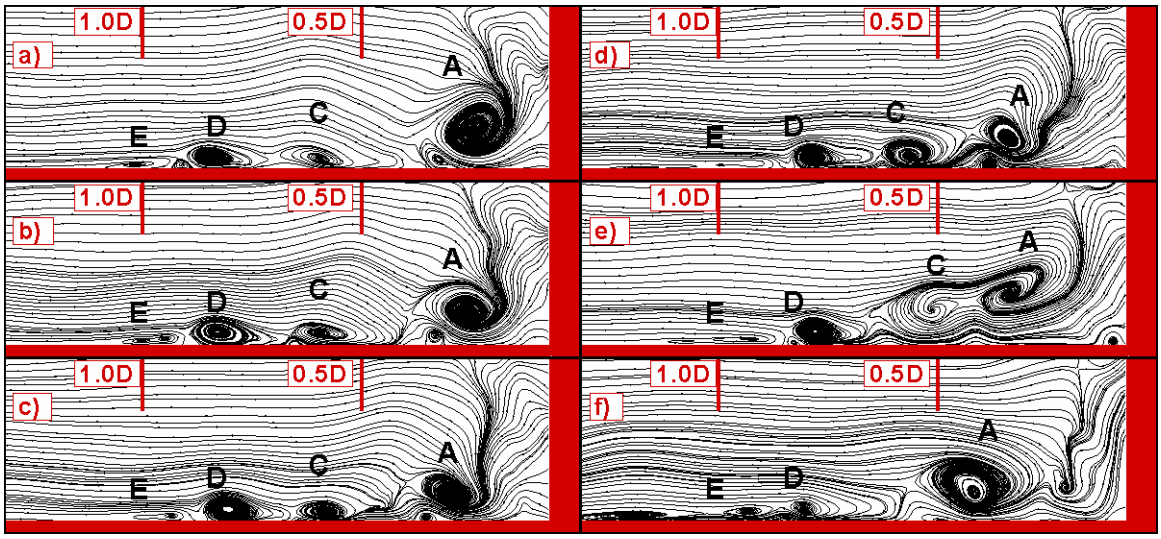

Figure 5.31. Temporal evolution of instantaneous HV system (submerged case) in a vertical plane making a 35^0 angle with lateral wall. a) 1.28 D/U; b) 1.44 D/U; c) 1.6 D/U; d) 1.76 D/U; e) 1.92 D/U; f) 2.36 D/U.

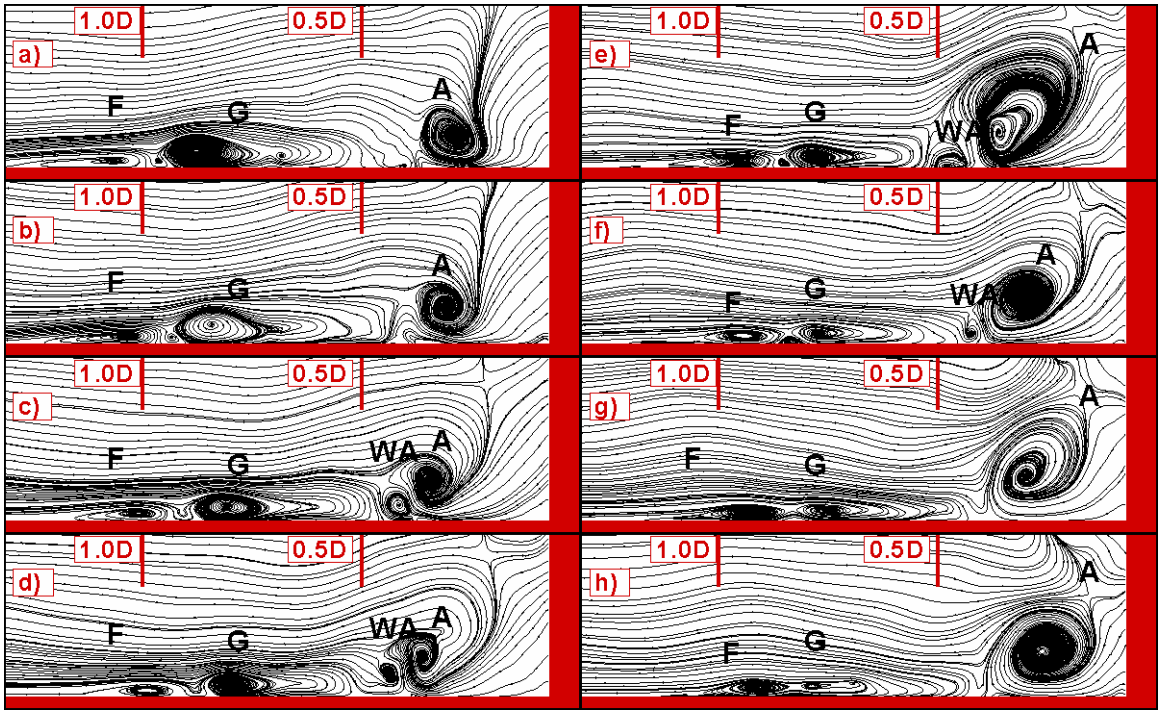

Figure 5.32. Temporal evolution of instantaneous HV system in a vertical plane making a 35^0 angle with lateral wall. a) 0.12 D/U; b) 0.28 D/U; c) 0.44 D/U; d) 0.6 D/U; e) 0.76 D/U; f) 0.92 D/U; g) 1.08 D/U; h) 1.24 D/U. Time origin is different from the one used in Figure 5.31.

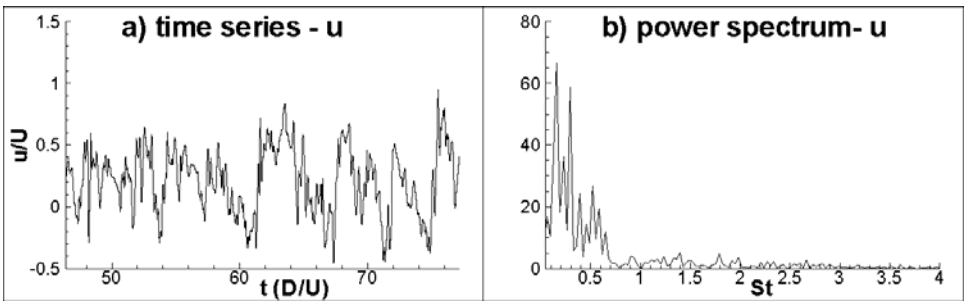

Figure 5.33. Time series and power spectrum of u-velocity at point p20 situated inside the HV system (position of point p20 is shown in Figure 5.27e). a) time series; b) power spectrum.

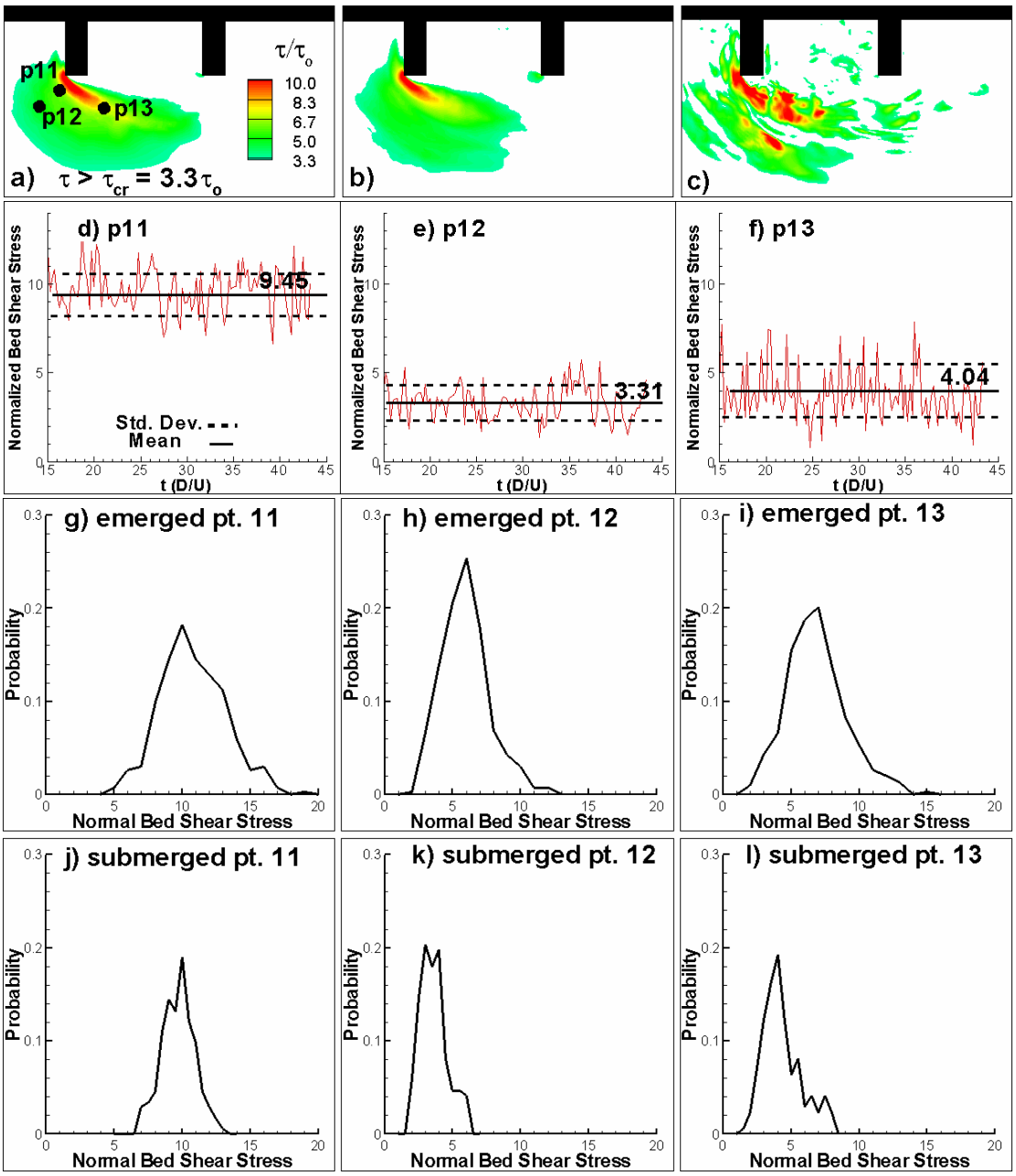

Figure 5.34. Non-dimensional bed shear stress distribution showing region where entrainment occurs. a) mean values, emerged case; b) mean values, submerged case; c) instantaneous values, submerged case; d) bed shear stress time series at point p11, submerged case; d) bed shear stress time series at point p12, submerged case; f) bed shear stress time series at point p13, submerged case; g) histogram of bed shear stress at point p11, emerged case; h) histogram of bed shear stress at point p12, emerged; i) histogram of bed shear stress at point p13, emerged case; j) histogram of bed shear stress at point p11, submerged case; k) histogram of bed shear stress at point p12, submerged; l) histogram of bed shear stress at point p13, submerged case.

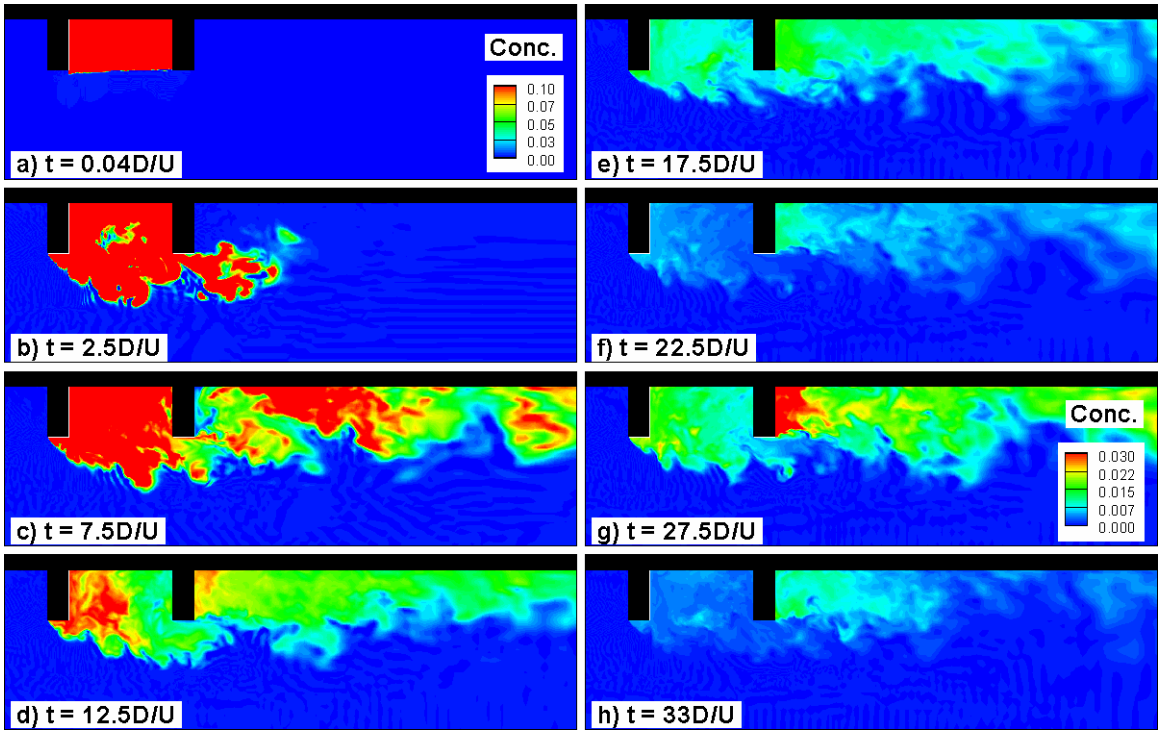

Figure 5.35. Instantaneous contours of contaminant concentration at groyne mid-depth level (z/D = 0.5). Mixing starts at t=0D/U when the concentration in the embayment is set to C/C_0=1.0. a) t = 0.25D/U; b) t = 2.5D/U; c) t = 7.5D/U; d) t = 12.5D/U; e) t = 17.5D/U; f) t = 22.5D/U; g) t = 27.5D/U; h) t = 33.0D/U. Note: The contour levels are changed in frames g and h.

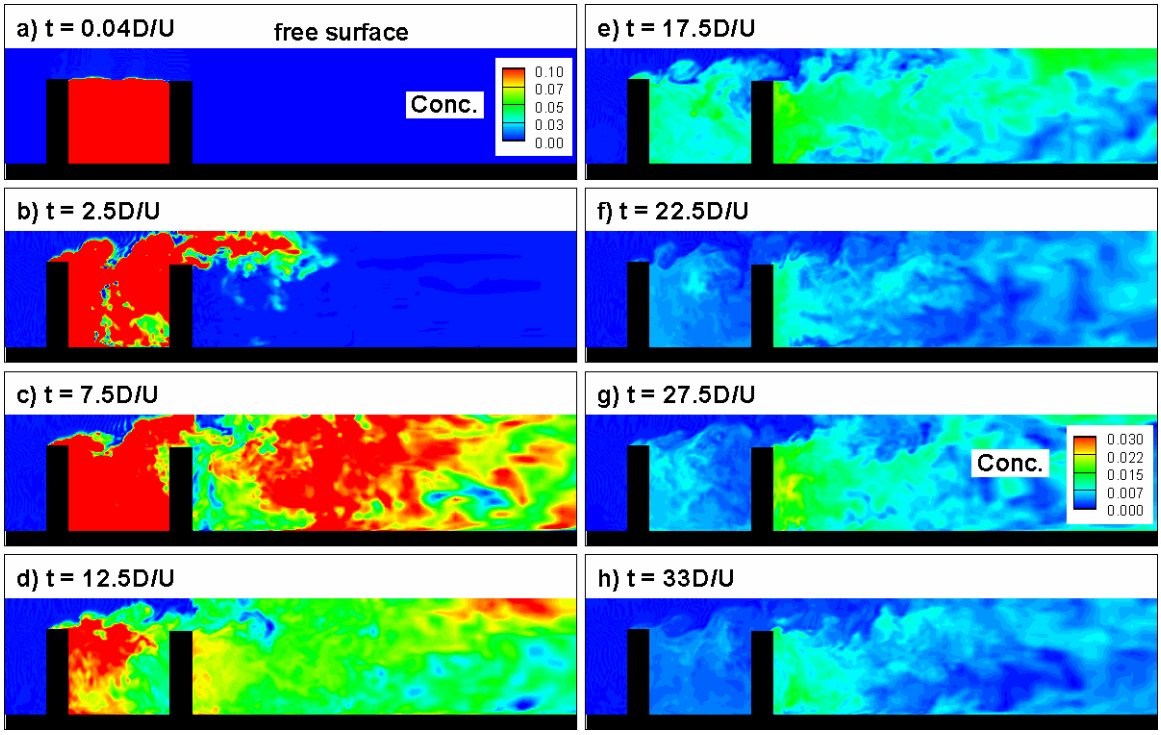

Figure 5.36. Instantaneous contours of contaminant concentration at groyne mid-width level (y/D = 3.4375). Mixing starts at t=0D/U when the concentration in the embayment is set to C/C_0=1.0; a) t = 0.25D/U; b) t = 2.5D/U; c) t = 7.5D/U; d) t = 12.5D/U; e) t = 17.5D/U; f) t = 22.5D/U; g) t = 27.5D/U; h) t =33.0D/U. Note: The contour levels are changed in frames g and h.

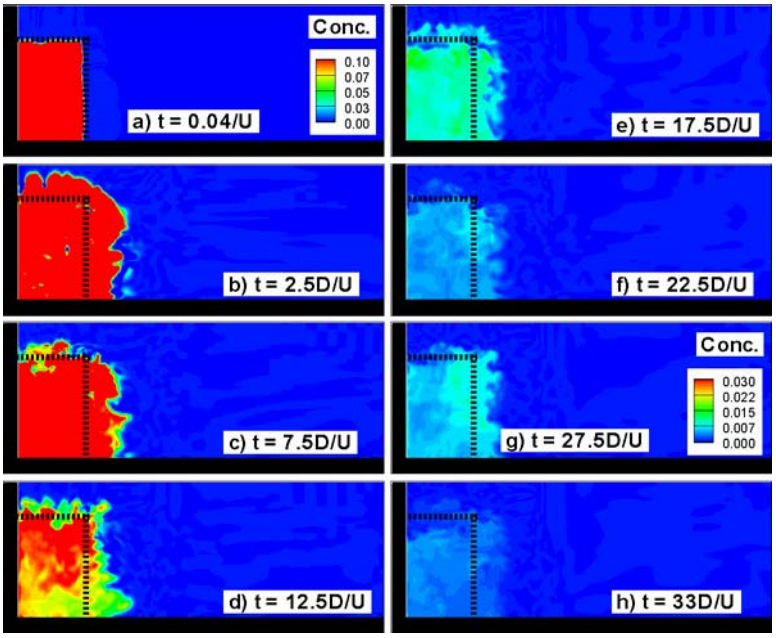

Figure 5.37. Instantaneous contours of contaminant concentration at embayment mid-length (x/D = 2.75). Mixing starts at t=0D/U when the concentration in the embayment is set to C/C_0=1.0. a) t = 0.25D/U; b) t = 2.5D/U; c) t = 7.5D/U; d) t = 12.5D/U; e) t = 17.5D/U; f) t = 22.5D/U; g) t = 27.5D/U; h) t = 33.0D/U. Note: The contour levels are changed in frames g and h.

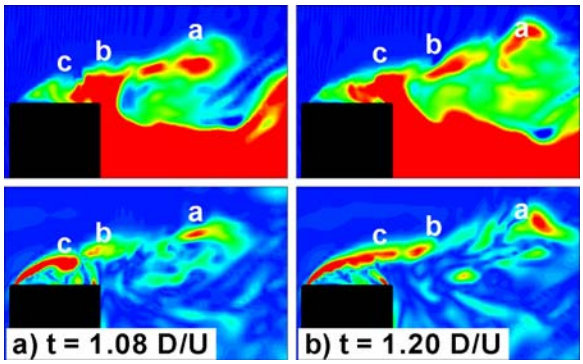

Figure 5.38. Contaminant concentration (top) and out of plane vorticity contours (bottom) in a vertical plane (y/D=3.3) cutting through the vertical DSL near the crest of the upstream groyne. a) t=1.08D/U; b) t=1.20D/U.

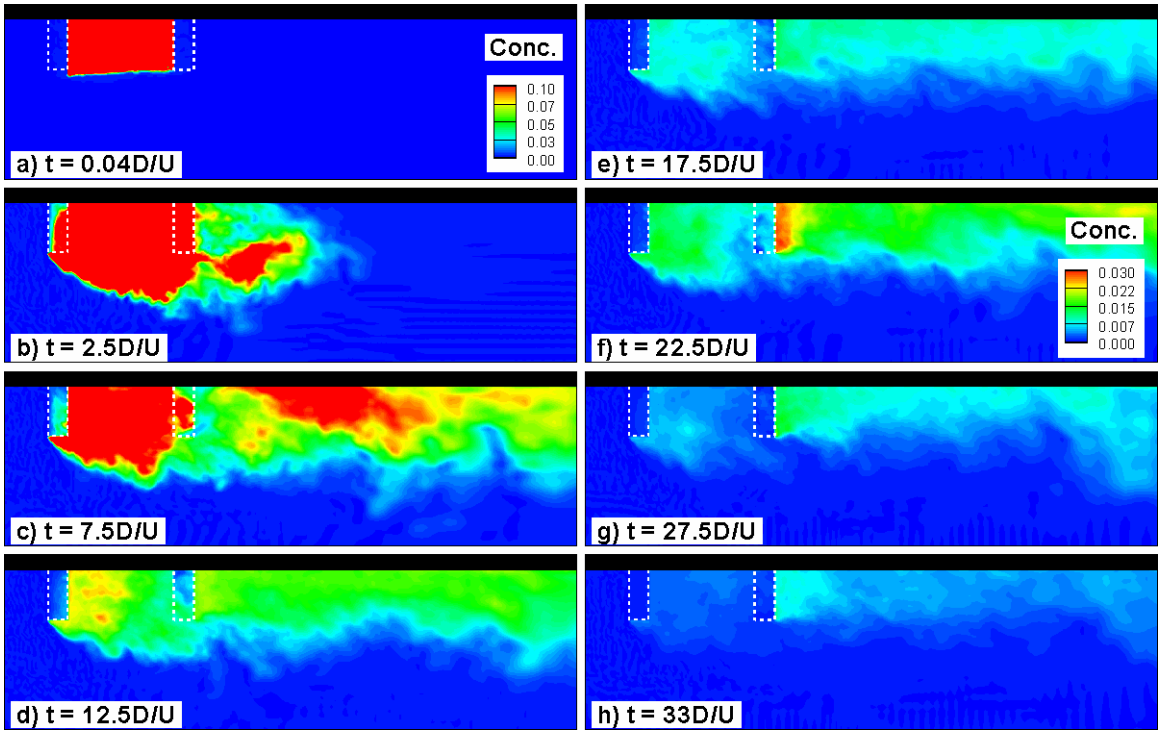

Figure 5.39. Instantaneous contours of depth-averaged contaminant concentration. Mixing starts at t=0D/U when the concentration in the embayment is set to C/C_0=1.0. a) t = 0.25D/U; b) t = 2.5D/U; c) t = 7.5D/U; d) t = 12.5D/U; e) t = 17.5D/U; f) t = 22.5D/U; g) t = 27.5D/U; h) t = 33.0D/U. Note: The contour levels are changed in frames f, g and h.

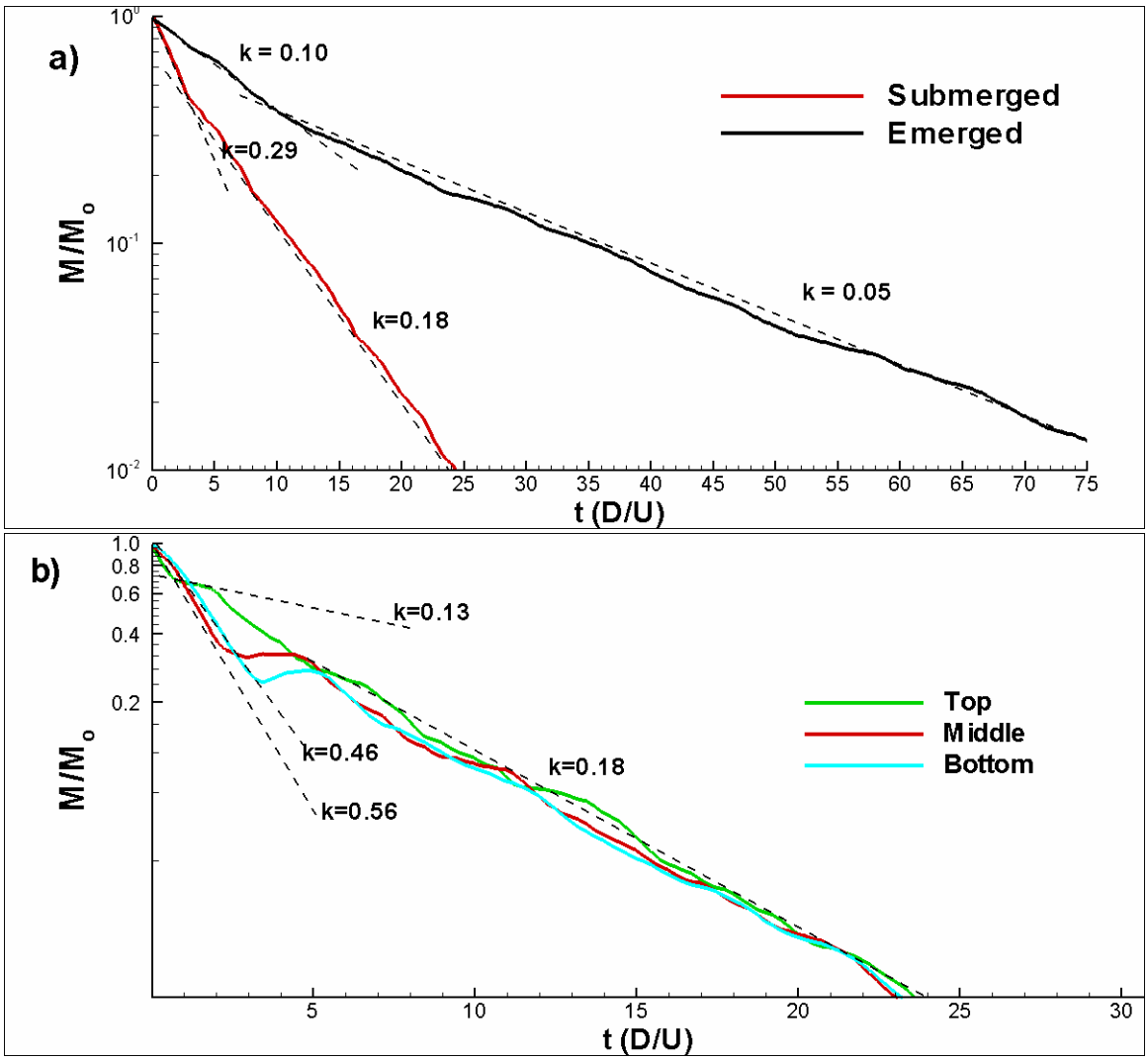

Figure 5.40. Contaminant mass decay. a) within the whole embayment volume for submerged and emerged cases; b) within top, middle and bottom embayment layers for submerged case.

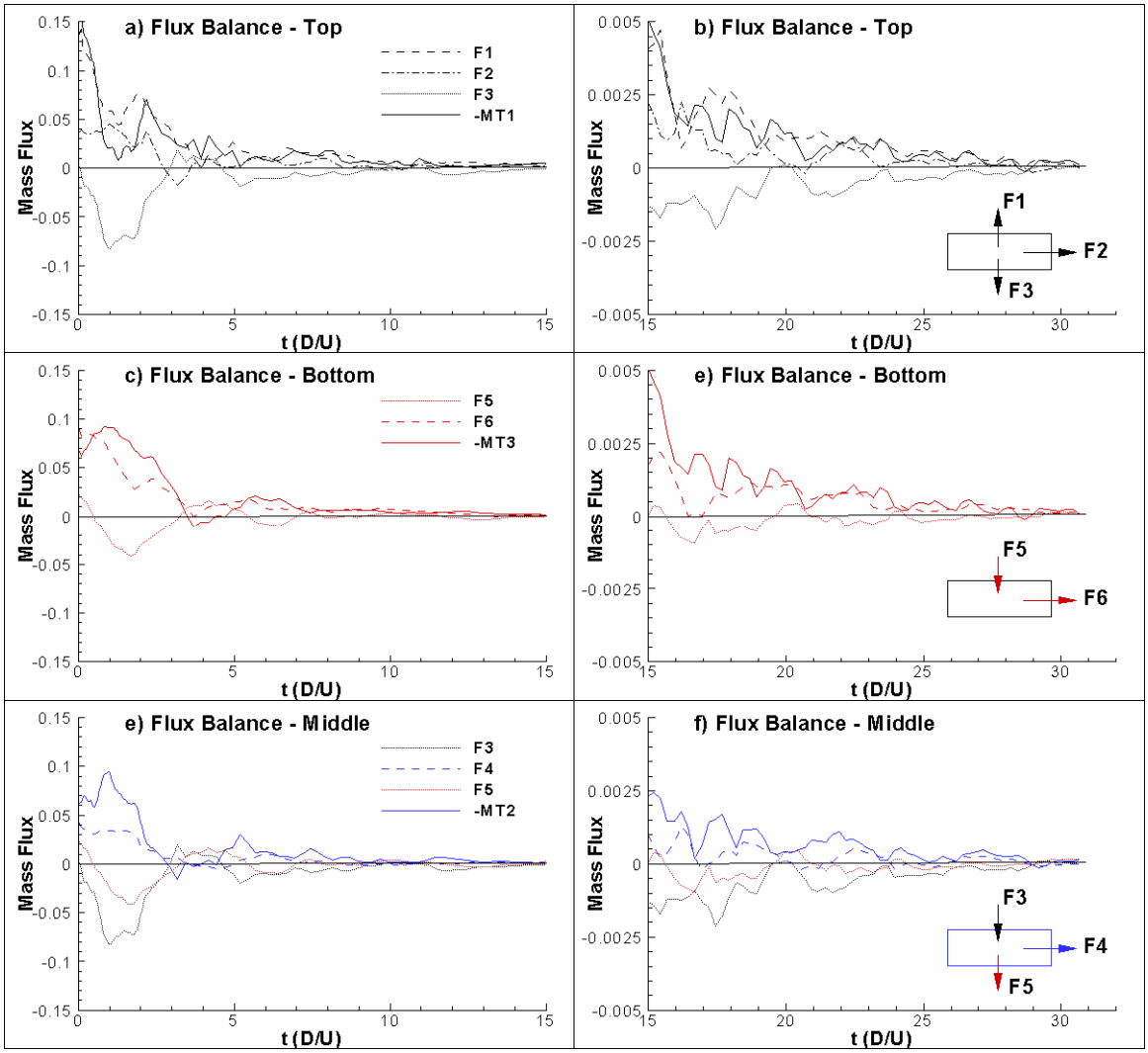

Figure 5.41. Contaminant mass fluxes within each layer of the embayment (submerged case). a) top (t = 0 to t = 15); b) top (t = 15 to t = 30); c) bottom (t = 0 to t = 15); d) bottom (t = 15 to t = 30); e) middle (t = 0 to t = 15); f) middle (t = 15 to t = 30).

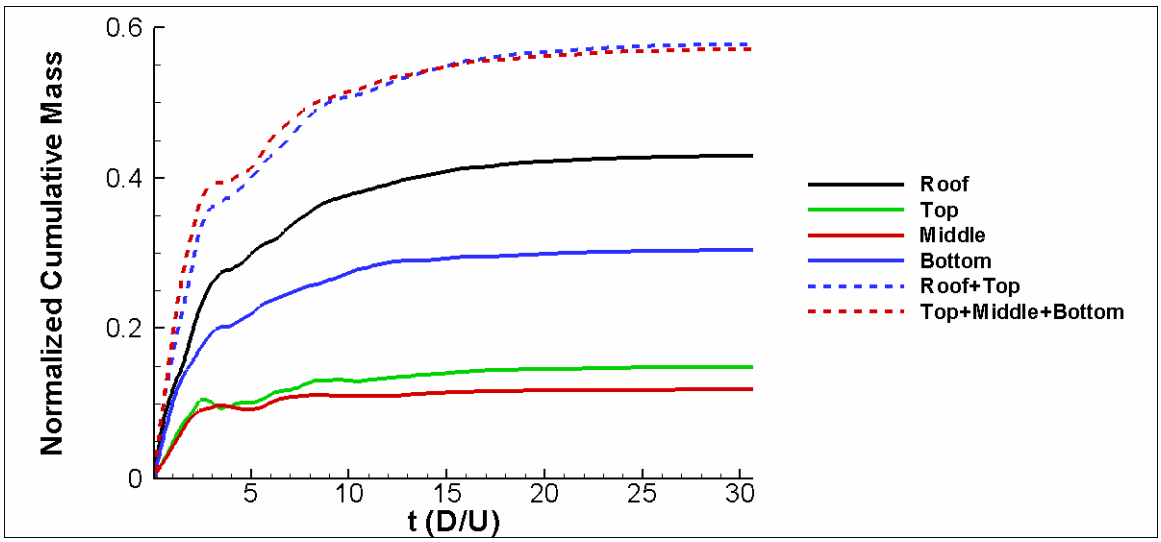

Figure 5.42. Temporal evolution of cumulative contaminant mass transport into the channel through the corresponding embayment-channel interfaces (submerged case).

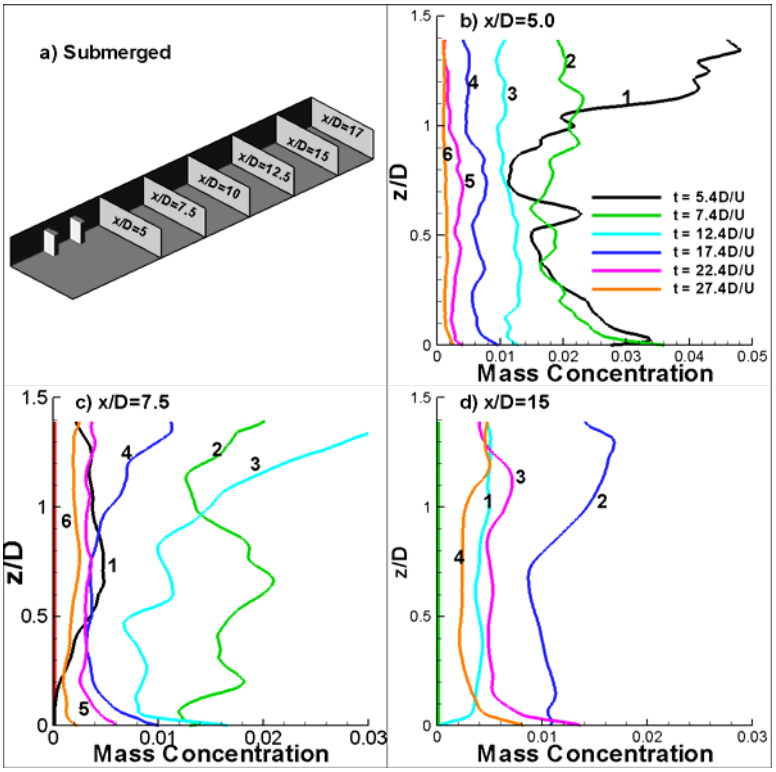

Figure 5.43. Analysis of contaminant advection through main channel. Temporal evolution of width-averaged concentration profiles in various cross sections. a) positions of cross sections; b) x/D=5; c) x/D=7.5; d) x/D=15. x/D is measured from the inlet section.

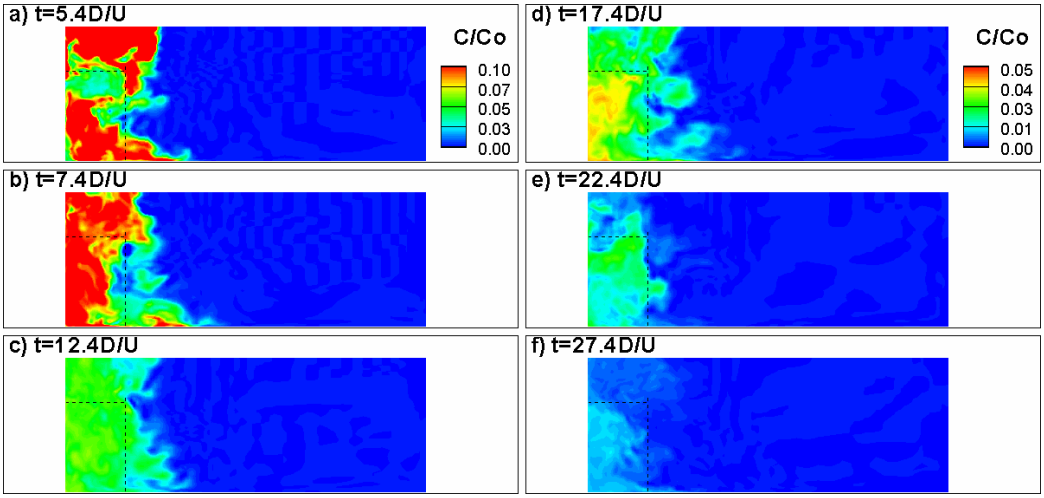

Figure 5.44. Instantaneous contours of contaminant concentration at section x/D = 5.0. a) t = 5.4D/U; b) t = 7.4D/U; c) t = 12.4D/U; d) t = 17.4D/U; e) t = 22.4D/U; f) t = 27.4D/U.

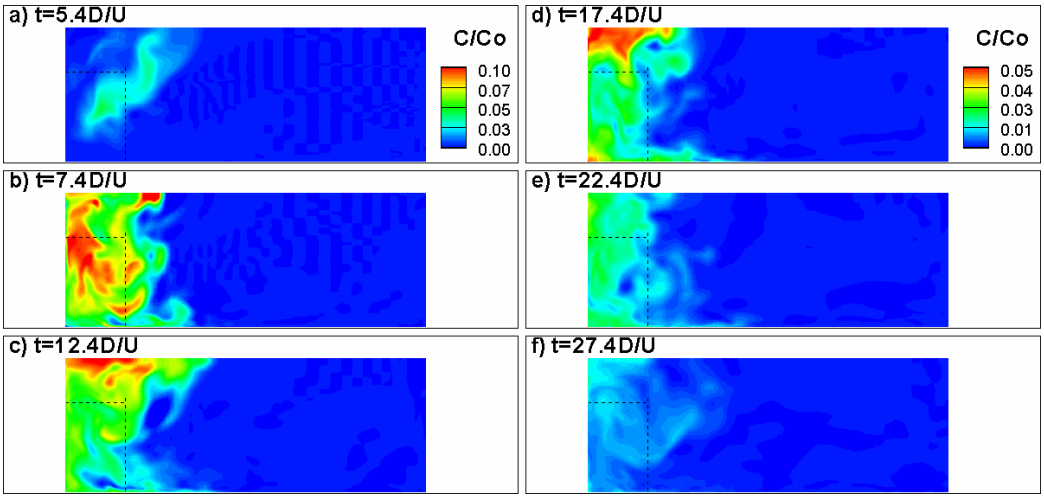

Figure 5.45. Instantaneous contours of contaminant concentration at section x/D = 7.5. a) t = 5.4D/U; b) t = 7.4D/U; c) t = 12.4D/U; d) t = 17.4D/U; e) t = 22.4D/U; f) t = 27.4D/U.

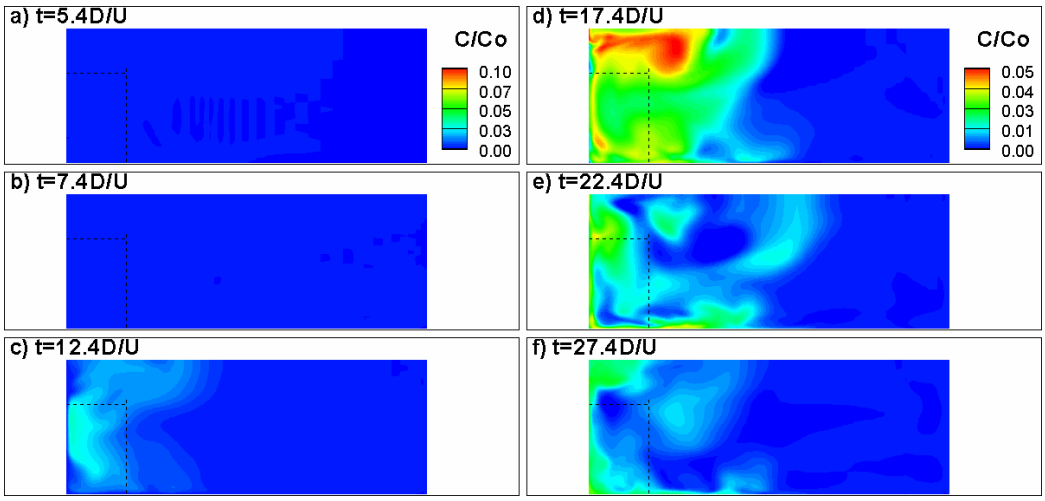

Figure 5.46. Instantaneous contours of contaminant concentration at section x/D = 17.0. a) t = 5.4D/U; b) t = 7.4D/U; c) t = 12.4D/U; d) t = 17.4D/U; e) t = 22.4D/U; f) t = 27.4D/U.

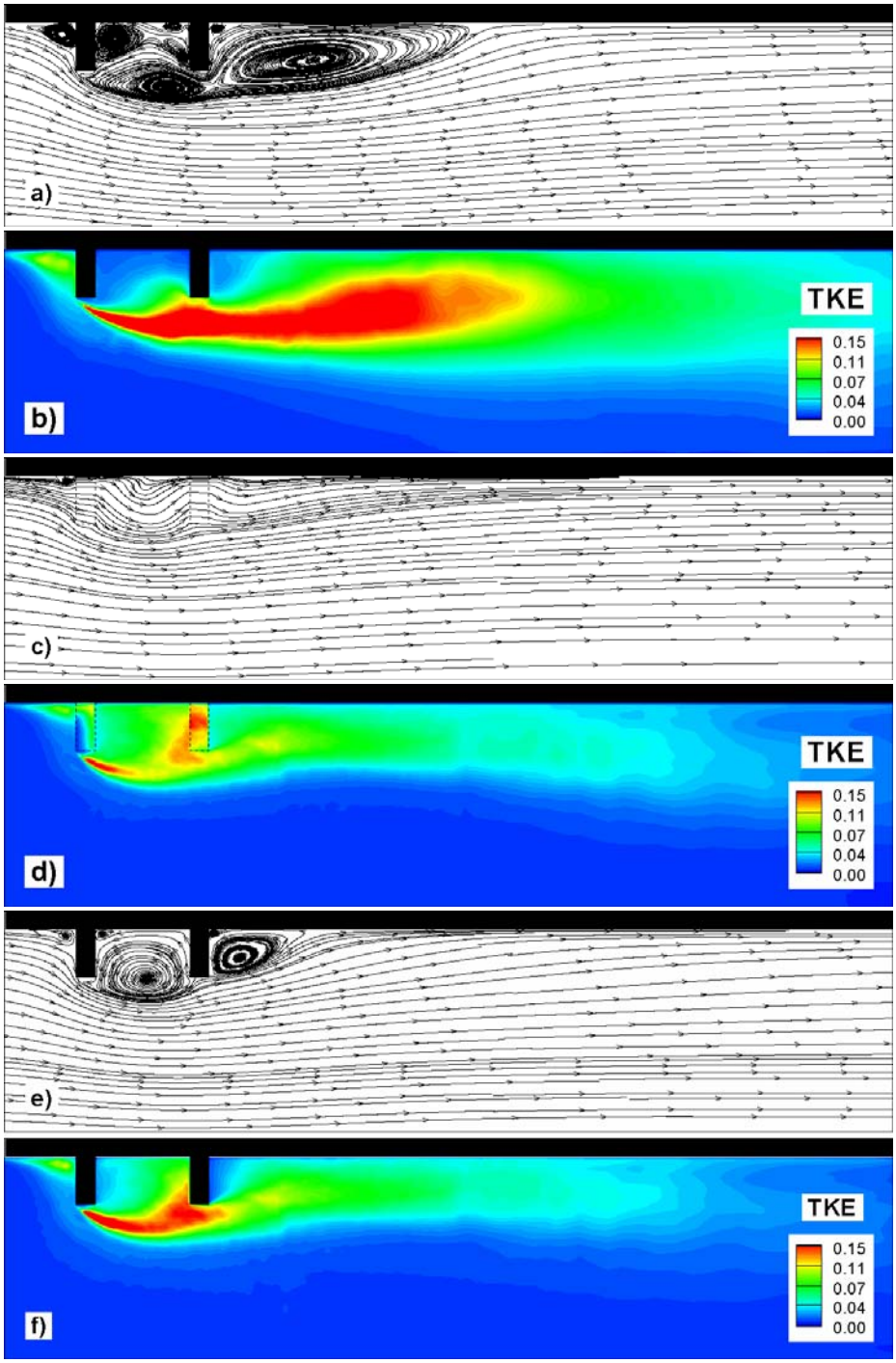

Figure 5.47. Streamlines and TKE distributions in depth averaged flow. a) streamlines, emerged case; b) TKE, emerged case; c) streamlines, submerged case; d) TKE, submerged case; e) streamlines, submerged case, depth averaging only over embayment depth; f) TKE, submerged case, depth averaging only over embayment depth.

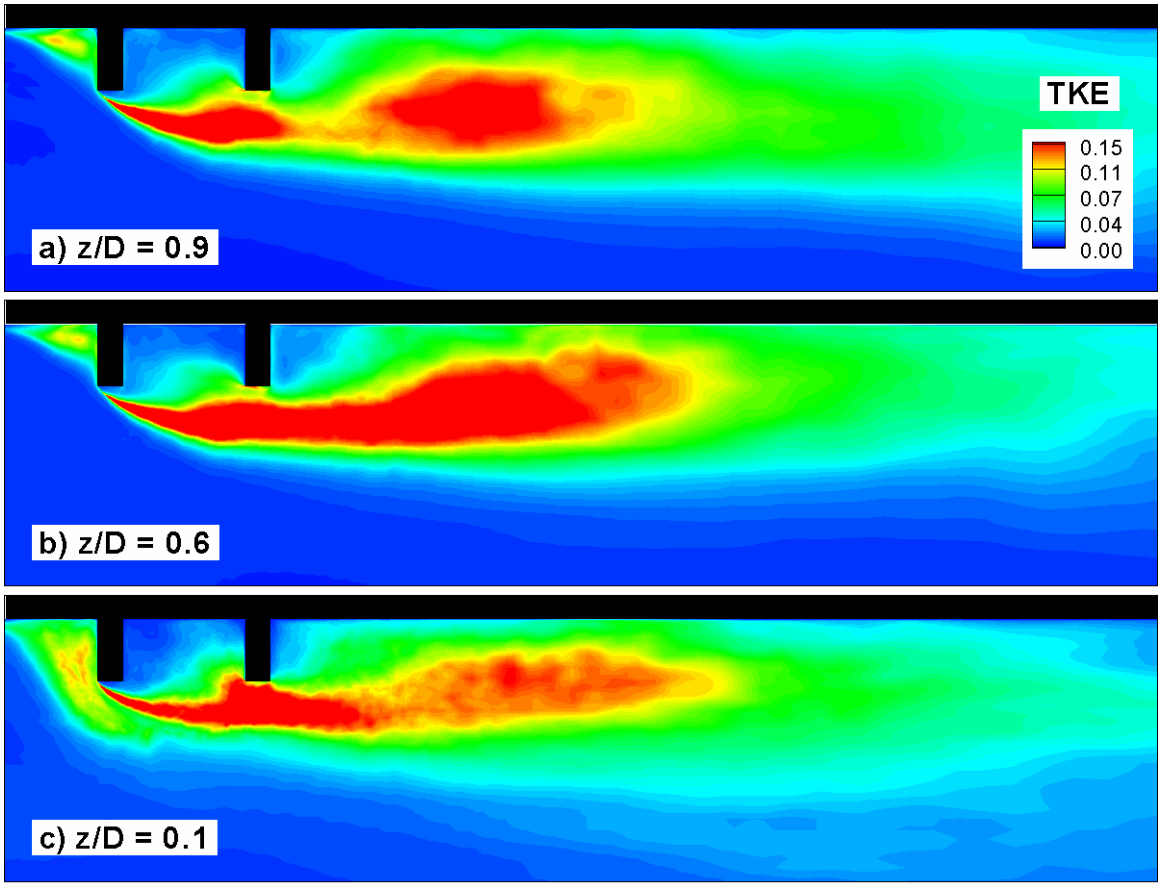

Figure 5.48. TKE distribution for emerged case in various horizontal planes. a) z/D = 0.9; b) z/D = 0.6; c) z/D = 0.1.

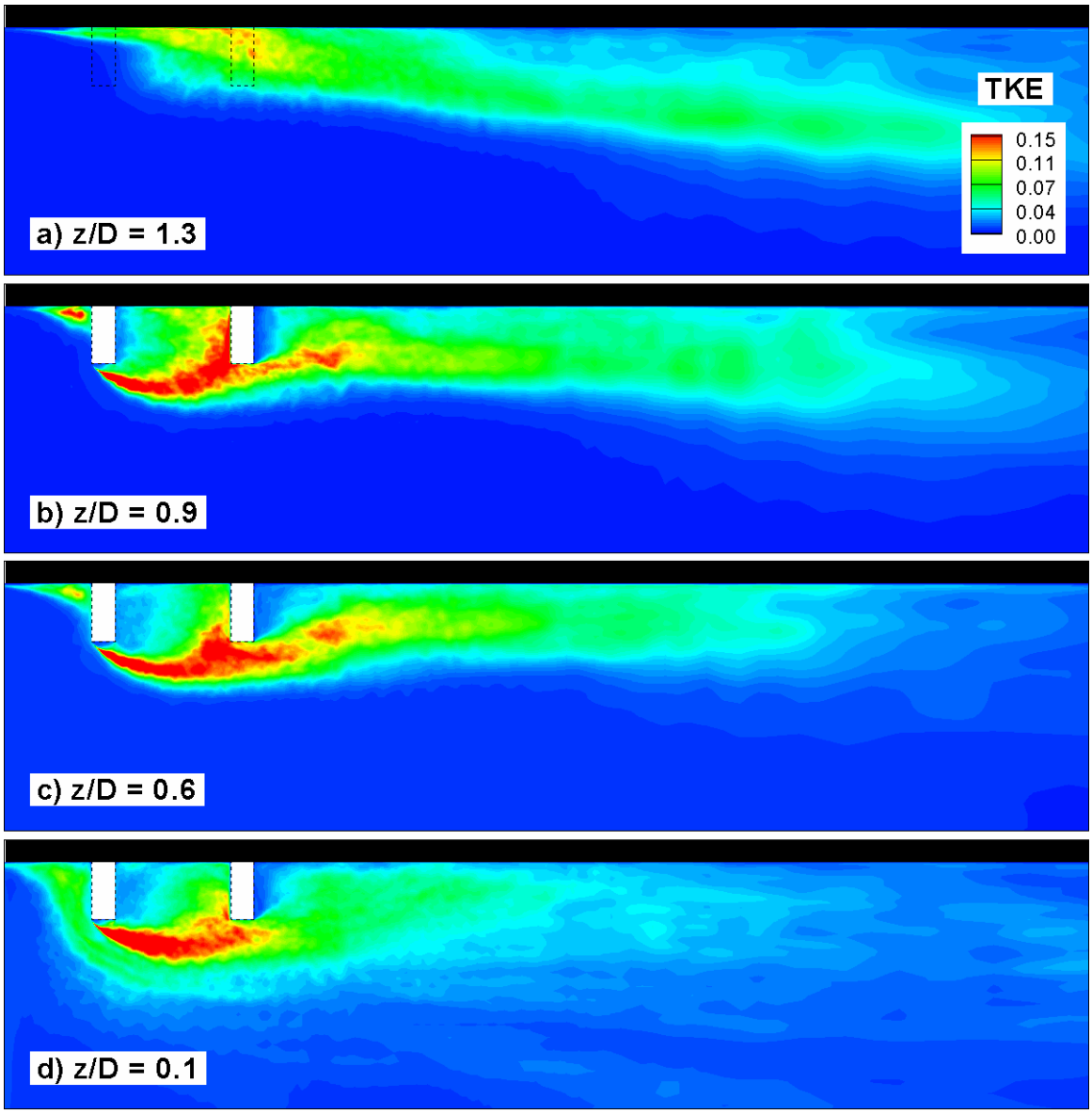

Figure 5.49. TKE distribution for submerged case in various horizontal planes. a) z/D = 1.3; b) z/D = 0.9; c) z/D = 0.6; d) z/D = 0.1.

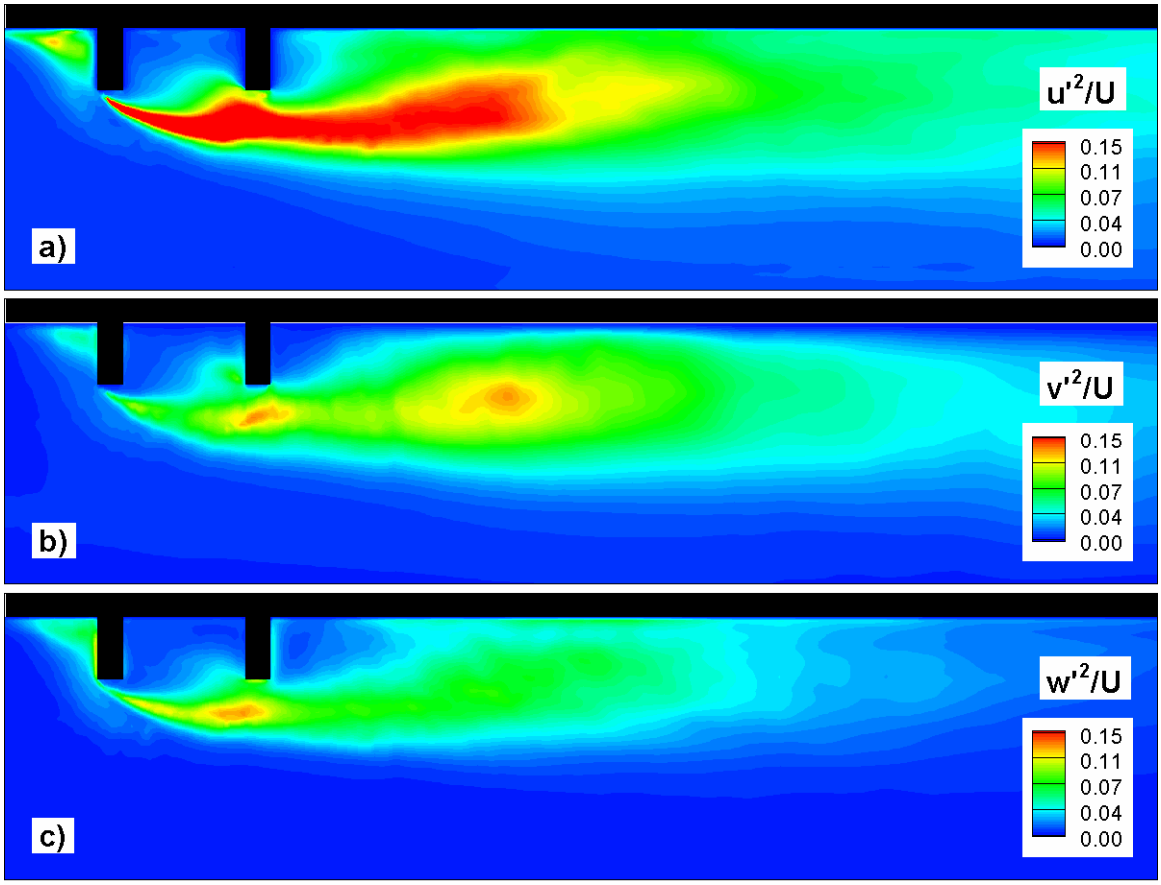

Figure 5.50. Resolved normal Reynolds stresses in the depth-averaged emerged groyne case. a) streamwise velocity fluctuations; b) spanwise velocity fluctuations; c) vertical velocity fluctuations.

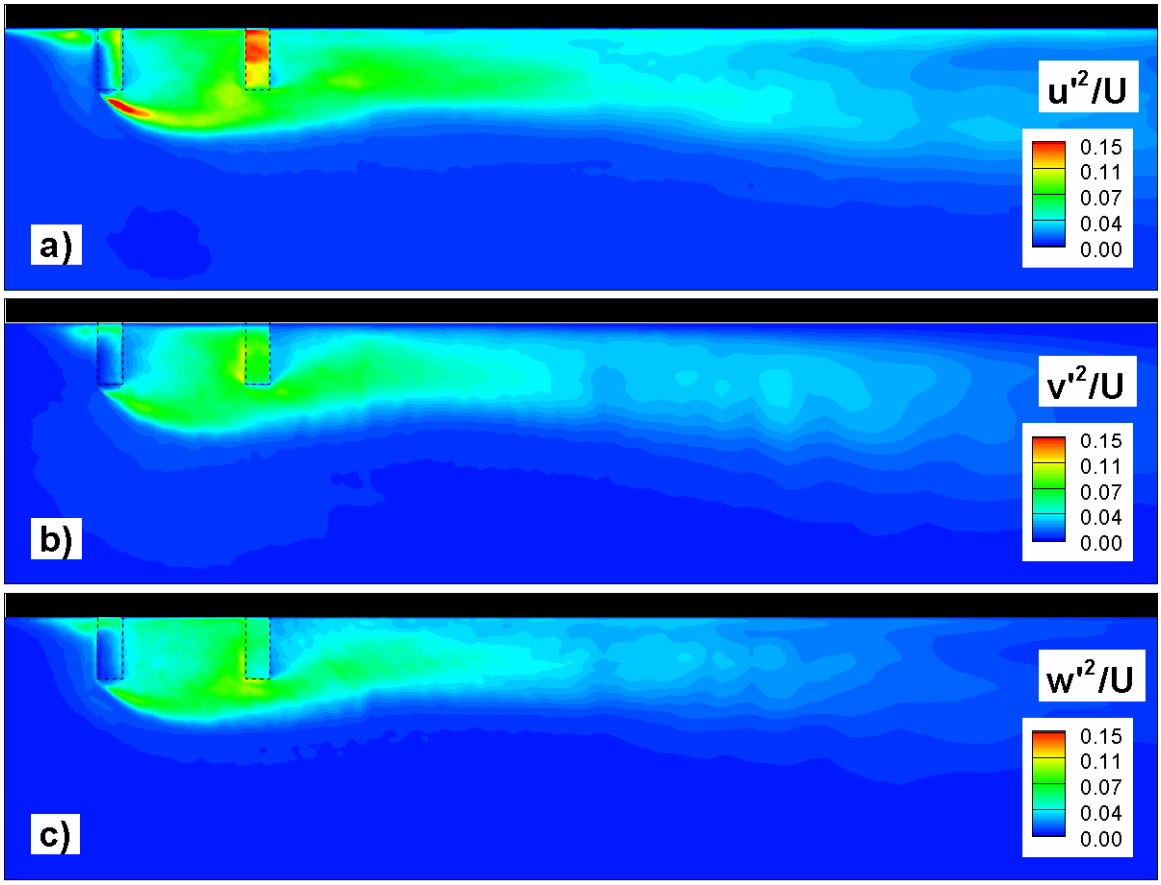

Figure 5.51. Resolved normal Reynolds stresses in the depth-averaged submerged groyne case. a) streamwise velocity fluctuations; b) spanwise velocity fluctuations; c) vertical velocity fluctuations.

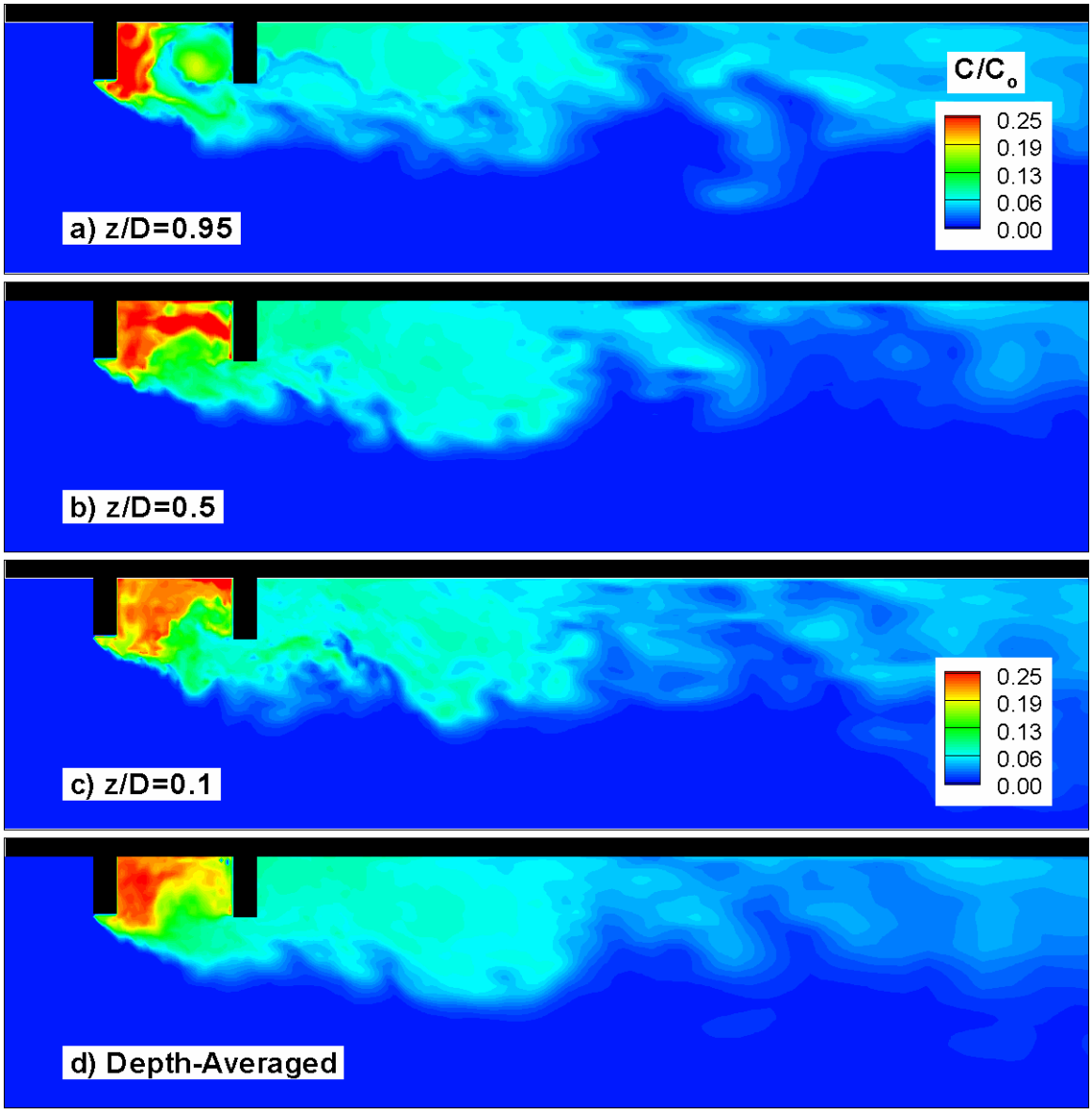

Figure 5.52. Instantaneous contaminant concentrations at t = 22D/U (emerged groyne case). a) z/D = 0.95; b) z/D = 0.5; c) z/D = 0.1; d) depth-averaged.

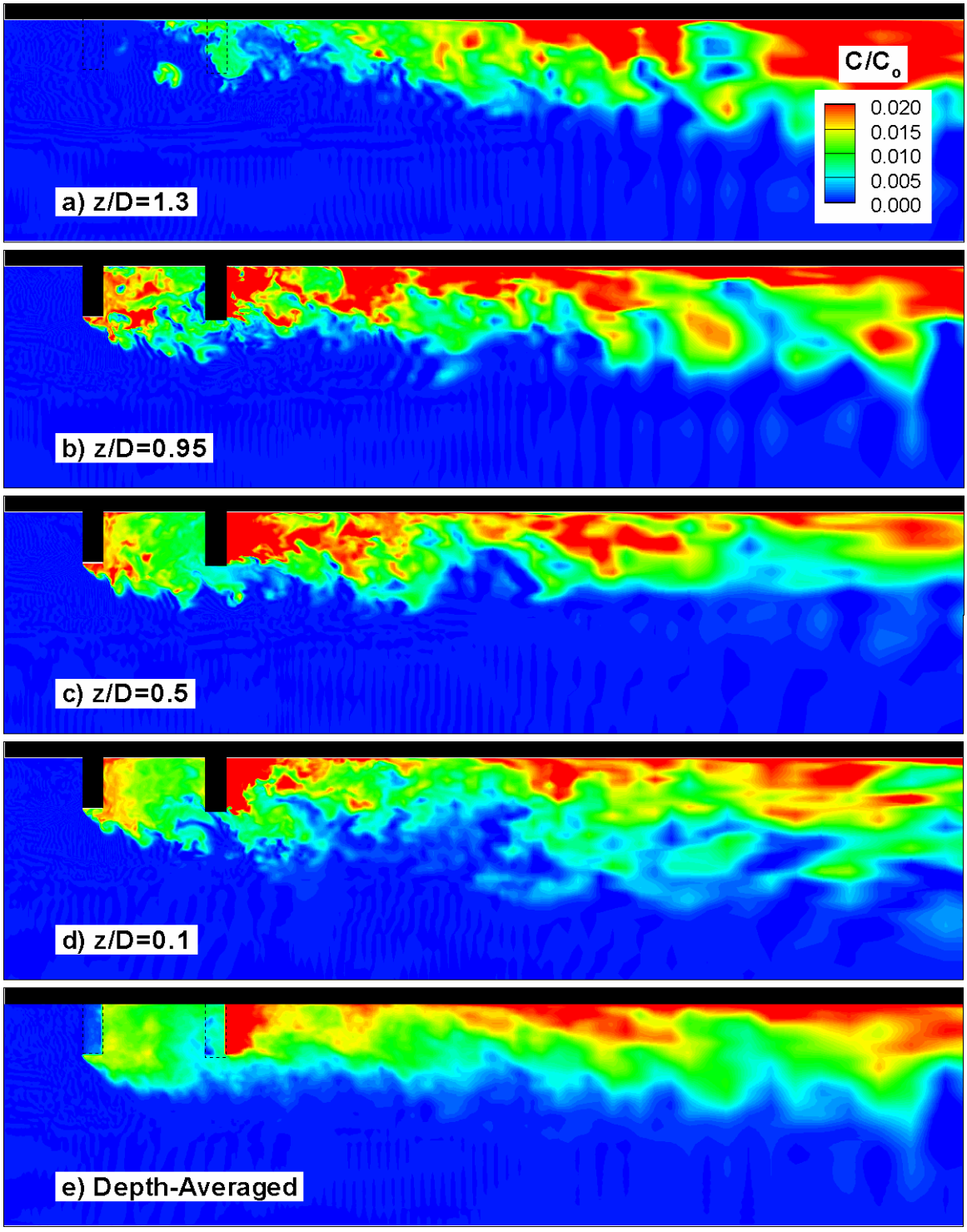

Figure 5.53. Instantaneous contaminant concentrations at t = 22D/U (submerged groyne case). a) z/D=1.3; b) z/D = 0.95; b) z/D = 0.5; c) z/D = 0.1; d) depth-averaged.

CHAPTER 6

RESULTS: SIMULATION OF FLOW AND MASS EXCHANGE AROUND A MULTIPLE-EMBAYMENT GROYNE FIELD

6.1 Introduction

In this section, Large Eddy Simulation (LES) is used to investigate the instantaneous and mean flow fields around a series of vertical non-permeable groynes situated on one side of a flat-bed open channel and the mass exchange processes between the various embayments and the main channel. The test case is characteristic of flow past series of groynes encountered in natural rivers where the embayment region is shallower than the main channel. The depth in the embayment is not constant, the embayment bed has a small slope toward the channel and the mean depth in the embayment regions is half the one in the main channel. The length and width of the embayments are much larger than the mean depth in the embayment region, so the flow inside the embayments can be considered shallow. The present generic geometry has been studied experimentally by Uijttewaal et al. (2001) at similar Reynolds numbers and with similar fully turbulent inflow conditions in the context of an investigation of flow around river groynes in the Dutch River Waal. Particle Tracking Velocimetry (PTV) was used in the experiment to collect velocity information at the free surface in several embayments. Based on these measurements, the horizontal mean velocity components and the velocity r.m.s. fluctuations were estimated at the free surface. The results of both the experimental study and the present numerical investigation are subject to scale effects. In natural rivers, the Reynolds numbers are one to two orders of magnitude higher than in the experiments.

The main topics discussed in the results section are: 1) validation of the numerical model using data from the scaled model study of Uijttewaal et al. (2001); 2) a description of the vortical structure of the flow in the embayment and mixing layer using the

instantaneous and time-averaged flow fields and a discussion of the variation of the mixing layer properties with the embayment rank; 3) a discussion of the degree of two-dimensionality of the main recirculation motions within the embayment and of the degree of three-dimensionality of the flow in the interface region between the interior of the embayments and the channel flow; 4) a study of the mean bed shear stress distribution inside the embayments and of related erosion phenomena around the groynes; 5) a discussion of the mechanisms of momentum and mass exchange between the quasi 2D flow in the center of the embayments and the main channel; 6) a quantitative study of the exchange of dissolved matter (passive contaminant) between the various embayments in the groyne field and the main channel; 7) an investigation of how the mass exchange at the channel-embayment interface takes place over the embayment depth and a description of the contaminant transport within the embayment; 8) an estimation based on LES results of the mass exchange coefficients used in simple mass exchange models for the present geometry; and 9) a description of the advection inside the main channel of the contaminant removed from the second embayment of the groyne field.

6.2 Computational Domain and Mesh

6.2.1 Computational Domain

The computational domain (Figure 6.1) and flow conditions correspond to test 8 of the physical model study of a schematized river reach containing rectangular groynes with smooth surfaces conducted by Uijttewaal et al. (2001). The sidewalls are vertical, and the groynes are emerged and oriented perpendicular to the mean flow direction. The flow depth, D, in the main channel is constant. To reduce the computational resources needed to perform the simulation, only the first 6 embayments out of the ten considered in the experiment and only half of the channel width were part of the computational domain. As a consequence, the lateral boundary on the side without groynes was

simulated as a symmetry plane rather than a wall. The domain extends 7.5D upstream of the first embayment and 25D downstream of the last embayment.

The depth in the main channel, D=0.1m, was chosen as the length scale. The mean velocity, U=0.35m/s, in the main channel, was chosen as the velocity scale. The Reynolds number was $Re=UD/\nu=35{,}000$ in both experiment and simulation. In the computational domain, x is the streamwise direction. The inflow section is located at x/D=12.5. In the transversal direction, y/D=0 corresponds to the sidewall (Figure 6.2a). The vertical direction, z, is measured from the channel bottom. The thickness of the groynes is 0.5D. As the width (w=7.5D) over length (l=10.75D) ratio of each embayment is 0.7, a one-gyre circulation pattern was observed inside the embayments in the experiment. For this configuration, the mixing-layer eddies are expected to play the predominant role in the momentum exchange between the embayment and channel. For longer embayments (w/l<0.5) where a two-gyre pattern is present, Uijttewaal et al. (2001) observed that larger-scale eddies are shed from the tip of the groynes and interact strongly with the upstream recirculation gyre in an irregular way. This mechanism is generally absent for embayments with w/l>0.5.

The depth in the embayment area increases linearly from 0.4D at the sidewall to a_i=0.6D at the channel-embayment interface (Figure 6.2b). This corresponds to a bottom slope toward the channel of 2:75. As the ratios between the horizontal dimensions of the embayment and the mean depth in the embayment region (a_m=0.5D) are larger than 15, the embayment can be considered shallow, and the large scale motions inside the embayment are expected to have a strong 2D character. The physical Reynolds number inside the embayment region was around 3,000-6,000. The interaction between the vertical groyne elements with the main channel flow and the presence of the sudden change in flow depth between the embayment and the main channel are likely to induce strong 3D effects.

6.2.2 Boundary and Initial Conditions

The flow in the inlet section in both the experiment and simulation was fully turbulent. In the simulation, the instantaneous velocity fields corresponding to a precalculated fully-developed open channel flow simulation conducted at the same channel Reynolds number with periodic conditions in the streamwise direction were fed in a time-accurate way through the inflow section. This ensured that the incoming turbulent channel flow upstream of the groyne field contained realistic coherent structures. A convective outflow boundary condition was used at the exit section. The velocity components on all solid boundaries were set equal to zero. As the Froude number was smaller than 0.35 over the whole domain, free surface deformation effects are not important, and the free surface was simulated as a rigid lid (zero horizontal shear stress and zero normal velocity).

The removal of a passive (conservative) contaminant initially introduced inside embayments 2 and 5 was studied similarly to the previous two cases (one-embayment geometry) using an advection-diffusion equation that was solved for the non-dimensional concentration C ($0<C<1$). The contaminant was introduced instantaneously over the whole depth of the embayment after the flow inside the computational domain became statistically steady. That time was chosen as the initial starting time ($t=0D/U$) of the mixing process. The viscous Schmidt number, Sc, was taken equal to 1. The non-dimensional concentration was set to zero at the inflow section over the whole duration of the contaminant removal process and equal to one at $t=0D/U$ within the embayment in which the contaminant was introduced. At all the other boundaries (walls, free surface, exit), the concentration mass flux was set to zero. The simulation was run for an additional 800D/U until less than 10% of the initial mass of contaminant was left inside embayment 2 and 5, respectively.

6.2.3 Computational Mesh

The total number of cells in the computational domain is around 4 million; the number of cells in the vertical direction in the embayment region is 22; and in the channel it is 42. Figure 6.2a-b shows the computational mesh in the free surface plane and in a vertical spanwise plane (x/D=36.6), respectively. Figure 6.2c shows a partial view of the mesh in a horizontal plane around one of the embayments. Figure 6.2d shows a detailed view of the mesh in a vertical plane around the interface. The first row of cells off the walls is located at around 3 wall units from the solid surfaces assuming $u_{\tau 0}/U \sim 0.045$. The maximum mesh spacing in the vertical direction is around 22 wall units. In the horizontal plane, the typical dimension of the mesh cells in the region around the head of the groynes is close to 8 wall units. The horizontal cell size is close to 220 wall units at point c1 (Figure 6.2c) inside the embayment region, which is acceptable because the physical Reynolds number inside the embayment is a couple of times smaller than the one in the channel.

The time step in the simulation was 0.002D/U, and the maximum Courant number was 0.12. The simulation was run for nearly 200D/U until the transients were eliminated. Then statistics were calculated using the instantaneous flow fields over the next 250D/U.

6.3. Analysis of Mean and Instantaneous Flow Structure, Flow Changes along the Groyne Field and 3D Effects in the Interface Region

6.3.1 Free Surface Flow

Figure 6.3a shows the distribution of the mean streamwise velocity, u, in the free surface plane. The mixing layer growth is relatively linear on the channel side until the end of the third embayment. Starting with the fifth embayment, the variation in the width of the mixing layer is much smaller, suggesting the flow is relatively periodic in the streamwise direction with the wavelength equal to the embayment length.

The TKE distribution in Figure 6.3b confirms that starting with the fifth embayment the flow is practically independent of the embayment rank. As expected, the highest turbulent fluctuations are present inside the strong shear layer around the embayment-channel interface, particularly around the head of the groynes. This is because some of the large-scale energetic eddies convected inside the mixing layer are interacting with the groynes (see also discussion of Figure 6.10) and because new eddies are shed from the tip of each groyne. The convection of these coherent structures into the embayment parallel to the face of the downstream groyne explains the relatively high values of the TKE in that region. The turbulence within the shear layer dominates the one associated with the fully turbulent flow within the main channel. The amplification ratio is around ten. In the first embayment, the TKE values are high over the whole length of the embayment around the interface. For embayments of the higher rank, there is a clear decay of the TKE levels over the downstream half of the embayment length until very close to the groyne edge.

Figure 6.4 provides more details on the variation of the 2D streamlines patterns, vorticity magnitude, streamwise and transverse normal Reynolds stresses with the embayment rank in the free surface plane. The mean dimensions of the main recirculation eddy (gyre) change very mildly with the rank of the embayment. Consistent with the experiment, for the embayment aspect ratio of the present geometry, a one-gyre circulation pattern is observed. The main recirculation eddy in Figure 6.4a occupies most of the embayment volume except the two corners where secondary counter-rotating eddies are present. The main difference between the embayments is that the inclination of the streamlines relative to the streamwise direction, and thus the values of the transverse velocities on the interface line, are smaller in the first embayment. This implies that more of the embayment fluid is entering the main channel region near the free surface in the embayments of higher rank.

The mean vorticity magnitude distribution shows that starting with embayment 4, the vorticity decay past the tip of the upstream groyne in the vorticity sheet at the channel-embayment interface is much faster compared to the decay in the first and second embayments. The fact that the vorticity sheet is weaker in the embayments of higher rank means that the eddies near the interface can penetrate more easily across the interface. Consequently, the mass exchange near the free surface is expected to be slightly higher in these embayments. As the mean transverse velocity is oriented toward the channel, it is expected that the prevalent direction of mass exchange in the region is from the embayment toward the channel. The amplification observed around the tip of the downstream groyne is due to the interactions between the eddies in the mixing layer and the downstream groyne.

Comparison of the streamwise and transversal resolved Reynolds stresses in Figure 6.4c-d shows that the streamwise fluctuations are generally larger in the mixing layer. These fluctuations are associated with the convection of the large-scale eddies inside the mixing layer in a direction that is relatively parallel to the interface. However, for the higher rank embayments, it is the transverse fluctuations that are larger in the vicinity of the downstream groyne away from its tip. The amplification of the transverse fluctuations is due primarily to the random but continuous injection and convection of the mixing layer eddies parallel to the wall of the downstream groyne rather than the small scale turbulence present in the embayment region. In the context of the mass exchange, these eddies carry high-vorticity, low-concentration channel fluid inside the embayment. As these eddies are convected parallel to the embayment walls, they mix with the higher concentration embayment fluid that is recirculated by the main gyre. This is the main mechanism through which the high concentration fluid from the center of the embayment gets diluted over time.

Figure 6.5 compares the mean velocity vector fields predicted by the numerical simulation and the ones measured in the experiment (Uijttewaal et al., 2001). Figures

6.5a and 6.5c show the computed velocity vector fields in the first embayment and the sixth embayment. Figures 6.5b and 6.5d display the measured velocity vector fields in the first and the eighth embayment. The main difference between the simulated and measured mean velocity vector fields occurs in the upstream corner of the higher rank embayments as observed form comparison of Figures 6.5c and 6.5d where the size of the secondary recirculation cell is underpredicted in the simulation by about 30%. One should also notice that both experiment and simulation predict a much smaller size secondary recirculation cell in the first embayment. The size of this secondary eddy inside the first embayment is well predicted by the simulation.

Figure 6.6 compares the streamwise velocity profiles in the free surface plane between simulation and experiment (Uijttewaal et al., 2001) in the first embayment (frames b to h) and in embayment 6 (frames j to p). The experimental data collected in embayment 8 (measurements were not available in embayment 6, and the computational domain contains only six embayments) is used to validate the numerical predictions in embayment 6 because they correspond to embayments situated far from the start of the series of groynes where the flow is only very slightly dependent of the embayment rank. Results from a RANS simulation using the k-ω model (no wall functions were used) obtained on the same mesh as the one used in LES, and in which similar boundary conditions were used, are also plotted in Figure 6.6 to put the predictive capabilities of LES in better perspective.

Comparing the streamwise velocity decay across the mixing layer at equivalent x/D positions in embayments 1 and 6 (Figure 6.6), one can see that the gradient is larger across the first groyne. This is fully consistent with the overall distribution of the mean streamwise velocity in Figure 6.3a. Overall, good agreement is observed in the profiles parallel to the sidewall and the groynes in both embayments. In the first embayment, the main disagreement occurs inside the jet-like flow parallel to the sidewall (the jet-like flow is toward the upstream groyne). The velocity is underestimated by the simulation

between x/D=24 and x/D=28. Interestingly, the predictions are in excellent agreement with the experiment in embayment 6. However, in this embayment, it is the velocity gradient across the mixing layer that is overestimated in the simulation. One can speculate that the agreement would improve if all ten embayments would have been simulated. The overestimation of the velocity gradient across the mixing layer is considerably higher in the RANS results. Additionally, the agreement with the experiment is poorer for 0<y/D<4 in both embayments.

Error! Reference source not found. compares the r.m.s. streamwise velocity fluctuations in the free surface plane. No data is available from RANS. The position of the sections relative to the two embayments is shown in Figure 6.6a and 6.5i. In both embayments, the LES simulation predicts the amplification of the streamwise velocity fluctuations along the mixing layer well (its center is situated at y/D~7.5 in embayment 1 and at y/D~8 in embayment 6). Though the simulation captures the relative maximum associated with the jet-like flow parallel to the sidewall, the values are somewhat underpredicted, and the position of the peak is situated closer to the sidewall compared to experiment, especially in the first embayment. In embayment 6, the predictions at the upstream part of the jet-like flow parallel to the sidewall are in excellent agreement with experiment (x/D=84 and x/D=83), but then the streamwise fluctuations decay too fast (x/D=82 and x/D=79). The streamwise fluctuations at the center of the embayment are underpredicted.

Figure 6.8 shows the validation for the transverse velocity. Consistent with the underestimation of the streamwise velocity in the jet-like flow near the sidewall in embayment 1, the transverse velocities in the LES simulation are also underestimated in the jet-like flow parallel to the upstream groyne (Figure 6.8b between x/D=20 and x/D=22). Figure 6.7c shows that as the mixing layer is approached, the agreement improves. By contrast, the agreement is excellent in embayment 1 for the upstream part of the jet-like flow that is parallel to the downstream groyne (Figure 6.8b between

x/D=28 and x/D=31). Very good agreement is observed in embayment 6 between LES predictions and experimental data. The RANS predictions in embayment 1 show a similar level of agreement with experiment. However, in embayment 6, RANS underpredicts the width of the jet-like flow parallel to the downstream groyne (see Figure 6.8f and 6.7g for x/D>84) compared to experiment and LES.

Figure 6.8i-l contains several profiles of the transverse r.m.s. velocity fluctuations. The experiment shows that the intensity of the transverse velocity fluctuations in the jet-like flow parallel to the downstream groyne is decaying with the embayment rank. Though the LES simulation captures the amplification of the transverse fluctuations in this region, it does not capture the strong amplification present in embayment 1 (y/D =3 for x/D>29 in Figure 6.8i). In contrast, very good agreement is observed in the prediction of the transverse fluctuations in both embayments across the mixing layer and across the jet-like flow parallel to the sidewall (see profiles at x/D=27 and x/D=83 in Figure 6.8j and 6.7l). The transverse velocity fluctuations are also underestimated in the region close to the upstream groyne in both embayments (Figure 6.8i and 6.7k). Despite some differences, the level of agreement observed for the streamwise and transverse r.m.s. fluctuations in the free surface plane for such a complex flow is very good. It also suggests that the mesh used to conduct the LES simulation was fine enough to capture the dynamic eddy content of the mixing layer and the interaction of these eddies with the groynes.

Figure 6.8 compares several TKE profiles obtained from experiment, LES and RANS. In both embayments, RANS predicts a higher amplification of the TKE at the center of the mixing layer. The decay of the fluctuations on both sides of the mixing layer is, however, too rapid (RANS underpredicts the width of the mixing layer) compared to experiment. LES does a better job overall of capturing the distribution of the TKE across the mixing layer, especially over the downstream half of the embayment length (Figure 6.9c-d for embayment 1 and Figure 6.9g-h for embayment 6).

Because the groynes are fully emerged and impermeable, the momentum transport occurs uniquely via the mixing layer at the channel-embayment interface. As discussed in Figure 6.4, a large quasi-2D recirculation eddy is present inside the embayment. More details on the main mechanism through which mixing takes place in the embayment region can be inferred from Figure 6.10, which shows the instantaneous distributions of the streamwise velocity and vorticity magnitude in embayments 1, 2 and 6 close to the free surface. The turbulence content of the interfacial mixing layer is of great importance for the momentum and mass exchange processes between the embayments and the main channel. Large-scale eddies that form in the mixing layer and then interact with the tip of the groynes control and modulate the momentum exchange between the wall-attached jet-like flow that forms starting at the tip of the downstream groyne (e.g., several patches of high vorticity are convected parallel to the downstream groyne toward the sidewall in embayment 1 in Figure 6.10b) and the main recirculation eddy. The jet-like flow follows the embayment boundaries (see also corresponding mean velocity distribution in Figure 6.6 and Figure 6.8). The role of the jet-like flow for the mixing within the embayment is very important because, for the present geometry, the aspect ratio w/l is relatively large (short embayment). The large value of w/l is the main reason why in both experiments and animations of the instantaneous vorticity fields obtained from the simulation, the mixing-layer eddies do not grow into a very large eddy that can strongly interact with the main recirculation eddy inside the embayment (see discussion in Uijttewaal et al., 2001). Thus, the mixing mechanism observed for embayments with small w/l is practically absent. Animations also show that though large deformations of the shape of the main recirculation eddy are present in the instantaneous flow, the dominant one-gyre structure is preserved at all times.

6.3.2 Vortical Structure of the Flow in the Detached Shear Layer and Embayment Region

Despite the fact that the motions associated with the main recirculation eddy have a strong 2D character, the flow in the interface region and the interactions between the mixing-layer eddies and the groynes are highly unsteady and three-dimensional. The size of most of the strongly coherent eddies is of the order of the channel depth for the present geometry. However, from time to time larger eddies can form via pairing inside the mixing layer (e.g., observe the eddy approaching the tip of the downstream groyne in embayment 2 in Figure 6.10b). Their effect on the interfacial momentum exchange and on the intensity of the jet-like flow within the embayment is dependent on the nature of their interaction with the tip of the groyne (see Lin and Rockwell, 2001).

In some cases, the eddies are convected past the groyne on the channel side of the mixing layer without interacting with the groyne tip (total escape event). In other cases, as a result of the interaction with the tip of the groyne, the eddy is split into two vorticity patches. One of these patches is injected inside the embayment and convects momentum and fluid particles with it from the channel into the embayment, while the other is convected downstream in the mixing layer. This second patch of vorticity is stretched and dissipates, or it can merge with other eddies before interacting with one of the subsequent groynes in the field. Finally, in some cases, the mixing-layer eddy is convected entirely inside the embayment (total clipping event) parallel to the downstream groyne surface where it forms the above-mentioned wall jet-like current. The process through which these patches of highly vortical fluid from the mixing layer are forming the jet-like flow is random. A detailed discussion of the relationship between the occurrence of these events and the pressure and vorticity distributions and flow patterns inside the cavity/embayment is given in Chang et al. (2006). These eddies progressively lose their coherence as they are convected toward the sidewall and then parallel to it due to the small-scale turbulence and interaction with the shallow bottom. The vorticity

levels inside the center of the main recirculation region virtually always remain low, indicating that these eddies cannot penetrate toward the center of the embayment. Thus, the fluid inside the center of the embayment is expected to have significantly larger residence times. However, these eddies are very efficient at enhancing the mixing at the boundary with the main recirculation region.

The following discussion of 3D effects in Figure 6.11 and Figure 6.12 is based on results corresponding to embayment 5, but the flow phenomena are similar starting with embayment 1. The 2D mean velocity streamline patterns shown in Figure 6.11a-c at the free surface, at mid-depth level and a distance of 0.1D from the inclined bottom clearly demonstrate the non-uniformity of the transverse velocity component over the depth in the interface region. If close to the free surface the flow is on average oriented from the embayment toward the channel, at deeper levels the trend is reversed over practically the whole length of the embayment, as observed in Figure 6.11c and especially in Figure 6.11b. As expected, if the depth averaged flow is considered (Figure 6.11d), the size of the region where the streamlines are deflected toward the channel (upstream half of the embayment) is roughly equal to that where the streamlines are deflected toward the embayment (downstream half of the embayment). This is to be expected due to continuity as the flow is incompressible. The one gyre circulation pattern is observed at all depths within the embayment.

The distribution of the mean transverse velocity in the interface section (the vertical scale was distorted 4:1 in Figure 6.12a) gives a more quantitative picture of the non-uniformity of the mean momentum exchange between the embayment and the channel. Consistent with the qualitative trends in Figure 6.11a, in the free surface layer ($z/D>0.83$) the transverse velocity is oriented toward the channel over practically the whole length. The largest values are recorded over the upstream half length of the embayment. Below $z/D=0.83$, the transverse velocity is oriented predominantly toward the embayment over most of the embayment length. This strong non-uniformity of the

transverse velocity over the depth has important consequences for the mass exchange processes. In the case in which contaminant is ejected from the embayment, it is expected that most of it will leave the embayment through the upstream half of the free-surface layer. Thus, once outside the embayment, the contaminant concentration will be high predominantly near the free surface before the contaminant disperses into the main channel.

The mean transverse velocity distribution in Figure 6.12 also explains why the global mass exchange coefficient determined based on the convection of floating particles out of the embayment was considerably larger than the one estimated based on measurements of the depth-averaged concentration of dye introduced within the embayment volume in the experiments of Uijttewaal et al. (2001). The transverse flow toward the main channel in the surface layer is the reason for this. The mean transverse velocity averaged over the embayment length in a thin layer close to the free surface is close to 0.033U. This translates into a dimensional velocity of 0.011m/s, which is very close to the estimate of 0.01m/s given by Uijttewaal et al. (2001) needed to account for the quantitative difference between the exchange coefficients estimated with the two methods. Still, one should keep in mind that in reality the transverse velocity distribution is not uniform over the length of the top layer. Figure 6.11d-e gives more details on the transverse velocity distribution in the free surface plane and at the mid-embayment level (z/D=0.6). Even away from the interface, the distribution of the transverse velocity is not exactly the same at the two depths.

The regions within the embayment where 3D effects are important can be educed using the distributions of the mean vertical velocity. The plane at z/D=0.67, (Figure 6.12b) situated at mid embayment depth, is representative. The maximum vertical velocity on both sides of the interface is around 0.03U. Relatively large vertical velocities are observed in the regions associated with the jet-like flow parallel to the groyne walls, in particular close to the downstream one where the vertical velocity is

around 0.05-0.08U. Even in the depth-averaged flow shown in Figure 6.12c, the magnitude of the depth-averaged vertical velocity is of the order of 0.05U. As the typical magnitude of the horizontal velocity inside the embayment is of the order of 0.2-0.3U, the importance of 3D effects outside the center of the embayment where the flow is quasi-2D cannot be ignored.

The distribution of the TKE (Figure 6.13) also shows some strong variations over the depth, especially in the region around the interface. As observed from Figure 6.13a (the vertical scale is distorted 4:1), which shows the distribution in the interface section, the turbulent fluctuations are the highest downstream of the groyne tip between the bottom and z/D=0.83. Then they decay by more than twice in the top layer (0.83<z/D<1). This is confirmed by comparing the TKE distributions in a plane close to the free surface (z/D=0.95) and at mid-depth level (z/D=0.67), as shown in Figure 6.13b and 6.12c, respectively. In contrast, the TKE amplification upstream of the tip of the downstream groyne, related to the injection of patches of vorticity from the mixing layer, is larger near the free surface.

Analysis of the instantaneous and time-averaged data fields suggests that the flow inside the main gyre within the embayment is predominantly 2D. This is consistent with the shape of the energy spectrum of the transverse velocity component in Figure 6.14c at point C situated inside the eddy. The exact position of point C is shown in Figure 6.13b. The spectrum contains a -3 subrange along with a short Kolmogorov -5/3 inertial subrange. The presence of a -3 subrange is associated with the decaying of the large-scale quasi-2D structures. By comparison, the velocity spectra in the channel and inside the mixing layer (e.g., points A and B), shown in Figure 6.14a and 6.13b, contain only the -5/3 inertial range associated with a typical 3D turbulent flow. This form of the energy spectrum observed in the embayments is very similar to the one determined from experimental velocity measurements in shallow embayments by Engelhardt et al. (2004). One should also make the observation that in cases when the large scale eddies inside the

separated shear layer remain quasi 2D a -3 subrange is expected to be observed inside this region. However, because of the sudden change in bed elevation in the interface region, the flow becomes highly 3D in the present configuration and no such quasi 2D eddies are observed to form in the separated shear layer over the depth of the channel.

Figure 6.15 shows the mean transverse and vertical velocities, the 2D streamlines and the TKE in three spanwise sections cutting through embayment 5. The sections are situated close to the upstream wall (x/D=67.7), close to the middle of the embayment (x/D=70.4) and close to the downstream wall (x/D=73.1). The strong variations of the transverse velocity component in the streamwise direction and over the depth in the interface region are clearly visualized in Figure 6.15a-c. The thickness of the free surface layer where the mean transverse velocities are oriented toward the channel decreases as one goes from the upstream groyne toward the downstream groyne. Outside the embayment, the tranverse velocity maintains the same orientation in the thin free surface layer. On the other hand, even at x/D=67.7, the transverse velocity is oriented toward the embayment over the bottom half of the embayment in the interface section. By x/D=73.1, the transverse velocity in the interface region is oriented toward the embayment over most of the embayment depth. The change in the direction of the tranverse velocity inside the embayment (compare Figure 6.15a and 6.14c) is due simply to the change in the orientation of the velocity vectors in the large recirculation eddy (one gyre pattern). In all the sections, the vertical velocities are strongly amplified in the embayment interface region. The region on the embayment side where large vertical velocities are observed has a length of 1-1.5D. The maximum values of w and total surface of the regions where w is relatively high ($|w|>0.02U$) increase in the streamwise direction as one approaches the location of the downstream embayment wall (Figure 6.15d-f). By contrast,the TKE amplification in the interface region decays in the streamwise direction, as shown by comparing the distributions in Figure 6.15g-i. This is simply because of the strong detached shear layer forming downstream of the upstream

groyne head of each embayment. Past the initial one third of the embayment length, the TKE decay is relatively sharp in the DSL.

The combined effect of the transverse and vertical velocity distributions in the interface region and of the non-uniformity of v over the depth is to induce relatively strong secondary motions in these spanwise planes (e.g., see streamlines patterns in Figure 6.15j-l where several recirculation cells are present). These secondary motions can play an important role in the overall momentum and mass exchange between the embayments and the main channel.

6.3.3 Bed Shear Stress Distribution

LES has the advantage that it can provide information on the distribution of the mean and instantaneous distributions of the bed shear stress that are very difficult to evaluate from experiments. Knowledge of these distributions allows determination of the regions where scour will potentially occur. Designs can be evaluated using numerical simulation results to minimize the formation of scour.

Figure 6.16a-b shows the mean bed shear stress, τ, in embayment 5 and in the corresponding part of the main channel, respectively, nondimensionalized by the mean value of the bed shear stress in the incoming fully developed flow in the main channel, τ_0. In the main channel, τ/τ_0 peaks close to the interface in between the groynes. However, the amplification is only of the order of 10% compared to the mean value. In the embayment, the largest values of τ/τ_0 occur close to the downstream groyne starting at its tip. The largest mean values of the bed shear stress are of the order of $0.6\tau_0$ due to the smaller mean velocities in the embayment area. Given the mean sediment size encountered in the embayment region in rivers, these bed-stress values are often above the critical value for sediment entrainment.

The other interesting observation is that in the region where scour may occur inside the embayment, the instantaneous values of the bed shear stress can be much larger

than the mean values. For instance, in Figure 6.16c, the largest values of τ/τ_0 are larger than one. These variations are not due to the usual fluctuations associated with a turbulent flow. Rather, they are produced by the convection of large-scale eddies parallel to the downstream groyne. It is the passage of these eddies that are expected to play the main role in the development of the scour hole.

6.4. Mass Exchange Processes

6.4.1 General Description

The temporal evolution of the depth-averaged concentration contours in Figure 6.17 serves to illustrate the contaminant removal from embayment 5, its subsequent convection into the main channel and the secondary mass exchange between the channel and embayment 6. The main feature the concentration distributions have in common, past the initial stages of the contaminant removal process, is that the largest concentrations are always recorded in the center of the embayment, corresponding to the center of the main recirculation eddy. In this region, the TKE is low, the flow is quasi-2D and the residence times are very large compared to other regions inside the embayment. Consistent with the mean flow patterns, the reduction in the concentration levels up to 300D/U is largest in the downstream part of the embayment due to the continuous injection of patches of low-concentration fluid from the channel via the mixing layer and the interactions with the head of the downstream groyne. Conversely, the higher concentration fluid that is ejected by entrainment into the mixing layer close to the face of the upstream groyne is then convected past the downstream groyne of embayment 5.

As the flow hydrodynamics past embayments 5 and 6 are practically identical, patches of high vorticity fluid from the mixing layer are entrained into embayment 6 parallel and close to the downstream groyne in this embayment. The mixing layer contains patches of relatively high concentration fluid ejected from embayment 5. Part of

these patches (corresponding to total or partial clipping events) will be injected into the jet-like flow in embayment 6 (see Figure 6.17a). Again, the mixing inside embayment 6 is nonuniform, in the sense that the lowest concentration levels are consistently observed near the center regions until t~400-500D/U, when the small scale eddies mix most of the recirculated fluid within the embayment. For t>500D/U, the average concentration levels in embayment 6 start decaying, signifying that the mass of contaminant in embayment 6 starts decaying because the mass of contaminant ejected into the mixing layer from embayment 6 is larger than the one entrained into embayment 6 via the same mixing layer.

Figure 6.18 shows snapshots of the concentration distribution in a spanwise plane cutting around the middle of embayment 5. As expected, the largest values of the concentration are observed in the center region of the main recirculation eddy inside the embayment. Even in these regions, the concentration field is not exactly uniform over the depth, as smaller concentration values are observed near the bottom over the duration of the contaminant removal process.

Figure 6.19 gives more details on the variation of the instantaneous concentration fields at different levels within embayment 5. The concentration fields at t=380D/U show that the large scale features of the concentration distributions are similar at all depths in the embayment region. However, the main difference is that the concentration values are larger by about 20-30% inside the center of the main gyre close to the free surface compared to the corresponding values observed in sections situated close to the embayment bottom. Still, the depth-averaged distribution gives a good description of the concentration distributions at all levels within the embayment with the exception of the interface region.

The contour plots in Figure 6.18 clearly show that the non-uniformity of the concentration distribution over the depth is the largest for a length close to 1D on both sides of the interface region. This is also confirmed by the concentration distribution in

the interface plane shown in Figure 6.20 at two representative time instances (t=200D/U and t=500D/U) during the contaminant removal process.

The phenomena are qualitatively very similar for the contaminant removal process in embayment 2. The temporal evolution of the depth-averaged instantaneous concentration contours is shown in Figure 6.21. Figure 6.22 shows the instantaneous distributions at the free surface, and Figure 6.23 shows the instantaneous distributions in a plane parallel to the embayment bottom situated at a distance of 0.1D from it. As observed from comparison of Figure 6.17 and Figure 6.21, the depth-averaged concentration distributions at equivalent times after the start of the ejection process are similar in embayments 2 and 5 and in embayments 3 and 6, respectively. This will be confirmed quantitatively later when the temporal variation of the total mass of contaminant in these embayments will be analyzed. Of course, for the case in which the contaminant was introduced in embayment 2, there will be contaminant exchange not only with embayment 3, but also with all of the downstream embayments via the mixing layer in the region past embayment 2. As expected, the concentration fields in Figure 6.21 show that the amount of contaminant entrained into the downstream embayments decreases with the rank of the embayment. However, the process is qualitatively similar in all these embayments, as contaminant is predominantly entrained in the region close to the downstream groyne of each embayment and is ejected back into the mixing layer in the region close to the upstream groyne.

Another mechanism that is directly responsible for momentum and mass exchange between the embayment and the main channel is the presence of intermittent intrusions of channel fluid into the embayment. These intrusions develop close to the position of the sudden change in the bottom elevation and have time scales that are much smaller than the one associated with significant changes of the concentration distribution in horizontal planes inside the embayment. This is illustrated in Figure 6.24, where the free surface distributions in embayment 5 between t_0=205D/U and t_0+8D/U are quite

similar away from the interface. However, that is not the case for the concentration distributions on both sides of the interface as observed from Figure 6.25, in which the concentration fields are shown in a vertical spanwise plane situated toward the downstream end of embayment 5 cutting at the same time instances.

In Figure 6.25a, one can see that there is a sharp interface between the high and low concentration fluids associated with the embayment and the main channel. The interface is situated at that time instance on the channel side. In Figure 6.25b-c, the gradient across the interface decreases as local mixing becomes significant. Concomitantly, an intrusion of channel fluid starts penetrating into the embayment close to the embayment bottom. The intrusion on the embayment side attains its peak at $t= t_0+5D/U$. Then, the turbulent eddies and large scale motions in the interface region start mixing the higher concentration embayment fluid with the low concentration fluid that penetrated from the mixing layer, as illustrated in Figure 6.25e and 6.24f. The mixing process also takes place on the channel side of the interface, where the streak of high concentration observed in Figure 6.25a is stretched (see Figure 6.25c) and then mixes with the surrounding channel fluid. On the side containing the lateral embayment wall, a streak of high concentration fluid that penetrated close to the lateral wall is mixing with the lower concentration fluid convected parallel to the lateral wall by the jet-like flow inside the embayment. This process is also non-uniform over the depth of the embayment.

The intrusions are driven by the random formation of strong streaks of vorticity within the mixing layer that migrate laterally around the interface section. The vorticity magnitude field in the same spanwise section (x/D=73.1) at time $t=t_0$ (Figure 6.26a) shows the presence of a continuous streak of vorticity originating at the edge, where the bottom elevation changes, and ending at the free surface. Clearly, this streak delineates the region between the embayment fluid and the channel fluid at that instant of time, as seen by comparing Figure 6.25a and Figure 6.26a. At $t=t_0+2D/U$, the streak has detached

from the bottom edge. As in the mean flow field, the transverse velocity is on average toward the embayment (see corresponding contours in Figure 6.15c), and it is expected that low concentration channel fluid will start intruding into the embayment. Indeed, this is what is happening in Figure 6.25b. At $t= t_0+3D/U$ (Figure 6.26c), the original streak becomes oriented relatively parallel to the free surface, and a new streak is forming at the bottom of the embayment close to the interface. As no continuous vorticity streak is present across the embayment depth, channel fluid is expected to continue to be advected into the embayment. In this way, the size of the intrusion continues to grow in Figure 6.25c. By $t= t_0+5D/U$, the transverse extent of the intrusion has reached its maximum, and the embayment region close to the interface contains several large patches of vorticity. The length of the penetration on the embayment side is of the order of the total channel depth, D, and relatively close to that observed in the concentration contours in Figure 6.25. This region also corresponds to the area where large vertical velocities are observed in the mean flow, as shown in Figure 6.15f. The wide range of highly energetic vortices present in the intrusion region mixes the fluid. The process is highly three-dimensional. Most of the mixing takes place between $t= t_0+5D/U$ and $t= t_0+8D/U$, by which time the intensity of the vorticity patches in the interface region has decayed considerably. The vertical velocity distribution and the secondary flow patterns in Figure 6.15l strongly suggest that the sudden bottom elevation change at the interface is one of the main reasons for the formation of these intrusions. Examination of animations shows that though the occurrence of these intrusions is not periodic, their time scales are of the order of 5-20D/U.

The intrusion process takes place over most of the embayment length. The corresponding vorticity magnitude (Figure 6.27) and concentration (Figure 6.28) contour plots in a spanwise plane situated in the upstream part of embayment 5 (x/D=67.7) show that low concentration intrusions occur near the embayment bottom over practically the whole length of the embayment. The fluid intrusion peaks when patches of strong

vorticity magnitude do not obstruct the interface (e.g., see Figure 6.27b and Figure 6.27c). In the following two frames of Figure 6.27, the vorticity is strongly amplified in the interface region and the embayment and intrusion fluids mix. The embayment fluid starts pushing the mixed fluid back into the mixing layer in Figure 6.28f. Observe also that while inside the interior of the embayment the variation of the concentration fields over 8D/U is not significant (Figure 6.24), the contaminant distribution over the embayment depth is far from uniform.

The discussion of Figures 6.16 to 6.27 shows that 3D effects are predominantly found in the interfacial region while the flow inside the embayments away from the channel-embayment interface remains largely 2D with the exception of the jet like flow propagating close to the upstream groyne wall and then parallel to the lateral wall. It is highly probable that the presence of the sudden change in the bottom elevation in the interface region is responsible to a large degree for the large three-dimensionality of the flow in the interface region. It is this local effect that is responsible for the fact that most of the contaminant leaves the groyne field through the upper layer. It is expected that this phenomenon will be greatly reduced for configurations in which there is a mild variation between the water depths in the embayment and the main channel.

6.4.2 Temporal Variation of the Mean Contaminant Concentration within Embayments 2 and 5

The decay of the contaminant mass, or equivalently of the mean concentration, within embayments 2 and 5 is shown in Figure 6.29a. Past the initial stages of the removal process, the decay is very similar in both embayments. The experimental data of Uijttewall et al. (2001) is also shown. The comparison is quite good, especially for the higher rank embayments (e.g., embayment 5 from simulation and embayment 8 from experiment). Unfortunately, no estimation of the accuracy of the estimated mean concentration in the embayment was available from experiment to get a more precise idea

of how well the numerical solution predicts the experimental data. It is not clear if the differences observed in the experiment between embayments 2 and 5 are due to the scatter associated with the method (Uijttewaal et al., 2001, concludes that the differences between the contaminant decay in the various embayments of this experiment are hardly significant) or to differences in the mixing layer characteristics along the interface of the two embayments. The simulation results suggest that the effect of the embayment rank on the overall contaminant ejection process is very small.

Similar to the analysis performed in the previous two chapters, dead-zone theory models are employed to characterize the contaminant ejection process for the present geometry in which the depth of the embayment is not constant and the mean depth is smaller than the main channel depth. Again, by assuming the rate of decay of the mean concentration inside the embayment, M, is proportional to the mean concentration difference between the embayment and the channel, M_r (=0 in the present case where the main channel is assumed to have a very large volume compared to the embayments), one can write the following global mass conservation equation (see also Uijttewall et al. 2001):

$$l\,w\,a_m \frac{\partial M}{\partial t} = -k\,l\,a_i\,U\left(M_r - M\right) \tag{6.1}$$

where k is the dimensionless exchange coefficient. Equation (6.1) can be rewritten as:

$$\frac{\partial M}{\partial t} = -\frac{1}{T}\left(M_r - M\right) \tag{6.2}$$

where the characteristic time constant T is obtained from eqn. (6.1):

$$T = \frac{a_m w}{a_i U k} \tag{6.3}$$

As in the previous two test cases, the constant, T, is determined by measuring the decay of the mean concentration inside the embayment experimentally or numerically. Equation (6.3) is then used to estimate *k* (=6.25D/TU in the present case. The definition

is not identical to the one used in the previous chapters to make our analysis consistent with the way the experimental results were presented in the paper by Uijttewaal et al., 2001). The numerical simulation results suggest that there is a change in the slope of the decay around t=550D/U (t~180s) in both embayments. This change of slope, around t~180s, is also suggested by the decay observed in experiment, especially in embayment 8. In both experiment and simulations, the decay rate is smaller in the later stages of the removal process.

In the case of the numerical simulations, the inferred values of the nondimensional exchange coefficient are k=0.018 over the initial phase and k=0.014 over the final phase of decay. Over the initial phase of decay in which about 75% of the initial mass of contaminant leaves the embayment, the corresponding values inferred from the experimental data are k=0.016 for embayment 8 and k=0.013 for embayment 2. The removal of contaminant from an embayment (emerged groynes) in which a one gyre circulation pattern is observed can be characterized by the presence of two distinct regimes over which the mean concentration decay is exponential, but the value of the global mass exchange coefficient is different. This is consistent with the field measurements in irregular embayments of the River Elbe conducted by Engelhardt et al. (2004) and with the results in the previous two chapters for single embayment geometry in a straight channel. Engelhardt et al. (2004) related the presence of different exponential decay regimes to the fact that the mixing inside the embayment is characterized by multiple mean residence times.

Figure 6.29b further details the decay of the mass of contaminant within the embayment by considering separately the temporal evolution of the mean concentration in the top, middle and bottom embayment layers. All three layers have equal volumes, and the interfaces between the three layers are horizontal. The mean exponential decay associated with the full embayment volume over the initial phase starts at t~100D/U in the middle and top layers and at t~140D/U in the bottom layer. Before that, the values of

k in the three layers are somewhat variable. Figure 6.28c gives the values of k estimated from the mean concentration curves in each layer. The change in slope around t=600D/U occurs in all the three layers.

6.4.3 Non-Uniformity of the Mass Exchange Process over the Embayment Depth

More details on the dynamics of the contaminant transport among the different layers and between the embayment and the main channel can be inferred from Figure 6.30 in which the interface fluxes (F1, F2 and F3), the flux between the bottom and middle layer (F4) and the flux between the middle and top layer (F5) are plotted along with the rates of change (positive if mass leaves the embayment) of the contaminant mass within the top, middle and bottom layers (-MT1, -MT2, -MT3). The interface fluxes are considered positive when the transport is from the embayment toward the channel, while F4 and F5 are positive when they are oriented toward the free surface.

In embayment 1, F1 is always positive and has the largest magnitude compared to F5 and –MT1. The variation of F5 is strongly correlated to that of F1 at most times, in the sense that they increase and decrease in a similar way. The mean levels of -MT1 and F5 over large time scales are comparable. This means that much of the fluid exiting the embayment through the top layer of the embayment-channel interface is due to contaminant being advected from deeper levels. The rate of change of the mass inside the top embayment is positive at most times, though several short periods are observed when $-MT1<0$ because the influx of contaminant from the middle layer is slightly higher than the flux leaving the top layer through the channel-embayment interface.

In the bottom layer, the flux through the interface changes direction fairly regularly, which means that contaminant from the mixing layer along the embayment length is sometimes re-entrained inside the embayment, especially past the upstream groyne region. This is mostly because, as shown in Figure 6.12a, the mean transverse

velocity in the interface region is oriented toward the embayment. Thus, very little contaminant leaves the embayment through the bottom part of the embayment-channel interface (see also discussion of Figure 6.31). Most of the mass decay within this layer is due to the flux advected vertically toward the middle layer (F4). There are brief periods of time when F4<0. Over the time periods when contaminant is advected back into the embayment through the channel-embayment interface, the flux through the interface between the bottom and middle layers increases substantially. When F3>0, at most times F4 is larger than F3, meaning that most of the decay in the mass of contaminant inside the bottom layer is due to the flux of contaminant through the top interface.

In the middle layer, the flux of contaminant leaving the embayment through the middle part of the channel-embayment interface (F2) is significant at most times. However, the flux from the bottom layer F4 is positive over large periods of time, and its magnitude is comparable and many times higher than that of F2, especially for t<120D/U. The largest flux is the one toward the top layer, F5. Its variation is similar to that of F4, especially for t<200D/U. This means there is a general upwards motion of the contaminant from the bottom layer toward the top layer. As the rate of decay of the mass of contaminant inside the middle layer, -MT2, is generally close to or smaller than F2, on average some of the contaminant situated initially in this layer is also advected upwards toward the top layer (see also discussion of Figure 6.31). This is consistent with the fact that at most times F5>F4.

Figure 6.30 shows there is a clear advection of contaminant from the bottom of the embayment toward the top layer. This is also confirmed in a quantitative way by the temporal evolution of the cumulative mass of contaminant exiting the embayment volume through the top, middle and bottom layers of the interface. The values in the line plots in Figure 6.31 are non-dimensionalized by the initial mass of contaminant inside the embayment, $M_0=40.31D^3C_{0,}$ where C_0 is the initial concentration of the contaminant. The results for embayment 5 are shown with the continuous line. The cumulative mass

advected at t=800D/U, when about 90% of the initial mass of the contaminant has left the embayment volume, through the bottom layer of the interface is about 13 times smaller than the one advected through the top layer. At t=800D/U, about 66% of the initial mass left the embayment through the top layer, 20% through the middle layer and only about 4% left through the bottom layer. Thus, very little of the contaminant situated initially inside the bottom layer left the embayment through the corresponding bottom interface layer. Even in the case of the middle layer, only about two thirds of the contaminant initially present inside this volume left through the corresponding middle interface layer. By contrast, more than twice the initial mass of contaminant initially situated inside the top layer left the embayment through the top interface layer. This is consistent with the mean distribution of the transverse velocity in the interface region.

The process is similar regardless of the rank of the embayment. For instance, in the case of embayment 2 (dashed lines in Figure 6.31), the only difference is that the amount of contaminant ejected through the middle layer of the interface is slightly higher than the one in embayment 5. At t=800D/U, 27% of the initial mass of contaminant left embayment 2 through the middle layer interface, compared to only 20% in the case of embayment 5. Compared to embayment 5, the cumulative mass in the top and bottom layers of embayment 2 at the same time instance is smaller by about 4% in the top layer and by about 3% in the bottom layer.

6.4.4 Mass Transport through the Channel

Figure 6.31b-d shows temporal variation of the width-averaged concentration profiles at different spanwise locations (see Figure 6.32a) in between the embayments (x/D=42, immediately past embayment 2, x/D=65, immediately past embayment 4) and at a location (x/D=100) past the groyne field at several time instances (100D/U<t<800D/U) for the case in which the contaminant was introduced in embayment 2. These time instances are labeled with numbers (1 to 8) in the line plots in

Figure 6.32 to make it easier to follow the vertical distribution of the width-averaged profiles in time. The corresponding concentration distributions in these spanwise sections at the same time instances are shown in Figure 6.33 to Figure 6.35. They contain information on the lateral extent of the contaminant cloud over and past the groyne region, maximum and mean concentration values in these sections, etc

This information on the spatial and temporal distribution of the concentration within the main channel as the cloud of contaminant is advected out of one of the embayments and then disperses into the main channel and the downstream embayments is important for pollution studies in cases in which the contaminant could be harmful to the river. For example, knowledge of the spatial and temporal distributions of the contaminant levels in the channel can be used to estimate the regions where the concentration levels are above the allowed values and the period over which they will remain above these values.

In the section at x/D=42, the largest width-averaged concentrations are observed near the free surface. This is to be expected, as the section is situated just downstream of embayment 2, from which the contaminant is convected into the main channel primarily through the top layer of the embayment-channel interface. As shown in Figure 6.33, the contaminant cloud intrudes laterally over a distance of about 1.5D into the channel. The largest concentration levels in that section are close to 0.5 and occur for $t<200D/U$. In the later stages of the removal process, the concentration becomes more uniformly distributed inside the intrusion both laterally and vertically, as also observed in profiles 4 to 8 in Figure 6.32b.

Several qualitative changes are observed in the distribution of the width-averaged concentration profiles in the section situated at x/D=65. For $200D/U<t<600D/U$, the concentration distribution over the depth appears to be close to linear with a mild slope corresponding to slightly higher values near the free surface. For $t>600D/U$, the width-

averaged concentration away from the free surface (profiles 7 and 8) is practically constant.

The mean levels in the profiles at t=100D/U and t=200D/U are comparable. However, the concentration distribution in this section at the two time instances is very different (Figure 6.32a-b). At t=100D/U, the cloud of contaminant intrudes less laterally compared to t=200D/U, but the concentration levels are sensibly higher (maximum values around 0.2), especially near the channel-embayment interface. Interestingly, the maximum lateral intrusion of the contaminant cloud is observed at t=200D/U (~3.7D). By t=400D/U, the concentration distribution inside the contaminant cloud is relatively uniform in both directions. The mild slope in the width-averaged profiles at t>400D/U is due primarily to the interface between the cloud of contaminant and the channel fluid that is tilted such that the width of the intrusion is about 1.3D larger at the free surface than at the channel bottom.

It appears that past the groyne field region (e.g., at x/D=100), the form of the width-averaged concentration profiles varies very little in time (at least over the duration over which most of the contaminant is convected through that section). For t<600D/U, the width-averaged concentration can be approximated as linear, with the largest values occurring at or near the free surface. Between t=100D/U and t=400D/U, very little variation is observed among the width-averaged profiles at all depths. The lateral extent of the intrusion in this section is close to 6D (see Figure 6.35) due to the lateral dispersion of the contaminant cloud as it is advected downstream. For t>400D/U, the contaminant appears to be well-mixed vertically over the first 1.5D from the lateral wall on the groyne field side. For t>600D/U, the width-averaged concentration is practically constant for z/D<0.6. The mild slope observed in the width-averaged concentration profiles is due to slightly larger concentration values observed near the free surface away from the lateral wall and to the tilting of the interface between the cloud of contaminant and the channel fluid. These trends are consistent with the expected dispersion of a cloud of contaminant

advected into a shallow channel where the contaminant is expected first to mix vertically and then laterally.

The temporal evolution of the amount of contaminant present in each of the embayments in shown in Figure 6.36. There is a significant amount of contaminant that is entrained into embayments 3 to 6 as the contaminant is ejected from embayment 2. For example, the amount of contaminant present inside embayment 3 can be as high as 8.5% of the total amount of contaminant introduced into embayment 2. This maximum occurs at t~250D/U. As the embayment rank increases, the maximum amount of contaminant mass present in that embayment is smaller and the maximum occurs later. For example, in the case of embayment 4, the maximum percentage is close to 5.5% and is observed around 340D/U. In the same figure, the orange curve corresponds to the total mass of contaminant present in the channel (supposing the channel has infinite length downstream of the groyne field).

The dashed red curve corresponds to the amount of contaminant in the channel that has left the groyne field region (x/D>100). The total mass of contaminant in the channel increases rather sharply between t=0D/U and t=100D/U as most of the contaminant leaves embayment 2 to enter the channel. Then the slope decreases sharply for about 30D/U as a substantial part of the contaminant from the channel is advected into embayments 3 to 6. Over this period, the flux of contaminant entering the channel via the embayment 2 interface is only slightly higher than the sum of the fluxes of contaminant from the channel to embayments 3 to 6. Then, for 130D/U<t<500D/U, the rate of growth of the amount of contaminant present in the channel is relatively constant as the net flux of contaminant from the channel to embayments 3 to 6 is either small or negative (contaminant leaves these embayments and enters the main channel). The maximum percentage of the amount of contaminant present in embayments 3 to 6 at a given moment is equal to about 20%. These peak values are observed between t=200D/U and t=300D/U. The mass of contaminant that left the groyne field area is practically

equal to zero until t~100D/U when the upstream part of the pollutant cloud reaches the end of the groyne field region.

The mass of contaminant past x/D=100 increases sharply until 180D/U. Then, the rate of growth decreases to values that are close to or slightly higher than the ones observed for the variation of the amount of contaminant present in the whole channel. Between t=400D/U and t=800D/U, the difference decreases from about 20% to less than 10%. This represents the amount of contaminant present inside the main channel in the groyne field region.

6.5. Summary

The mean velocity and r.m.s. velocity fluctuations at the free surface were found to be in good agreement with the experimental results. The analysis of the hydrodynamics allowed inferences of several important consequences related to mass transfer phenomena.

As expected, the flow inside the shallow embayments (aspect ratio w/l=0.7) was shown to have a strong 2D character, and a one-gyre circulation pattern was observed consistent with experiment. The predominant 2D character was also confirmed by the transverse velocity spectra inside the main recirculation region that contained a -3 subrange associated with quasi-2D shallow flows. However, the intensity of the secondary motions and the importance of 3D effects in the region close to the embayment-channel interface were shown to be more important than originally thought.

The bed shear stress inside the cavity was found to peak in the region close to the downstream groyne of each embayment and to show a high variability around the mean values due to the interaction of the mixing layer eddies with the head of the groynes and their convection parallel to the groyne wall.

The transverse velocity distribution was found to be strongly non-uniform over the depth at the embayment-channel interface. The flow in the top layer was found to be

oriented predominantly toward the channel, while the flow at the deeper levels was oriented predominantly toward the embayment. Consistent with these trends in the distribution of the mean transverse velocity, it was found that most of the contaminant introduced inside the embayment will leave the embayment volume close to the free surface. The amount of contaminant leaving the embayment through the bottom third of the interface section was estimated to be 12 times lower than the amount leaving through the top layer. This amount accounted for about 70% of the total mass of contaminant initially present inside the embayment. Comparatively, the mass leaving through the middle layer interface accounted for about 24% and the bottom layer for the remaining 6%. This is consistent with the observed presence of a mean upward circulation of contaminant within the embayment.

The transverse velocity distribution in the interface also explains why the mass exchange coefficients are overestimated when they are predicted using methods that employ floating particles as a tracer. In fact, the predicted mean transverse velocity close to the free surface was found to agree with the value estimated from experiments needed to account for the difference in the global mass exchange coefficients determined using floating particles and depth-averaged concentration fields.

Related to the strong three-dimensionality of the flow and contaminant distribution in the interface region, it was found that strong vortical eddies are formed, stretched and then destroyed on both sides of the channel-embayment interface. During this process, low-concentration channel fluid can penetrate laterally inside the embayment over distances of the order of the total channel depth before being mixed with the embayment fluid by the small scale turbulence. The process was found to be random, though the time scales associated with these intrusions were estimated to be of the order of 5-20D/U.

The other phenomenon responsible for momentum and mass exchange between the fluid inside the main recirculation eddy and the channel fluid was the injection of

patches of high-vorticity, low-concentration mixing layer fluid into the embayment in the form of a wall-attached jet-like flow parallel to the downstream groyne and then to the sidewall. The intensity of this jet-like flow was strongly modulated by the injection of these energetic coherent structures. As they were convected parallel to the embayment walls, these eddies mixed with the higher-concentration fluid from the edge of the main recirculation region.

For the embayments situated downstream of the one where the contaminant was introduced, there is substantial mass exchange between the mixing layer containing higher concentration fluid and the lower concentration fluid inside these embayments. For example, the maximum value of the total amount of contaminant mass that was present inside embayments 3 to 6, for the case in which the contaminant was introduced into embayment 2, was found to be close to 20% of the total initial mass of contaminant and to considerably slow the overall advection of the cloud of contaminant past the groyne field region.

The mechanisms of mass exchange are similar to the ones responsible for ejection of contaminant from the embayment in which the contaminant was initially introduced. In particular, the interactions between the mixing layer eddies containing relatively high-concentration, high-vorticity fluid and the downstream groyne of each of these embayments were identified as the main mechanism through which the contaminant ejected into the channel is entrained into the higher rank embayments. At a certain point, the mass exchange process in these embayment reverses, in the sense that on average more contaminant is leaving these embayments than is entering through the corresponding channel-embayment interface. This transition occurs after most of the contaminant is ejected from the embayment in which the contaminant was originally introduced and occurs at a later time in each successive embayment. The numerical simulation results suggest that the mass decay is very slightly dependent on the embayment rank. The decay of the contaminant in the embayment in which it was

initially introduced appears to be exponential, but there is a small change in the corresponding exchange coefficient (decay rate) close to 550D/U when about 20% of the initial mass of contaminant is left inside the cavity. This change in the decay rate is also present in the experimental data obtained at embayment 8 by Uijttewaal et al. (2001). It is also consistent with previous LES investigations of the flow and mass exchange processes in a channel with a single embayment (see Chapter 4) and with the results of the field study conducted by Engelhardt et al. (2004). In all these studies, a one-gyre circulation pattern was observed inside the relatively high aspect ratio embayments. The inferred value of the non-dimensional mass exchange coefficient over the initial phase of decay, k=0.018, was found to be close to the values determined based on experimental measurements of the mass decay in embayments 2 (k=0.016) and 8 (k=0.013).

The LES database was used to better understand the way the contaminant cloud is advected and disperses inside the main channel. This detailed information allows estimation of the concentration distribution within the channel, the lateral extent of the pollutant cloud and the time periods and spatial extent of the regions where the concentration values are above the threshold values corresponding to environmental policy. It was found that in the main channel past the embayment region, the width-averaged concentration profile appeared to be relatively linear over the depth, with largest concentrations present near the free surface. This was due to both the tilting of the lateral interface between the contaminant cloud and the main channel, and to the slightly higher concentrations present in the layer close to the free surface as a result of the fact that most of the contaminant leaves the embayment close to the free surface.

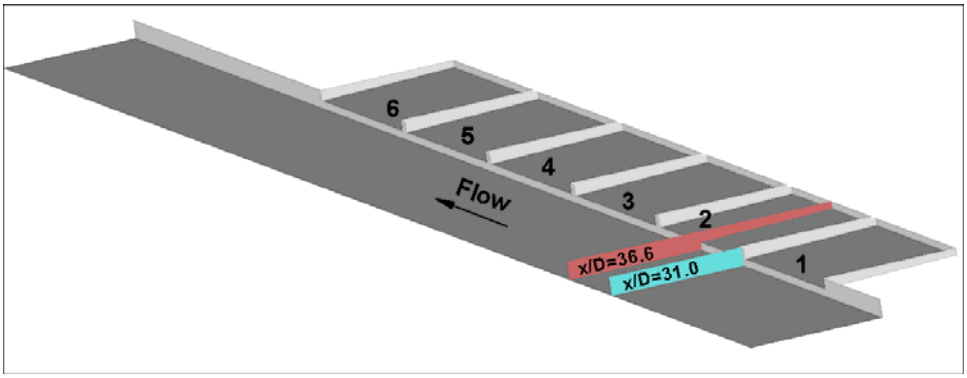

Figure 6.1. Sketch showing computational domain with six shallow embayments on one side; the position of two cross sections is also shown.

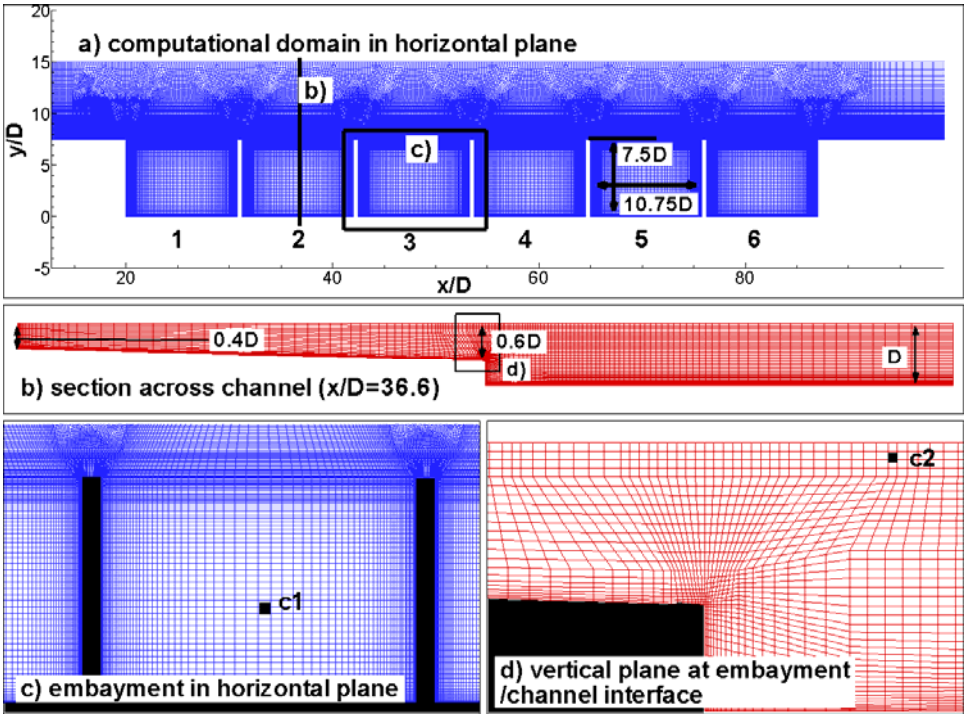

Figure 6.2. Computational mesh. a) mesh in a horizontal plane near the free surface; b) mesh in a vertical cross-section cutting through the embayment; c) detail showing horizontal mesh within one embayment; d) detail showing vertical mesh around the channel-embayment interface.

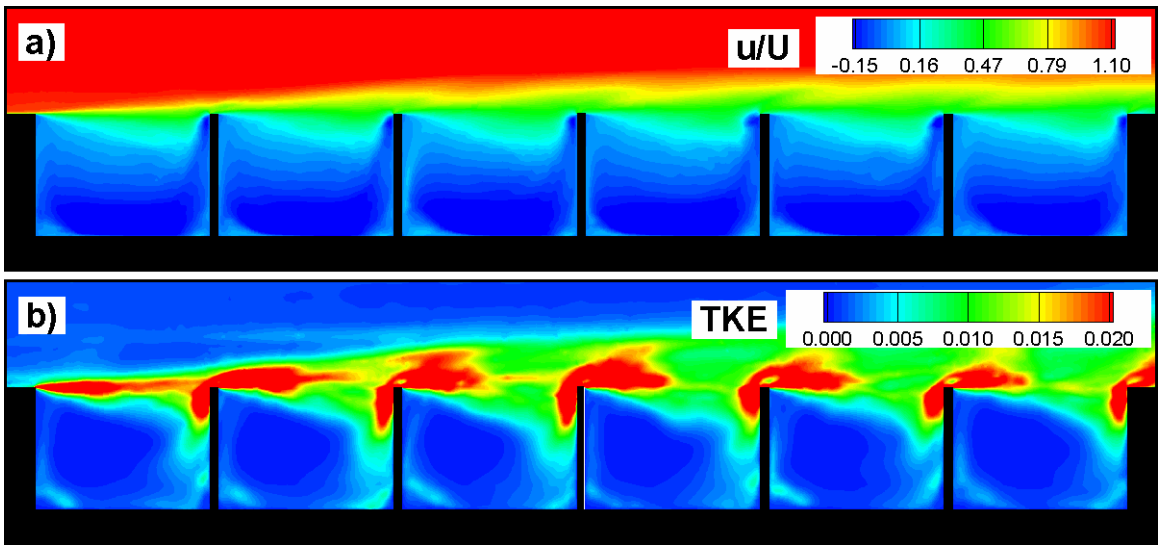

Figure 6.3. Distributions of mean flow variables in a plane near the free surface (z/D=0.95). a) streamwise velocity; b) TKE.

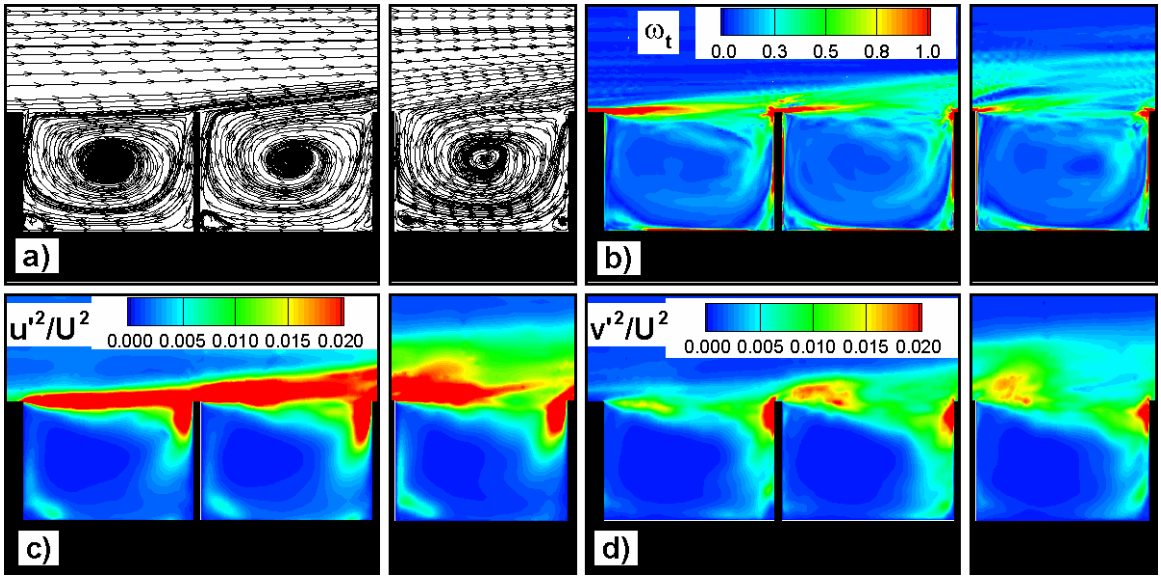

Figure 6.4. Effect of the embayment rank on the mean flow in a plane near the free surface (z/D=0.95). Embayments 1, 2 and 6 are shown. a) 2D streamlines; b) total vorticity magnitude; c) $\overline{u'^2}/U^2$; d) $\overline{v'^2}/U^2$.

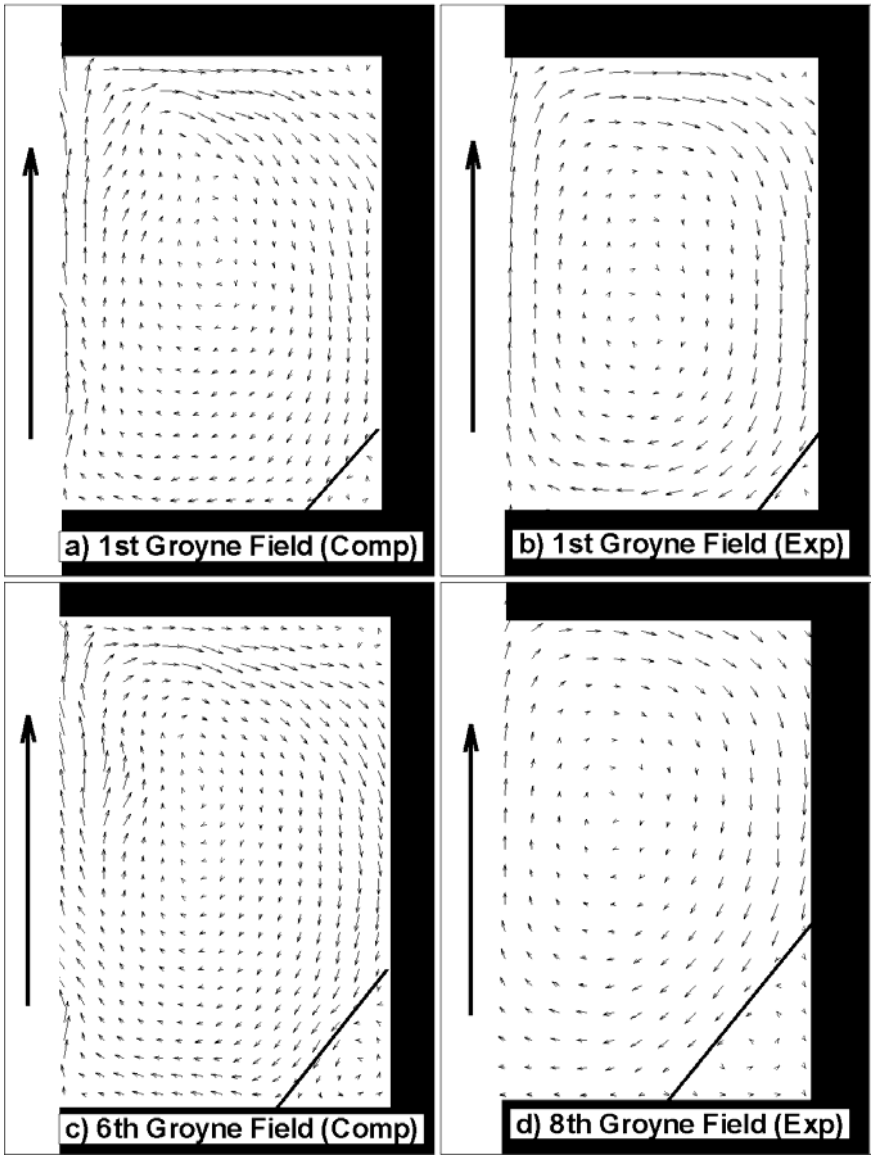

Figure 6.5. Comparison between predicted (a, c) and measured (b, d) mean velocity vectors at the free surface inside the first embayment and inside one of the higher rank embayments.

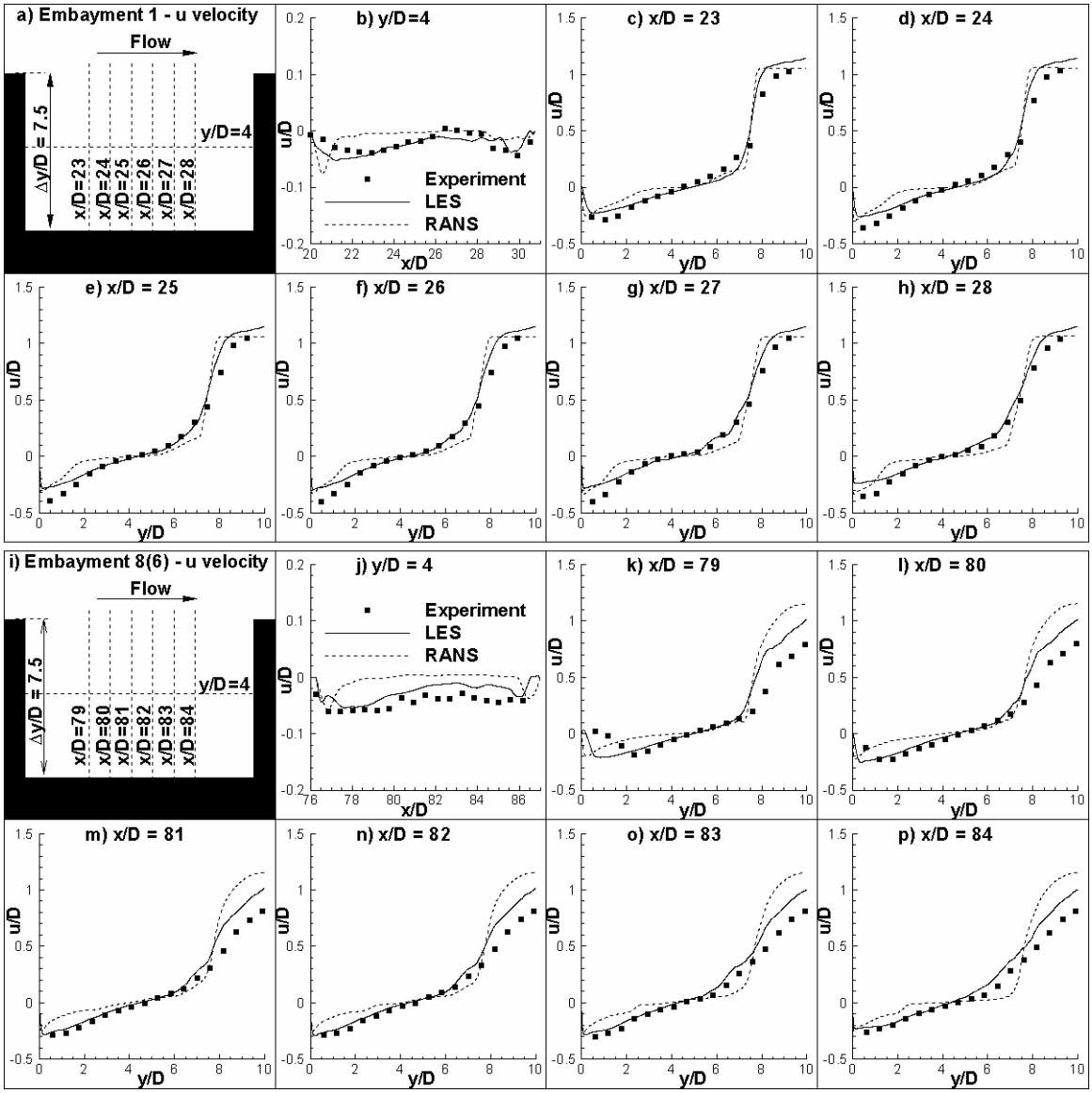

Figure 6.6. Comparison between numerical predictions (continuous line) and experiment (symbols) for the streamwise velocity profiles, u/U, in embayment 1 (frames b-h) and embayment 6 (frames j-p). The position of the sections is shown in frames a and i, respectively.

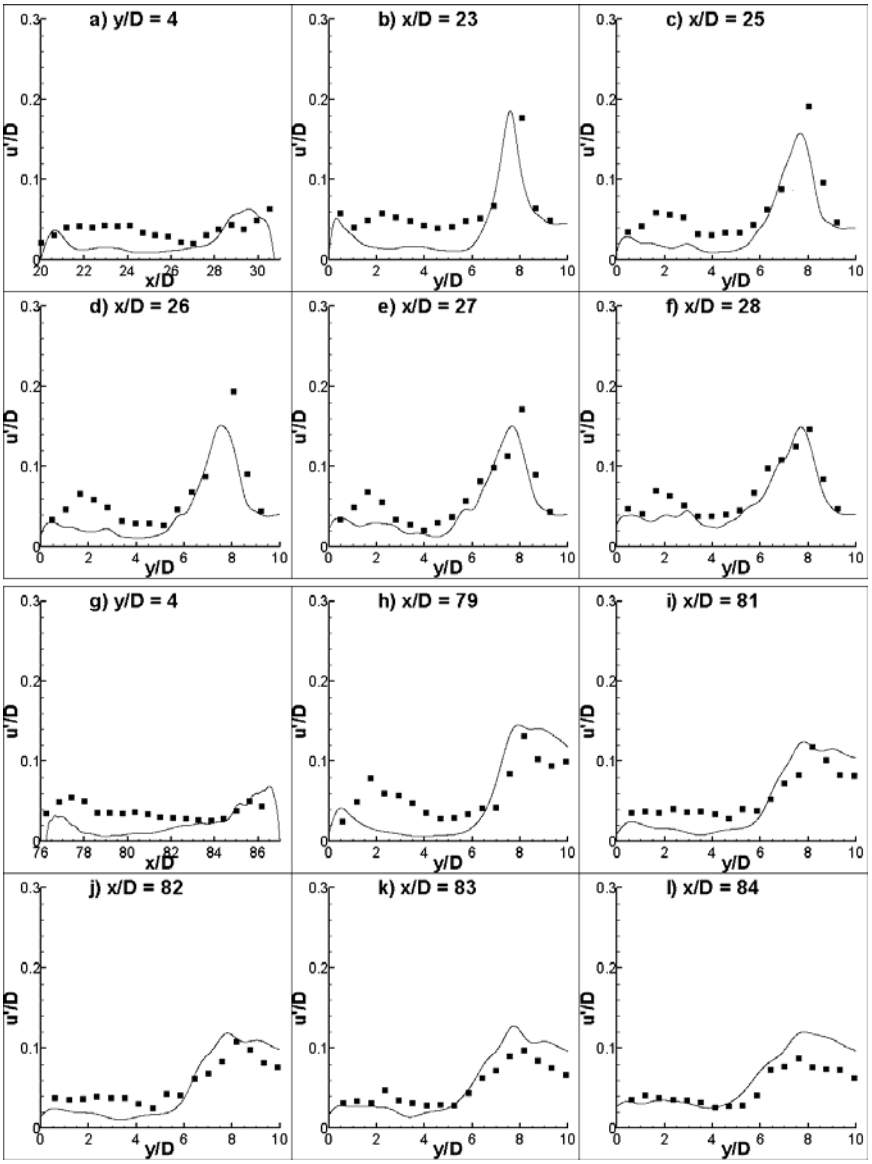

Figure 6.7. Comparison between numerical predictions (continuous line) and experiment (symbols) for the r.m.s. of the streamwise velocity fluctuations in embayment 1 (frames a-f) and embayment 6 (frames g-l). The position of the sections is shown in frames a and i in Figure 6.5.

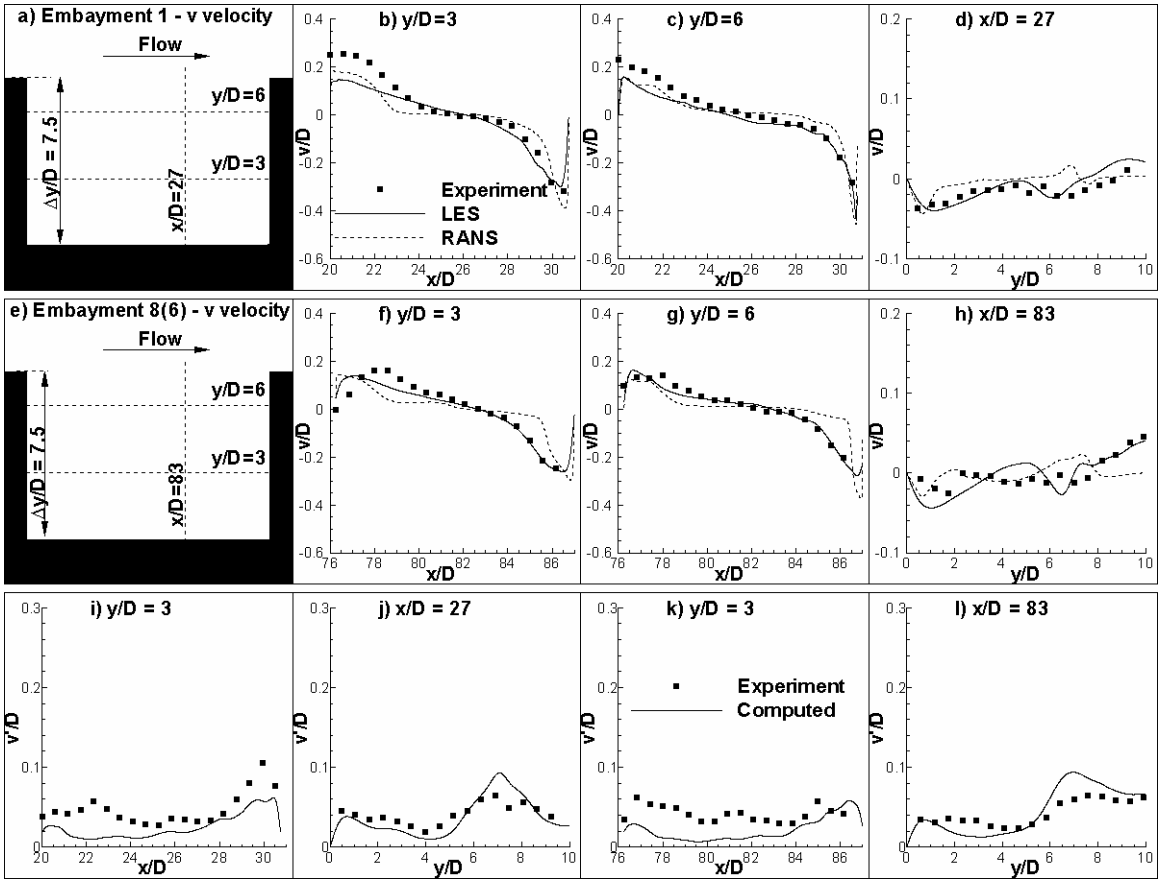

Figure 6.8. Comparison between numerical predictions (continuous line) and experiment (symbols) for the transverse velocity, v/D, and transverse r.m.s. velocity fluctuations, v'/D, in embayment 1 (frames b-d and i-j) and embayment 6 (frames f-h and k-l). The position of the sections is shown in frames a and e, respectively.

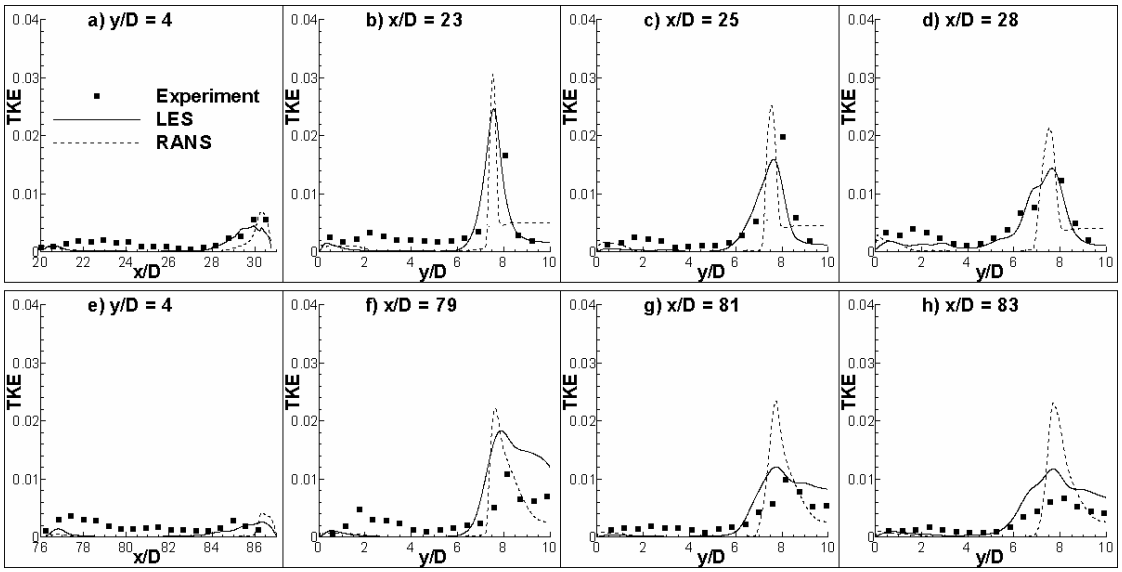

Figure 6.9. Comparison between numerical predictions (continuous line) and experiment (symbols) for TKE in embayment 1 (frames a-d) and embayment 6 (frames e-h). The position of the sections is shown in Figure 6.5.

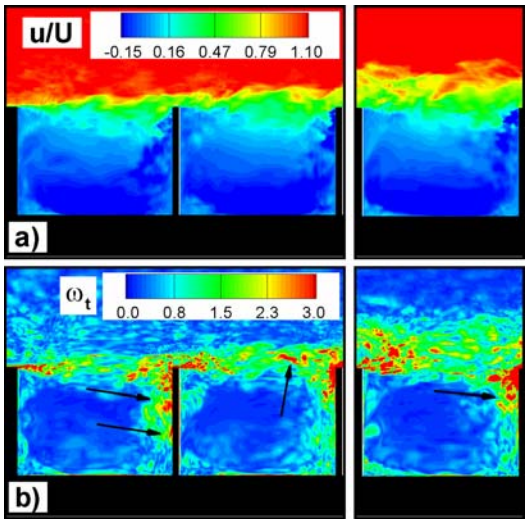

Figure 6.10. Visualization of instantaneous flow in a plane near the free surface (z/D=0.95). Embayments 1, 2 and 6 are shown. a) streamwise velocity; b) total vorticity magnitude.

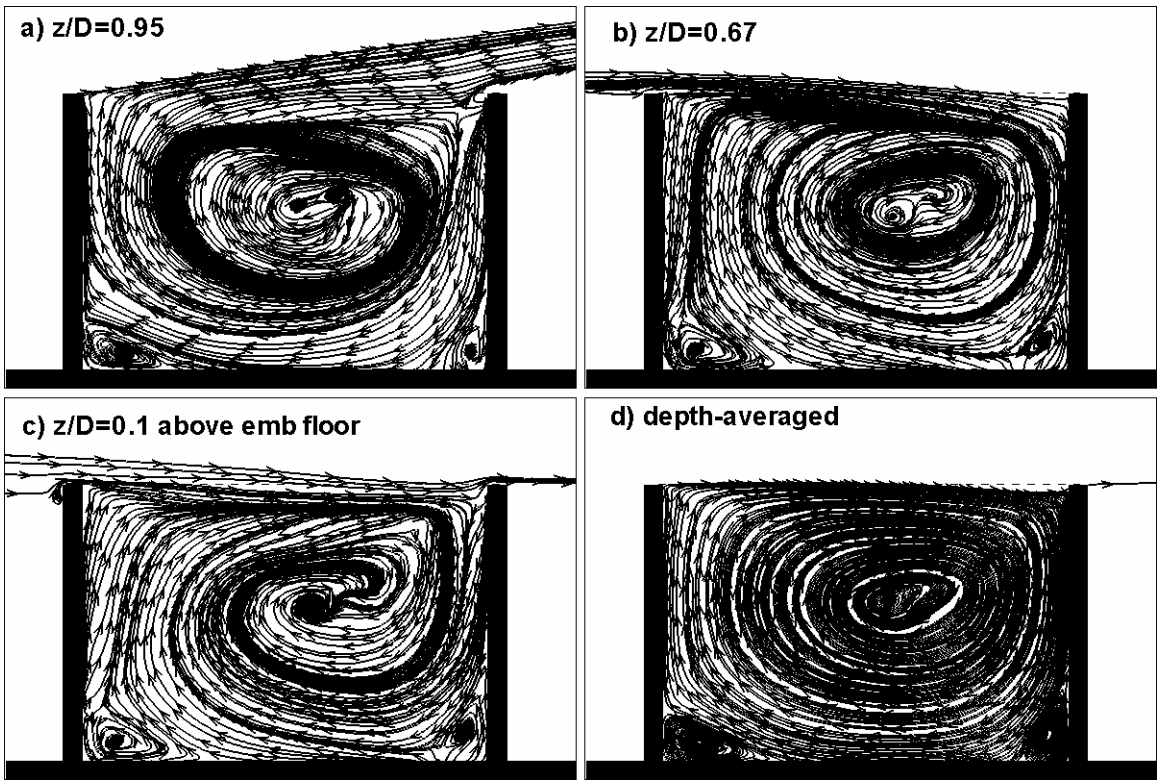

Figure 6.11. Mean 2D streamlines in embayment 5. a) z/D=0.95; b) z/D=0.67; c) at a distance of 0.1D from the embayment bottom; d) depth-averaged.

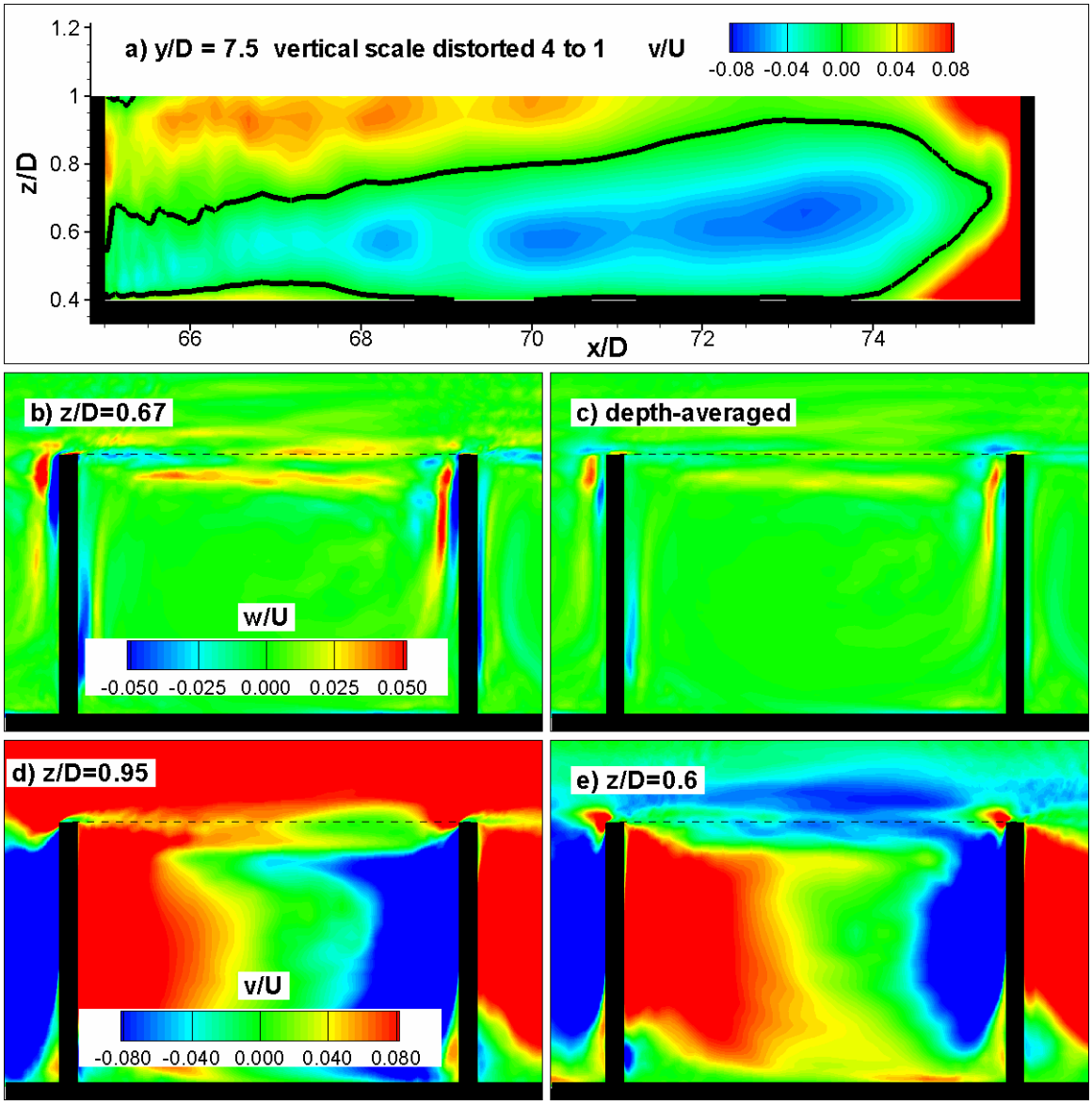

Figure 6.12. Velocity distribution in embayment 5. a) transverse velocity at the channel-embayment interface (scale is distorted 4:1 in the vertical direction); b) vertical velocity at z/D=0.83; c) depth-averaged vertical velocity; d) transversal velocity (z/D=0.95); e) transversal velocity (z/D=0.60).

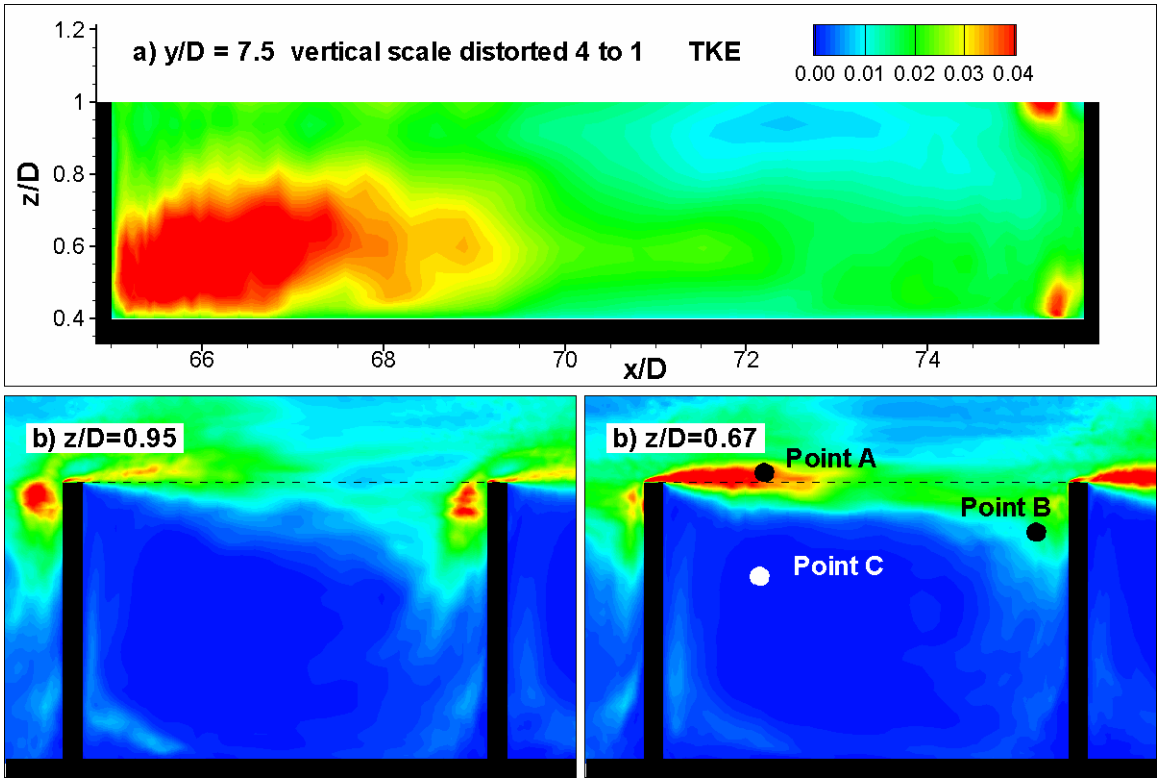

Figure 6.13. TKE distribution in embayment 5. a) channel-embayment interface (scale is distorted 4:1 in the vertical direction); b) z/D=0.95; c) z/D=0.67.

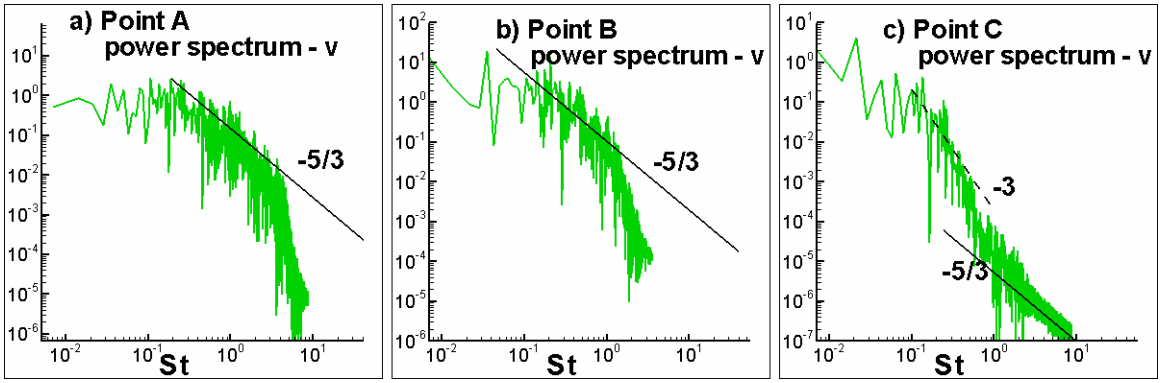

Figure 6.14. Power spectra of transversal velocity at several points situated near mid-depth level in embayment 5. a) Point A; b) Point B; c) Point C. Position of points is shown in Figure 6.12c.

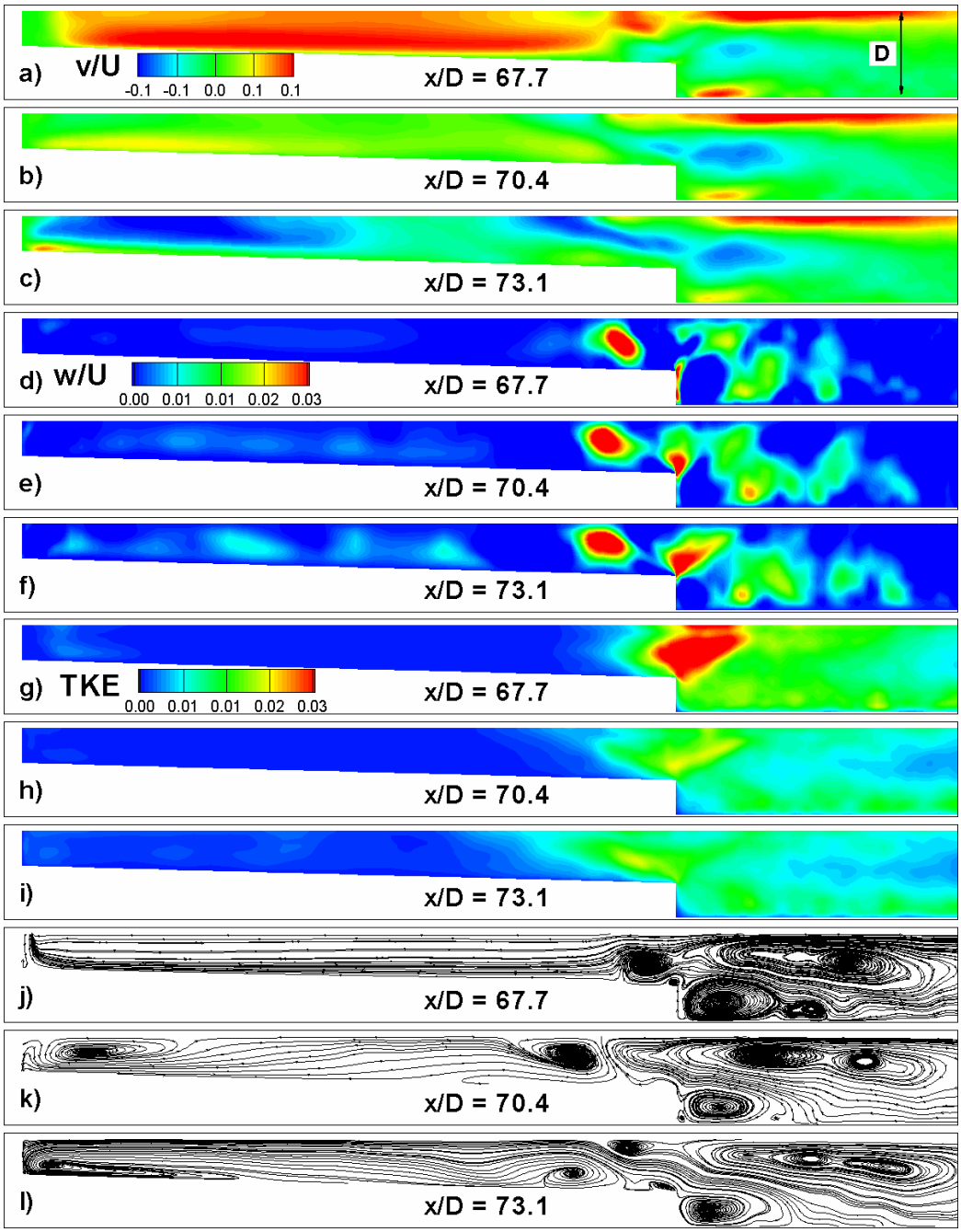

Figure 6.15. Visualization of the mean flow variables in crosswise sections cutting through embayment 5. a) v/U, x/D=67.7; b) v/U, x/D=70.4; c) v/U, x/D=73.1; d) w/U, x/D=67.7; e) w/U, x/D=70.4; f) w/U, x/D=73.1; g) TKE, x/D=67.7; h) TKE, x/D=70.4; i) TKE, x/D=73.1; j) 2D streamlines, x/D=67.7; k) 2D streamlines, x/D=70.4; l) 2D streamlines, x/D=73.1.

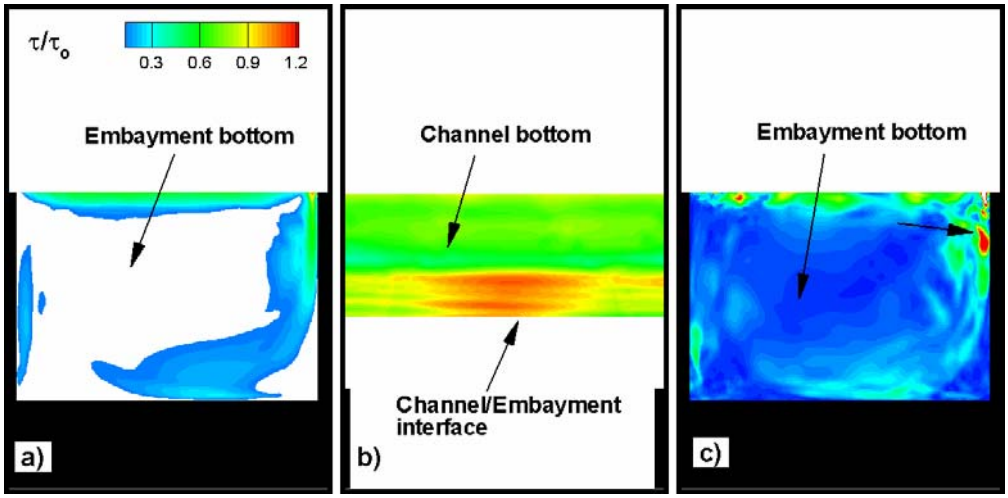

Figure 6.16. Bed shear stress distributions, τ/τ_0, in the region corresponding to embayment 5. a) mean distribution inside embayment; b) mean distribution inside channel; c) instantaneous distribution inside embayment.

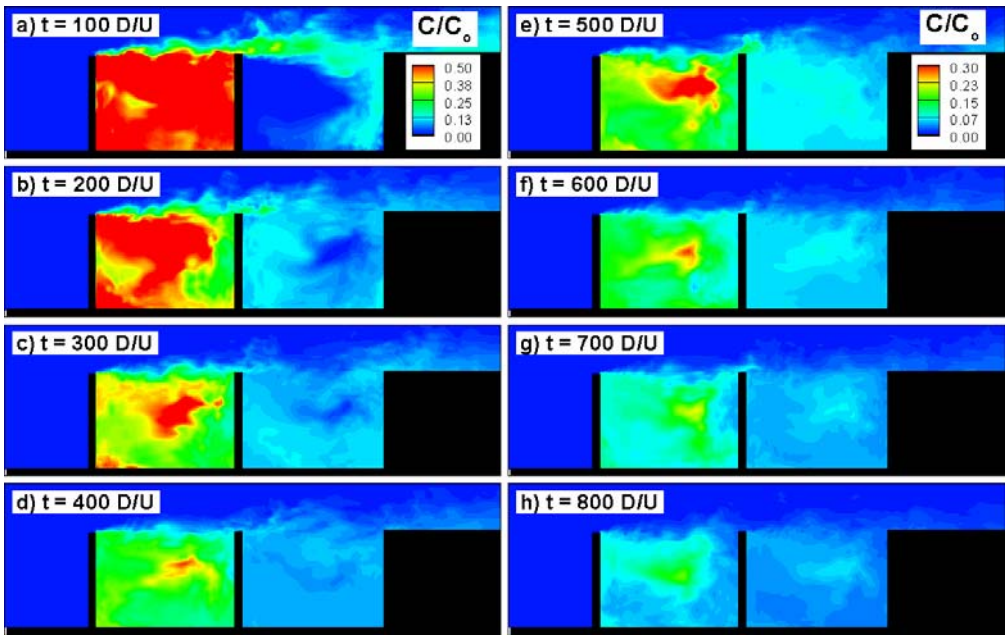

Figure 6.17. Depth-averaged contours of contaminant concentration around embayment 5 (contaminant is introduced initially into embayment 5). a) t=100D/U; b) t=200D/U; c) t=300D/U; d) t=400D/U; e) t=500D/U; f) t=600D/U; g) t=700D/U; h) t=800D/U.

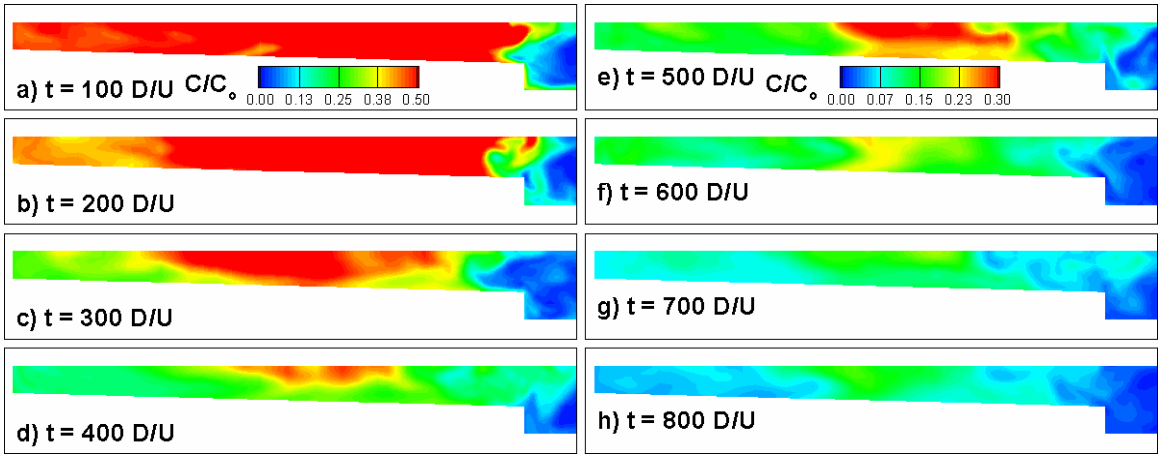

Figure 6.18. Contours of contaminant concentration in a spanwise section (x/D=70.4) situated near the mid-length of embayment 5 (contaminant is introduced initially into embayment 5). a) t=100D/U; b) t=200D/U; c) t=300D/U; d) t=400D/U; e) t=500D/U; f) t=600D/U; g) t=700D/U; h) t=800D/U.

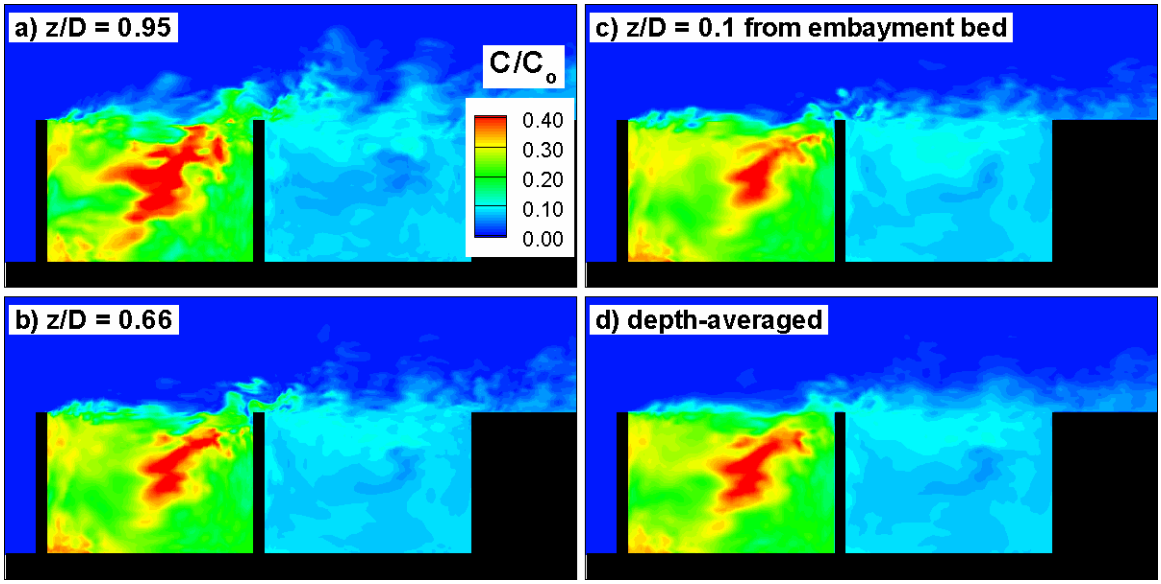

Figure 6.19. Contours of contaminant concentration at t=380D/U around embayment 5 (contaminant is introduced initially into embayment 5). a) z/D=0.95; b) z/D=0.66; c) z/D=0.1 from the bed; d) depth-averaged.

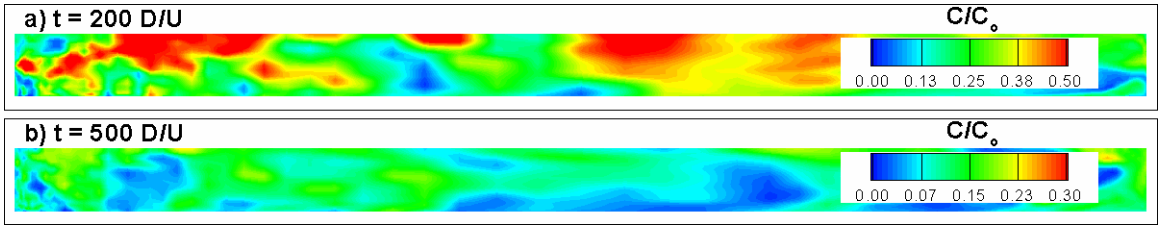

Figure 6.20. Contours of contaminant concentration at the interface (y/D=7.5) between embayment 5 and the channel (contaminant is introduced initially into embayment 5). a) t=200D/U; b) t=500D/U.

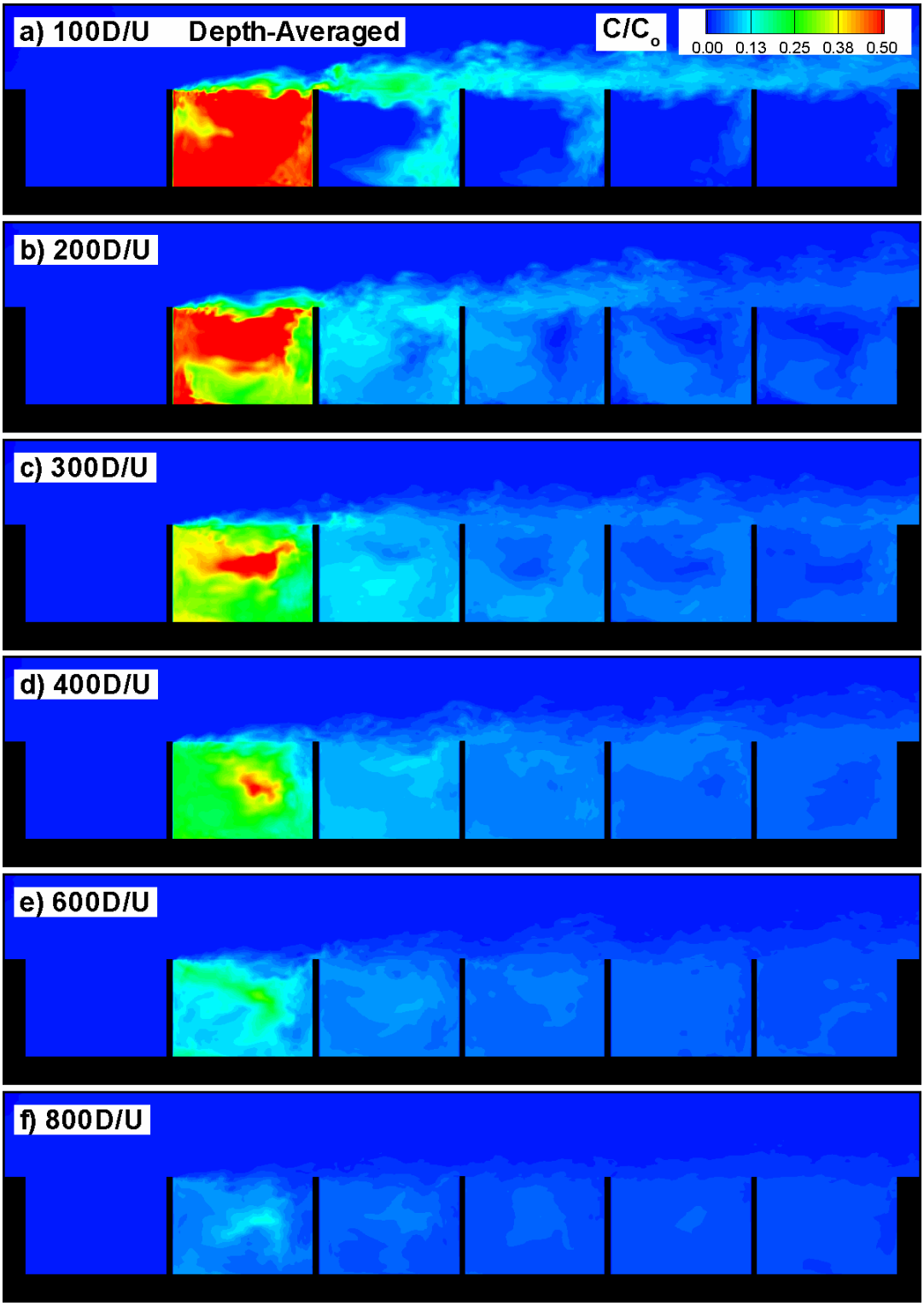

Figure 6.21. Depth-averaged contours of contaminant concentration (contaminant is introduced initially into embayment 2). a) t=100D/U; b) t=200D/U; c) t=300D/U; d) t=400D/U; e) t=600D/U; f) t=800D/U.

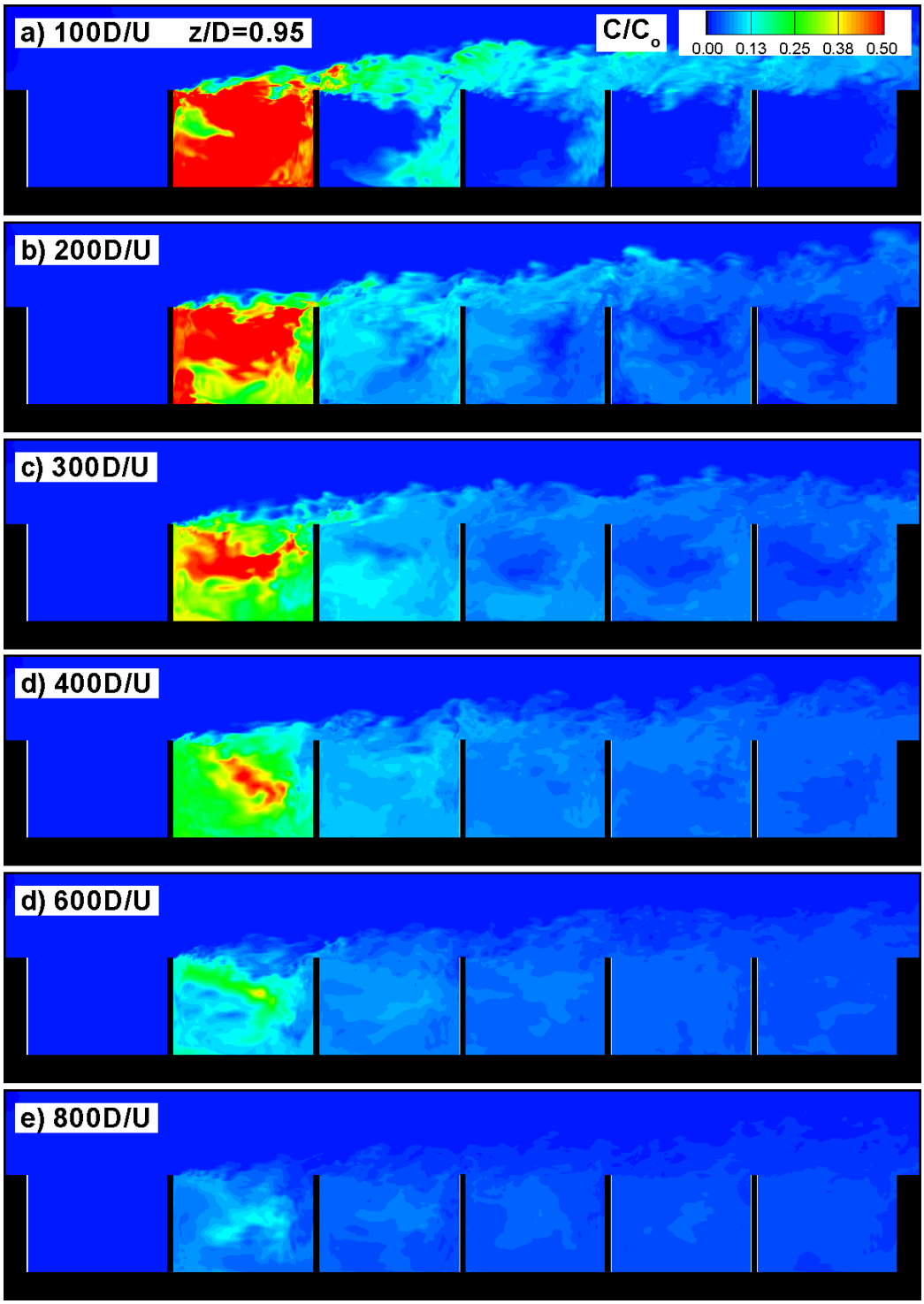

Figure 6.22. Contours of contaminant concentration at z/D=0.95 (contaminant is introduced initially into embayment 2). a) t=100D/U; b) t=200D/U; c) t=300D/U; d) t=400D/U; e) t=600D/U; f) t=800D/U.

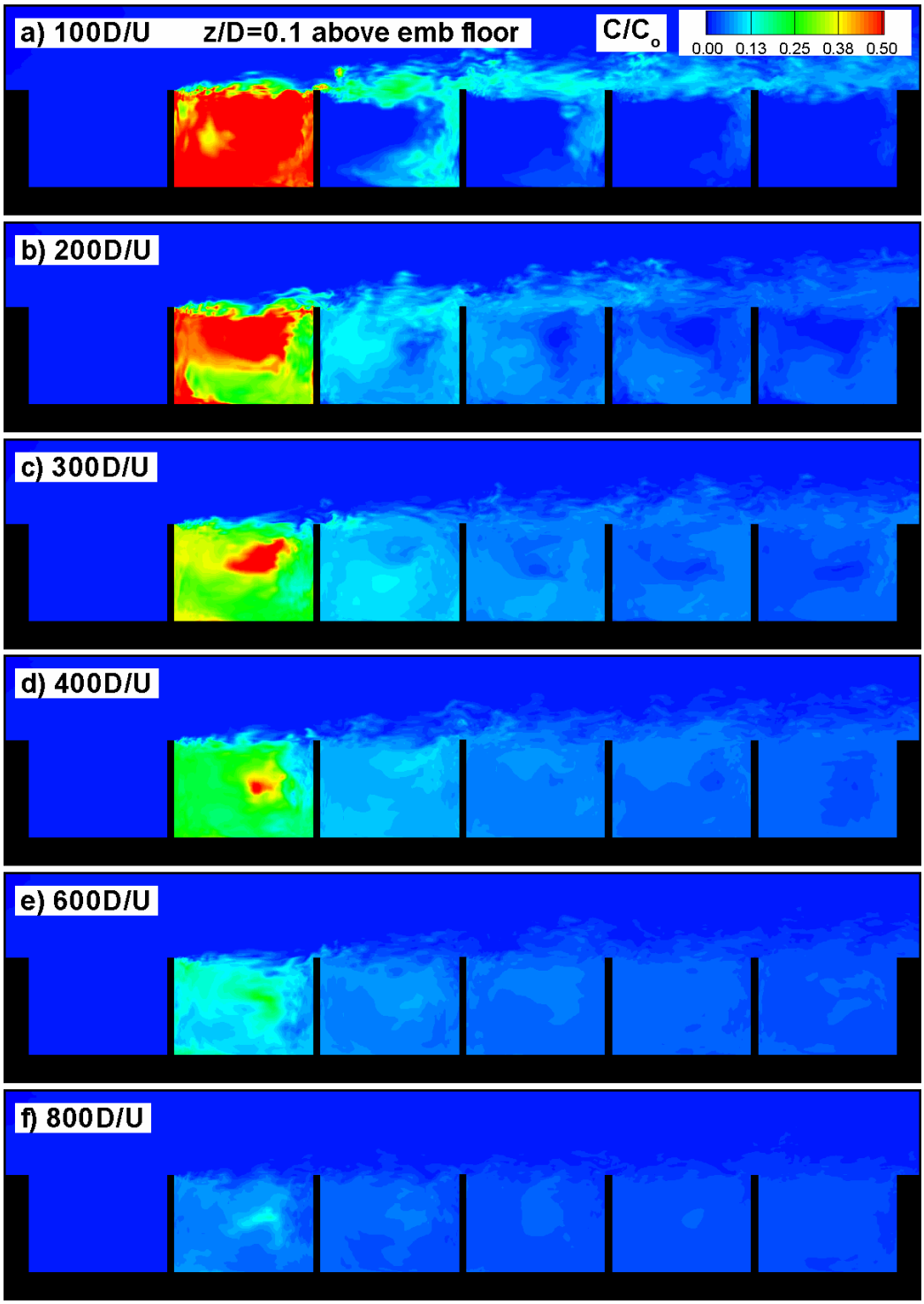

Figure 6.23. Contours of contaminant concentration in a plane situated at z/D=0.1 from the embayment bottom (contaminant is introduced initially into embayment 2). a) t=100D/U; b) t=200D/U; c) t=300D/U; d) t=400D/U; e) t=600D/U; f) t=800D/U.

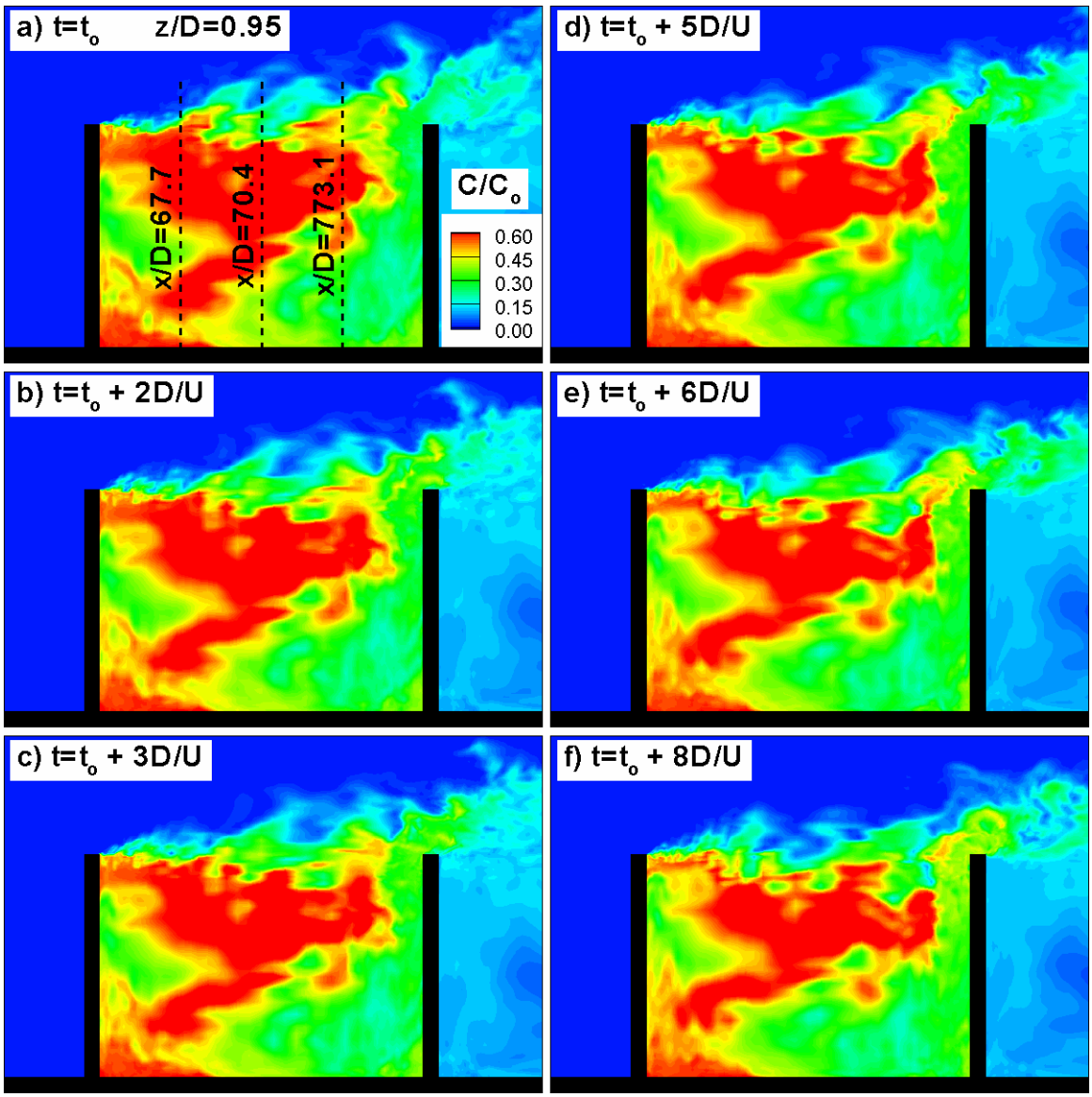

Figure 6.24. Contours of contaminant concentration at z/D=0.95 in embayment 5 (contaminant is introduced initially into embayment 5), t_0=205D/U. a) $t=t_0$; b) $t=t_0$+2D/U; c) $t=t_0$+3D/U; d) $t=t_0$+5D/U; e) $t=t_0$+6D/U; f) $t=t_0$+8D/U.

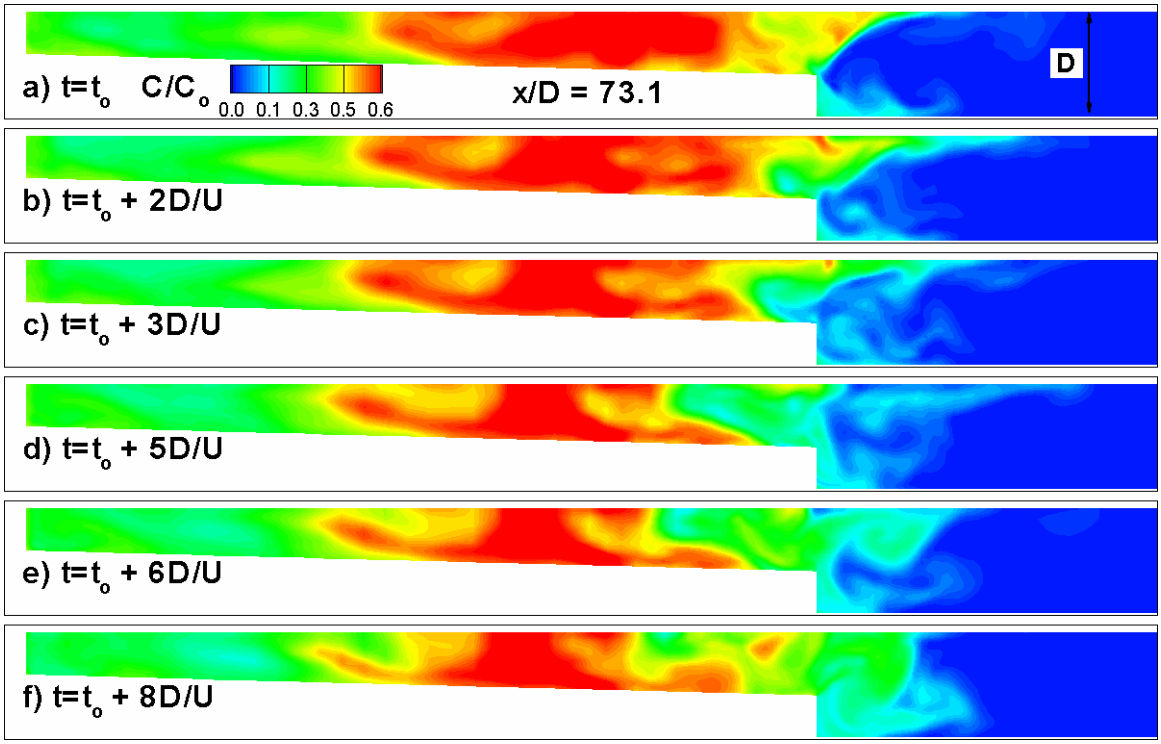

Figure 6.25. Contours of contaminant concentration at x/D=73.1 in embayment 5 (contaminant is introduced initially into embayment 5), t_0=205D/U. a) t=t_0; b) t=t_0+2D/U; c) t=t_0+3D/U; d) t=t_0+5D/U; e) t=t_0+6D/U; f) t=t_0+8D/U.

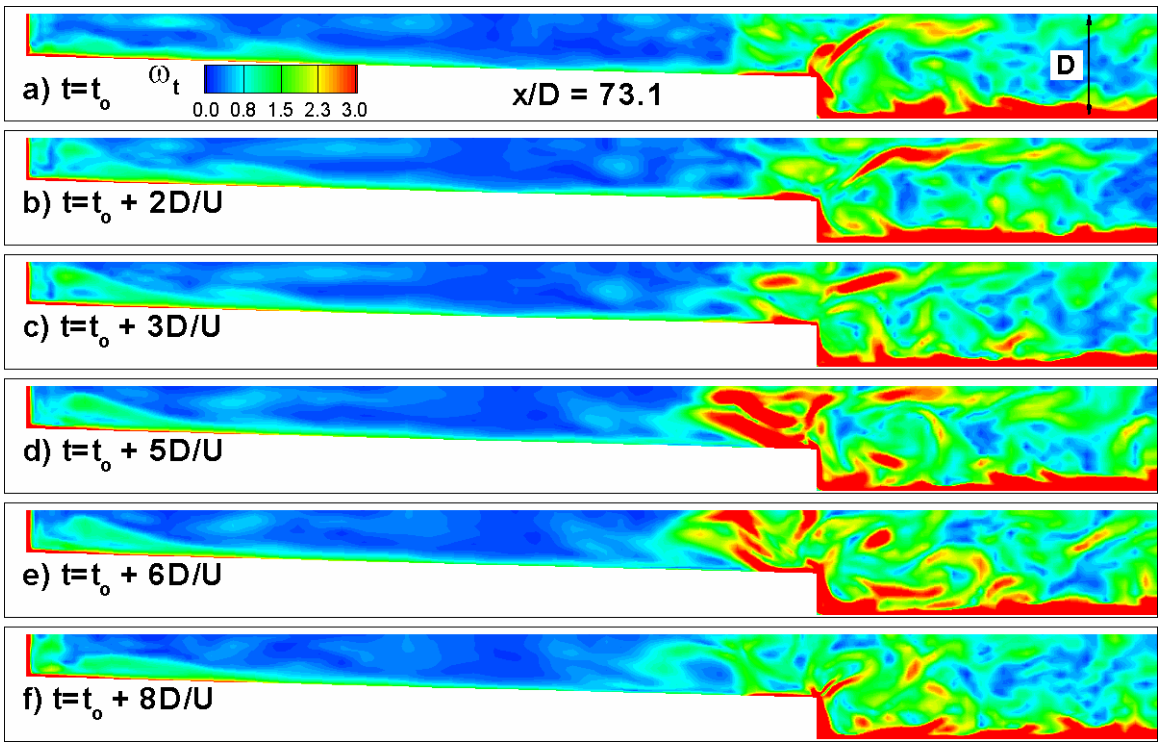

Figure 6.26. Contours of total vorticity magnitude at x/D=73.1 in embayment 5 (contaminant is introduced initially into embayment 5), t_0=205D/U. a) $t=t_0$; b) $t=t_0$+2D/U; c) $t=t_0$+3D/U; d) $t=t_0$+5D/U; e) $t=t_0$+6D/U; f) $t=t_0$+8D/U.

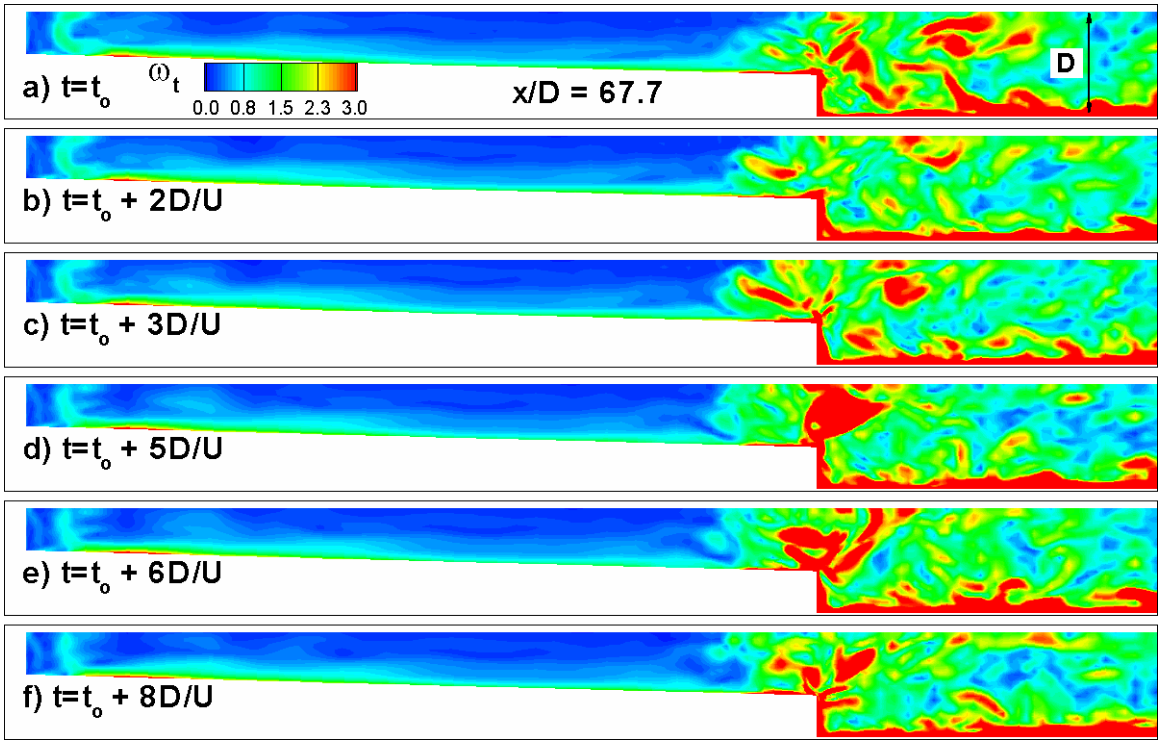

Figure 6.27. Contours of total vorticity magnitude at x/D=67.7 in embayment 5 (contaminant is introduced initially into embayment 5), t_0=205D/U. a) t=t_0; b) t=t_0+2D/U; c) t=t_0+3D/U; d) t=t_0+5D/U; e) t=t_0+6D/U; f) t=t_0+8D/U.

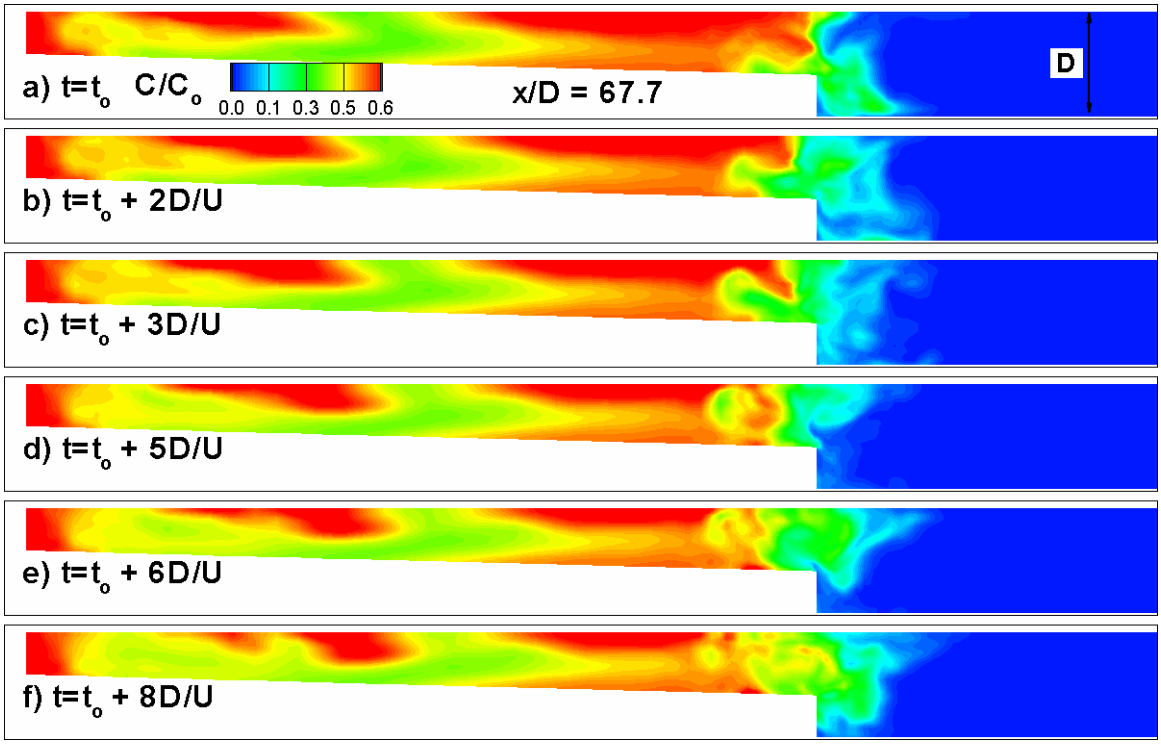

Figure 6.28. Contours of contaminant concentration at x/D=67.7 in embayment 5 (contaminant is introduced initially into embayment 5), t_0=205D/U. a) t=t_0; b) t=t_0+2D/U; c) t=t_0+3D/U; d) t=t_0+5D/U; e) t=t_0+6D/U; f) t=t_0+8D/U.

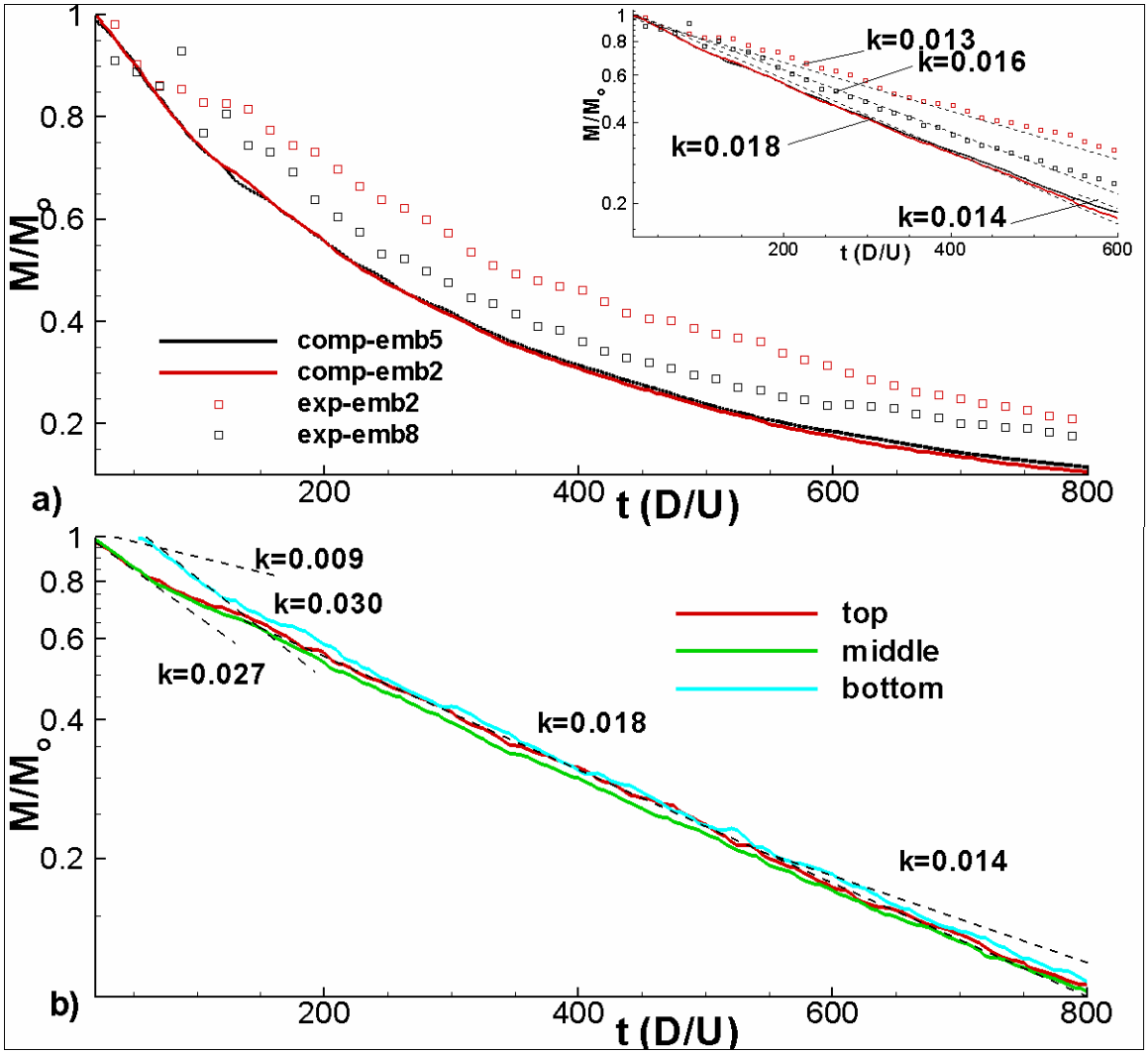

Figure 6.29. Contaminant mass decay within embayment 5. a) linear-linear scale with inset showing mass decay in log-linear scale; b) log-linear scale showing the decay of the mass of contaminant in the top, middle and bottom layers of embayment 5. The inferred values of the nondimensional exchange coefficient, k, are also shown.

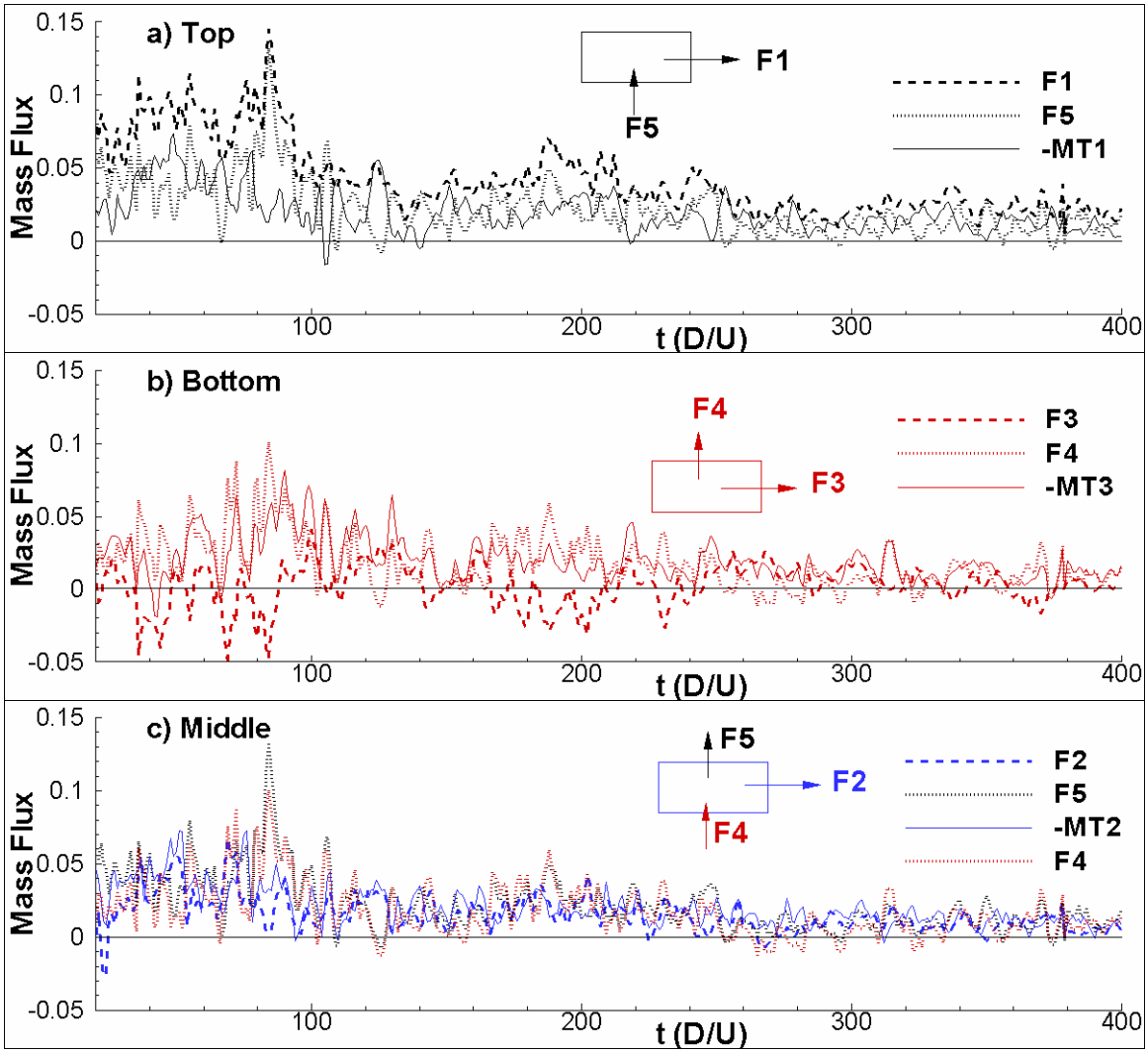

Figure 6.30. Contaminant mass fluxes through the corresponding layer of the channel-embayment interface (contaminant is introduced initially into embayment 5). a) top; b) bottom; c) middle.

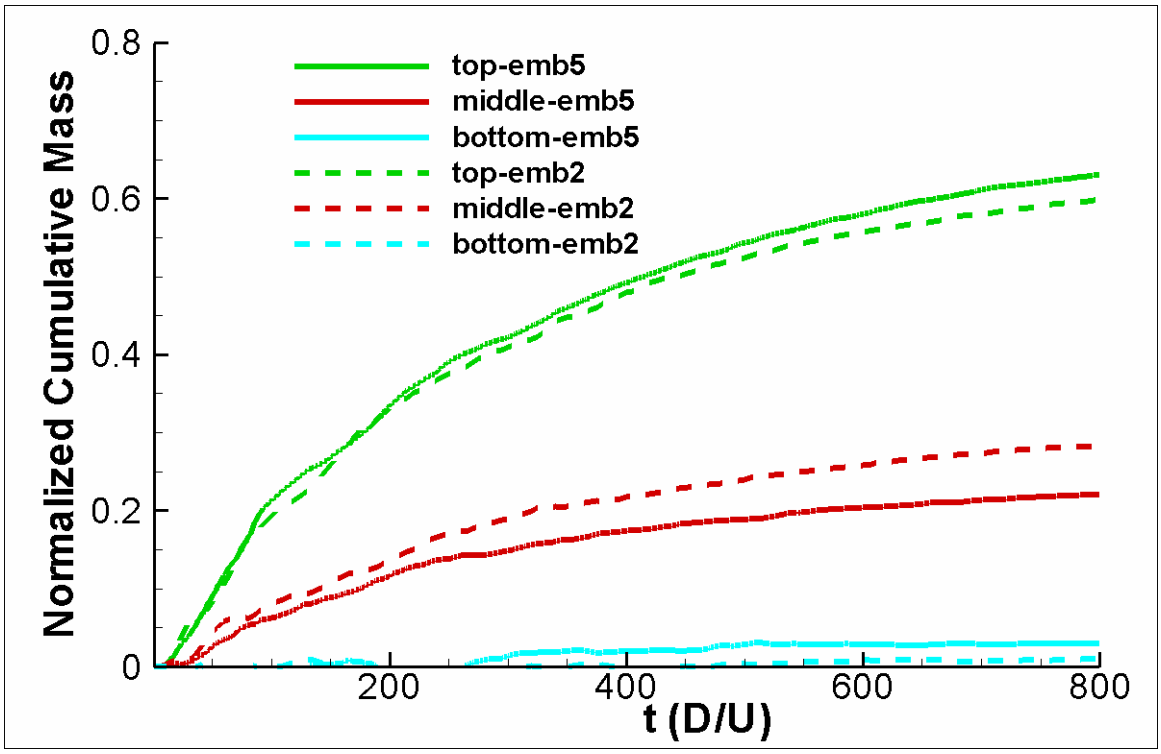

Figure 6.31. Temporal evolution of cumulative contaminant mass transport into the channel through the corresponding layer of the embayment-channel interface for the case when the contaminant is introduced into embayment 2 (dashed line) and into embayment 5 (continuous line).

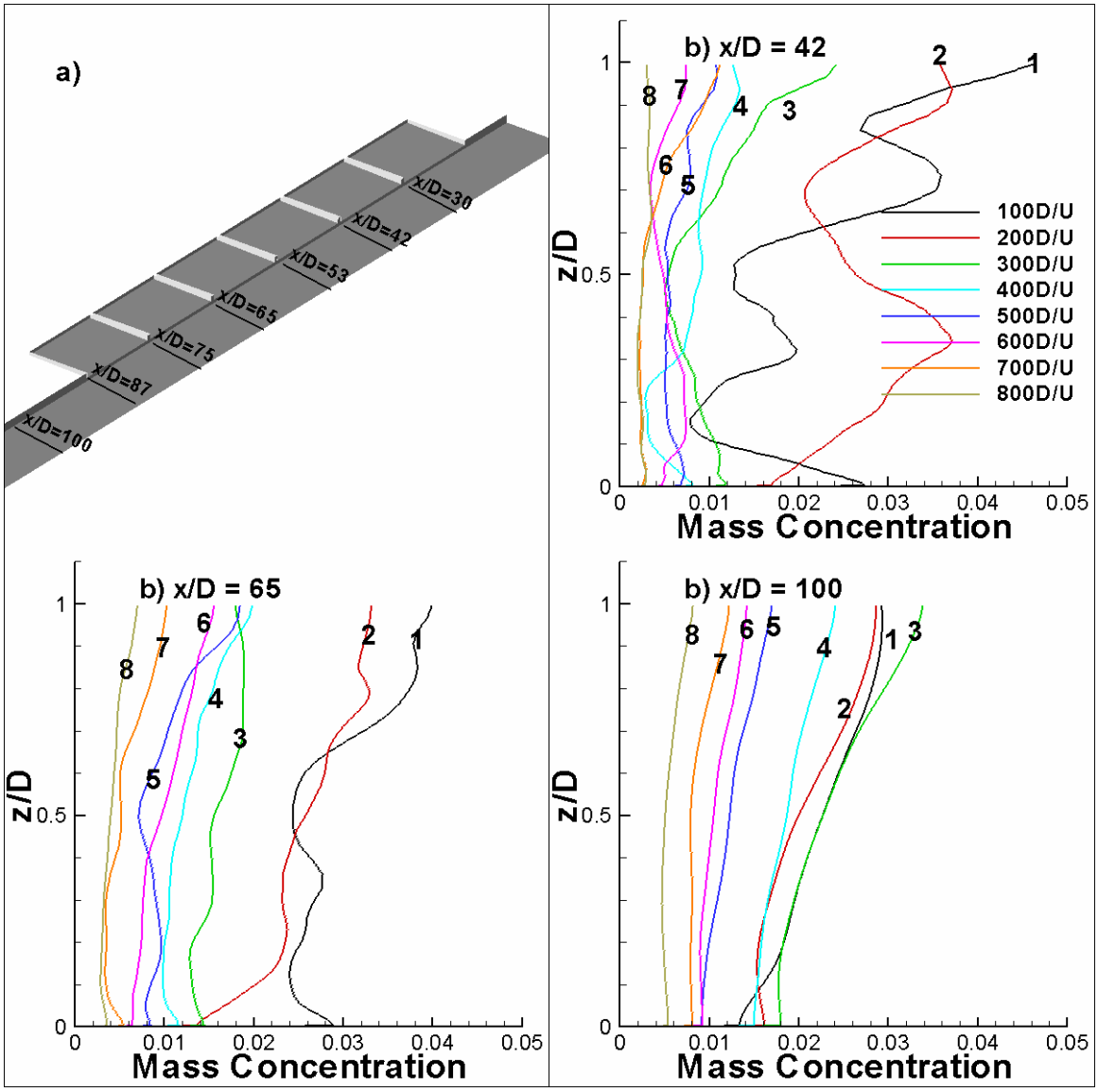

Figure 6.32. Temporal evolution of the width-averaged concentration profiles in various spanwise sections for the case when the contaminant is introduced into embayment 2. a) sketch showing position of the spanwise sections; b) x/D=42; c) x/D=65; d) x/D=100.

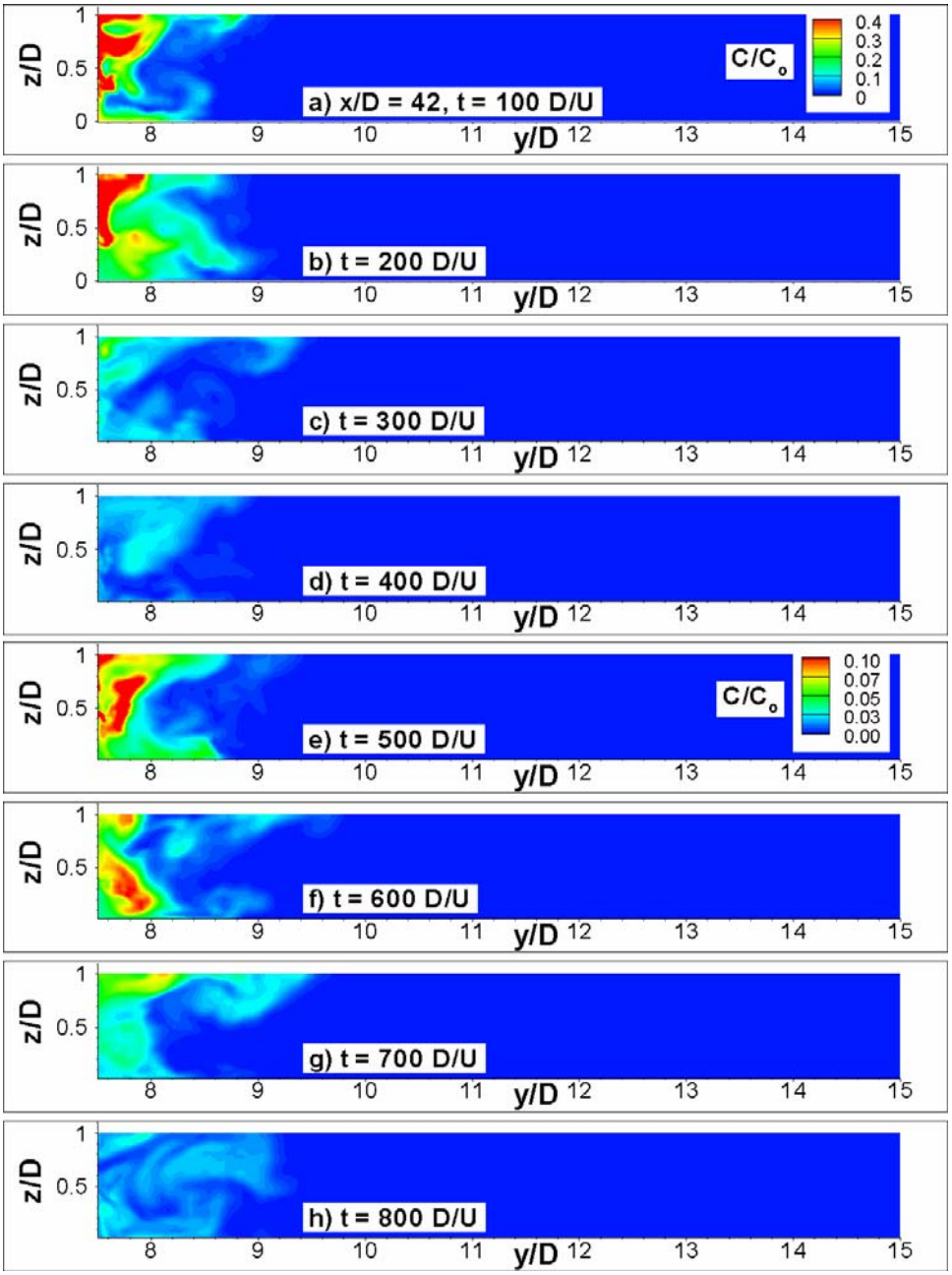

Figure 6.33. Contours of contaminant concentration at x/D=42 (contaminant is introduced initially into embayment 2). a) t=100D/U; b) t=200D/U; c) t=300D/U; d) t=400D/U; e) t=500D/U; f) t=600D/U; g) t=700D/U; h) t=800D/U.

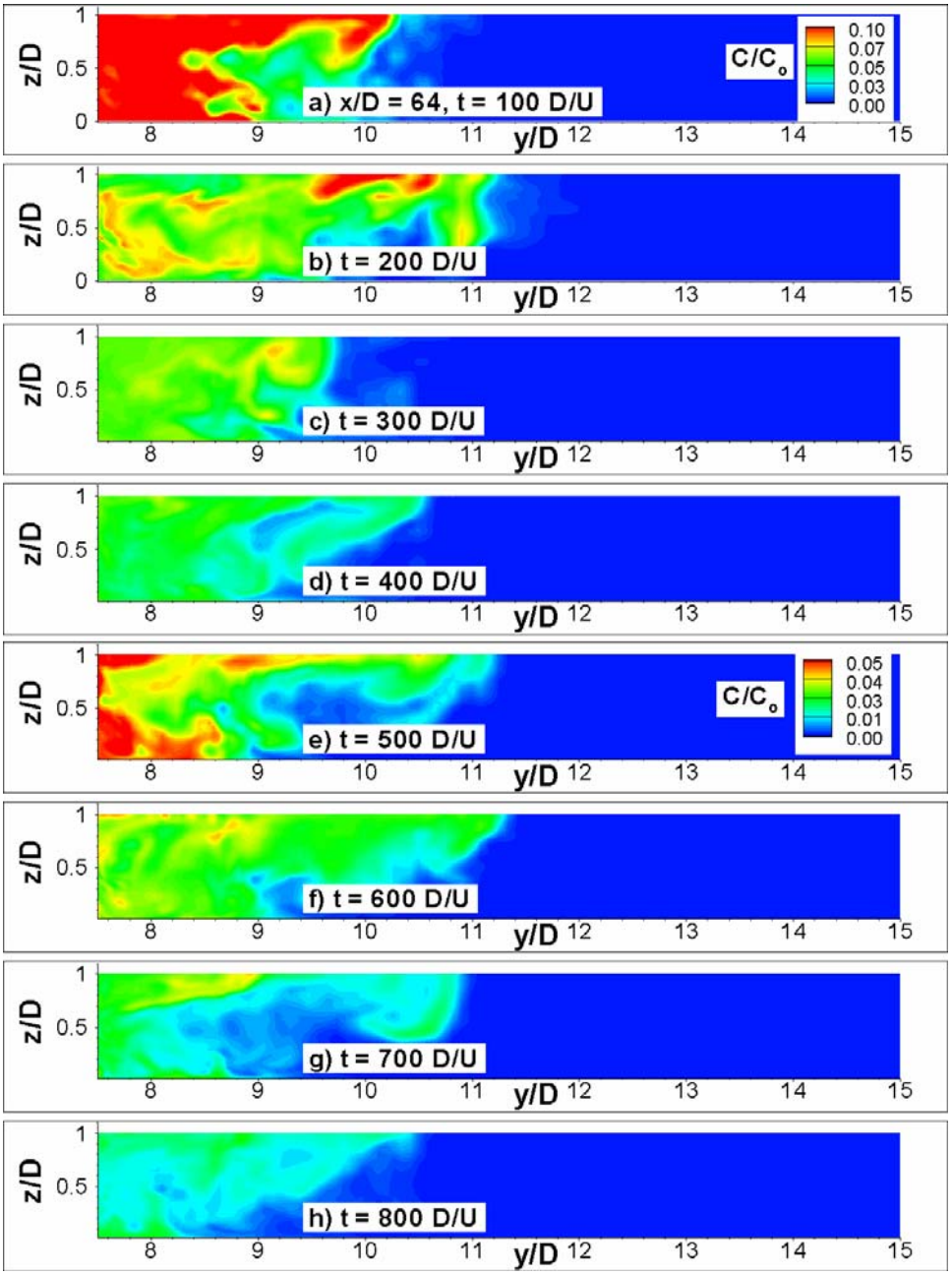

Figure 6.34. Contours of contaminant concentration at x/D=65 (contaminant is introduced initially into embayment 2). a) t=100D/U; b) t=200D/U; c) t=300D/U; d) t=400D/U; e) t=500D/U; f) t=600D/U; g) t=700D/U; h) t=800D/U.

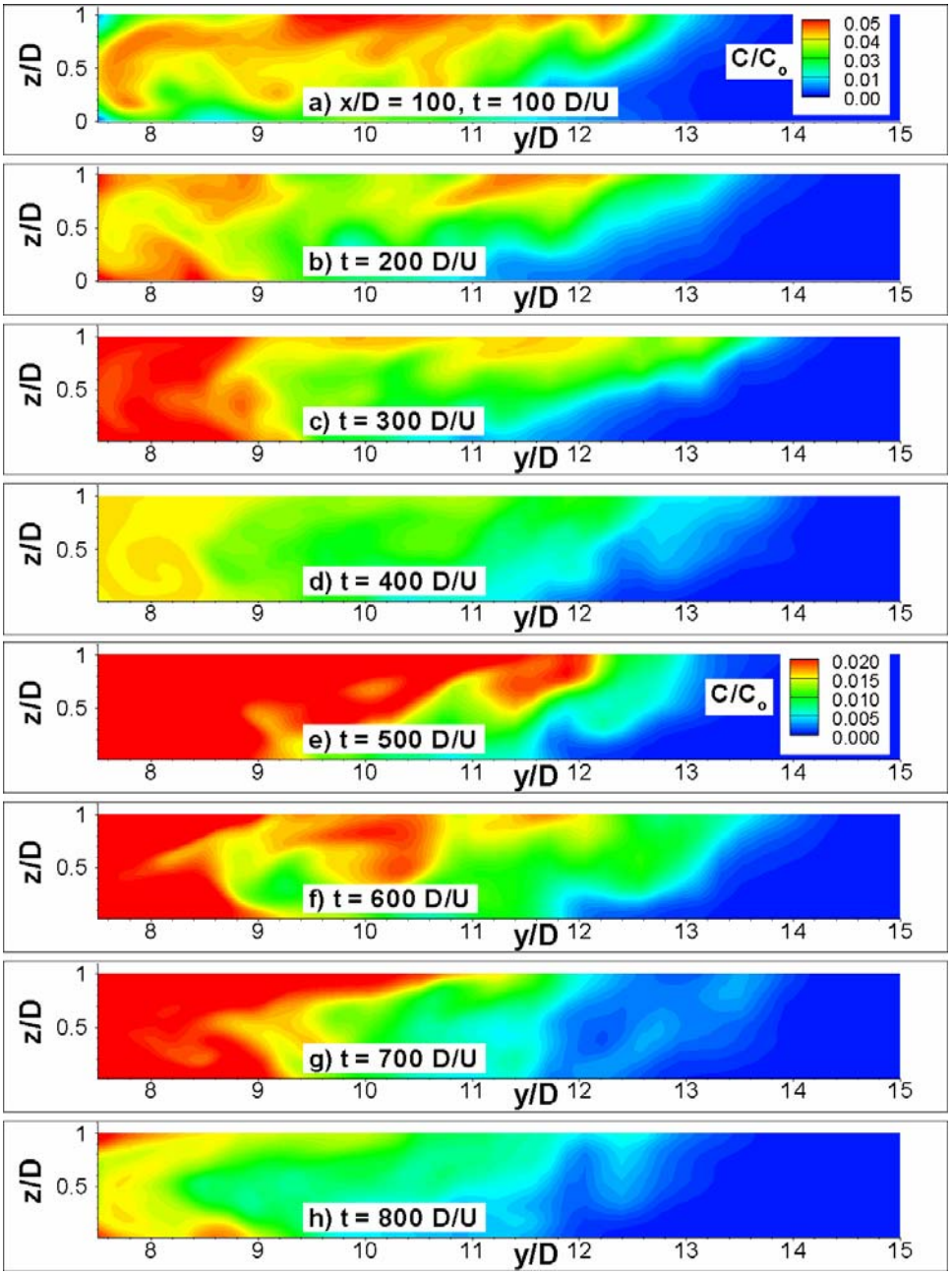

Figure 6.35. Contours of contaminant concentration at x/D=100 (contaminant is introduced initially into embayment 2). a) t=100D/U; b) t=200D/U; c) t=300D/U; d) t=400D/U; e) t=500D/U; f) t=600D/U; g) t=700D/U; h) t=800D/U.

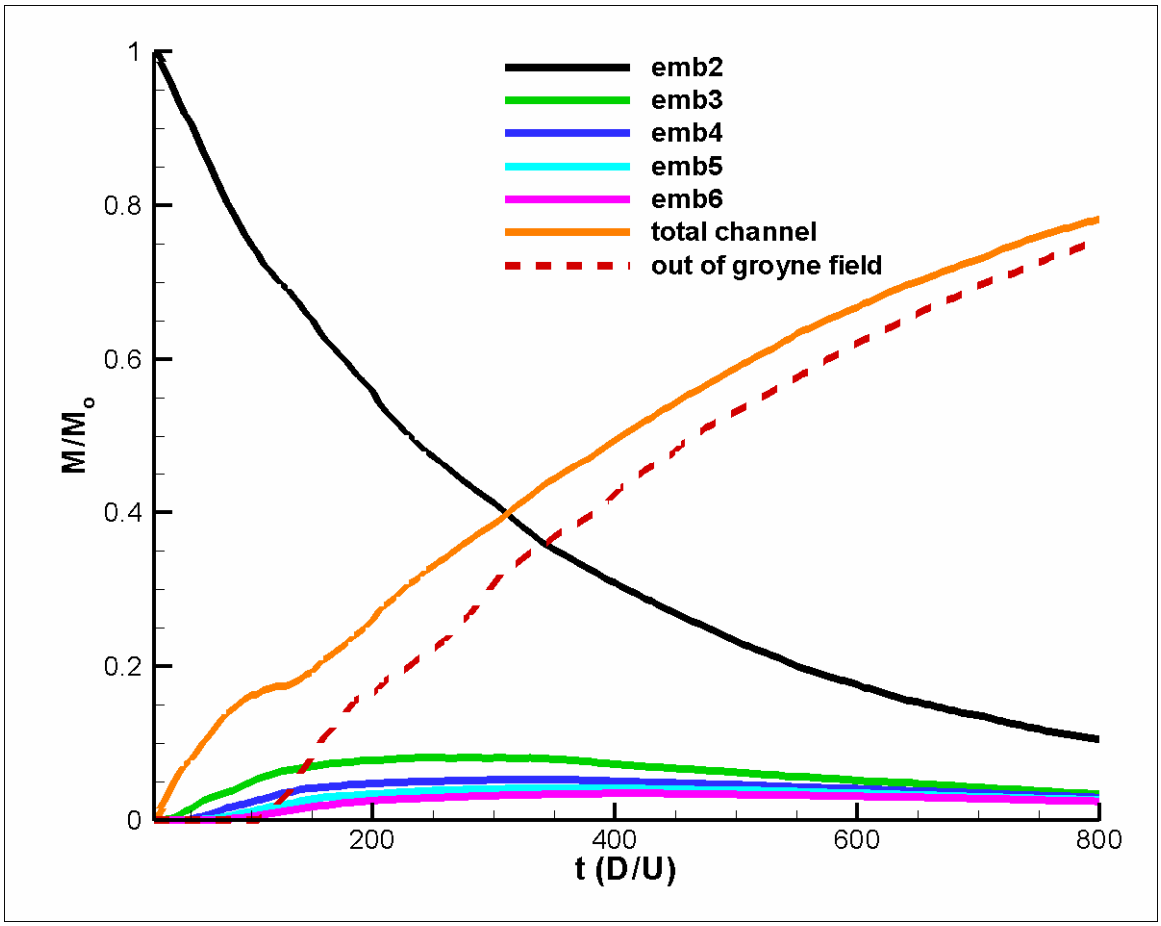

Figure 6.36. Temporal variations of the mass of contaminant within the various embayments, in the region past the groyne field and in the main channel for the case when the contaminant is introduced into embayment 2.

CHAPTER 7

CONCLUSIONS AND RECOMMENDATIONS

7.1 Conclusions

The 3D LES simulations conducted in the present study have shown that LES used in conjunction with a non-dissipative viscous solver and meshes that are fine enough to resolve the dynamically important structures in the turbulent flow can predict most of the instantaneous and averaged free-surface flow features observed in previous experimental investigations of similar flows. Additional information was obtained on the flow and large-scale dynamics inside the embayment and in the embayment-channel interface region, on the role of these coherent structures and macroturbulence events in the mass transport process, and on the distribution of the bed shear stress.

The study of the flow and mass exchange processes in a channel with two emerged or submerged groynes has shown:

1. In both cases, the mass exchange between the embayment region and the channel flow was controlled by the injection of patches of high-vorticity low-concentration fluid from the detached shear layers into the embayment, close to the downstream groyne. The frequency of occurrence of these interactions (total escape, total clipping or partial clipping events), the thickness of the detached shear layers and the turbulence amplification within these detached shear layers were found to be dependent on whether the groynes were emerged or submerged and on the relative geometrical dimensions of the embayment. However, the structure of the vertical detached shear layer over the embayment in the submerged case was found to be qualitatively similar to that of the lateral detached shear layer.
2. As expected, the three-dimensionality of the flow was found to be larger and the ejection of the contaminant introduced inside the embayment volume to be faster

in the submerged case due to the presence of an additional exchange surface (embayment roof) through which contaminant was advected out of the embayment.

3. The structure of the horseshoe vortex (HV) system at the base of the upstream groyne was found to be highly variable and the turbulence was strongly amplified inside the HV region. However, a main necklace vortex was observed to be present at most times. The largest values of the bed shear stress were found to be present in the strong acceleration region around the tip of the upstream groyne and beneath the main necklace of the HV system.
4. The contaminant removal process was found to be highly non-uniform over the depth in both cases. In the emerged case, it was shown that the mass of contaminant leaving the embayment through the top third of the embayment-channel interface is three times larger than the mass of contaminant leaving through the bottom third of the interface. In the submerged case, it was found that more contaminant leaves the embayment through the top interface than through the middle and top layers of the lateral interface. A large-scale mean upward contaminant transport was observed over most of the depth in the emerged case and over the top two-thirds of the embayment depth in the submerged case.
5. The decay of the mean concentration inside the embayment was found to be exponential in both cases, which is consistent with dead zone theory models. However, also consistent with experimental studies in which a one-gyre circulation pattern was observed inside the embayment, the decay was characterized by two different values of the mass exchange coefficient corresponding to an initial phase, in which about 65% of the initial mass of contaminant was removed from the embayment, and to a final phase in which the value of the non-dimensional mass exchange coefficient was smaller.

6. The simulations provide a comprehensive data set for future investigations of the flow physics for single embayment configurations with emerged and submerged groynes or for the flow around the first groyne of a multiple-embayment groyne field. The data set is especially valuable for validation of codes used to predict flow around groyne fields in realistic configurations as this geometry can be simulated using 3D RANS based codes on relatively coarser meshes, especially if wall functions are used. A similar argument holds for 2D LES or RANS simulations. One of the main advantages of such a validation study is that the distribution of the flow variables (mean velocity, turbulence quantities, depth-averaged quantities) at the inflow required by the 3D RANS or 2D LES/RANS model can be obtained from the LES database containing the instantaneous flow fields without any simplifying assumptions. The statistics from the 3D LES simulation allows not only a direct assessment of the capabilities of a simpler (e.g., RANS) model to predict quantities such as the mean velocity components and the TKE, but also allows a more in depth study of the reason why the different models fail to predict lower order statistics in a certain region. This can be done by calculating the modeled terms in the transport equations solved in RANS models and comparing them with the corresponding quantity from LES that does not require modeling except for the small scale contribution that can generally be ignored. Using the LES statistics one can also easily investigate the need for the use of low-Reynolds-number versions of RANS models to simulate flow past groyne like geometries by performing simulations using both wall functions and low-Reynolds-number corrections.

The study of the flow and mass exchange processes in a channel with multiple emerged groynes containing six relatively shallow embayments has shown:

1. The mean and r.m.s. velocity fluctuations at the free surface were found to be in good agreement with experimental results. The mean flow fields and turbulence statistics in the groyne field region became relatively independent of the embayment rank past embayment 4.
2. The mean flow distribution and transverse velocity spectra confirmed that the flow was quasi two-dimensional in the embayment region away from the interface. However, the flow was found to be three-dimensional in the interface region on both the embayment side and the channel side. In particular, the mean transverse velocity was found to be predominantly oriented toward the channel in the upper free surface layer and toward the embayment at lower depths. This explained why the mass exchange coefficients predicted by methods that use floating particles at the free surface are larger than the ones predicted using more accurate methods that measure the depth-averaged dye concentration within the embayment.
3. Two main mechanisms through which low concentration channel fluid penetrate inside the embayment were identified. The first mechanism is due to the partial or total injection of patches of high vorticity fluid from the mixing layer close to the tip of the downstream groyne of the embayment (similar to 2D cavity flows). This regular injection of patches of relatively high-momentum high-vorticity mixing-layer fluid produces a jet-like flow parallel to the downstream groyne face and then to the lateral wall of the embayment. Mixing takes place at the interface of the jet-like flow with the main recirculation eddy inside the embayment. The second mechanism is due to the random formation of highly vortical eddies in the interface region. At times, these eddies facilitate the intrusion of low-concentration fluid inside the embayment over lateral distances of the order of the channel depth. As these eddies were stretched and broken into small-scale turbulence, local mixing of the fluid in the jet-like flow with the high-

concentration embayment fluid occurred. The time scales associated with the second mechanism were estimated to be between 5 and 20D/U.

4. The bed shear stress was found to peak near the face of the downstream groyne, close to the tip of the groyne, where patches of highly vortical fluid were injected inside the embayment. Because this process is intermittent, the instantaneous bed shear stress values associated with these events were found to be substantially higher than the mean values. This explains why scour can develop inside shallow embayments where the mean velocities are lower than inside the main channel.
5. Consistent with the distribution of the mean tranverse velocity, it was found that most of the contaminant left the embayment through the top layer of the embayment-channel interface. It was shown that a strong mean upward circulation of contaminant within the embayment was present.
6. The decay of the mean concentration inside the embayment was found to be characterized by a non-unique value of the mass exchange coefficient, similar to the other two simulations. However, the difference in the value of the non-dimensional exchange coefficient between the initial and final phase of decay was found to be relatively small. The value of the non-dimensional mass exchange coefficient over the main initial phase was found to be relatively close to the value inferred from the experiment of Uijttewaal et al. (2001). However, the LES simulations suggest that the variation of the mass exchange coefficient with the embayment rank is smaller than the one observed in experiment.
7. In the case in which the contaminant was introduced inside embayment 2, it was found that a substantial amount of contaminant (up to 20% of the initial mass) can be reinjected into the downstream embayments before being ejected back into the main channel. The lateral extent of the contaminant cloud in the groyne field region and immediately past it was determined at the different stages of the process.

8. Use the instantaneous flow fields and statistics from LES along with the available flow measurements at the free surface for validation of simpler numerical models as discussed for the one-embayment geometry simulations.

The present numerical investigation using 3D LES highlighted the need for conducting parallel numerical and experimental investigations using eddy resolving techniques (e.g., PIV) of complex flows around hydraulic structures and, in particular, of flow past groyne fields. Validation of 3D LES codes requires high quality measurements of mean flow and higher order statistics (e.g., TKE) in relevant flow regions where highly coherent coherent structures are present (e.g., in several vertical planes perpendicular to the core of the main horseshoe vortex around the most upstream groyne) along with measurements of velocity spectra. In particular, there is a need for detailed measurements of the velocity and turbulence flow fields at a section situated upstream of the groyne region as the flow past the groynes and mass exchange processes are sensible to the characteristics of the incoming turbulent flow (e.g., presence of large scale secondary motions, level of turbulence, etc.) and in many cases the incoming flow is close but not exactly fully developed and totally free of large scale secondary motions in the flume in which the experiments are conducted.

Additional instantaneous data in several horizontal planes visualizing the dynamics of the main vortices and their relation to the transport of contaminant within these planes as well as in and out of them would be very valuable toward making sure that the LES can capture the correct dynamics. Once the model is validated based on information available in several representative planes then the LES results can be used confidently toward elucidating the flow physics and the interactions among the main vertical systems in the flow. This is mainly because collecting PIV data in plane surfaces is quite expensive and the interrogation area is generally limited. In this regard until experimental techniques (e.g., 3D PIV) that can determine the velocity and concentration

distributions within the embayment in several planes spanning the depth of the channel at practically the same time will be applied for groyne field geometries, 3D LES remains the best tool toward understanding and quantifying the mass exchange processes within and around the embayments.

In this regard, it will be very helpful if the mean transverse velocity distribution at the channel-embayment interface would be available from experiments. The analysis of the mass exchange processes bases on the 3D LES results showed a strong non-uniformity of this quantity over the depth of the embayment especially for the multiple groyne case in which the embayment depth was smaller than the channel depth. Though it was shown that the higher transverse velocity (oriented from the embayment toward the channel) predicted by LES explained the larger mass exchange coefficients predicted by experimental techniques based on free-surface measurements compared to experimental techniques based on estimation of the depth averaged concentration fields, a direct comparison of the predicted and measured mean transverse velocity profiles at the embayment-channel interface would strengthen the conclusion reached in this purely numerical study.

The present study allowed a better understanding of the flow and mass exchange processes for two generic geometries. The idealized form of the geometries considered (in particular the one used for the one-embayment case) is an obvious limitation of the present study. Still, the simulations conducted in the present study allowed gaining more insight into:

1. The mass exchange processes between the channel and the embayments in particular on the non-uniformity of the mass exchange processes over the depth and on the contaminant mass flow within the embayment. The link between the mean transverse velocity in the interface plane and the non-uniformity of the mass exchange processes over the depth was demonstrated. This also allowed a

quantitative explanation of why the mass exchange coefficients predicted based only on free-surface measurements are overestimated.

2. The structure of the horseshoe vortex system at the base of the first groyne was investigated for the emerged case and a case in which the submergence was relatively high. It was found that the pressure fluctuations and TKE. was strongly amplified in the HV region and that the main reason of the spatial and temporal variations in the intensity of the main necklace eddy was the interactions of this eddy with secondary necklace vortices shed form the separation region of the incoming boundary layers. This large scale variation in the overall intensity of the main necklace structures translated into large variations of the local bed shear stress values. Though the mean bed shear stress value can be lower than the critical value for sediment entrainment sediment particles can be still entrained each time the instantaneous bed shear stress exceeds the critical value. This has an obvious consequence for RANS models that cannot capture the unsteady dynamics of these necklace vortices. To increase the accuracy of these models, they should be modified to incorporate a transport equation that will allow the variance of the bed shear stress along with its mean value to be estimated as part of the calculation. The simulations of the emerged and submerged geometry (Chapters 4 and 5) showed that if the mean flow velocity in the incoming channel remains the same the intensity of the HV system will diminish in the submerged case. This is because part of the flow that would be entrained into the upstream recirculation motion is convected over the submerged groynes rather than feeding flow and momentum into the HV system. However at flooding conditions the mean velocity increases the HV system is expected to be stronger than the one observed in the emerged case. This explains the fact that most of the scour occurs at flooding conditions.

Future studies using the present model in which more realistic geometries are considered are possible because the present solver uses unstructured meshes that allow performing simulations in very complex geometries. Several relevant such simulations are proposed as topics for future research in the next section. However, if LES without wall functions is to be used the Reynolds numbers at which these simulations can be conducted will have to remain low (of the same order with the ones at which model studies are generally conducted) due to the steep increase in the mesh requirements with the Reynolds number. Thus, one cannot investigate scaling effects. To perform eddy resolving simulations at higher Reynolds number one should either use LES with wall functions or hybrid RANS-LES approaches like Detached Eddy Simulation. Of course, in all these approaches the amount of empiricism in the model is larger, thus detailed validation of the model is an even more important task.

In LES and hybrid RANS-LES models the use of an isotropic model for the unresolved scales is fully justified as the main energy containing scales in these simulations are directly resolved. However, in the case of a time-accurate or steady 3D RANS model it is likely the use of an anisotropic closure will result in more accurate predictions based on the large anisotropy of the flow fields predicted by LES. Still the use of a non-hydrostatic anisotropic RANS model is unlikely to accurately predict the mean structure of the horseshoe vortex system or to predict the ejection and dispersion of the contaminant in the channel. This is because for massively separated flows in which large adverse pressure gradients are present and in which large scale unsteady phenomena are present RANS models have been shown to be relatively unsuccessful. Evidence of this was shown in the present work when the RANS and LES predictions at the free surface were compared with the experimental predictions. The capabilities of RANS to predict the mean flow in the horseshoe vortex region or the mean transverse velocity distribution at the channel embayment interface for configurations in which the flow is

strongly non-uniform in that region are expected to be even lower than the ones observed for the free surface flow. Thus the use of 3D hybrid RANS-LES simulations using non-zonal or zonal approaches appears to be the best tool available today for simulation of flow around groyne-like geometries at realistic Reynolds numbers.

The present LES simulations also provide strong evidence that the 2D approach (used in conjunction with LES or RANS) is likely to result in poor predictions of the depth averaged flow not only for the submerged case where the limitations of this approach are evident but also for the emerged case. Effects related to the nonuniformity of the transverse velocity distribution or on the vertical large scale advection of contaminant within the embayment cannot be accounted for properly in these models. Thus, developing a general 2D model that does not have to be calibrated each time a new type of geometry is considered is unlikely.

Another important limitation of the present study is the absence of a parametric study. In particular, conducting two detailed parametric studies in which the ratio between the embayment length and the embayment width is varied and in which the submergence depth is varied would be a very interesting study that can also be of real use to practitioner engineers. Related to the parametric study in which the submergence depth is varied from zero (emerged case) to large values, an obvious limitation of the present code will be the simulation of cases with a low submergence depth where free surface effects are important (e.g., the flow past the top of the groynes resembles that over a weir). Though Hinterberger (2004) showed that for the emerged case the rigid lid approximation can be used while successfully capturing the seiching motions inside the embayments (these motions were estimated using the predicted pressure field on the rigid free surface plane and the hydrostatic pressure assumption), it is unlikely that simulations with low relative submergence depths would successfully capture the time variations of the free surface deformations deduced using the hydrostatic assumptions and their effects on the flow beneath them. A deformable free surface capability (e.g., using level sets)

should be added to make accurate simulations of these cases possible. For larger relative submergence depths like the one considered in the present study it is likely that the rigid lid approximation will not modify considerably the flow dynamics away from the free surface.

Though the data related to the time evolution of the concentration flow fields was used to predict the temporal variation of the contaminant mass flux and the variation of the width averaged concentration at several vertical sections situated downstream of the embayment region, the information available from the present LES simulations is much more comprehensive and can be used in obtaining quantitative answers related to the usual questions asked in river pollution studies. The database can be mined to calculate not only the amount of pollutant exiting an embayment and being re-entrained in a subsequent embayment or the maximum concentration recorded in a certain sub-region but, more importantly, to determine the amount of time the concentration was higher than a certain threshold value in a given region. This is very important as most of the river pollution guidelines in U.S. are formulated in this form. Though this was beyond the scope of the present work, the database can be used to perform a more detailed study of the dispersion past the embayment region and of the occurrence of situations when the environment can be considered at risk due to the passage of the contaminant, given a certain set of environmental constraints.

7.2 Recommendations

The present simulations served to elucidate several aspects of flow past groynes that are very difficult or expensive to determine or study experimentally. The model can be further used to investigate other relevant geometries related to groyne field flow and enhanced to allow study of more general mass exchange processes between the embayments and the main channel. The findings from these numerical studies can be used in conjunction with experiments to optimize the groyne position and shape with

respect to navigation, bank stability, flood prevention or ecological contribution of the groyne field to the sustainability of the river ecosystem. Some of the future areas of research related to use of full 3D simulations with eddy-resolving techniques, such as LES, include:

1. A study of flow and mass exchange processes in a channel with a groyne field containing embayments with smaller aspect ratios (width over length) where a two or three gyre mean circulation pattern is observed. As shown experimentally (Uijttewaal et al., 2001), in this case some of the eddies contained in the detached shear layer can strongly interact with the main recirculation eddies inside the embayment and significantly enhance the mass exchange. A numerical investigation may help elucidate several aspects of their formation dynamics and the form of the interactions between these flow structures and their contribution to the overall mass exchange process.
2. A study of flow in a channel containing a multiple-embayment groyne field in which the depth transition between the embayment region and the main channel is smooth such that a horseshoe vortex system can form at the base of the groynes.
3. A more complete study of the effect of the submergence depth ratio, especially for channels with series of groynes, and consideration of a case where the groynes are permeable.
4. Consideration of the case of a groyne field in a curved channel.
5. Consideration of the case in which the channel and embayment bottom are loose and the study of mass exchange processes at equilibrium conditions and/or the flow and bed shear stress distributions at different stages of the scouring process for different groyne designs.
6. Consideration of the case in which the channel section increases considerably during a flood (submerged groynes).

7. Consideration of the case in which the contaminant is initially present only in a layer close to the bottom. For negatively buoyant contaminants or for some particular geometries, the contaminant is not expected to mix uniformly inside the embayment before leaving it.
8. Consideration of the dispersion of particulate matter in a Lagrangian-Eulerian framework. The study of the dispersion of individual particles of various sizes will allow a more realistic description of these processes in which both the effect of drag on the particles and the effect of particles on the turbulent flow can be modeled.
9. Consideration of cases relevant to the dynamics of phytoplankton in natural rivers where the presence of embayments is linked to a localized enhancement of phytoplankton abundance (local residence times that are essential in these kind of studies can be much more easily determined from numerical simulations in which particles are tracked using a Lagrangian approach).
10. Simulation of flows at Reynolds numbers closer to field scale using hybrid RANS-LES approaches like Detached Eddy Simulation, which will allow investigation of scale effects.

REFERENCES

Apte, S., Mahesh, K., Ham, F., Constantinescu, S.G., and Moin, P. (2003a). "Large eddy simulation of multiphase flows in complex combustors." Computational Methods in Multiphase Flow II, Eds., A.A. Mammoli and C.A. Brebbia, pp. 53-62, WIT Press, U.K.

Alfrink, B.J. and van Rijn, L.C. (1983). Two-equation turbulence model for flow in trenches. Journal of Hydraulic Engineering. 109(7), 941-958.

Apte, S., Mahesh, Moin, P. and Oefelein, J. (2003b). "LES of swirling particle laden flows in a coaxial jet combustor." International Journal of Multiphase flow, Vol. 29(8), 1311-1331.

Apte, S., Mahesh, K. and Lundgren, T. (2004). "Modeling finite size effects in LES/DNS of two phase flows." IUTAM Symposium on computational approaches to disperse multiphase flows, Argonne National Laboratory, Oct 4-7, 2004.

Babu, P and Mahesh, K. (2005). "Upstream entrainment in numerical simulation of spatially evolving round jets." Phys. Fluids 16, 3699-3705.

Biglari, B. and Sturm, T. (1998). "Numerical modeling of flow around bridge abutments in compound channels." Journal of Hydraulic Engineering, Vol. 124, No. 2, 156-164.

Chang, K.S., Constantinescu, S.G., and Park, S. (2005). "Influence of inflow conditions on the development of the flow and pollutant transport for the flow past an open cavity." Proc. of 4th Int. Conf. on Computational Heat and Mass Transfer, Cachan, France.

Chang, K., Constantinescu, G., and Park, S. (2006a). "The purging of a neutrally buoyant or a dense miscible contaminant from a rectangular cavity. Part II: The case of an incoming fully turbulent overflow." submitted to Journal of Hydraulic Engineering.

Chang, K., Constantinescu, G., and Park, S. (2006b). "Analysis of the flow and mass transfer process for the incompressible flow past an open cavity with a laminar and a fully turbulent incoming boundary layer." Journal of Fluid Mechanics, Vol 561, 113-145.

Chen, F. and Ikeda, S. (1997). "Horizontal separation flows in shallow open channels with spur dikes." Journal of Hydroscience and Hydraulic Engineering, Vol 15, No. 2, 15-29.

Cheng, N., and Chiew, Y. (1998). ‘‘Pickup probability for sediment entrainment.’’ Journal Hydraul. Eng., 124~2!, 232–235.

Chrisohoides, A., Sotiropoulos, F., and Sturm, T. W. (2003). “Coherent structures in flat-bed abutment flow: computational fluid dynamics simulations and experiments.” Journal of Hydraulic Engineering, Vol. 129, No. 3, 177-186.

Chrisohoides, A., and Sotiropoulos, F. (2003). “An experimental technique for visualizing lagrangian coherent structures in aperiodic flows.” Physics of Fluids, Vol. 15, No. 3, 25-28.

Coleman, S., Lauchlan, C., and Melville, B. (2003). “Clear-water scour development at bridge abutments.” Journal of Hydraulic Research, Vol. 41, No. 5, 521-531.

Dancey, C.L., Diplas, P., Papanicolaou, A., and Bala, M. (2002). “Probability of individual grain movement and threshold condition.” Journal of Hydraulic Engineering 128(12), 1069-1075.

Dargahi, B. (1990). "Controlling mechanism of local scouring." Journal of Hydraulic Engineering, Vol. 116, No. 10, 1197-1214.

Devenport, W. J., and Simpson, R. L. (1990). "Time-dependent and time-averaged turbulence structure near the nose of a wing-body junction." Journal of Fluid Mechanics, Vol. 210, 23-55.

Engelund, F., and Fredsoe, J. (1976). "A sediment transport model for straight alluvial channels." Nordic Hydro., 7, 293-306.

Englehardt, C., Kruger, A., Sukhodolov, A., and Nicklisch, A. (2004). "A study of phytoplankton spatial distributions, flow structure and characteristics of mixing in a river reach with groynes." Journal of Plankton Research, Vol. 26, No. 11, 1351-1366.

Elwady, E., Michiue, M., and Hinokidani, O. (2000). “Experimental study of flow behavior around submerged spur-dike on rigid bed.” Annual Journal of Hydraulic Engineering, Vol. 44, 539-544.

Elwady, E., Michiue, M., and Hinokidani, O. (2001). “Movable bed scour around submerged spur-dikes.” Annual Journal of Hydraulic Engineering, Vol. 45, 373-378.

Fox, J.F., Papanicolaou, A. N., Kjos, L. (2005a). “Eddy Taxonomy methodology around a submerged barb obstacle within a fixed rough bed.” Journal of Engineering Mechanics vol. 131, no. 10, pp1082-1101.

Fox, J.F., Papanicolaou, A. N., Hobbs, B., Kramer, C., Kjos, L. (2005b). "Fluid-sediment dynamics around a barb: an experimental case study of a hydraulic structure for the Pacific Northwest." Canadian Journal of Civil Engineering 32, pp 853-867.

Fredsoe, J., and Deigaard, R. (1992). Mechanics of coastal sediment transport. World Scientific Publishing co., River Edge, N.J.

Gessler, J. (1971) "Beginning and ceasing of sediment motion." In River Mechanics, Volume I, Edited and Published by Shen H.W. Fort Collins, Colorado.

Ham, F., Apte, S., Iaccarino, G., Wu, X., Hermann, S., Constantinescu, S.G., Mahesh, K., and Moin, P. (2003). "Unstructured LES of reacting multiphase flows in realistic gas-turbine combustors." Annual Research Briefs 2003. Center for Turbulence Research, Stanford, CA.

Harlow, F.H., Welch, J.E. (1965). "Numerical calculation of time-dependent viscous incompressible flow of fluid with free surface." Phys. Fluids, 8, 2182-2189.

Hinterberger, C. (2004). Three-dimensional and depth-average large eddy simulation of shallow water flows, Ph.D. Dissertation, Karlsruhe, Germany.

Hussain, A.K.M.F., and Reynolds, W.C. (1975). "Measurements in a fully developed turbulent channel flow." J. Fluids Eng., 97, 568-578.

Jiang, G.S. and Peng, D. (2000). "Weighted ENO schemes for Hamilton Jacobi equations." *SIAM J. of Sci. Comput*. 21, 2126-2143.

Kawahara, Y., Peng, J, and Fujii, K. (1998). "Three-dimensional calculation of flow through submerged spur dikes." Collected papers of river and environmental engineering laboratory, University of Tokyo, 141-146.

Keshavarzy, A., and Ball, J. (2000). ''An application of image processing in the study of sediment motion.'' J. Hydraul. Res., 37~4!, 559–576.

Kimura, I., Hosada, T., Onda, S. (2001). "Numerical simulations of flow structures around skewed spur dikes." Japanese Society of Computational Fluid Dynamics.

Kimura, I., Hosada, T., Onda, S. (2003)." 3D numerical analysis of unsteady flow structures around inclined spur dikes by means of a nonlinear k-e model." Proc. of the Int. Symp. on Shallow Flows Delft, The Netherlands.

Kirkil, G., Constantinescu, G., and Ettema, R. (2005a). "The Horseshoe Vortex System around a Circular Bridge Pier on Equilibrium Scour Bed." ASCE-EWRI World Water and Environmental Resources Congress, Alaska.

Kirkil, G., Constantinescu, G., and Ettema, R. (2005b). "The Horseshoe Vortex System around a Circular Bridge Pier on a Flat Bed." XXXIst International Association Hydraulic Research Congress, Seoul, Korea.

Kirkil, G., Constantinescu, G., and Ettema, R. (2006). "Investigation of the Velocity and Pressure Fluctuations Distributions inside the Turbulent Horseshoe Vortex System around a Circular Bridge pier." Proc. River Flow 2006.

Koken, M., Constantinescu, S.G. (2006). "Investigation of flow around a bridge abutment in a flat bed channel using large eddy simulation." World Environmental and Water Resources Congress 2006, Omaha, Nebraska.

Kothyari, U. and Rangaraju, K. (2001). "Scour around spur dikes and bridge abutments." Journal of Hydraulic Research, Vol. 39, No. 4, 367-373.

Kuhnle, R., Alonso, C., and Shields, F. (1997). "Geometry of scour holes around spur dikes, an experimental study." Proceedings of the Conference on Management of Landscapes Disturbed by Channel Incision, 283-287.

Kuhnle, R., Alonso, C., and Shields, F. (1999). "Geometry of scour holes associated with 90^{o} spur dikes." Journal of Hydraulic Engineering, Vol. 125, No. 9. 972-978.

Kuhnle, R., Alonso, C., and Shields, F. (2002). "Local scour associated with angled spur dikes." Journal of Hydraulic Engineering, Vol. 128, No. 12. 1087-1093.

Kurzke, M., Weitbrecht, V., and Jirka, G.H. (2002). "Laboratory concentration measurements for determination of mass exchange between groin fields and main stream." Proceedings of River Flow 2002, Louvain-la-Neuve, Belgium, 369-376.

Kwan, R. T. F. (1984). Study of abutment scour, Rep. No. 328, School of Engineering, The University of Auckland, New Zealand.

Kwan, R. T. F., and Melville, B. W. (1994). "Local scour and flow measurements at bridge abutments." Journal of Hydraulic Research, Vol. 32, No. 5, 661-673.

Lilly, D.K. (1992). "A proposed modification of the Germano subgrid scale closure method." Phys. Fluids A 4 (3), 633-635.

Lim, S. and Cheng, N. (1998). "Prediction of live-bed scour at bridge abutments." Journal of Hydraulic Engineering, Vol. 124, No. 6, 535-538.

Lim, S. (1997). "Equilibrium clear-water scour around an abutment." Journal of Hydraulic Engineering, Vol. 123, No. 3, 237-243.

Lin, J. C. & Rockwell, D. (2001). "Organized oscillations of initially turbulent flow past a cavity." *AIAA J.*, 39, 1139-1151.

Liu, J., Tominaga, A., and Nagao, M. (1994). "Numerical simulation of the flow around the spur dikes with certain configuration and angles with bank." Journal of Hydroscience and Engineering, Vol. 12, No. 2, 85-100.

Mahesh, K., Constantinescu, S.G., and Moin, P. (2004). "A numerical method for large eddy simulation in complex geometries." Journal of Comp. Physics 197, 215-240.

Mahesh, K., Constantinescu S.G., Apte, S., Iaccarino, G., Ham, F., and Moin, P. (2006). "Large eddy simulation of reacting turbulent flows in complex geometries." accepted for publication, J. of Appl. Mechanics.

Marson, C., Caroni, E., Fiorotto, V., and Da Deppo, L. (2003). "Flow field analysis around a groyne." Proceedings of the 30th IAHR Congress, Thessaloniki, Greece, Theme C, 377-383.

Mansour, N.N., Moin, P., Reynolds, W.C., Ferziger, J.H. (1979). "Improved methods for large-eddy simulation of turbulence," in: F. Durst, B.E. Launder, F.W. Schimdt, J.H. Whitelaw (Eds.), Proceedings of the Turbulent Shear Flows I, Springer, Berlin, 1979, pp. 386-401.

Meijer, C. (1685). "L'arte di restituire a roma la tralasciata nauigatione del suo teuere." In Roma: Stamperia del Lazari Varese.

Melville, B. W. (1997). "Pier and abutment scour: integrated approach." Journal of Hydraulic Engineering, Vol. 123, No. 2, 125-136.

Miller, R., Roulund, A., Sumer, B., Fredsoe, J., Truelsen, C., Michelsen, J. (2003). "3-d numerical modeling of flow around a groin." Proceedings of the 30th IAHR Congress, Thessaloniki, Greece, C: 385-392.

Moin, P. (2001). "Fundamentals of Engineering Numerical Analysis." Cambridge University Press.

Moin, P., Squires, K., Cabot, W., and Lee, S. (1991). "A dynamic subgrid-scale model for compressible turbulence and scalar transport." Phys. Fluids A3, 2746-2757.

Muppidi, S. and Mahesh, K. (2005a). "Study of trajectories of jets in cross flow using numerical simulations." J. Fluid Mech. 530, 81-100.

Muppidi, S. and Mahesh, K. (2005b). "Direct numerical simulation of round turbulent jets in cross flow." Journal of Fluid Mechanics (2005b), in review.

Muto, Y., Baba, Y., and Fujita, I. (2002). "Velocity measurements in rectangular embayments attached to a straight open channel." Proceedings of River Flow 2002, Louvain-la-Neuve, Belgium, 1213-1219.

Neill, C. R., and Yalin, M. S. (1969). ''Qualitative definition of beginning of bed movement.'' Journal of the Hydraulics Division, ASCE 95, 585–587.

Nezu, I., Onitsuka, K., and Yano, M. (2002). "PIV measurements in side-cavity open-channel flows with and without sediment transport." Proceedings from the 10th International Symposium on Flow Visualization, Kyoto, Japan, 2002.

Ohmoto, T. and Hirakawa, R. (2003). "Effects of water surface oscillations on flow characteristics in open channel with spur dikes." Proceedings of the 30th IAHR Congress, Thessaloniki, Greece, Theme C, 401-408.

Ouillon, S. and Dartus, D. (1997). "Three-dimensional computation of flow around a groyne." Journal of Hydraulic Engineering, Vol. 123, No. 11, 962-970.

Papanicolaou, A.N., Diplas, P., Evaggelopoulos, N., and Fotopoulos, S. (2002). "Stochastic incipient motion criterion for spheres under various bed packing conditions." Journal of Hydraulic Engineering, 128(4), 369-380.

Peng, J., and Kawahara, Y. (1997). "Numerical simulation of flow in river with spur dikes." Collected Papers of River and Environmental Engineering Laboratory, University of Tokyo, 1997, 88-89.

Peng, J., Kawahara, Y., and Huang, G. (1999a). "Evaluation of modified k-e models in simulating 3d flows over submerged spur dikes." Turbulence and Shear Flow - 1, First International Symposium, Banerjee and Eaton, Editors, Santa Barbara, CA.

Peng, J., Tamai, N., Kawahara, Y., and Huang, G. (1999b). "Numerical modeling of local scour around spur dikes." Proceedings of the 28th IAHR Congress, Graz, Austria.

Pierce, C. D. and Moin, P. (2001). "Progress-variable approach for large-eddy simulation of turbulent combustion." Mech. Eng. Dept. Rep. TF-80, Stanford University.

Rajaratnam, N. and Nwachukwu, B. (1983). "Flow near groin-like structures." Journal of Hydraulic Engineering, Vol. 109, No. 3, 463-479.

Reynolds, C.S. (1988). "Potomoplankton: paradigms, paradoxes, prognoses," in Algae and Aquatic Environment, Biopress, Bristol, 285-311.

Shvidchenko, A.B. and Pender, G. (2000). "Flume study of the effect of relative depth on the incipient motion of coarse uniform sediments." Water Resources Research 36(2), 619-628.

Scott, S., Jia, Y., and Wang, S. (2001). "3d numerical simulation of flow in Mississippi River and validation using field data." Proceedings from 29th Congress of IAHR. Beijing, China.

Shields, F., Cooper, C., and Knight, S. (1995). "Experiment in stream restoration." Journal of Hydraulic Engineering, Vol. 121, No. 6, 494-502.

Shields, F., Knight, S., and Cooper, C. (1994). "Effects of channel incision on base flow stream habitats and fishes." Environmental Management, Vol. 18, No. 1, 43-57.

Shields, F., and Cooper, C. (1997). "Stream habitat restoration using spurs added to stone toe protection." Proceedings of the Conference on Management of Landscapes Disturbed by Channel Incision, 667-672.

Skelnar, P. (2002). "Evaluation of flow resistance in a straight channel with a group of spur structures." Proceedings of River Flow 2002, Louvain-la-Neuve, Belgium, 385-393.

Simpson, R.L. (2001). "Junction flows." Annual Review of Fluid Mechanics, 33, 415-443.

Strayer, D. L., Downing, J.A., Wendell, R.H., King, T.L., Layzer, J.B., Newton, T.J., Nichols, J.S. (2004). "Changing Perspectives on Pearly Mussels, North America's Most Imperiled Animals." BioScience. Vol. 54. No. 429, 429-439.

Sukhodolov A., Uijttewaal W.S.J., and Engelhardt C. (2002). "On the correspondence between morphological and hydrodynamical patterns of groyne fields." Earth Surface Processes and Landforms Vol. 27, 289-305.

Sukhodolov, A., Engelhardt, C., Kruger, A., and Bungartz, H. (2004). "Case study: turbulent flow and sediment distributions in a groyne field." Journal of Hydraulic Engineering, Vol. 130, No. 1, 1-9.

Tamai, N., Kawahara, Y., Aoki, M. Matumoto, A., Ishikawa, Y., Yasuda, M. (1996). "Ecohydraulics of spur dikes in Ushizu River, Kyushu Region, Japan." Proceedings from the 2nd International Symposium on Habitat Hydraulics, Quebec, Canada, Volume B, 631-542.

Tokyay, T. and Constantinescu, S.G. (2005a). "Coherent structures in pump intake flows: A Large Eddy Simulation study." XXXIst International Association Hydraulic Research Congress, Seoul, Korea, September 2005.

Tokyay, T. and Constantinescu, S.G. (2005b). "Large Eddy Simulation and Reynolds Averaged Navier Stokes Simulations of flow in a realistic pump intake: A

validation study." World Water and Environmental Resources Congress, Alaska, May 2005.

Tokyay, T. and Constantinescu, S.G. (2006). "Validation of a large eddy simulation model to simulate flow in pump intakes of realistic geometry." Accepted for publication in J. Hydraul. Engrg.

Tominaga, A., Nakano, Y., and Fujita, T. (2000). "Visualization analysis of flow structures in submerged spur dikes." Annual Journal of Hydraulic Engineering, Vol. 44, 1041-1045.

Tominaga, A., Ijima, K., and Nakano, Y. (2001a). "Flow structures around submerged spur dikes with various relative height." Proceedings of the 29th IAHR Congress, Beijing, China.

Tominaga, A., Ijima, K., and Nakano, Y. (2001b). "PIV analysis of flow structures around skewed spur dikes." Annual Journal of Hydraulic Engineering, Vol. 45, 379-381.

Uijttewall, W. (2005). "Effects of groyne layout on the flow in groyne fields: laboratory experiments." Journal of Hydraulic Engineering, Vol. 131, No. 9, 782-791.

Uijttewaal, W., Lehmann, D., van Mazijk, A. (2001). "Exchange processes between a river and its groyne fields: model experiments." Journal of Hydraulic Engineering, Vol. 127, No. 11, 928-936.

Uijttewall, W. and van Schijndel, S.A.H. (2004). "The complex flow in groyne fields: numerical modeling compared with experiments." Proceedings of River Flow 2004, Naples, Italy, 1331-3838.

Van Haveren, B.P. Jackson, W. L. (1986). "Concepts in Stream Riparian Rehabilitation." Transactions 51st North American Wildlife and Natural Resources Conference.

Wallast, W., Uijttewaal, W., Van Mazijk, A. (1999). "Exchange processes between groyne field and main stream." Proceedings from the 28th IAHR Congress, Graz, Austria.

Wei, T., and Willmarth, W.W. (1989). "Reynolds-number effects on the structure of a turbulent channel flow." J. Fluid Mech., 204, 57-95.

Weitbrecht, V. and Jirka, G. (2001a). "Flow patterns and exchange processes in dead zones of rivers." Proceedings of the 29th IAHR Congress, Beijing, China, 2001, 439-445.

Weitbrecht, V. and Jirka, G. (2001b). “Flow patterns in dead zones of rivers and their effect on exchange processes.” Proceedings of the 2001 International Symposium on Environmental Hydraulics.

Weitbrecht, V., Kuhn, G., and Jirka, G. (2002). “Large scale PIV-measurements at the surface of shallow water flows.” Flow Measurement and Instrumentation, Volume 13. 237-245.

Weitbrecht, V., Uijttewaal, W. and Jirka, G.H. (2003). “2d particle tracking to determine transport characteristics in rivers with dead zones.” Proceedings Int. Symp. Shallow Flows, Delft, The Netherlands. Vol. II, 103-110.

Xu, Y., Wang, S., and Jia, Y. (2002). “Numerical simulation of the three-dimensional flow structure around submerged dikes.” Proceedings of the International Conference on Hydroscience and Engineering, Warsaw, Poland, 2002.

Yossef, M., Klaassen, G. (2002). “Reproduction of groynes-induced river bed morphology using LES in a 2-d morphological model.” Proceedings from River Flow 2002, Louvain-la-Neuve, Belgium, 1099-1108.

Yossef, M. and Uijttewall, W. (2003). “On the dynamics of the flow near groynes in the context of morphological modelling.” Proceedings of the 30th IAHR Congress, Thessaloniki, Greece, Theme C, 361-368.

Young, N. (2005). “Characterizing mussel habitats using field measurements and hydrodynamic simulation.” Ph.D Dissertation, The University of Iowa, IIHR-Hydroscience and Engineering.